Methods for the Monitoring of Peroxy Radicals and Measurement of NO_2 Photolysis in the Atmosphere

Robert Vernon Gladstone

A thesis submitted for the degree of

Doctor of Philosophy

Department of Chemistry

University of York

March 1995

"If you know the enemy and know yourself, you need not fear the result of one hundred battles. If you know yourself but not the enemy, for every victory gained you will also suffer a defeat. If you know neither the enemy nor yourself, you will succumb in every battle."

<div align="right">

Sun Tzŭ, 500BC [*Tzŭ*, 1990]

</div>

"The secret to happiness is short-term, stupid self-interest!"

<div align="right">

Calvin, 1993 [*Waterson*, 1993]

</div>

Abstract

Chemical amplification, which has been investigated as a method for detecting atmospheric peroxy radicals is based on the following chain reaction, where RH is an organic species:

$$HO_2 + NO \rightarrow OH + NO_2 \qquad (1)$$

$$OH + RH \rightarrow R + H_2O \qquad (2)$$

$$R + O_2 \rightarrow RO_2 \qquad (3)$$

Previous work has used carbon monoxide (CO) as a chain carrier, although larger chain lengths, and thus greater sensitivity, can be a expected for certain organic species. This is predicted by faster rates for reaction (3) that would reduce the influence of chain termination reactions, and more complex secondary chemistry, that could yield more than one peroxy radical for each cycle of the chain.

The experimental work used dimethyl ether (DME) as the chain carrier, as well as CO for comparison, while radicals were generated by the photolysis of ethanal in the presence of oxygen. Under identical conditions DME gave a chain length (1400) almost three times that of CO (475). The responses of the system to the initial concentration of NO (0.6-10pmm), and to the duration of the photolysis (1-25ms) were also investigated. It was found that, over the range of concentrations investigated, greater concentrations of NO gave longer chain lengths although longer photolysis periods produced shorter chain lengths.

Computer models used to simulate the chemistry were found to closely reproduce the experimental data. In addition, models were constructed for several other organic species; ethene, propene, ethanol and ethyne. Using these models, all six compounds were examined for their responses to reactor conditions and interference from pollutants, such as ozone, peroxyacetyl nitrate (PAN) and peroxynitric acid (PNA). While the alkenes gave consistently higher chain lengths under pollutant-free conditions, they were also the most susceptible to interferences. The best combination of high chain length, and low interference was shown by DME.

In addition, the photolysis of NO_2 in the presence of 2-butyne ($CH_3C{\equiv}CH_3$) was investigated, as a means of simplifying the measurement of the ambient NO_2 photolysis rate. If the concentration of 2-butyne is chosen correctly, all the $O(^3P)$ produced by the photolysis reacts with it, rather than with more NO_2.

Contents

Acknowledgments

I would like to sincerely thank my supervisor, Dr. Chris Anastasi, for his constant advice and support during the course of my studies. Also, thanks go to Terry Chamberlain, Clive Brookes, Roy Noakes and Brian Smith for the vital work done to keep everything working, despite my best efforts.

In addition, the help, advice and friendship of the other members of the Gas Kinetics Group has been a constant aid. In particular I would like to thank Moray Stark, Mike Sanderson, Gary Knight, Debbie Bird, Adam Heathfield and John Busby for their invaluable support.

Finally, I would like to thank the instructors and staff of the University of York Karate Club, without whom this would not have been completed.

Declaration

The work contained in this thesis is entirely my own, with the following exceptions:

The chemical models used in this work, with the exception of the nitrogen dioxide and ethanal models, were developed by *Sanderson* [1994]. The two exceptions are my own work.

The preliminary nitrogen dioxide photolysis measurements in Chapter 5 were performed by *Vipond* under my supervision.

Some of the work contained herein has been the subject of a journal publication [*Anastasi et al.* 1993].

Glossary

A-D	Analogue to Digital
CL	Chain Length
DP	Discriminating Power
I/O	Input/Output
LIF	Laser-induced fluorescence
MMS	Molecular Modulation Spectrometer
PM tube	Photomultiplier tube
ppm	part per million by volume (1×10^{-6})
ppb	part per billion by volume (1×10^{-9})
ppt	part per trillion by volume (1×10^{-12})
UV	Ultraviolet
hυ	light
λ	wavelength
[species]	concentration of a species

Introduction

1.1   Basic Atmospheric Chemistry

The work described here is a study of one aspect of the phenomenon of Photochemical Air Pollution (PAP).   There are many, complex aspects to this problem, but it is important to begin with a few simple definitions. Air pollution in general is described by *Butler* [1979] as:

> "The presence in breathable air of chemical elements or compounds
> in sufficient quantity to constitute injury to health or life over short or
> long time periods."

This is a reasonable, though limited definition. The air of the upper atmosphere is not breathable, not only because of its distance from the surface of the Earth, but because it contains insufficient oxygen. As will be discussed later, however, the presence of Man-made chemicals in this region is believed to result in the depletion of ozone, which may then allow greater quantities of harmful ultraviolet (UV) radiation to reach the surface. Thus, the presence of chemicals in non-breathable air can also result in deleterious effects.

Bearing this in mind, perhaps a better idea can be obtained from the definition of a pollutant provided by *Manahan* [1991]:

> "...a pollutant is a substance present in greater than natural
> concentration as a result of human activity and having a net
> detrimental effect upon its environment or upon something of value
> in that environment."

As such, this definition distinguishes between a pollutant and a contaminant, which is a substance whose abundance is greater than natural, but which has no harmful effects. It should be noted that the "detrimental effect" need not be of a definite physical nature. The existence of a malodour, say from a sewage treatment plant, though not actually damaging, causes a reduction in 'quality of life' and as such, is pollution.

The general emphases of these definitions are, however, the same: that human activity can result in the environment containing sufficient quantities of materials that cause harm. The time scale can vary widely: dense smoke from cigarettes can cause eye irritation in a matter of seconds, while inhaled asbestos dust accumulates in lungs over many years before any ill effects are felt. Nor need the harm be to humans, the damage to animals and plants is also of great concern.

1.1.1 Air Pollution in the Past

Although the problem of air pollution has only come to prominence in the last thirty years, it would be a mistake to think it was a new phenomenon. The blue haze of the Smokey Mountains, although purely natural in origin and therefore not pollution by the definitions above, is believed to involve the same kind of chemical reactions as the anthropogenic photochemical pollution of urban environments [*Wayne*, 1991]. While eye irritation became a serious problem in Los Angeles after the Second World War, it was first reported there in 1868 [*Wayne*, 1991].

The first cause of air pollution was the burning of wood, and other biomass, as fuel. In fact, the combustion of organic material is still arguably the largest source of air pollution. Now, however, it is the use of fossil fuels that is the greatest concern.

The arrival of the industrial revolution and the switch from wood to coal as the main fuel brought more significant pollution. The smoke from wood contains mainly organic compounds, while coal usually has a high sulphur content. Consequently,

the smoke from burning coal has much higher levels of sulphur oxides, including sulphur dioxide, SO_2. These are highly soluble in water, where they can form sulphurous and sulphuric acids.

The combination of sulphurous smoke and fog results in what is known as smog (an acronym from SMoke and fOG), the thick 'pea-soupers' that, although once common in large cities, are always associated with London. Fogs are usually formed in very still air, with little vertical mixing so the smoke and sulphur compounds are trapped close to the ground, producing a very acidic mix, sometimes with a pH as low as 2 [*Finlayson-Pitts and Pitts*, 1986]. These smogs were harmful not only because of their acidity, but also because of the much reduced visibility that accompanied them. It was not uncommon for visibility to be only a few feet, and the number of accidents that occurred during smogs rose as visibility decreased.

The most infamous smog incident occurred in London in 1952. It lasted for five days and is thought to have been responsible for around 4000 deaths, mainly among the young and elderly. The Clean Air Act (1952) was introduced as a consequence of such episodes and aimed to prevent their re-occurrence. Although the still air and fog were essentially natural, on their own they cause only a minor hazard due to the reduction in visibility. By controlling the use of fuels, particularly coal, in urban regions the quantities of two of the major ingredients, smoke and sulphur compounds, were eventually reduced and the occurrence of sulphurous smogs greatly reduced. Today, they no longer occur.

Confusion can arise over what is meant by the word smog. The word was originally used to refer to the kind of pollution episodes described above but has also come to be used for an entirely different form of pollution. Photochemical air pollution, which is the focus of this work, can and does occur in the absence of fog, and is chemically very different from the sulphurous smog. Its principal cause is the photochemically initiated degradation of hydrocarbons, typically unburned fuel in motor vehicle exhausts, in the presence of nitrogen oxides. The only features it has in common with the sulphurous smogs are that it requires the burning of fuel for its

source of materials, and that it needs a stable air mass with little vertical mixing to concentrate the pollutants close to the ground. The details of the chemistry involved in the formation of this smog will be discussed in detail in section 1.1.5 below.

Photochemical air pollution was first recognised as a problem in the Los Angeles area after the Second World War, although it is likely that it had occurred to lesser degrees prior to that. The topographical and meteorological features of the area, combined with the widespread use of cars, served to create conditions that favoured PAP. Los Angeles is surrounded on three sides by the San Bernadino mountains with the Pacific Ocean on the fourth. Breezes blow off the ocean onto the land and are trapped by the mountains, thus forming a stable mass of air. The intense sunlight of the region initiates the photochemistry and the unburned fuel trapped in the air mass is oxidized. While the primary pollutants, those actually emitted to the atmosphere, are frequently not harmful in the concentrations encountered, their secondary and tertiary degradation products, for example ozone, aldehydes and peroxynitrates, can be very damaging.

The result is often referred to as photochemical smog, but it is also known by the location where it was first characterised. Hence it can be referred to as 'Los Angeles smog' while the sulphurous smogs formed by coal burning are called 'London smog', though once again, this can be misleading as photochemical smogs are not uncommon in London and many other cities. They are also not limited just to city areas, so called 'European smogs' can extend over entire countries and are formed when anticyclones that can cover a quarter of Europe trap the pollution from the heavily industrialised region.

Before considering the details of the chemistry involved in photochemical smog formation, it may be useful to spend some time considering the general structure of the atmosphere, and some of the other problems effecting it.

1.1.2 The Structure of the Atmosphere

The Earth's atmosphere is vertically divided into distinct regions, each characterised by different physical and chemical processes. The two regions most commonly of interest to the atmospheric chemist are the troposphere, the region from the surface to a height which varies from around 11 to 15km, and the stratosphere which extends from the top of the troposphere to around 50km [*Finlayson-Pitts and Pitts*, 1986].

The stratosphere, as its name suggests, is characterised by a very layered structure. The temperature at its lowest altitude is around 220K and this rises to around 275K at the top. Because the cold, more dense, air is below the warmer air there is very little vertical mixing, and hence the layered structure. The other principal feature of the stratosphere is the existence of very strong horizontal winds that result in very fast mixing within each layer.

Between 15 and 30km, the stratosphere contains high concentrations of ozone. The UV radiation incident on the atmosphere photolyses molecular oxygen:

$$O_2 + h\upsilon \ (\lambda < 230nm) \rightarrow 2 \ O \qquad\qquad 1.1$$

The O atom produced can then react with more oxygen to form ozone:

$$O + O_2 \ (+M) \rightarrow O_3 \ (+M) \qquad\qquad 1.2$$

where M is an inert third body. A cycle, known as the Chapman cycle, is completed by the photolysis of ozone by longer wavelength radiation [*Turco*, 1975], and the reaction of the O atom with ozone itself:

$$O_3 + h\upsilon \ (\lambda < 1180nm) \rightarrow O(^3P) + O_2 \qquad\qquad 1.3$$
$$O_3 + h\upsilon \ (\lambda < 310nm) \rightarrow O(^1D) + O_2 \qquad\qquad 1.4$$
$$O + O_3 \rightarrow 2 \ O_2 \qquad\qquad 1.5$$
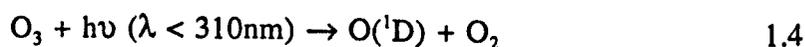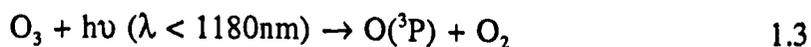
The trapping of radiation by molecular oxygen and ozone is the cause of the heating through the stratosphere, and also serves to filter out effectively all the incident radiation of wavelength less than 290nm which would be damaging if it reached the surface. Radiation with wavelengths less than around 300nm can cause skin cancers and cataracts in humans and animals, and can damage the chloroplasts in vegetation.

The troposphere contains 90% of the mass of the entire atmosphere and is the most chemically diverse region. Almost all the emissions of trace gases into the atmosphere occur in the boundary layer (up to approximately 1000m) of the troposphere, and it is this region of the atmosphere that has the most direct effect on the biosphere.

The air in the troposphere is largely transparent to UV (with $\lambda > 290$nm) and visible radiation from the Sun so this passes through and is absorbed or reflected by the surface. Some of this radiation is then re-emitted from the surface at longer wavelengths that can be absorbed by species in the atmosphere, primarily water vapour and carbon dioxide (CO_2) [*Wayne*, 1991]. Consequently, the air close to the surface is warmed and is at a higher temperature than the air in the upper troposphere. This gives rise to convection currents which mean that, in contrast to the stratosphere, the troposphere is vertically well mixed.

Topographical and surface conditions in the troposphere mean that the extent of the radiative heating can vary over much shorter distances than in the stratosphere so horizontal mixing by wind is more localised. Solar radiation with wavelengths greater than 338nm is not absorbed in the troposphere, but it can be scattered. The shorter the path the incident radiation has between the top of the atmosphere and the surface, the less absorption in the stratosphere and the less scattering in the troposphere can occur, and the stronger the heating at the surface. Consequently, the regions where the Sun is overhead, around the Equator, are heated more strongly than those at higher latitudes, where the Sun is at a more oblique angle, and thus the strongest convection currents arise around the Equator.

As the air from the Equatorial regions rises it cools and expands, spreading north and south as it does so. Eventually it cools sufficiently to begin falling again, around the mid-latitudes, resulting in constant circulation patterns of air known as Hadley cells. One of the effects of this circulation is that winds tend to blow toward, rather than across, the Equator, leading to poor atmospheric mixing between the northern and southern hemispheres.

1.1.3 Meteorology

The above section has given a brief indication of how large-scale atmospheric conditions can effect the make-up of the troposphere and stratosphere. In this section, the effect of meteorology on the chemistry of the troposphere will be considered.

Clouds have a profound effect on the processes of the troposphere. Their most apparent role is that of shielding the planet's surface from the Sun's light, the familiar shade of a cloud passing overhead. It is, not surprisingly, too simplistic to say that clouds block out the light from the Sun; what it they do is scatter radiation in all directions. Incident solar radiation is scattered, preventing heating at the Earth's surface, but outgoing heat is also scattered and so reduces cooling. Hence the cloudless skies above deserts provide both maximum insolation and maximum radiation and so give rise to the extreme difference in temperature between day and night.

For those interested in tropospheric chemistry, it is the effect on the incident UV radiation that is of greater interest than the temperature changes. Cloud cover reduces the amount of radiation that reaches the boundary layer and so reduces the generation of for example, OH radicals [*Spinherne and Greene*, 1978; *Demerjian et al.*, 1980; *Madronich*, 1987]. Interestingly, within the cloud itself, photolysis rate coefficients can actually exceed their clear-sky equivalents [*Madronich*, 1987].

The other major influence of clouds on tropospheric chemistry is that they provide an aqueous environment for reactions to take place. This is of particular importance to the degradation processes of sulphur compounds in the atmosphere. Sulphur dioxide, SO_2, is highly soluble in water droplets where it is hydrolysed to sulphuric acid, H_2SO_4. Also, reaction rates may vary between vapour and aqueous environments, and if this is not properly accounted for, models of atmospheric processes may yield inaccurate results.

Dissolution into water droplets, and subsequent deposition on the Earth's surface through precipitation ('wet deposition') is one of the principle processes through which materials are transferred from the atmosphere to the biosphere. The chain processes described below oxidise the reduced or partially oxidised species emitted into the atmosphere, and so increase their solubility in water.

The presence of aerosols is central to the formation of clouds. These small particles provide condensation nuclei around which water droplets can form. Without them, cloud formation would be very difficult as it would require a degree of supersaturation that is greater than that normally reached [Wayne, 1991].

This nucleation effect is another reason why the sulphurous 'London' smogs were so dense. The soot from the coal fires, and indeed sulphur compounds themselves, make excellent condensation nuclei and so promoted the formation of the fog.

The final aspect of meteorology to be considered is responsible for trapping pollutants close to the ground and so preventing their dispersion. The normal temperature profile of the troposphere shows that temperature falls with altitude and thus allows vertical convection currents. Temperature inversions occur where the temperature begins to fall as the altitude increases but then warms again higher up before beginning to re-cool, as associated with large-scale meteorological conditions. The result is a warmer, less dense region above a colder, more dense one. Convection currents cannot then mix the two air masses and the lower one is 'trapped'.

Inversions can be formed by very rapid radiative cooling of the surface or by the passage of a warm air mass over a region of cold air. In the case of Los Angeles the cool breezes that blow off the Pacific Ocean are trapped under the warmer air of the land, in effect putting a lid on the box formed by the surrounding mountains. The steady emission of pollutants into this still air, from traffic, power generation and industry, can result in concentrations of the primary pollutants significantly higher than those normally encountered.

1.1.4   Atmospheric Pollution Phenomena

In addition to photochemical air pollution and the now rare 'London smog', there are three major atmospheric concerns: acid rain, stratospheric ozone depletion, and global warming. These will now be considered very briefly.

Acid rain is a phenomenon largely confined to the northern hemisphere. It is a result of the burning of fossil fuels releasing nitrogen and sulphur oxides into the troposphere. In clouds these are ultimately converted to nitric and sulphuric acids, lowering the pH of the rainwater from the clouds. This been blamed for the destruction of Scandinavian and North American lakes and forests.

Acid rain neatly illustrates many of the problems associated with attempting to address atmospheric pollution problems. Both the nitrogen and sulphur compounds have significant natural sources so acid rain is not an entirely Man-made feature. The problems arise from human perturbations to the natural system.

The effect of the acidic rainfall is exacerbated by local conditions. In the regions most affected the local bedrock is of a granitic nature which is unable to buffer the local water. In limestone regions the acid can be buffered by the bedrock. The most apparently simple solution would be to add lime to the affected areas to neutralise the acid artificially. However, the scale and cost of such an operation would be prohibitive, it would not provide a long-term solution and the addition of further material to an already polluted region would be unpopular with the general public.

The final, and perhaps biggest, problem is that the combustion that adds the nitrogen and sulphur to the atmosphere, and so causes the acid rain, often takes place in a different country to that in which the rain falls. Britain was largely held responsible for the destruction of the Scandinavian lakes and forests, with other European countries also being blamed. Thus, national interests and politics are added to an already complicated chemical system.

As mentioned earlier in this chapter, the stratospheric cycling of oxygen between molecular oxygen (O_2) and ozone (O_3) absorbs UV radiation which would otherwise be harmful to life on the surface. However, the presence in the stratosphere of several man-made pollutants is upsetting the balance of the Chapman cycle.

Most pollutants emitted at the surface of the planet do not survive long enough to be transported into the stratosphere. However, some species, and in particular the chlorofluorcarbons (CFCs) and nitrous oxide (N_2O), are sufficiently chemically inert to survive degradation in the troposphere. In the stratosphere, they are photolysed by the UV radiation and form radical species that destroy ozone catalytically. The reaction chains shown below are greatly simplified and are for illustration only.

$$CF_2Cl_2 + h\upsilon \rightarrow Cl + CF_2Cl \qquad 1.6$$

$$Cl + O_3 \rightarrow ClO + O_2 \qquad 1.7$$

$$ClO + O \rightarrow Cl + O_2 \qquad 1.8$$

and:

$$N_2O + h\upsilon \rightarrow O + NO \qquad 1.9$$

$$NO + O_3 \rightarrow NO_2 + O_2 \qquad 1.10$$

$$NO_2 + O \rightarrow NO + O_2 \qquad 1.11$$

Although mean ozone levels have been dropping by around 3% each decade since 1970 [*WMO*, 1991], the decline was originally only noticeable above the Antarctic where the weather conditions amplified the effect. Increasingly, reductions in the amount of stratospheric ozone are also being found in the northern hemisphere [*WMO*, 1991].

As indicated earlier, some trace gases in the troposphere absorb radiation emitted by the surface and so warm the atmosphere. Without this warming, known as the 'Greenhouse Effect', the average temperature of the Earth's surface would be around 253K, approximately 30K cooler than it is now. There is growing concern that the build up in the troposphere of trace gases will increase the amount of heat trapped and so upset the Earth's radiation balance.

Most of the attention is focused on carbon dioxide, CO_2, because fossil fuel combustion is increasing its atmospheric loading by 0.4% each year [*Houghton et al.*, 1992]. The other species considered important are methane, nitrous oxide and the chlorofluorocarbons. The concentrations of these molecules are also increasing steadily and their infrared absorption coefficients are often larger than those of CO_2. The CFCs may well become the centre of attention in the future because they absorb in an atmospheric 'window' region, a part of the Earth's emission spectrum where, at present, little atmospheric absorption occurs.

The consequences of the build up of the so called 'Greenhouse Gases' are far from certain. Indeed, the existence of a problem is still disputed. Models have been used to try to establish future concentrations which can then be used in other models to predict their effects. Some consensus has been reached, e.g. that the pre-industrial revolution concentration of CO_2 (260ppm) will be doubled by around the middle of the 21st century. By the middle of the next century, the average global temperature is expected to rise by between 2K and 6K, resulting in the melting, to some extent, of polar icecaps and a rise in sea levels. The world's climatic zones are also expected to shift [*Houghton et al.*, 1992].

While such changes in temperature have occurred before in the planet's history, it is unlikely that they have done so over the short space of time anticipated. What effects such changes will have on the planet's ecosystems are unknown, but they are likely to be extensive.

Although the above discussion treats these phenomena as isolated and independent of each other, it should be apparent that this is not the case. The absorption of radiation in the stratosphere affects the chemistry of the troposphere, while the chemistry of the troposphere determines the atmospheric lifetimes of trace species, and hence the chemical content of the stratosphere. 'Greenhouse Gases' are often also involved in the chemistry of the troposphere.

1.1.5   The Tropospheric Chemistry of Peroxy and Oxy Radicals

During daylight hours, the hydroxy radical (OH) is the predominant oxidant in the troposphere. It initiates oxidation chains that ultimately degrade most trace species in the troposphere to CO_2 and H_2O.

The sole primary source of OH in the troposphere is via the photolysis of ozone, to produce $O(^1D)$. This tropospheric ozone accounts for 10% of the total atmospheric load and has two sources. In the higher troposphere, a small amount of mixing across the tropopause results in the transport of some stratospheric ozone into the troposphere. In the boundary layer above the Earth's surface the main source of ozone is via the photolysis of NO_2:

$$NO_2 + h\upsilon \ (\lambda < 420nm) \rightarrow O(^3P) + NO \qquad 1.12$$

$$O(^3P) + O_2 \ (+M) \rightarrow O_3 \ (+M) \qquad 1.2$$
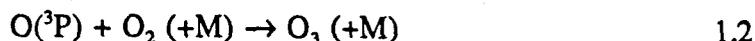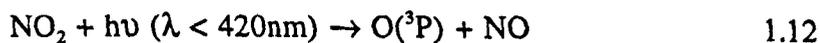
Stratospheric ozone does not completely shield the troposphere from UV radiation and consequently some photolysis of low lying ozone does occur:

$$O_3 + h\upsilon \ (\lambda < 310nm) \rightarrow O(^1D) + O_2 \qquad 1.4$$
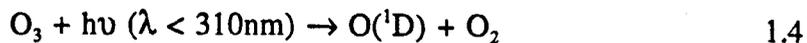
Most of the $O(^1D)$ formed is quenched to the ground state, $O(^3P)$, through collision with an inert body (M), primarily nitrogen or oxygen:

$$O(^1D) \ (+ M) \rightarrow O(^3P) \ (+ M) \qquad 1.13$$
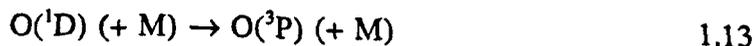
However, some reacts with water vapour to give OH:

$$O(^1D) + H_2O \rightarrow 2\ OH \qquad\qquad 1.14$$

Because of their relative abundance, reactions with CO and CH_4 consume most of the OH:

$$OH + CO\ (+M) \rightarrow H + CO_2\ (+M) \qquad\qquad 1.15$$
$$OH + CH_4 \rightarrow H_2O + CH_3 \qquad\qquad 1.16$$
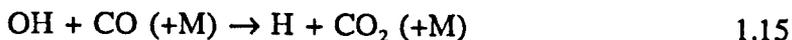
In a 'clean', unpolluted environment CO and CH_4 would account for approximately 70% and 30% of the OH respectively [*Wayne*, 1991]. The radical products, H and CH_3, combine with the oxygen in the atmosphere to form peroxy radicals:

$$H + O_2\ (+M) \rightarrow HO_2\ (+M) \qquad\qquad 1.17$$
$$CH_3 + O_2\ (+M) \rightarrow CH_3O_2\ (+M) \qquad\qquad 1.18$$
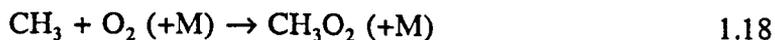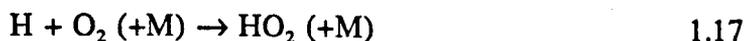
In the absence of nitrogen oxides, the primary fate of the peroxy radicals is their reaction with each other:

$$CH_3O_2 + HO_2 \rightarrow CH_3OOH + O_2 \qquad\qquad 1.19$$
$$HO_2 + HO_2 \rightarrow H_2O_2 + O_2 \qquad\qquad 1.20$$
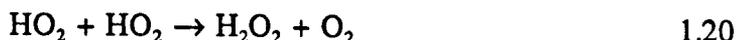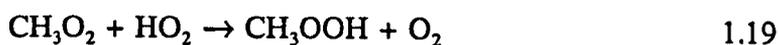
Both CH_3OOH and H_2O_2 are water soluble and, therefore, can act as sinks for the radicals through rainout. However, they are also both photolabile, and so can reform oxy radicals.

When NO is present, the chemistry changes. The peroxy radicals can react with the NO:

$$HO_2 + NO \rightarrow OH + NO_2 \qquad\qquad 1.21$$
$$CH_3O_2 + NO \rightarrow CH_3O + NO_2 \qquad\qquad 1.22$$

These are very important reactions as they convert NO to NO_2 while regenerating the oxy radicals. As has already been mentioned, the photolysis of NO_2 is the principal source of ozone, and consequently OH, in the troposphere. Generally, therefore, as the concentration of NO_2 increases, so does the concentration of OH.

The methoxy radical, CH_3O, formed in reaction 1.22 combines with molecular oxygen to generate more hydroperoxy radicals, and methanal:

$$CH_3O + O_2 \rightarrow HO_2 + HCHO \qquad\qquad 1.23$$

At first sight the methanal appears to be a stable product, but in fact, is itself photolabile at wavelengths available in the troposphere, and can therefore also generate more hydroperoxy radicals:

$$HCHO + h\upsilon \ (\lambda < 338nm) \rightarrow H + CHO \qquad\qquad 1.24$$
$$CHO + O_2 \rightarrow CO + HO_2 \qquad\qquad 1.25$$

Thus, the presence of nitrogen oxides is of crucial importance to the oxidation of trace gases in the air. The formation of OH depends on the photolysis of NO_2, while the recycling back to OH of the peroxy radical products of the OH reactions depends on NO. It is estimated that the average lifetime of HO_x (combination of OH and HO_2) is 45s, during which it will be cycled between OH and HO_2 five times [*Ehhalt*, 1994]. Each 'incarnation' of the OH radical is believed to last around 1s in the cleanest air, and around 1ms in the most polluted [*O'Brien and Hard*, 1993].

All the chemistry above occurs in unpolluted air, as the oxides of nitrogen have significant natural sources, such as anaerobic decay of biomass in soils, forest fires and electrical storms. On a global scale the contributions from natural and anthropogenic sources are approximately equal [*Houghton et al.*, 1992 and references therein]. However, on a smaller scale, humans can be responsible for 90% of the nitrogen oxides in industrial areas [*Houghton et al.*, 1992 and references therein].

In this environment, the relative concentrations of NO_x and O_3 are controlled by the following reactions:

$$NO_2 + h\upsilon \ (\lambda < 420nm) \rightarrow O(^3P) + NO \qquad 1.12$$

$$O(^3P) + O_2 \ (+M) \rightarrow O_3 \ (+M) \qquad 1.2$$

$$O_3 + NO \rightarrow NO_2 + O_2 \qquad 1.10$$
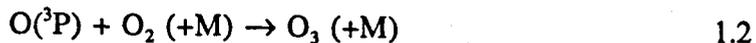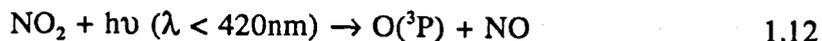
and are thus defined by the Photostationary State Equation:

$$[O_3] = \frac{J[NO_2]}{k[NO]}$$

where J is the photolysis rate constant for NO_2, and k is the rate constant for the reaction between NO and O_3.

Although NO_2 and ozone can both cause health problems in their own right [*Lippmann*, 1991], the concentrations encountered in 'clean' air are low enough to be effectively harmless. The main concerns arise when hydrocarbons are added to the mixture. The degradation chains initiated by OH, and maintained by HO_2 and NO_x can lead to the production of concentrations of ozone elevated to a level where they can cause damage, and also generate aldehydes and peroxynitrates which are more harmful. The chemistry involved in these chains is illustrated by the general scheme shown below.

$$RH + OH \rightarrow R + H_2O \qquad 1.26$$

$$R + O_2 \ (+M) \rightarrow RO_2 \ (+M) \qquad 1.27$$

$$RO_2 + NO \rightarrow RO + NO_2 \qquad 1.28$$

$$RO + O_2 \rightarrow R'CHO + HO_2 \qquad 1.29$$

$$R'CHO + OH \rightarrow R'CO + H_2O \qquad 1.30$$

$$R'CO + O_2 \ (+M) \rightarrow RCOO_2 \ (+M) \qquad 1.31$$

Peroxyacyl radical

15
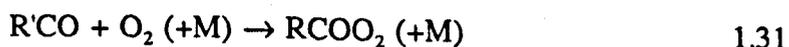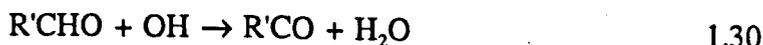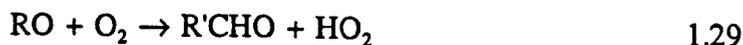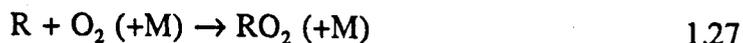
Peroxyacyl radicals can undergo the reaction with NO analogous to that of RO_2, but they can also add NO_2 to give $RCOO_2NO_2$. In the case of the peroxyacetyl radical, the most common of the peroxyacyl radicals, the product is peroxyacetyl nitrate, PAN, a strong lachrymator:

$$CH_3COO_2 + NO_2 \ (+M) \ \rightleftharpoons \ CH_3COO_2NO_2 \ (+M) \qquad 1.32$$

As a packet of air cools, the peroxyacyl radical and the NO_2 combine to form the stable adduct, which can survive for much longer than free NO_2, until the packet temperature rises and the NO_2 is released. Its importance in atmospheric chemistry, other than its harmful nature, is that this adduct provides a stable reservoir for NO_2, thereby allowing its transport into otherwise 'clean' areas.

Human activities are not the only source of hydrocarbons. Many plants also emit them and importantly they are often very reactive unsaturated compounds, such as terpenes. As well as the H abstraction shown above, unsaturated compounds can provide an alternative reaction route for OH, as it can add across a double bond:
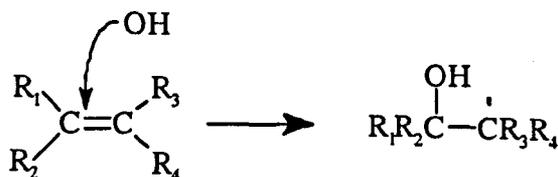
For the lower alkenes, such as ethene, this then will add O_2, as with an alkyl radical. The larger alkenes and other unsaturated compounds undergo fission at the site of the double bond before further reactions take place.

1.1.6 Summary

The discussion above has demonstrated the pivotal role of both alkoxy and hydroperoxy radicals (particularly OH and HO_2) radicals in the troposphere, and the importance of the chemistry of nitrogen oxides in their formation and propagation.

Summary of the important reactions involved in photochemical air pollution.

$$O_3 + h\nu\ (\lambda < 310nm) \longrightarrow O_2 + O(^1D) \xrightarrow{+M} O(^3P)$$

$$\downarrow + H_2O$$

$$OH + OH$$

$$+CO\diagup(+M) \quad \downarrow +RH \quad \diagdown +CH_4$$

$$HO_2 \xleftarrow{+O_2} H + CO_2 \qquad R + H_2O \qquad H_2O + CH_3 \xrightarrow{+O_2} CH_3O_2$$

$$NO \longrightarrow NO_2 \qquad\qquad \downarrow +O_2 \qquad\qquad NO \longrightarrow NO_2$$

$$\downarrow \qquad\qquad RO_2 \qquad\qquad\qquad CH_3O$$

$$OH \qquad NO \longrightarrow NO_2 \qquad O_2 \longrightarrow H_2O$$

$$RO \qquad\qquad\qquad HCHO$$

$$O_2 \longrightarrow HO_2 \qquad \downarrow + h\nu\ (\lambda < 338nm)$$

$$R'CHO \qquad\qquad H + HCO$$

$$OH \longrightarrow H_2O \qquad O_2 \longrightarrow HO_2$$

$$R'CO \qquad\qquad\qquad CO$$

$$\downarrow +O_2$$

$$R'CO.O_2 \underset{(+M)}{\overset{+NO_2}{\rightleftharpoons}} R'CO.O_2.NO_2$$

$$NO \longrightarrow NO_2$$

$$R'O_2$$
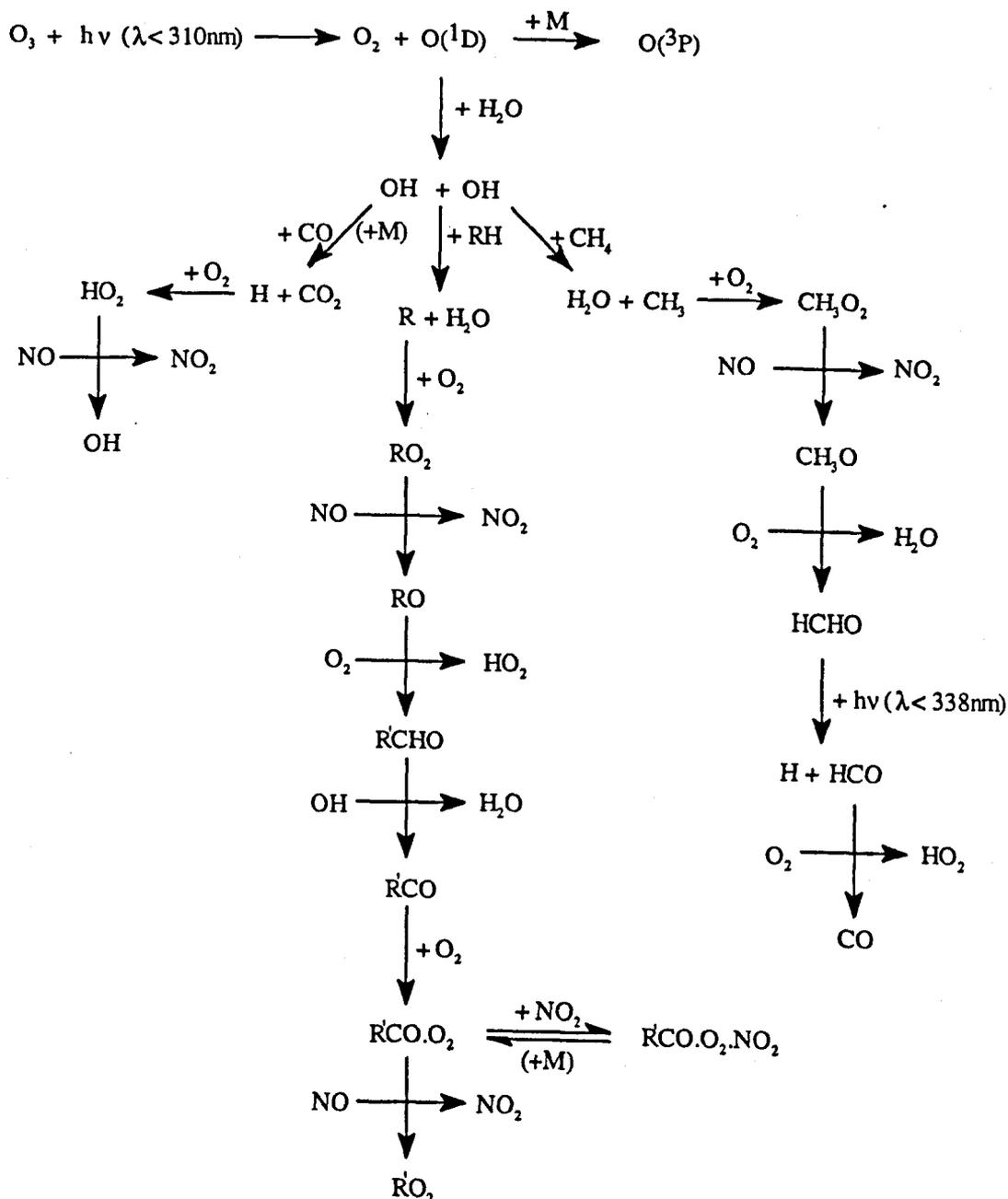
As these radicals are the primary daylight oxidants in the troposphere it is of vital importance to atmospheric sciences that their precise roles are understood. Laboratory studies can elucidate reaction mechanisms and rate constant data but it is also necessary to know the concentrations of these species that exist in the troposphere. In addition, the ability to measure, or predict, the photolysis rate of NO_2 would help in the accurate forecasting of the severity of photochemical air pollution, and thus allow the implementation of measures to alleviate such events.

As yet, there have been several attempts to determine radical concentrations, particularly OH, but the uncertainties involved are still significant. Neither has a method been developed that allows the accurate measurement of atmospheric photolysis rates to be made on a routine basis. Difficulties exist in both fields and in the following sections the work to date on these topics will be discussed.

1.2   Atmospheric Radical Monitoring

1.2.1   Overview

Most interest in monitoring of radicals in the atmosphere has, so far, focused on the detection of OH radicals. There are two basic methods that are under development for measuring OH concentrations, and these are spectroscopic analysis (including both absorption and fluorescence techniques) and chemical tracing. In addition, atmospheric modelling has been used to infer radical concentrations. Work on monitoring HO_2, the species of interest in the present study, has been less extensive, involving research into three main areas: far-infrared spectroscopy, matrix isolation followed by electron spin resonance spectroscopy, and chemical amplification. Methods that measure OH concentrations using an air stream sampling apparatus can also be used to measure HO_2, by adding excess NO to the sample to reduce the HO_2 present to OH before reaching the detector.

The main problems arise as a result of the very low concentrations involved. Most estimates for OH suggest that its tropospheric concentration is around 10^6 cm^{-3} [e.g. *Altshuller*, 1989 and *Eisele and Bradshaw*, 1993] so any reliable detection technique would require a limit of detection of around 10^5 cm^{-3}, a mixing ratio of 1 in 10^{14} [*Hoell et al.*, 1984]. The principal advantage in measuring HO_2 concentrations is that, while the role of HO_2 is also crucial in tropospheric trace gas oxidation, its mixing ratio is believed to be around 100 times greater than that of OH (around 10^8 cm^{-3} [e.g. *O'Brien and George*, 1992 and references therein, and *Cantrell et al.*, 1993]).

1.2.2   Laser-Induced Fluorescence of OH

In principle this is one of the simpler techniques attempted for the detection of OH and is one of the most studied [e.g. *Wang et al.*, 1975, 1981 and *Davis et al.*, 1976]. The OH radicals are excited from their ground state to a higher electronic state by absorption of radiation. The excited state then relaxes back to the ground state, radiating the excess energy. Because the excited state undergoes some rotational or vibrational relaxation before relaxing fully by radiation, the re-emitted energy is of a longer wavelength than that absorbed. Quenching of the fluorescence can occur when the excited state gives up the excess energy in a collision with another body.

In OH there are two excitation bands available with existing lasers, at 282nm and 308nm, both resulting in fluorescence around 309nm. The first attempts, using 282nm excitation, suffered serious interference problems from artificially generated OH. The excitation laser caused the production of $O(^1D)$ by the photolysis of ambient ozone. The subsequent reaction of the $O(^1D)$ with water vapour produced OH (reactions 1.4 and 1.14 above). Although much effort was put into solving this problem, [e.g. *Davis et al.*, 1981; *Wang and Davis*, 1982; and *Smith and Crosley*, 1990] it was concluded in 1987 that it was still not possible to make reliable OH measurements using LIF [*Beck et al.*, 1987]. Switching excitation sources to 308nm greatly reduced the artificial OH interference but made distinguishing between the fluorescence signal and scattering from the excitation laser much more difficult.

Two methods were developed in order to get around the problem. The first utilises sequential excitation of OH by two lasers, neither of which is capable of dissociating ambient ozone and so cannot generate artificial OH [*Bradshaw et al.*, 1984]. Theoretical work to date suggests that this technique has potential although sufficiently powerful lasers in the 1.4-2.9μm region are not available at present. An alternative method uses two lasers, one tuned to the excitation wavelength, 'on line' and one tuned close to it, 'off line'. The 'on line' laser generates an OH fluorescence signal, including interferences, while the 'off line' laser generates only the interferences. Subtraction of the of the 'off line' signal from the 'on line' signal yields

the genuine OH fluorescence. The pulses from the two lasers are timed to be around 500µs apart to ensure that they both sample the same air parcel. In tests a detection limit of 1×10^6 cm^{-3} was achieved with the system, although calibration has proved difficult [Rodgers et al., 1985].

The second method explored involved reducing the pressure of the sample, known as Fluorescence Assay with Gas Expansion (FAGE). It was reported that expanding a sample through a nozzle to reduce the pressure to around 6 mbar improved the sensitivity of the system [Hard et al., 1984]. Although the reduced pressure means that there is less OH in the excitation region, it also means that the fluorescence efficiency and lifetimes are increased. The increased lifetimes allow the potential use of delayed, gated detection to reduce the influence of scattered radiation. Discrimination against scattering is also improved as Raman, Rayleigh and Mie scattering are reduced proportionally with pressure. False signals from artificial OH are reduced because the reduced pressure slows the kinetics of the formation reactions: at the lower pressures it is harder for any $O(^1D)$ produced to collide with a water molecule before it relaxes or is quenched.

The claimed extent of this reduction in OH generation has been disputed [Shirinzadeh et al., 1987] but the system has been developed further [Hard et al., 1986, 1989, and Chan et al., 1990] and ambient measurements of both OH and HO$_2$ (following reduction by NO to OH) have been made recently [Hard et al., 1992a, 1992b]. The measured concentrations were 2.5-8 $\times 10^6$ cm^{-3} for OH and 1-2 $\times 10^8$ cm^{-3} for HO$_2$. The principal disadvantage of the FAGE system is that the passage of the sample through the nozzle may alter the concentration of radicals in the air stream.

The advantages of low sample pressure have been used by Wennberg et al. [1994] to monitor OH and HO$_2$ (following titration with NO) in the upper troposphere and lower stratosphere using fluorescence excited by a pulsed dye-laser at 282nm. The method appeared to work well, with signal-to-noise ratios of greater than thirty reported.

1.2.3 Absorption Techniques

An alternative spectroscopic technique to fluorescence is provided by ultraviolet (UV) absorption. Like the LIF idea, the principles involved are relatively simple. Radiation from a source of known intensity is passed through the sample vapour and the drop in intensity at wavelengths where the analyte absorbs is monitored. The concentration of the analyte is provided by the Beer-Lambert Law:

$$\text{Absorbance, } A = -\ln\left(\frac{I_t}{I_o}\right) = \sigma c d$$

where I_t is the transmitted radiation intensity, I_o is the incident intensity, σ is the absorption coefficient of the species at the desired wavelength, c is the concentration, and d is the path length of the radiation.

In studies of atmospheric radicals, the very low concentrations involved mean that path lengths have to be very long in order for a suitable absorption strength to be obtained. The light source, commonly a laser or powerful xenon lamp, and the detector are sited together, with a reflector over a kilometre away. Ozone formation is avoided by expanding the beam, so reducing the photon flux density.

In one method the spectral region around the OH absorption at 308nm is scanned over a path length of between 3 and 10km. Absorption features due to other species are sometimes detected, such as those due to SO_2 or HCHO. When the source of these features can be determined, they can be deconvoluted from the spectrum, otherwise they are added to the background, reducing the signal-to-noise ratio [e.g. *Hübler et al.*, 1984; *Perner et al.*; 1987; *Platt et al.*, 1988; *Platt*, 1991; *Ehhalt et al.*, 1991 and earlier references by the same workers). Observation of several spectroscopic features reduces the potential interferences, and measurements of ambient OH have been made [*Hofzumahaus et al.*, 1991] that suggest a peak value of 7×10^6 cm^{-3}. In the apparatus of *Mount* [1992] a portion of the exiting beam is split off and monitored with the returning beam so that the change in intensity of the laser can be monitored directly.

21

Problems arise, not only from the absorbance of other species in the air sample, but also from scattering of the radiation by aerosols and turbulence. This can be countered by using Differential Optical Absorption Spectroscopy (DOAS). Two lasers, tuned to two close, but separate, wavelengths, can be used [e.g. *Perner et al.*, 1976; *Zellner and Hägele*, 1985]. As with the LIF work of *Rodgers et al.* [1985] described above, the lasers are tuned so that one is on an absorption band of OH, usually at 308nm, while the other is just off it. The difference in the intensities of the two returning lasers can then be attributed to the absorption of OH alone. This is valid if the interferences have a broad wavelength dependence, so that any feature that effects the 'off line' beam will also effect the 'on line' one equally.

Armerding et al. [1990, 1991, 1992] have used a system that varies from this in two ways. The first difference is that only one laser is used and in order to achieve the differential adsorption, the laser is rapidly (1.3kHz) scanned over a narrow wavelength band (7 cm^{-1}) centred around 308nm.

The second difference is that instead of using a long path through the atmosphere with a single retroreflector, they use a multipass apparatus. Mirrors at either end of the path reflect the laser back and forth, so that an effective path length of 800m can be achieved over much shorter distances. This solves a potential problem of long path techniques, that the concentrations measured are the average concentrations over the entire path length. As has already been shown, this can be as much as 10km. Other atmospheric species, such as NO_x, SO_2 and O_3 are frequently measured with point sampling devices, which measure the concentrations at a particular place, rather than over a region. The integration of point and average data into a model can cause problems. The reported OH detection limit of 2-5 x 10^5 cm^{-3} [*Armerding et al.*, 1994] is sufficiently below the expected concentrations to provide a reasonable test for the predictions of OH concentrations under a variety of conditions.

Recently, the DOAS technique has been used to measure the concentrations of the halogenated radicals ClO, IO and BrO as well as OH [*Platt and Hausmann*, 1994] as these are also believed to play a significant role in tropospheric oxidation.

The principal advantage of absorption techniques is that they are 'absolute' and require no calibration, provided that care is taken to account for the pressure dependence of the absorption coefficients. Also, the reported sensitivities have been good. The disadvantages are that it provides spatially averaged, rather than point, data, and the cost of DOAS equipment (approximately £100,000) is prohibitive for general atmospheric monitoring.

1.2.4 Chemical Tracer Methods

Chemical tracer methods utilise the high reactivity of OH to label it with a specific isotope that can then be detected. At present, two techniques have been tried and both show good promise.

In the first, ^{14}CO is added to the sampled air and $^{14}CO_2$ is formed (reaction 1.15). After various reaction times, samples are removed and cryogenically stored for later analysis at a radionuclide laboratory. For the method to be reliable the purity of the ^{14}CO tracer has to be high with respect to both other compounds that contain ^{14}C (e.g. $^{14}CH_4$) and other nuclides that may be present, such as ^{222}Rn. The $^{14}CO_2$ has to be chemically separated from the unreacted ^{14}CO, again with a high degree of accuracy, and the walls and other surfaces of the equipment must not catalyse the conversion of the tracer to $^{14}CO_2$ that would add to the measured OH concentration.

Initial work on the system contained several problems associated with the treatment of the stored samples that led to large uncertainties in the results [Campbell et al., 1979, 1986]. Development of the technique greatly improved its reliability, with sample times of 100s giving standard errors in the counting equivalent to 2×10^5 cm^{-3} in measured OH concentrations of 2-9 $\times 10^6$ cm^{-3} [Felton et al., 1988]. Improvements in the purities have increased the precision of the system further [Felton et al., 1990] and OH concentrations in clean air have been measured as 5.6 $\times 10^6$ cm^{-3} with an error of only $\pm 0.1 \times 10^6$ cm^{-3} [Felton et al., 1992].

23

Instead of reacting OH with radiolabelled CO, *Eisele and Tanner* [1991] used $^{34}SO_2$, which forms $H_2^{34}SO_4$ in air containing OH, oxygen and water. Although the reaction involves 3 steps, they occur rapidly in ambient air and the conversion is complete within 10-20ms. The air flow is then analysed by a quadrupole mass spectrometer. Although the system is new, it appears to offer a detection limit of 1×10^5 cm^{-3} [*Eisele and Tanner*, 1991] and initial comparisons with other OH detection methods have been favourable [*Mount and Eisele*, 1992].

Although more work is needed on the $^{34}SO_2$ titration method, it appears to have potential for the future. The ^{14}CO tracer method provides very reproducible results but in its present form cannot provide real-time data, even though the collection time for a sample is short (100s). Also, the collection of data over a period of time cannot be done, except by using a large number of sample containers with the obvious potential for inaccuracy and inconvenience.

1.2.5 Deduction of OH Concentrations Using Atmospheric Modelling

This is similar in idea to the chemical tracer methods. If the amount of a material added to the troposphere, and the kinetics of its loss processes are known, then measuring its concentration after a given time can determine the concentration of the attacking species. Since for almost all trace gases this attacking species is primarily OH, this can provide a method of deducing the OH concentration.

Estimates of the average OH concentration over approximately a kilometre can be made by releasing two compounds simultaneously. The compounds are chosen so that one reacts with OH while the other does not, and ideally they have no other loss processes. Therefore, when the concentrations of the two are measured a number of hours later, the difference in concentration can be attributed to the reaction with OH [*Prinn*, 1985]. For global estimates of average OH concentrations species released by industrial processes can be used, provided they have a long tropospheric lifetime. The organochloride CH_3CCl_3 has been suggested for this purpose as it has a long

lifetime and is lost primarily through reaction with OH, although at present its emission inventory is not sufficiently well established [*Singh*, 1977; *Volz et al.*, 1981; *Derwent and Eggleton*, 1981 and *Prinn*, 1987].

Other researchers have used measurements of reactive hydrocarbons to determine the OH concentrations [*Calvert*, 1976; *Singh et al.*, 1981 and *Roberts et al.*, 1984]. It was found that this method tended to predict lower concentrations of OH when more reactive hydrocarbons were used. *McKeen et al.* [1990] found that for species emitted from a continuous source, vertical transport and horizontal diffusion could not be assumed to be independent of species reactivity, and that to do so could lead to OH concentrations being underestimated by up to a factor of 2.

Ehhalt [1994] used a simple model of tropospheric chemistry, along with data for the concentrations of various trace species including non-methane hydrocarbons (NMHC). Poor correlations were obtained between the model predictions for OH concentration based on the photolysis rate of O_3 and that measured by long path absorption, with the model overpredicting the OH concentration. The correlation for a 'clean', rural environment was better than that for an urban one, where greater spatial differentiation of sources and turbulence occurs. Despite the poor correlation over the data sets, the predicted OH concentration was never more than a factor of 2 higher than that measured. Better correlations between the predicted OH concentrations and those measured by long path absorption were obtained *Poppe et al.* [1992,1994] by using a more complex model.

A detailed, time-dependent model, incorporating physical characteristics of the troposphere such as temperature, pressure and solar intensity, as well as the primary reactions has been developed by *Lu and Khalil* [1991] which provides OH concentrations over the Earth. The results of the model are in good agreement with other assessments. A variation on this theme is provided by *Kanakidou* [1991] who used a reaction model, incorporating estimates of radical concentrations, to determine the annual emission of ethane and propane to the troposphere.

25

1.2.6   Matrix Isolation/ Electron Spin Resonance

Laboratory studies of aqueous chemistry commonly use the technique of Electron Spin Resonance (ESR, also known as Electron Paramagnetic Resonance, EPR) spectroscopy to detect the presence and character of radicals. As the name implies, it uses the resonance frequency of the magnetic field induced by the unpaired electrons on radicals in a sample. The exact frequency and nature of the signals indicate the species of radical being detected.

The technique has been adapted for the detection of atmospheric peroxy radicals by *Mihelcic* and co-workers [*Mihelcic, et al.*, 1978a, 1978b, 1985, 1990, 1993; and *Helton, et al.* 1984;]. The sample of air, around 20 litres, is cryogenically trapped in a matrix of H_2O and CO_2 on a liquid nitrogen cooled cold finger and returned to the laboratory for analysis. Because of the sampling and analysis methods, the technique is known as Matrix Isolation-Electron Spin Resonance (MIESR) detection.

Although modifications to the method have meant that the data have become more reliable, the MIESR detection limit is around 10^8 cm^{-3}, so it cannot be used, as yet, in relatively clean air. Another problem is that NO_2 has a strong ESR signal which has to be removed from the analysis and so decreases the accuracy of the results. However, numerical fitting procedures now allow the signal to be differentiated to provide concentrations of HO_2, CH_3COO_2 (the peroxy precursor for PAN), and the sum of the concentrations of other peroxy radicals.
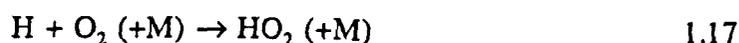
Watanabe [1982], used ESR to measure OH concentrations, though he used spin-trapping, rather than matrix isolation, to collect the samples. The OH was reacted with α-4-pyridyl-N-tert-butylnitrone α-1-oxide to form a stable adduct which was analysed later in a laboratory. A detection limit of 5×10^5 cm^{-3} was claimed for a sample of $200m^3$, with an uncertainty of ± 30%. However, no further work has been reported, although the same spin trapping method has also been used for OH detection in laboratory smog chamber studies with some success [*Stokes et al.*, 1994].

1.3   Chemical Amplification

1.3.1   Basic Principles of Chemical Amplification

Chemical Amplification was first proposed as a method for measuring ambient concentrations of hydroperoxy radical (HO_2) in the early eighties. It was so named as it is analogous to the electronic amplification used to measure weak electrical signals. The conditions in the monitor's reaction chamber are such that a chain reaction is set up that 'amplifies' the low concentration of HO_2 into higher concentrations of NO_2 that can then be monitored.

The chain reaction is brought about by adding carbon monoxide, CO, and nitric oxide, NO, to the sampled air stream so that the following reactions occur:

$$HO_2 + NO \rightarrow OH + NO_2 \qquad\qquad 1.21$$

$$OH + CO \rightarrow H + CO_2 \qquad\qquad 1.15$$

$$H + O_2 (+M) \rightarrow HO_2 (+M) \qquad\qquad 1.17$$

The sensitivity of the system is measured by the length of the reaction chain; the longer the chain, the more sensitive the system. The chain length is defined as:

$$\text{Chain Length, C.L.} = \frac{\Delta [NO_2]}{[HO_2]_o}$$

The system also measures other radicals, principally alkylperoxy, hydroxy and alkoxy radicals, as shown by reactions 1.28, 1.29 and 1.33.

$$RO_2 + NO \rightarrow RO + NO_2 \qquad\qquad 1.28$$

$$RO + O_2 \rightarrow HO_2 + R'CHO \qquad\qquad 1.29$$

$$RO + CO \rightarrow R + CO_2 \qquad\qquad 1.33$$

although the efficiency with which they are measured decreases as the size of the alkyl group increases as a result of greater competition from the addition reactions of NO [Cantrell et al., 1993]:

$$RO_2 + NO \rightarrow RONO_2 \qquad\qquad 1.35$$

$$RO + NO \rightarrow RONO \qquad\qquad 1.36$$

As the concentrations of OH and RO radicals in the troposphere are very much lower than those of the peroxy radicals (between 100 and 1000 times lower as indicated earlier) the chemical amplifier effectively monitors the sum of hydro- and alkylperoxy radicals. As such, the chain length is more properly defined as:

$$\text{Chain Length, C.L.} = \frac{\Delta[NO_2]}{([HO_2]_o + [RO_2]_o)}$$

The chain length depends on the balance between propagation and termination reactions. If all the peroxy radicals that entered the monitor, and all the OH radicals formed within it, reacted only with NO and CO respectively, the chains would be infinitely long. However, there are termination reactions, the most important of which were originally believed to be [Cantrell and Stedman, 1982; Cantrell et al., 1984]:

$$OH + NO \ (+M) \rightarrow HONO \ (+M) \qquad\qquad 1.37$$

$$HO_2 + HO_2 \rightarrow H_2O_2 + O_2 \qquad\qquad 1.20$$
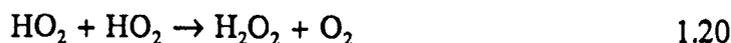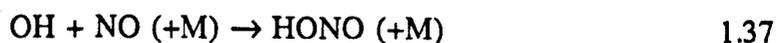
Also, the reversible formation of peroxynitric acid, PNA, in the chamber reduces the chain length by temporarily binding the NO_2:

$$HO_2 + NO_2 \ (+M) \rightleftharpoons HO_2NO_2 \ (+M) \qquad\qquad 1.38$$
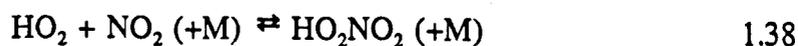
Later studies showed the importance of wall termination reactions in determining the chain length [Buhr, 1986; Ghim, 1988; Hastie et al., 1991; Cantrell et al., 1992; Cantrell et al., 1993]. As a result of different wall loss rates in the different experimental designs, measured chain lengths varied between 50 and 1500.

1.3.2 Chemical Amplifier Measurements

The basic operation of the chemical amplifier monitor is as follows. The air is drawn into the monitor by a pump, and CO and NO are added to the sampled air stream as it enters the reaction chamber. The chain reaction is allowed time to proceed as the stream passes through the chamber. *Cantrell et al.* [1993b] use a chamber size and flow rate that gives a residence time of around 10s, though it is only 1.1s in the equipment used by *Hastie* and co-workers [*Hastie et al.*, 1991]. The concentration of NO_2 in the sample as it leaves the chamber is measured using a chemiluminescent luminol detector described below [*Maeda et al.*, 1980; *Wendel et al.*, 1983].

Modulation techniques are used to distinguish between the NO_2 generated by the chemical amplification and the background NO_2 in the air stream. At periodic intervals the CO is switched with N_2, thus preventing the chain reaction and providing a measure of the background. This modulation allows for the removal of the signal from ambient NO_2 and that produced by the reaction of ambient ozone with the elevated levels of NO in the reactor:

$$O_3 + NO \rightarrow NO_2 + O_2 \qquad\qquad 1.10$$

However, the thermal decomposition of peroxyacetyl nitrate, PAN, and peroxynitric acid, PNA, in the reaction chamber can cause interferences that are not measured by this modulation technique. They can produce NO_2 and peroxy radicals in the chamber:

$$PAN\ (+M) \rightleftharpoons CH_3COO_2 + NO_2\ (+M) \qquad\qquad 1.32$$

$$PNA\ (+M) \rightleftharpoons HO_2 + NO_2\ (+M) \qquad\qquad 1.38$$
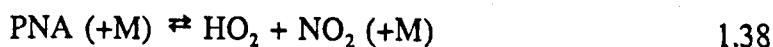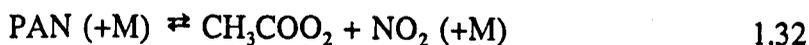
while the NO_2 will be measured as part of the background, the contribution from the peroxy radicals will not be, as the background is measured in the absence of amplification chemistry.

The interference from PAN and PNA thermolysis was reduced by *Hastie et al.* [1991] who modulated the signal merely by switching the position that the CO was added. In normal operation the CO and NO were added simultaneously, but their work showed that in the absence of CO, all the radicals react with NO within 40ms of the NO addition. Thus, when the CO was added 260ms after the NO, no amplification chemistry was observed. However, any radicals formed by the decomposition of PAN or PNA in the intervening time would be measured and so be removed as background. This system also had the added advantage of removing the need for a flow of N_2 that had to be precisely matched to that of the CO [*Hastie et al.*, 1991].

The luminol detector utilises the chemiluminescent oxidation of luminol (5-amino-2,3-dihydro-1,4-phthalazine dione) in an alkaline aqueous solution. The solution is pumped through a filter paper over which the sample flows as it exits the reaction chamber. The resulting chemiluminescence (between 400 and 500nm) is collected by a photomultiplier (PM) tube mounted 'face on' to the paper. The luminol detector was first proposed by *Maeda et al.* [1980] and with improvements since then [*Wendel et al.* 1983; *Walega et al.*, 1984; *Schiff et al.*, 1986; *Drummond et al.*, 1990; *Kelly et al.*, 1990] the detection limit is claimed to be around 2.5×10^8 molecule cm^{-3}. Improvements to the constituents of the solution for use in a chemical amplifier have been suggested by *Cantrell et al.* [1993b].

It is obviously very important to be able to calibrate the amplifier, so that the chain length can be determined. In ambient monitoring it is necessary to do this regularly, as the chain length can vary by a factor of 3 over a period of around a month [*Cantrell et al.*, 1993a]. The first chemical amplifier experiments were calibrated by passing dry air over hot nichrome wire [*Cantrell and Stedman*, 1982; *Cantrell et al.*, 1984], but this has since been abandoned in favour of measuring the thermal decomposition of H_2O_2 [*Cantrell et al.*, 1992; 1993b]. *Hastie et al.* [1991] have used a similar method for their calibrations, that is the thermal decomposition of PAN, and following their reported success this method is being investigated by Cantrell and co-workers [*Cantrell et al.*, 1993b].

1.3.3 Field Trials

With the exception of several isolated sets of measurements [*Cantrell and Stedman*, 1982; *Cantrell et al.*, 1984; *Hastie et al.*, 1991 and *Hu and Stedman*, 1994] there has been only one thorough field test of the chemical amplifier reported to date [*Cantrell et al.*, 1992]. This was conducted as part of the Rural Oxidants in a Southern Environment (ROSE) study in the USA during the summer of 1990. Also included in the study were measurements of the solar UV flux, various meteorological conditions, as well as the concentrations of NO, NO_2, O_3 and many hydrocarbons.

Throughout the study the amplifier worked reliably and a detection limit of 5×10^7 cm^{-3} was reported [*Cantrell et al.*, 1992]. However, it was found that the chain length varied greatly over the course of the study. Between June 16 and 29 the chain length was measured eight times, with a length of 51 ± 22, while between July 9 and 19 it was measured seven times, with an average length of 131 ± 30.

After the field trial the variability in the chain length was traced to changing wall loss rates as the reactor became 'conditioned'. Subsequently, the design of the reactor was changed so that it consisted of a thin inner wall of Teflon, inside a larger nylon tube, with the two separated by a galvanised wire mesh. A stream of nitrogen, passed through the mesh, filters through the inner Teflon wall into the chamber, creating a "nitrogen wall" intended to prevent the radicals reaching the teflon. In this way, wall conditioning was avoided and the chain lengths were found to be more stable ($\pm 26\%$ over 3 months).

The total peroxy radical concentrations ($HO_2 + RO_2$) measured were found to agree well with those predicted by modelling the concentrations of trace gases measured at the site, and showed a strong correlation with the measured photolysis rate of ozone. Daylight concentrations showed the expected diurnal variation, peaking around solar noon at between 2.5 and 6×10^9 cm^{-3} (100-250ppt). The measurements also showed a night-time concentration of around 5×10^8 cm^{-3}, but it was not clear if these were a result of a small non-linearity in the system, PAN interference or

genuine HO_2 produced by the reactions of NO_3. During daylight, little PAN interference was measured [Cantrell et al., 1992 and 1993a].

The results also showed a strong correlation between the photolysis rate of ozone, the precursor of OH and so HO_2, and the concentration of peroxy radicals. This is in agreement with the work of Feister [1994], who found a correlation between the solar UV flux and the concentration of OH.

Although the results of the ROSE study showed that chemical amplification was a viable method of monitoring peroxy radicals in the troposphere [Cantrell et al., 1992; 1993a and 1993b], there is still scope for improvements in the performance [Hu and Stedman, 1994]. Among these are the sensitivity and non-linearity of the luminol NO_2 detector under particular conditions, and the overall sensitivity of the apparatus. Detection of the NO_2 by laser-induced fluorescence could have advantages over the luminol system in terms of the linearity of response, although the quoted detection limits for the luminol method are lower than that for the LIF system (7.3×10^8 molecule cm^{-3} [Drummond et al., 1990] and 1.5×10^8 molecule cm^{-3} [Birnbaum, 1976] respectively). Increasing the chain length of the amplification chemistry would lead to an improvement in the overall sensitivity of the monitor. It has been suggested that the use of some simple organic species could yield such an increase [Anastasi et al., 1993] and this work is extended here.

1.4 NO_2 Photolysis Rate Determination

1.4.1   Theory

At a basic level the kinetics of NO_2 photolysis are very simple, depending only on the photolysis rate constant, J, and the concentration, $[NO_2]$:

$$-\frac{d[NO_2]}{dt} = J_{NO_2}[NO_2]$$

However, although the measurement of the concentration of NO_2 is now a relatively simple procedure, calculation of the photolysis rate constant, J, is more difficult as it depends on many factors. Provided the data are available it can be calculated from the following equation [Demerjian et al., 1980]:

$$J_{NO_2} = \int_{\lambda=290nm}^{420nm} I(\lambda)\sigma(\lambda)\phi(\lambda) \; d\lambda$$

where $I(\lambda)$ is the actinic irradiance (also called the actinic flux), $\sigma(\lambda)$ is the absorption cross-section and $\phi(\lambda)$ is the primary quantum yield of photolysis (all as a function of wavelength). It is important that the irradiance used is actinic (meaning spherically integrated) rather than planar, as molecules in the atmosphere are exposed to radiation from all directions, not merely that directly from the Sun. Failure to use the actinic flux can lead to erroneous photolysis rate determinations [Madronich, 1987].

The absorption cross-section and the photolysis primary quantum yield are physical properties of the NO_2 molecule and so can be, and have been, measured in the laboratory (e.g. cross-section: [Schneider et al., 1987; Koffend et al., 1987 and Leroy et al., 1987]; quantum yield: [Gardner et al., 1987]).

At the first level, the actinic flux is dependent on the solar spectrum and the solar zenith angle, which is itself dependent on latitude, altitude, day of the year and time of day. As these factors are well studied and documented it is possible to calculate a theoretical photolysis rate constant for NO_2 for any given location [Demerjian et al., 1980; Peterson, 1977]. Unfortunately, the discussion above neglects several important factors that influence the actinic flux.

For the flux to be properly calculated, the transfer of the radiation through the atmosphere needs to be considered. As discussed earlier in this chapter, not all the radiation incident at the top of the troposphere reaches the ground. It can be

scattered by molecules (Rayleigh scattering) or aerosols, as well as being absorbed by some species in the atmosphere, particularly ozone. Provided the concentrations of these species are known, their effect can be calculated with reasonable accuracy.

However, the strongest influence on the actinic flux comes from cloud cover. As mentioned earlier, clouds reflect both in-coming solar radiation and exiting radiation from the surface, as well as scattering light within themselves. Aerosols also scatter the radiation and so complicate the flux calculation. Modelling these effects has proved very difficult [*Spinherne and Greene*, 1978; *Mugnai et al.*, 1979; *Demerjian et al*, 1980; *Jones et al.*, 1981; *Madronich*, 1987; *Möller and Mauersberger*, 1992] and has not been successfully achieved to date.

In the absence of cloud cover, the influence of the other factors can be quantified and included in the calculations. Indeed, on cloud-free days calculations based on the measured UV flux are capable of reproducing measured NO_2 photolysis rates to within ±5% [*Parrish et al.*, 1983; *Madronich*, 1987 and *Shetter et al.*, 1992]. On days with cloud cover, however, the models are less reliable.

1.4.2 Measurement Techniques

In almost all of the previous measurements of the NO_2 photolysis rate, the chemical actinometers used a constant flow of dilute mixtures of NO_2 in a bath gas of either O_2 [*Jackson et al.*,1975; *Dickerson and Stedman* , 1980 and *Dickerson et al.*, 1982] or N_2 [*Zafonte et al.*, 1977; *Sickles et al.* , 1978; *Bahe*, 1980 and *Parrish et al.*, 1983]. Two groups have used different approaches: *Harvey et al.* [1977] used an air stream as the bath gas while *Madronich et al.* [1984] used pure NO_2 with no bath gas at all for reasons discussed below.

The advantage of nitrogen as a bath gas, instead of air or oxygen, is that in the absence of oxygen the secondary chemistry of the O atom produced by the photolysis is largely limited to:
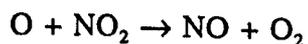
and so the effective quantum yield approaches 2. By reducing the pressure of their system to 60 mbar *Parrish et al.* [1983] were also able to reduce the contribution of the pressure dependent reactions:

$$O + O_2 \ (+M) \rightarrow O_3 \ (+M) \qquad\qquad 1.2$$
$$O + NO_2 \ (+M) \rightarrow NO_3 \ (+M) \qquad\qquad 1.39$$
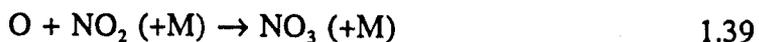
and they reported an effective quantum yield (or, as they called it, an actinometer efficiency) of 1.98. If air or oxygen are used as the bath gas, the production of O_3 through reaction 1.2, and its subsequent reaction with NO to reform NO_2 (reaction 1.10) would need careful consideration. With the exception of *Madronich et al.* [1984], the other studies were all carried out at a pressure of one atmosphere, although *Dickerson et al.* [1982] found that the photolysis rate was independent of the pressure of the system over the range 150 to 1200 mbar.

The photolysis cells used consisted of tubes of quartz (except *Sickles et al.* [1978] who used a bulb mounted on a 4m high pole) over a surface with a uniform albedo, usually matt black. To avoid the problem of 'end effects' which can be caused by the ends of the cell shading regions of the cell body, the tubes were designed to be long and narrow to minimise the diameter : length ratio.

It was also considered possible that reflections from the external and internal surfaces of the walls of the cell, as well as diffraction and focusing from the walls, would affect the transmittance of the light to the sample. However, many of the effects cancel and the transmission efficiency of this design of cell is taken to be 1 [*Parrish et al.*, 1983 and references therein].

Radiation scattered from adjacent surfaces and by atmospheric constituents makes a significant contribution to the photolysis process, as discussed above. If the intention of the measurement is merely to determine the NO_2 photolysis rate at a given point

and time, then provided care is taken to prevent interference from the actinometer itself, no special treatment of the albedo or diffuse irradiance of the sky is necessary. The advantage of the spherical cell used by *Sickles et al.* [1978] is that it can collect light from the full 4π steradians of scattered radiation. However, the uncertainties involved in the analysis of the data from this system are increased because the flow characteristics of the sphere are less well understood than the plug nature of the flow through the cylindrical cells.

Most of the previous studies have attempted to correlate the photolysis rate with the solar zenith angle for inclusion in atmospheric models. Consequently the actinometers have been designed to control the albedo effects by placing the cell over a surface with a uniform albedo of either 0 (black paint or felt [*Sickles et al.*, 1978; *Dickerson et al.*,1982 and *Parrish et al.*, 1983] or 1 (white zinc oxide paint [*Harvey et al.* 1977]. The cells were also usually sited so that they were shielded from reflections in order that they were only exposed to direct sunlight and the diffuse irradiance of the sky. The effect of the diffuse irradiance was demonstrated by *Dickerson et al.* when they performed measurements of the photolysis rate from an aircraft. They observed an apparent increase of around 15% over their ground-based data, which was believed to be due to the aircraft-mounted actinometer also being exposed to irradiance from $10°$ below the horizontal that their ground-based system was not [*Dickerson et al.*, 1982].

The method used by *Madronich et al.* [1984] was unique not only in that it did not make use of a bath gas, but also in that it is the only study not to utilise conventional chemiluminescent analysis to determine the final concentrations of NO and NO_2. Instead, the pressure increase in a static photolysis cell was used to deduce the extent of the conversion of NO_2 to NO and O_2. No bath gas was used, in order to maximise this difference.

Those studies that did use chemiluminescence did so with the analysers operating in the NO_x mode, where the measurement alternates between the concentration of NO_x and NO, with the concentration of NO_2 taken as the difference between the two.

This is, in fact, not strictly necessary as the total concentration of nitrogen oxides should remain constant throughout the experiments at the levels determined by the researchers. However, it can provide a useful check that there are indeed no variations in the concentration of NO_x.

1.4.3 Comparison of Measurements

The measurements described above have all been carried out at different locations and at different times of the year, so direct comparison between them is difficult. However, *Parrish et al.* [1983] have used the parameters of *Demerjian et al.* [1980] to adjust the data sets from these studies to a set of 'standard' conditions. Once this had been performed the agreement between the techniques was shown to be good, with an average value of the clear-sky photolysis rate of 8.5 x10^{-3} s^{-1} for a solar zenith angle of 30°. The values from the different studies were all with 6% of this figure, and it is also in excellent agreement with the value of 8.2 x10^{-3} s^{-1} calculated from first principals [*Demerjian et al.*, 1980].

The data from these studies have also been used by *Madronich* [1987] to develop a way of correlating measurements of the UV flux made using a radiometer with the photolysis rate. The radiometer consists of a UV filter and photocell behind a flat, opaque quartz diffuser plate. Because this plate is flat, the response of the radiometer to the angle of incidence of the light is cosine (rather than uniform) and so direct correlation of J values with the radiometer readings produces a curve which, because it is dependent on the location and time of the measurements, has proved difficult to reproduce. *Madronich* has found that if the ratio between the direct and diffuse radiation is considered, reproducible, linear correlations are obtained between the radiometer readings and J measurements. For cloud-free days the agreement between the prediction based on his analysis of the radiometer data and the previously reported actinometer measurements was within 5%, decreasing to 20% for cloudy days [*Madronich*, 1987].

This method was tested by *Shetter et al.* [1992] who made simultaneous measurements of the NO_2 photolysis rate with an actinometer (J) and a radiometer (J'). They found close agreement between the measurements with the ratio of the two, J'/J, being 1.01 ± 0.05 for clear days and 0.93 ± 0.09 when intermittent cloud cover was present.

Recently a radiometer with a uniform response over a hemisphere (rather than the cosine response of the standard radiometer) has been developed [*Junkermann et al.*, 1989] although at present its reliability is unknown.

Despite significant progress in recent years, there is at present no reliable and simple method of measuring the photolysis rate of NO_2. The chemical actinometers that have been used in previous studies are complex, while the interpretation of radiometer readings of the UV flux are not sufficiently precise. It is important to be able to monitor the photolysis as it is a fundamental part of tropospheric chemistry. The aim of the study described in Chapter 5 of this work was the development of a simple method of monitoring, based on static cells that can be easily transported to a site and exposed for a set time before being returned to a laboratory for analysis. It was intended that such a system should provide a reliable, simple and cheap method for making spot measurements. Preliminary studies, described in Chapter 5 and by *Vipond* [1994], have shown that such a system can be used to determine the atmospheric photolysis rate of NO_2 with reasonable accuracy.

Chapter 2

Experimental Methods

2.1   Introduction

The studies in this work involved some very complex sets of reactions. The reactions were initiated by ultra-violet (UV) photolysis and resulted in either a conversion of NO_2 to NO, or vice versa. The products were followed by three principal detection techniques, depending on the system: NO was detected by chemiluminescence analysis, NO_2 by its laser-induced fluorescence (LIF), and UV absorption was used for peroxy radicals.

In the first study, the method of chemical amplification was investigated as a means of monitoring very low concentrations of peroxy radicals, by generating them in the presence of NO and an organic chain carrying agent. The conversion of NO to NO_2 was followed by chemiluminescence analysis. The kinetics of the peroxy radical generation, and thus the concentration of the latter was studied using molecular modulation spectrometry (MMS).

In the second, related study computer modelling of reaction mechanisms was used to forecast the behaviour of alternative organic chain carriers in the chemical amplification method. Published rate data for the reactions believed to be involved were used to predict the product concentrations with time. This method of modelling was also used extensively to aid the elucidation of the mechanisms of other reactions studied experimentally.

The final study explored the reaction between the $O(^3P)$ atom, produced by photolysis of NO_2, and 2-butyne. The aim of this work was to reduce the uncertainties involved in making in-situ measurements of the atmospheric photolysis rate of NO_2. In systems containing only NO_2 and N_2 it is possible to get secondary chemistry that

effects the overall quantum yield. In this study 2-butyne was added in excess as an attempt to control the secondary chemistry, and so provide a quantum yield that remains constant over the course of the photolysis rate measurement.

2.2 Experimental Methods

2.2.1 Gas Handling

All the manipulation of gases was performed using a borosilicate glass (Pyrex) vacuum line. The manifold of the vacuum line was wrapped with nichrome electrical wire (resistance 4Ω m^{-1}) in order to warm it gently and so help limit the sticking of gases to the interior walls. All the taps were greaseless with Teflon fittings (Young's SPOR) as were all joints to removable bulbs, sample bulbs and gauges.

The vacuum line was pumped by a glass oil diffusion pump backed by an Edwards ED50 single stage rotary pump. These were connected to the line through a glass cryogenic trap surrounded by liquid nitrogen to freeze out any condensible gases. The vacuum in the line was monitored using an Edwards Pirani 14 gauge with a working range of <1 x 10^{-3} to 1 mbar. Pressures in the manifold, and elsewhere in the line, were measured using pressure transducers (Transinstruments BHL-4200 head with BHL-1420 controller (0.1-1000.0 mbar)).

Gases were stored in cylinders, lecture bottles or in purpose built glass bulbs. The cylinders and lecture bottles were connected to the line via copper tubing, or stainless steel tubing for corrosive gases such as NO_2, and brass needle valves. All the bulbs were covered in black tape to minimise the risk from implosion and to prevent the decay of any photolabile materials. In those cases where the vapour was to be taken from a liquid, the latter was stored in a sample bulb. These, and the removable bulbs occasionally used to store gases, were connected to the line with ball-and-socket or bayonet fittings, sealed with rubber O-rings.

Where necessary, materials were degassed to remove N_2 and O_2. This was done in either a sample bulb (for liquids) or a bulb with a "cold finger" (for gases) by repeated freeze-pump-thaw cycles, using liquid N_2 (77K) or CO_2/acetone (190K) cold temperature baths, as appropriate. It is common for cylinders of NO_2 to contain NO as an impurity, and vice versa. At temperatures around 253K and below, NO and NO_2 combine to form N_2O_3 which is clearly visible as a bright blue/green solid [*Greenwood and Earnshaw*, 1984]. It was found that by maintaining the sample at approximately 220K, the N_2O_3 remained solid and the appropriate amount of NO_2 or NO could be obtained. Refreezing of the NO_2 or NO showed no sign of the blue/green colour associated with the N_2O_3. Metal carbonyls (mainly $Fe(CO)_5$) were removed from the CO by passing it over activated charcoal.

2.2.2 Photolysis Methods

The reactions under investigation were all initiated by photolysis. Peroxy radicals for the chemical amplifier work were generated by the photolysis of ethanal in the presence of O_2, using between one and four low pressure mercury strip lamps (Philips TUV 15W, 450mm long). These lamps emit primarily at 254nm, though there are several other lines present in the spectrum. The lamps were arranged parallel to the cell, forming a cross-sectional square as shown in Figure 2.1a.

In the studies with 2-butyne, the $O(^3P)$ atoms were generated by the photolysis of NO_2. Two types of lamp were used, a "blacklamp" which has a broad emission centred around 350nm (Philips TL15W/08 450mm strip lamp), and a medium pressure mercury discharge bulb with several sharp lines between 250nm and 450nm. The emission spectra of all the lamps used were measured using a double beam monochromator, and are shown in Figure 2.2. The blacklamp was situated parallel to the cell, as with the low pressure mercury lamps above. Figure 2.1b shows the position of the mercury discharge bulb relative to the cell. In this position it provided a uniform irradiance of the cell.
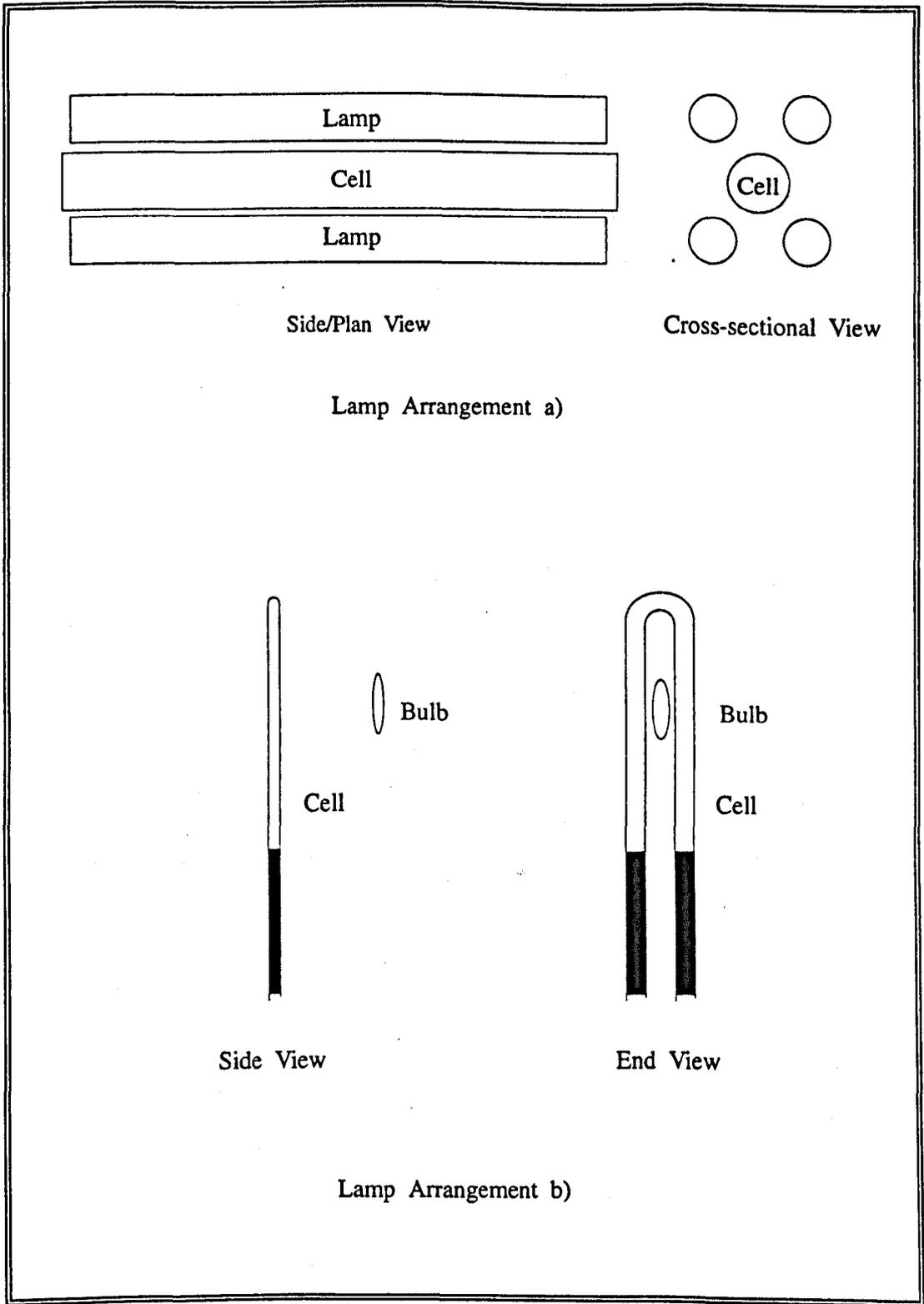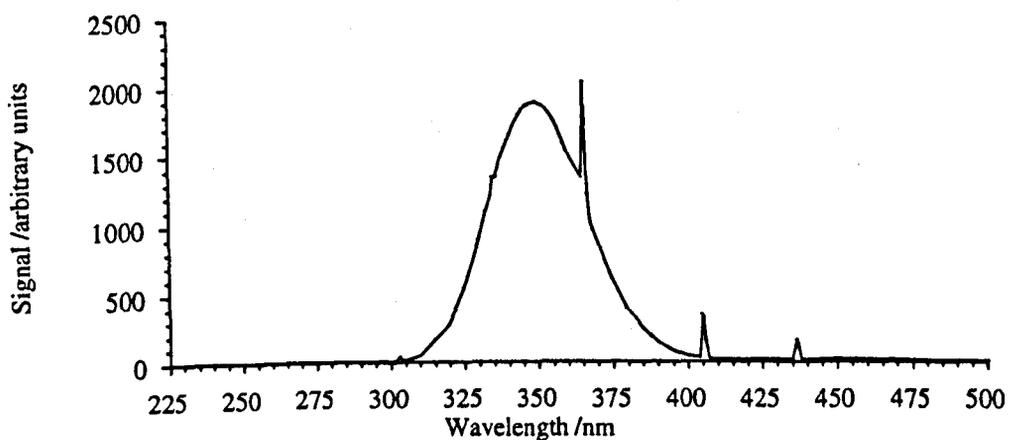
Figure 2.1 The different lamp/cell geometries used in this study
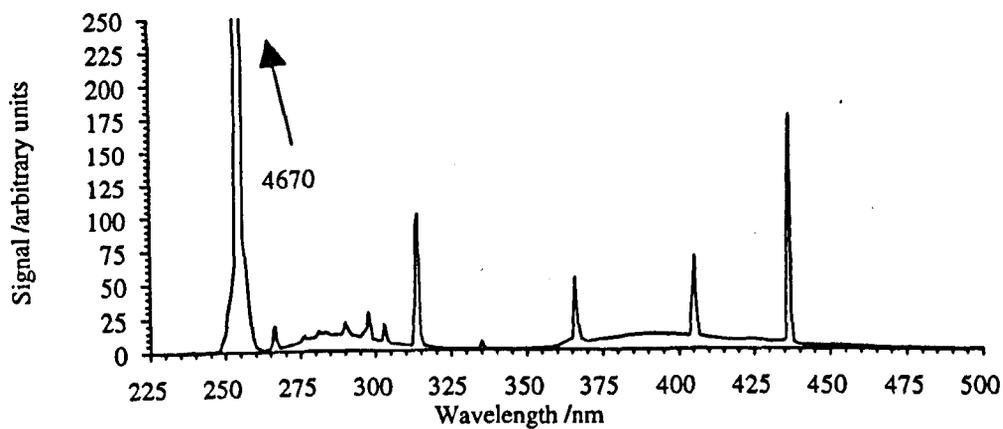
Spectrum a
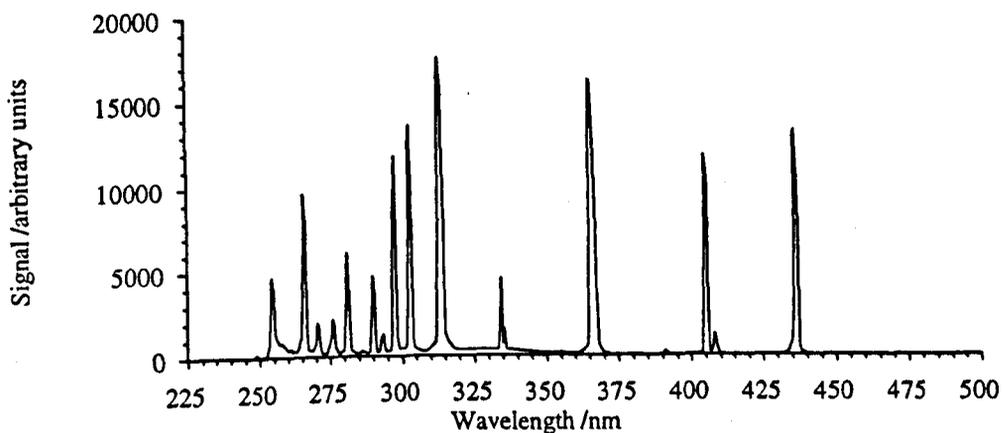
Spectrum b

Spectrum c

Figure 2.2   The spectra of the photolysis lamps used in this work. a: low pressure Hg arc; b: medium pressure Hg arc; c: "Blacklamp"

2.2.3   Materials

The materials used in this work are summarised below, along with their respective sources and purities. Figures in brackets were determined by gas chromatographic analysis.

Chemical	Supplier	Grade/Purity
NO_2	Matheson	99.5%
NO	Aldrich	98.5%
N_2	BOC	zero grade, 99.998%
Ar	BOC	zero grade, 99.998%
CH_3OCH_3	Matheson/Aldrich	99%/99%
CH_3CHO	Fisons	99% (>99.2%)
O_2	BOC	zero grade, 99.6%
CO	BOC	research grade, 99.95%
CH_3CCCH_3	Aldrich	99+% (>99.3%)
CH_2CH_2	Matheson	C.P. grade, 99.7%

2.3   Detection Techniques

2.3.1 NO_x Analysis using Chemiluminescence

Chemiluminescence analysers measure the concentration of nitric oxide, NO, using the gas-phase reaction between it and an excess of ozone, O_3. This reaction produces NO_2^*, an electronically excited state, which decays back to the ground state with the

emission of a characteristic luminescence. The intensity of the emission is linearly proportional to the concentration of NO in the reaction chamber.

$$NO + O_3 \rightarrow O_2 + NO_2^* \qquad (2.1)$$
$$NO_2^* \rightarrow NO_2 + h\upsilon \qquad (590 > \lambda > 3000nm) \quad (2.2)$$

This chemiluminescence is detected by a photomultiplier tube which feeds the signal via data processing electronics to a display and/or data logger.

The sample is drawn into the reaction chamber by a vacuum pump. In the NO mode it flows directly into the chamber, but in the NO_x mode it passes through a catalytic converter containing a screen of molybdenum at around 625K. This reduces NO_2, and other nitrogen containing species, to NO before they react with the O_3. For example, in the case of NO_2:

$$3 \, NO_2 + Mo \rightarrow 3 \, NO + MoO_3 \qquad (2.3)$$

The O_3 is produced by an electrical discharge across a stream of dried air, which is also drawn into the analyser by the vacuum pump. As O_3 is produced in excess to ensure all the NO reacts, the remaining O_3 is removed from the chamber exhaust using a scrubber between the reaction chamber and the pump. A schematic diagram of a chemiluminescent analyser is shown in Figure 2.3.

Two different analysers were used over the course of this study. In the chemical amplification experiments the concentrations of NO involved were low and a Thermo Electron Model 14B/E (10ppm full scale) was used. Due to the higher concentrations of NO generated in the experiments with 2-butyne and NO_2, a Thermo Electron 10A (10,000ppm full scale) was used. They were used almost entirely in the NO monitoring mode. In the NO_2 mode the sample gas stream alternates between passing directly into the chamber and entering the chamber via the converter. In this way the concentrations of NO and total NO_x respectively, are measured, and the concentration of NO_2 is taken as the difference between the two.

45

Sample inlet

Air inlet

Drying
Column

Ozone
Generator

Sample mode
switch

NOx
Converter

Reaction
Chamber

To vacuum pump

$$NO + O_3 \longrightarrow NO_2{}^* + O_2$$

$$NO_2{}^* \longrightarrow NO_2 + h\nu$$

Ozone
Scrubber

Filter

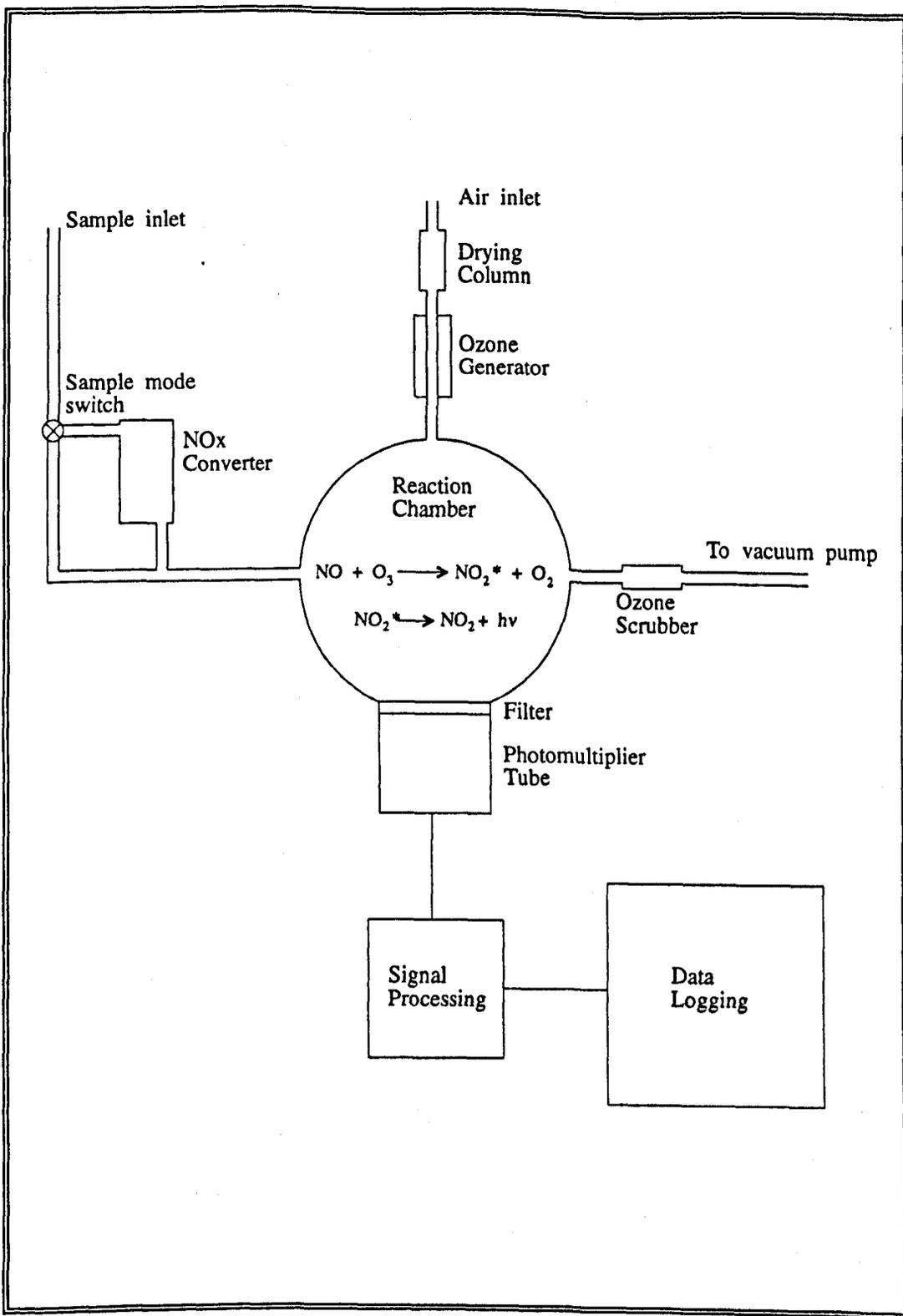Photomultiplier
Tube

Signal
Processing

Data
Logging

Figure 2.3   Schematic diagram of a chemiluminescent NO_x analyser

However, as indicated earlier, the conditions in the converter are severe enough that other oxides of nitrogen, such as nitric and nitrous acids, HNO_3 and $HONO$ respectively, may also be reduced to NO. Hence, any measure of the concentration of NO_2 will contain the concentrations of any other nitrogen oxides present. If the total NO_x concentration is already known, as it is in these experiments, then sampling through the converter provides no extra information.

In the NO_2/2-butyne experiments, discussed in Chapter 5, the aim of the chemiluminescence analysis was to measure the amount of NO produced after a set photolysis time. However, in the chemical amplification studies, it was the formation of NO_2 that was of primary interest, so this had to be calculated by taking the difference in the NO concentration before and after photolysis. Consequently, this increased the uncertainty in the measurements. This is discussed further in section 3.4.2.

In normal operation, analysers have a continuous sample flow, with perturbations to the level shown as fluctuations in the signal. It was not possible to do this as experiments were performed on isolated, static samples which were subsequently flushed through the analyser by a carrier gas, using a sample loop arrangement. This resulted in a pulse which appeared as a peak on an otherwise level baseline, similar to that obtained from a gas chromatograph. It was found that, provided the pulse was short (less than approximately 10s in duration) the peak width was constant, and that the height of the peak was linearly proportional to the concentration of NO in the sample. As measurement of the peak height is simpler than integrating the area from a chart recorder trace, where possible this method was used for assessing the concentration of NO. For longer pulses, where tailing effects were more significant, it was found that the peak height was no longer an accurate measure of the concentration, and so it was necessary to measure the area under the peak.

With the 10ppm analyser, for concentrations of NO up to around 1 ppm, the full peak could be integrated, but at higher concentrations the tailing became very severe, with the baseline taking over 1000s to return to its original level. During this tailing it
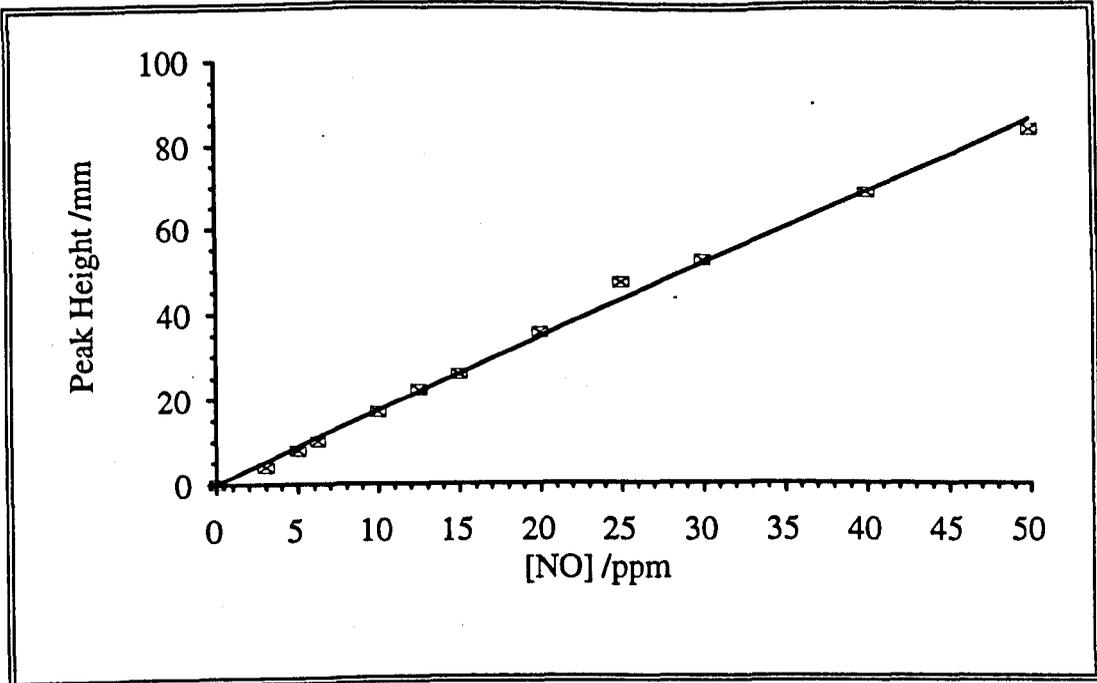
Figure 2.4 Calibration graph for the 10,000ppm NO_x Analyser (500mbar cell pressure). Flow rate = 470 ml min^{-1}
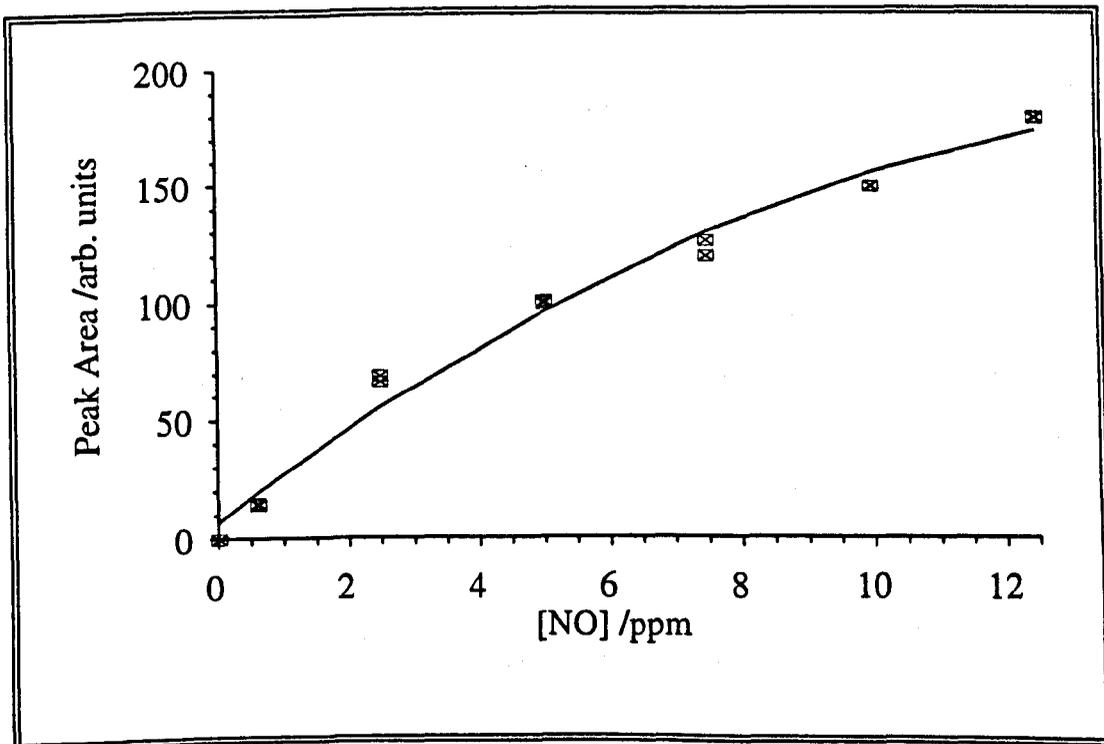

Figure 2.5 Calibration graph for the 10ppm NO_x analyser. Flow rate = 280ml min^{-1}

was found that redirecting the carrier gas flow, so that it no longer flushed through the loop, immediately returned the baseline to its original level. It was, therefore, assumed that this tailing was due to flushing the sample out of the parts of the loop not directly in the path of the gas, such as the side arm containing the pressure gauge. If this is the case, then the tailing would also have been present at the lower concentrations, but it was lost in the baseline noise.

However, in both cases it was found that good calibrations were possible, and they are shown in Figure 2.4 and Figure 2.5. As can be seen from Figure 2.5 the calibration for the 10ppm analyser is not linear, and actually fits, for the concentrations of interest, to a simple quadratic function. The results of the calibrations were as follows:

10,000ppm: (0.578 ± 0.022) ppm/mm

10ppm: Area = $7.25 + 20.8[NO] - 0.598[NO]^2$

where [NO] is the concentration of NO in ppm. The error in the calibration of the 10 ppm analyser is discussed in section 3.3.7.

2.3.2   Laser-induced Fluorescence of NO_2

Laser-induced fluorescence (LIF) provides a non-intrusive, in-situ method of monitoring species that can be both highly selective and very sensitive. The sensitivity of the system is greatly improved when it is linked to phase-sensitive detection.

The NO_2 molecule exhibits a broad absorption spectrum, extending from the ultra-violet through to the infrared [Herzberg, 1967]. The N-O bond has a photodissociation limit equivalent to the photon energy associated with 397.9nm radiation; however, it is observed that dissociation actually occurs at wavelengths up to 420nm. This has been attributed to the use of internal rotational energy to make

49

up the deficit in the photon energy. Reactions of electronically excited NO_2 with itself can also lead to very small amounts of dissociation at higher wavelengths [*Gardner et al.*1987; *Jones and Bayes*, 1973]. Such reactions are:

$$NO_2^{\bullet} + NO_2 \rightarrow 2NO + O_2 \qquad (2.4)$$

$$NO_2^{\bullet} + NO_2 \rightarrow NO + NO_3 \qquad (2.5)$$
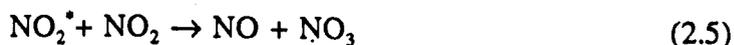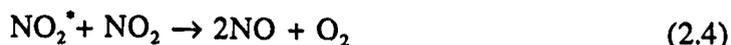
The fluorescence yield follows this wavelength dependence closely. Below 390nm there is no fluorescence, but the amount rises sharply between 390 and 410nm, before tailing off above 460nm [*Lee and Uselman*, 1972]. The intensity of the fluorescence is dependent on the pressure of NO_2 in the cell, and inversely proportional to the total of the products of the pressure of other species present, and their quenching coefficients, a,

$$I \propto \frac{[NO_2]}{\Sigma \, a_x[X]} \qquad \textbf{2.1}$$

This linear proportionality means that, for a given mixture, where only the concentration of NO_2 varies, calibration is easy. However, when the concentrations of the other species are also varying, calibration becomes more difficult. This can be corrected for if the quenching coefficients of each species are known.

Excitation was provided by a Liconix 4210 HeCd laser emitting radiation at 441.6nm with a beam width measured as approximately 5mm. Radiation of this wavelength excites the NO_2 through the $X^2A_1 \rightarrow {}^2B_1$ and $X^2A_1 \rightarrow {}^2B_2$ transitions, which are well characterised. The fluorescence lifetime at this excitation wavelength has been measured as 65μs [*Anastasi and Hancock*, 1988], 60μs [*Schwartz and Johnston*, 1969], and 70-75μs [*Sackett and Yardley*, 1970], so the signal is a real-time measure of the concentration of NO_2. Though the laser was rated as emitting 10mW, this was measured to be 5mW. Both the nominal and actual beam powers are low enough so that there is no significant loss of NO_2 through the reactions of its excited states, as discussed above.

The beam was attenuated by a Scitec Instruments chopper running at 497Hz and collimated by a series of concentric baffles before entering the cell. After exiting the cell, the beam passed through a further set of baffles, to reduce the back scattering of light, before being intercepted by a photodiode (Photophysics) that was used to monitor the laser power throughout the experiments.

Fluorescence from the excited NO_2 was collected perpendicular to the laser beam by a combination of a biconvex lens, iris diaphragm and cut-on filters. The exact arrangement of these optics differed between the experiments involving 2-butyne and those involving ethanal and DME in the chemical amplification work.

In the experiments where NO_2 was photolysed in the presence 2-butyne, the light was collected by a 40mm focal length lens mounted 40mm from the beam, and passed through a 2mm thick glass 590nm cut-on filter (Schott no. OG-590). The system was improved for the later chemical amplification experiments by changing the lens to one with a 20mm focal length mounted 40mm from the beam. This would focus light from the beam to a point 40mm from it, at which distance an iris diaphragm was placed. It was found that the optimum I_o-to-noise ratio was obtained with an iris 4mm in diameter. A combination of 495nm, 530nm and 590nm, 2mm thick glass cut-on filters (Schott no. GG495, GG530 and OG590 respectively) was used to remove stray laser radiation; the optical layout is shown in Figure 2.6. The fluorescence complex was situated at the centre of a long reaction cell which allowed for the photolysis, and also for absorption studies along the principal axis. As part of the system optimisation, it was also found that running the chopper at 793Hz gave an improved I_o-to-noise ratio. The details of the improvements made to the system, and the I_o to noise ratios achieved are given in section 3.3.2.

The signal was detected by an EMI 9813QB RF-shielded photomultiplier (PM) tube and passed to an EG&G PAC Model 5207 lock-in amplifier. The lock-in amplifier was also connected to the laser beam chopper and discriminated against any signal that did not have the pulse frequency of the chopper. The resultant signal was passed to an IBM compatible computer and logged as an ASCII text file using a BASIC programme provided by EG&G (Appendix 1). Regression and statistical analyses were performed using the Statgraphics v2.2 package on a microcomputer.
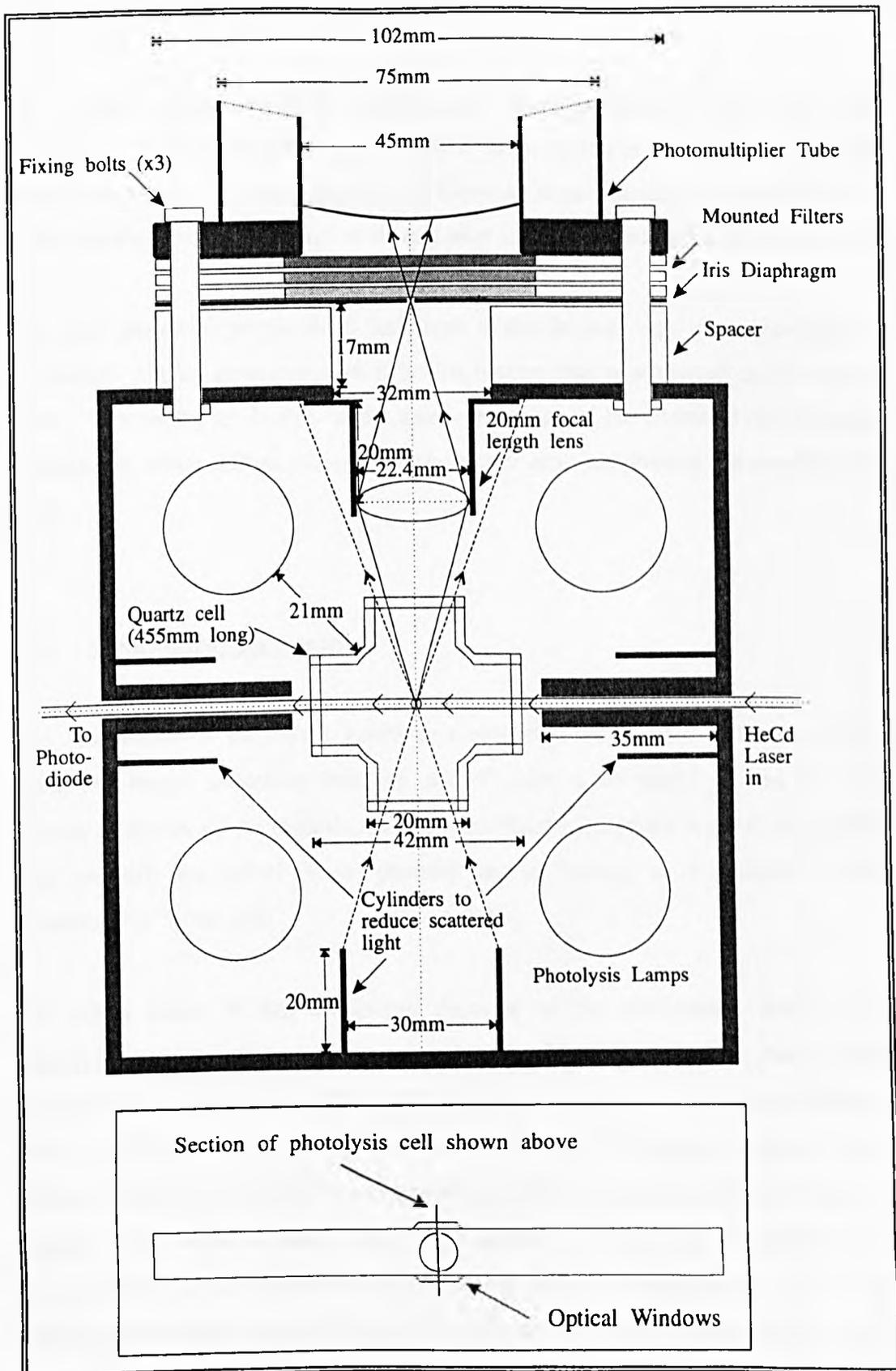
Figure 2.6   Diagram of the optimised LIF optical arrangement., showing the vertical cross-section.

2.4   Molecular Modulation Spectrometry

The theory behind the MMS technique has been covered in detail elsewhere [*Johnston et al.*, 1967; *Paukert and Johnston*, 1974; *Parkes et al.*, 1976] and, as such, will not be given a full treatment here. However, some discussion of how it is used in the present work is necessary as its role here is different from that in other studies.

The main advantage of the MMS technique is that known, very low concentrations of radicals can be generated, and it is this feature that is exploited in the present work. The ability to do this in the same apparatus as the chemical amplification experiments which follow, reduces the systematic error involved in the amplification study.

2.4.1   Experimental Technique

The electronics of the MMS generate a square wave form that is sent to the photolysis lamps, switching them on and off with a set period, τ, and for a set number of cycles, n. As radicals are formed when the lamps are on, and decay while they are off, the effect is to generate an oscillating, or modulated, radical concentration in the cell.

The actual shape of this oscillation depends on the relationship between the photolysis period and the rate of radical loss. If the radical loss rate is rapid compared with the period, τ, then a steady state concentration is quickly achieved while the lamps are on , and it dies away very quickly when the lamps are off. When this happens the radical concentration profile is very similar to that of the lamp output. At the other extreme, if the loss processes are very slow compared to τ, a steady concentration may not be reached, either while the lamps are on or off. The relationships between the lamp output and possible radical concentrations are shown in Figure 2.7.
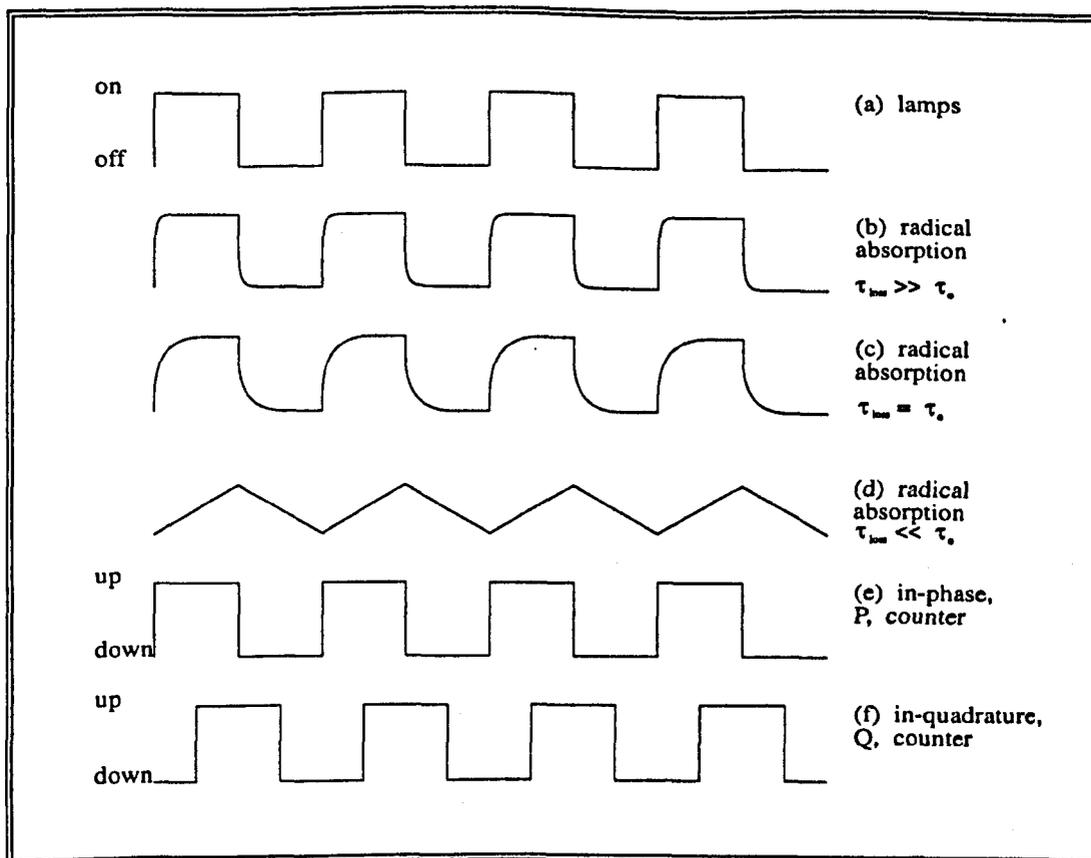
Figure 2.7 Timing relationships for MMS experiments

The concentration of the radicals was monitored using UV absorption. More detail on the actual apparatus used is given below in section 2.4.2. The signal from the PM tube is passed through an amplifier to a voltage-to-frequency (V-F) converter and then to two up-down counters. One of these is set to count in-phase with the lamps, up while they were on, down while they were off. The other counter is set a quarter phase (90°) behind the lamps. The rate at which they count depends on the frequency they receive, the lower the voltage from the PM tube (greater radical absorption), the greater the frequency output by the converter and the faster the count. The relationship between lamp switching and counter phase is also shown in Figure 2.7.

In all the experiments the total experimental time, T, was set as 100s, as this allowed a good signal-to-noise ratio to be achieved, and the photolysis period and number of cycles, n, were varied such that $n.\tau = T$ (e.g. 100 cycles at 1s period or 500 cycles

at 0.2s period). After each run the in-phase count, P, and the in-quadrature count, Q, were noted, τ and n were changed, and another run was performed. Suitable variation of τ leads to the different radical concentration profiles discussed above.

When the conditions in Figure 2.7b hold, i.e. during long photolysis periods, all the radical signal is in-phase, so P is at a maximum while Q approaches zero. At very short periods, the conditions for (d) hold, and the up and down counting are equal; hence both P and Q approach zero. Over a range of τ values the expected P and Q values are expected to show the dependence given in Figure 2.8.
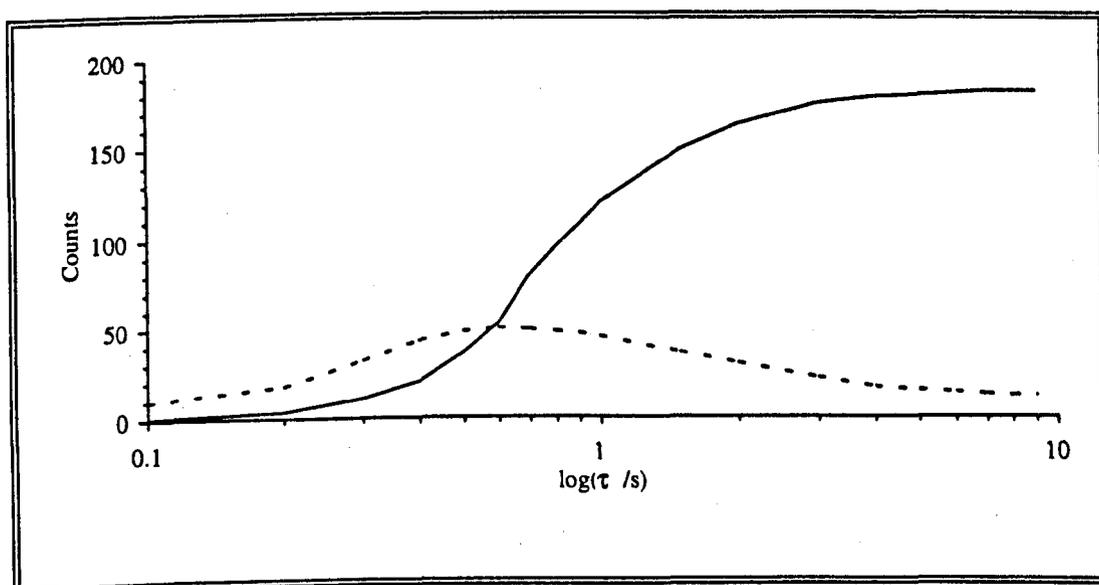
Figure 2.8   Expected dependence of P and Q counts on τ. The solid curve is the P count, the dotted curve is the Q count.

In a standard MMS study, the information from the P and Q counts can be related to the kinetic behaviour of the system. The factors of interest are primarily the photolysis period at which the P and Q counts are equal, τ_o, and the maximum number of P counts, which yields the maximum absorption A_o. A calibration must also be performed so that the number of counts can be related to an actual absorption. This is achieved by generating a square wave of known voltage, passing it directly to the V-F converter and noting the counts. By varying the size of the input voltage a graph of counts against voltage can be plotted (Figure 2.9), the gradient of which is the calibration factor.
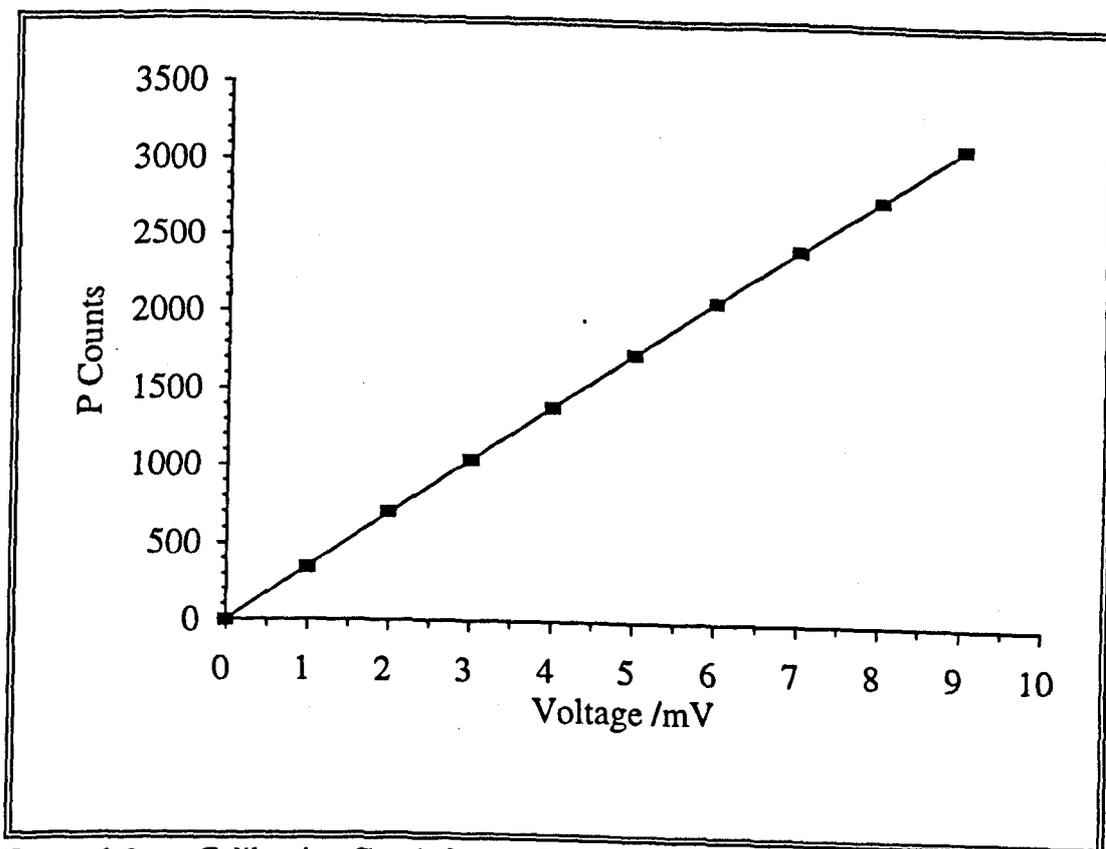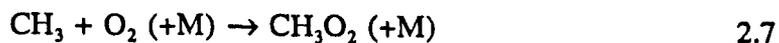
Figure 2.9 Calibration Graph for the MMS Apparatus. The gradient of the line, F = (348 ± 1) counts mV^{-1}. τ = 1.0s, n = 100, λ = 245nm.

The photolysis rate, B, of the radical precursor, is normally calculated by performing an experiment using a photolysis period that gives a square radical signal, over a long period of time. The fall in the absorption, shown by the decrease in the P count, over time due to consumption of the radical precursor can be monitored and yields the photolysis rate.

Changes in the absorption characteristics of the sample during an experiment can cause the DC voltage, on which the radical signal is superimposed, to change. If this happens the counts are affected but a simple correction can be used. The change can be due to consumption of the precursor, product absorption, or a change in the output power of the analysing lamp. In this work, such variations were limited, producing a small drop in the voltage, and the corrections were less than 5%.

2.4.2 MMS Apparatus

As has been stated earlier, the radicals in the chemical amplification studies were generated by the photolysis of ethanal in the presence of oxygen, by either one and four low pressure mercury strip lamps. This produced both hydroperoxy (HO_2) and methylperoxy (CH_3O_2) radicals.

$$CH_3CHO + h\upsilon \rightarrow CH_3 + CHO \qquad\qquad 2.6$$
$$CH_3 + O_2 \ (+M) \rightarrow CH_3O_2 \ (+M) \qquad\qquad 2.7$$
$$CHO + O_2 \rightarrow HO_2 + CO \qquad\qquad 2.8$$

Their concentration was monitored by UV absorption using the radiation from a D_2 analysing lamp, passed along the length of the cell. The light exiting the cell was focused by a lens through a slit into a double beam monochromator, set to pass radiation at 245nm. This wavelength was chosen to maximise the absorption by methylperoxy radicals while limiting the interference from absorption by hydroperoxy radicals, and the photolysis lamps. A schematic diagram of the equipment is shown in Figure 2.10

2.5   Computer Modelling

2.5.1   Introduction

Extensive use has been made in this work of computer modelling of the chemical systems under investigation. The results of such simulations can furnish valuable support for experimental data, and provide insight into the mechanisms involved in the chemistry. As such, they can be a very powerful tool. The following is a very brief discussion of the principles involved. A more thorough review is provided by *Sanderson* [1994] and references therein.
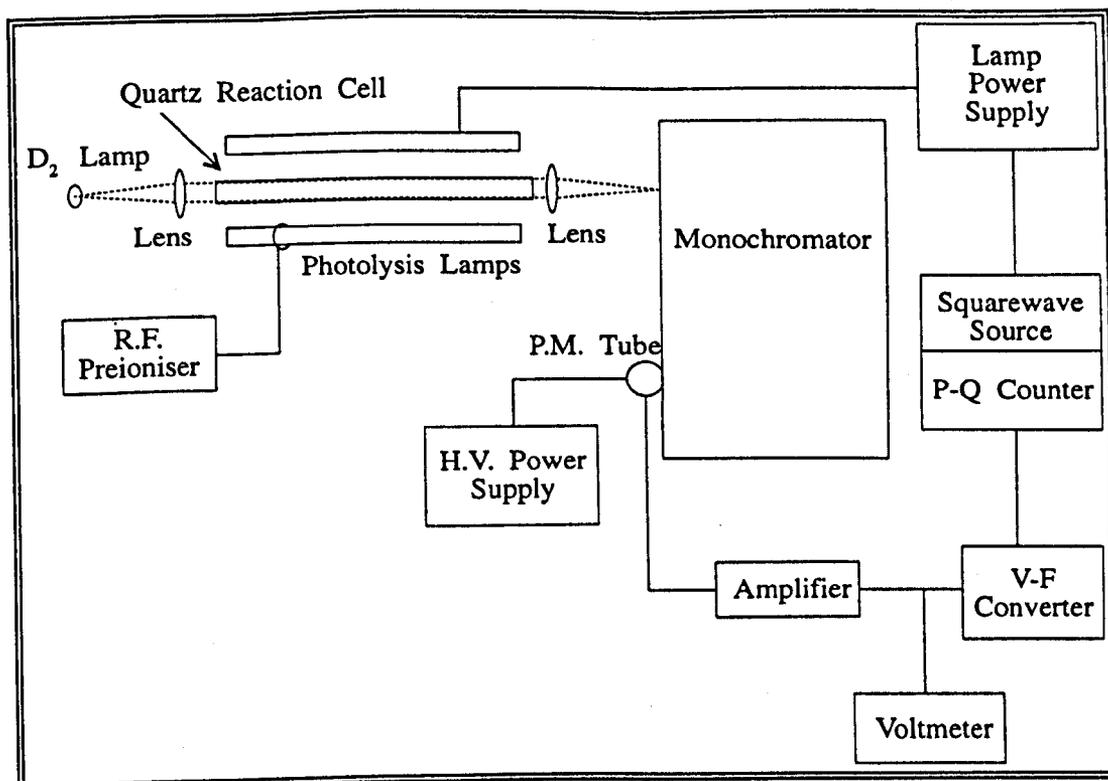
Figure 2.10 Schematic diagram of the Molecular Modulation Spectrometry apparatus

In this work a model was used in which it was assumed that mixing was very fast in comparison with reagent lifetimes, so that all concentrations are uniform over the reactor. Consequently, there are no functions for vertical or horizontal distributions, and hence the box is described as zero-dimensional. The desired initial concentrations of the reagents are input to the model, along with details of the reactions believed to play a role and their rate constants. The model is allowed to run for a set simulation time, after which the concentrations of any of the species involved may be read.

Any model, however, is only as good as the data used to construct it. If an important reaction is omitted, or an incorrect rate constant is used, then the model results will not be reliable. For this reason it is necessary to validate models, where possible, against existing data, such as that from experimental studies.

Not all reactions needed for a model may have published rate constants for the conditions of temperature and pressure of interest. It is frequently possible to

58

estimate values form existing data for different conditions, or from data for related compounds. While this can provide a satisfactory simulation, particularly if the estimated data are for reactions of little importance, it increases the uncertainty associated with any result. Also, as the number of unknown parameters increases, so does the risk of a non-unique solution.

2.5.2   The Processes of the Model

The programme uses the reaction mechanism and rate constant data to generate a series of ordinary differential equations (ODE), each one describing the behaviour of each individual reacting species. If the model scheme includes 50 different species, there will be 50 ODEs. Each one has to be integrated over a series of small time steps in order to derive the concentrations at the desired time.

There are several different methods for solving these equations. The software used here, SIMULA [*Rasmussen and Bjergbakke*, 1984], employs the CHECKIN programming code [*Prothero*, 1971]. Put simply, this solves the ODEs with the predictor-corrector method in which the value of each step is predicted by extrapolation of previous steps, then checked by using it in an integration of the ODEs.
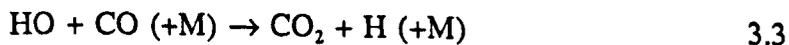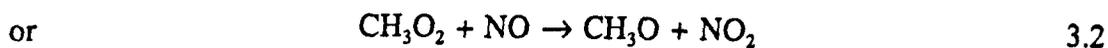
The size of the step is adjusted by the program to keep the difference between the predicted and checked values within set bands. While the accuracy of the result is improved by using very small steps, this involves very intensive computation, and hence large amounts of processor time. At times in the simulation where values are not changing rapidly, large integration steps can be used without significant loss in accuracy.

Chapter 3

Chemical Amplification:
Experimental Results for DME and CO

3.1   Introduction

Peroxy radicals form a crucial part of tropospheric chemical pathways. Along with the hydroxy radical, OH, they are responsible for the oxidation of almost all trace gases that are emitted to the troposphere. It is this radical oxidation that makes pollutants more water soluble and so aids their removal from the atmosphere by rain out.

Recently, there has been some interest in the detection of peroxy radicals in the atmosphere using chemical amplification; the technique has become known as the PERCA (Peroxy Radical measurement by Chemical Amplification) system. It is based on reacting peroxy radicals with NO to produce the corresponding alkoxy radical and NO_2. Carbon monoxide (CO) is used as the chain carrier to regenerate HO_2 radicals. Although this is discussed in more detail in Chapter 1, the principal reactions are shown below:

$$HO_2 + NO \rightarrow HO + NO_2 \qquad\qquad 3.1$$

or
$$CH_3O_2 + NO \rightarrow CH_3O + NO_2 \qquad\qquad 3.2$$

$$HO + CO\ (+M) \rightarrow CO_2 + H\ (+M) \qquad\qquad 3.3$$

$$H + O_2 \rightarrow HO_2 \qquad\qquad 3.4$$

The purpose of the work described in this chapter was to examine the viability of dimethyl ether (DME) as an alternative to CO as a chain carrier in the PERCA system.

The principal advantages of DME over CO are the faster rate constant for the reaction with OH, and that the chemistry subsequent to that reaction ultimately leads to the formation of more than one peroxy radical. Consequently, each cycle of the chain produces more peroxy radicals than the CO system, and so larger chain lengths, and greater sensitivity, are possible.
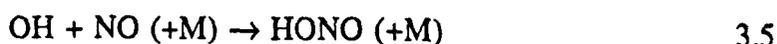
Before the performance of DME could be assessed, it was necessary to evaluate the kinetics of the radical production. Only if the number of radicals generated in each experiment was known, could a chain length be calculated. The MMS experiments described in this chapter were used to determine the photolysis rate of ethanal in this system. This could then be used to calculate the quantity of radicals produced when investigating the chemical amplification process in the experiments which followed.

Once a known concentration of radicals could be generated it was possible to perform the investigation of DME as a chain carrier for chemical amplification. In the first experiments the duration of the photolysis was varied as a means of generating different radical densities so that the effect of this on the chain length could be measured.

The role of NO in the chemical amplification system is crucial. Whilst it initiates the chain reaction with the peroxy radicals:

$$NO + HO_2 \rightarrow NO_2 + OH \qquad\qquad 3.1$$
$$NO + CH_3O_2 \rightarrow NO_2 + CH_3O \qquad\qquad 3.2$$

it is also a major sink for the OH radical:

$$OH + NO (+M) \rightarrow HONO (+M) \qquad\qquad 3.5$$

where M is an inert colliding body. The response of the system to the concentration of NO was, therefore, also examined.

A series of experiments was performed to provide a comparison between DME and CO. This would demonstrate whether any differences observed between the results of the experiments with DME and those reported for CO were genuine or caused by a systematic error in the experimental procedure.
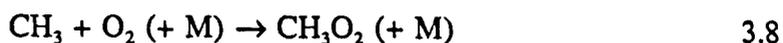
3.2 Radical Generation

3.2.1 MMS Experimental Procedure

The MMS technique and apparatus are described in detail in section 2.4.

In a traditional MMS investigation, two types of experiment are performed. In one, the photolysis rate of the radical precursor is found by photolysing a sample for a long period of time and following the drop in the precursor concentration. In the other, the radical loss rate constant is measured from the characteristic P-Q plot. In this study, theoretically, it was only necessary to do the first experiment although the second series can provide confirmation of the result.

Ethanal was used as the precursor for the peroxy radicals, because in the presence of oxygen, the photolysis of ethanal yields both hydroperoxy and methylperoxy radicals:

$$CH_3CHO + h\upsilon \rightarrow CH_3 + CHO \qquad 3.6$$
$$CHO + O_2 \rightarrow CO + HO_2 \qquad 3.7$$
$$CH_3 + O_2 (+ M) \rightarrow CH_3O_2 (+ M) \qquad 3.8$$

where M is an inert colliding body, such as N_2.

The advantage of ethanal is that it produces both hydro- and methylperoxy radicals, and so mimics genuine atmospheric conditions more closely than a precursor that yields a single radical species. An additional factor in the choice of ethanal as the precursor is that it can be easily obtained in high purity. The photolysis can be

achieved using 254nm radiation which is readily obtained from a Hg arc lamp. This wavelength was particularly suitable as it does not photolyse NO_2 significantly. However, because it is close to the wavelengths where the radical products absorb, it did limit wavelengths available for monitoring the radical concentrations through UV absorption.

The radical absorption was monitored at 245nm, at which the principal absorption is due to the methylperoxy radical. This wavelength is low enough so that there is no interference from the 254nm radiation from the Hg lamp, whilst being high enough to reduce the contribution from absorption by hydroperoxy. The absorption cross-sections for these species are discussed below, in section 3.2.5.

In a typical experiment 500mbar of a mixture containing 4% ethanal in oxygen was placed in the reaction cell and photolysed periodically for 100s by all four low pressure mercury lamps. The P and Q counters were started simultaneously with the photolysis, and their respective values were noted at the end of the 100s.

3.2.2   Analysis of the MMS Results

The results from the MMS are read as in-phase and in-quadrature counts, P and Q. In this form, it is difficult to relate the results to actual concentrations of radicals. The counts are converted into absorbances using the following formula:

$$A = \frac{P \ count}{F.I_o} \qquad (3.1)$$

where F is the calibration factor, (348.3 ± 1.4) counts mV^{-1}, and I_o is the base signal onto which the radical signal is superimposed. This base signal is measured as a voltage directly from the PM tube and is usually set in the absence of radicals to 1V, by adjusting the input voltage to the PM tube. In these experiments the actual value was 975mV, as any higher voltage resulted in squaring of the signal, due to its becoming too strong for the operating range of the V-F converter.

The absorbances can then be converted in to radical concentrations by using the Beer-Lambert Law:

$$\text{Absorbance, } A = \sigma.c.l \qquad (3.2)$$

where σ is the absorption cross-section, c is the concentration of the absorbing species, and l is the path length of the cell.

3.2.3 The Photolysis Rate of Ethanal

Two experiments were performed with the aim of determining B, the photolysis rate of ethanal in this system. The mixture of ethanal and oxygen was photolysed constantly for an extended period (around 5000s) using all four lamps. At intervals during this time the concentration of ethanal was monitored by performing a periodic photolysis, using a photolysis period, τ, that gave a steady state of radicals, and noting the P count. The experiments performed had τ values of 5.0s and 10.0s as it was believed that at these photolysis periods, such a steady state would be reached.

A plot of log(P count) against photolysis time is expected to give a straight line with a negative gradient. However, Figure 3.1 clearly shows that the results obtained in these experiments do not yield straight line plots. This is a consequence of secondary chemistry in the system, and it makes it more difficult to extract the information from the data in the normal way. The chemistry resulting from the ethanal photolysis is shown below.

While it was not possible to determine the ethanal photolysis rate from Figure 3.1, it can be seen that the results for the experiment with $\tau = 5.0$s and those from the experiment with $\tau = 10.0$s are very similar. This shows that A_o, the maximum absorbance by radicals, achieved when the radical signal approximates a square wave, has been reached with a photolysis period of 5.0s.
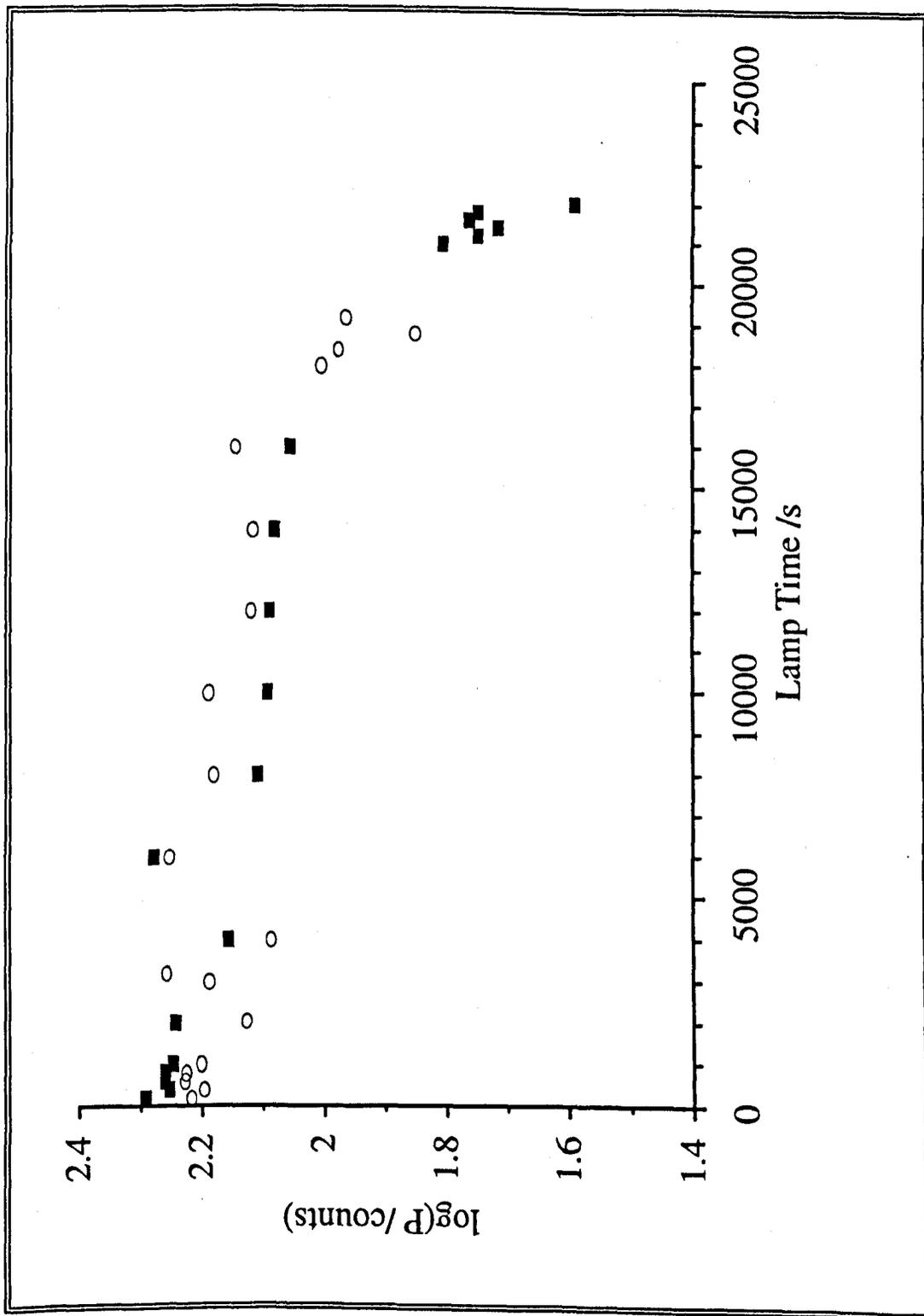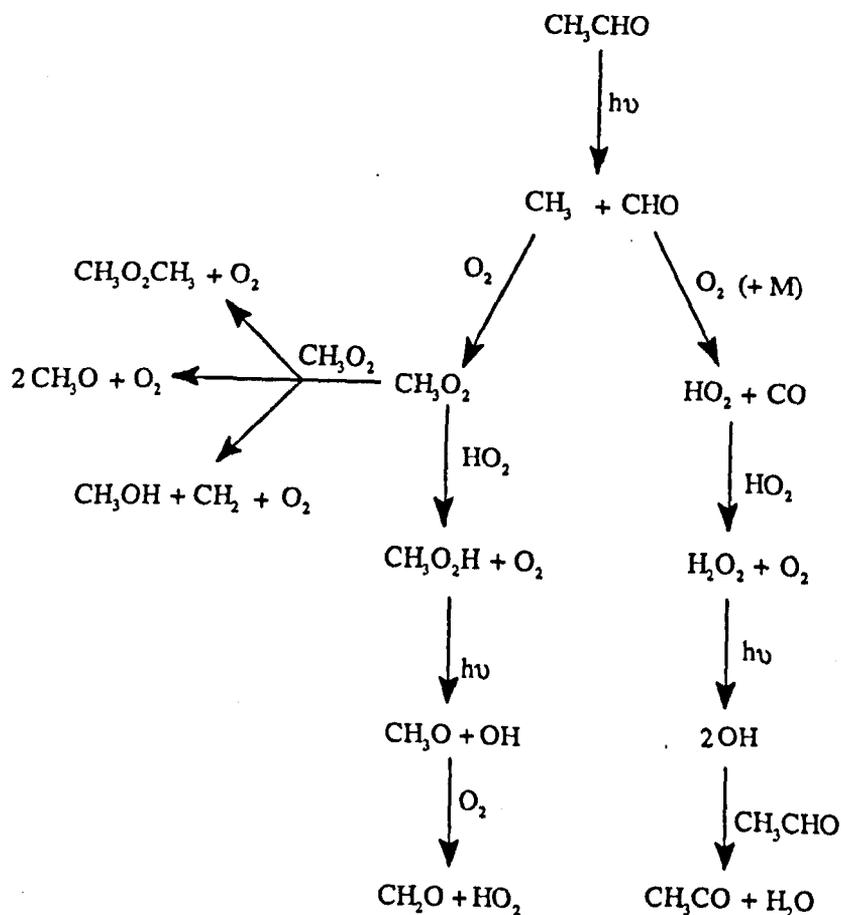
Figure 3.1 Decay of log(P) with Time. ■ $\tau = 5.0s$; ○ $\tau = 10.0s$; 500 mbar of 4% CH_3CHO in O_2; $\lambda = 245nm$; $I_o = 975mV$.

The main reactions that accompany the photolysis of ethanal in the presence of O_2

$$CH_3CHO$$

$\downarrow h\upsilon$

$$CH_3 + CHO$$

$O_2 \swarrow \qquad \searrow O_2 (+ M)$

$CH_3O_2CH_3 + O_2$

$2 CH_3O + O_2 \leftarrow \overset{CH_3O_2}{\nwarrow \leftarrow} CH_3O_2 \qquad HO_2 + CO$

$CH_3OH + CH_2 + O_2$

$\downarrow HO_2 \qquad\qquad \downarrow HO_2$

$CH_3O_2H + O_2 \qquad H_2O_2 + O_2$

$\downarrow h\upsilon \qquad\qquad \downarrow h\upsilon$

$CH_3O + OH \qquad 2 OH$

$\downarrow O_2 \qquad\qquad \downarrow CH_3CHO$

$CH_2O + HO_2 \qquad CH_3CO + H_2O$

3.2.4 Variation of Photolysis Period

A series of experiments was also performed to determine k_2, the second order rate constant for radical loss. In these, the photolysis period, τ, was varied while the total experiment time was kept constant at 100s. It was expected that this would provide a value of τ_0, the cross-over point of the P and Q lines. However, it can be seen from Figure 3.2 that the data for the cross-over region are too scattered to be reliably used in this case.

The scatter in the data is a consequence of noise from the internal multiplexing of the counter chip, caused by a fault. The switching operations in the chip itself produced electronic noise which interfered with the output line from the chip. As a result, the faster the switch rate, the greater the noise in the signal. In better quality chips the internal design prevents such noise from arising. Although attempts were made to filter out the noise by buffering the signal, these were not successful.

Further problems occur due to the mixed nature of the radicals produced. Traditional MMS experiments use a precursor that yields only one type of radical. This is not the case in these experiments, as two radical species are formed, which complicates the loss processes.

$$CH_3O_2 + CH_3O_2 \rightarrow Products \qquad\qquad 3.9$$
$$HO_2 + HO_2 \rightarrow Products \qquad\qquad 3.10$$
$$CH_3O_2 + HO_2 \rightarrow Products \qquad\qquad 3.11$$

The standard analysis procedure relies on the radical loss kinetics being either first or second order. Had reaction 3.9 been the sole loss channel, then the kinetics would indeed have been second order. However, this was not the case, as reactions 3.10 and 3.11 also play important roles, so in these experiments the radical loss kinetics were of mixed order. Analysis of the data was performed using computer modelling, as discussed in section 3.2.5 below.

At the longer photolysis periods ($\tau \geq 5.0s$), the noise is less significant so the value of A_o, the maximum absorption, is more reliable. A computer model of the chemistry involved was used in conjunction with published absorption cross-sections to determine a photolysis rate from this data. This is discussed in section 3.2.5 below.
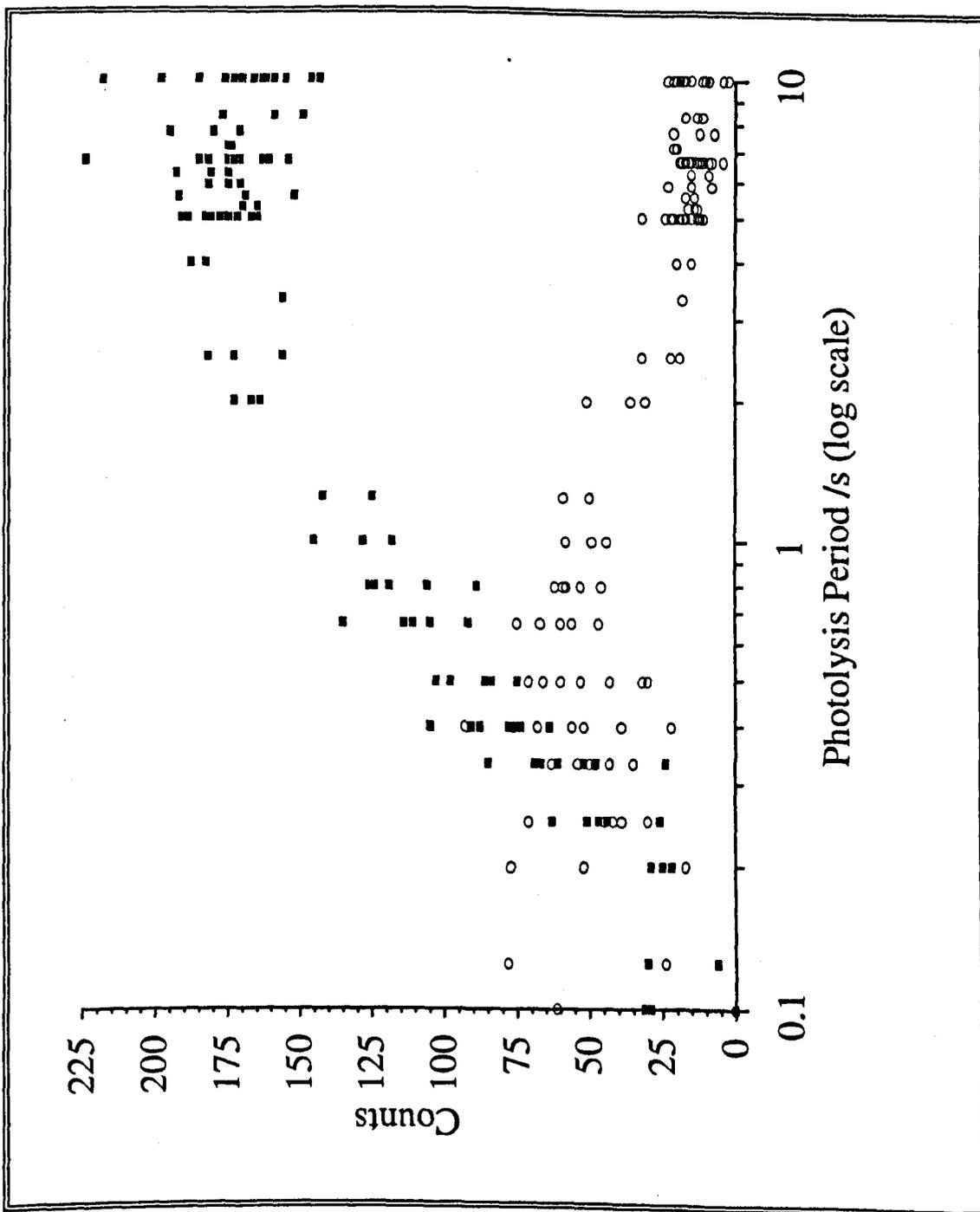
Figure 3.2   Variation of P and Q Values with τ. ■ P count: o Q count: 500mbar 4% CH_3CHO in O_2: $\lambda = 245nm$: $I_o = 975mV$

3.2.5 Computer Modelling of MMS Results

A scheme was developed to simulate the chemistry that took place upon photolysis of a reaction mixture. This was run in the Simula programme discussed in section 2.5 using published rate data. The model was run for 5s of reaction time and the concentrations of absorbing species were noted. These were combined, with the appropriate absorption cross-sections at 245nm to produce a total absorbance. The rate constant for the photolysis of ethanal was adjusted until the total absorbance matched that determined from the MMS experiments. The chemical model is shown in Table 3.i

The absorption cross-sections of the important absorbing species were as follows:

CH_3O_2 $\sigma_{245nm} = 4.38 \times 10^{-18}$ cm^2 molecule^{-1}

HO_2 $\sigma_{245nm} = 8.1 \times 10^{-19}$ cm^2 molecule^{-1}

$HOCH_2O_2$ $\sigma_{245nm} = 3.29 \times 10^{-18}$ cm^2 molecule^{-1}
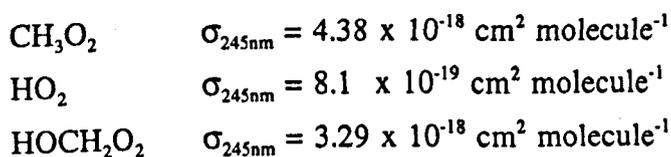
All absorption cross-sections are from *Lightfoot et al.* [1992]. The model also predicted that H_2O_2 ($\sigma_{245nm} = 1.00 \times 10^{-19}$ cm^2 molecule^{-1}) would absorb strongly. However, because H_2O_2 is a stable product, its absorption would be constant and not modulated by the lamp output. As such it would give equal counts in both the up and down phases and therefore would not influence the final result of the P-Q counters. The resultant total absorbance is plotted against the photolysis rate constant in Figure 3.3.

The analysis gives a gradient which is the product of the number of lamps, n, and the photolysis rate constant per lamp, γ.

$$n.\gamma = 2.52 \times 10^{-4} \text{ s}^{-1}$$

as n = 4,

$$\gamma = 6.3 \times 10^{-5} \text{ s}^{-1}$$

This is the photolysis rate constant for a uniform intensity output from the lamp over the entire flash duration and so can be used to calculate the number of radicals generated by a flash of much shorter length.

Table 3.i Reaction Scheme Used in Evaluating Data from MMS Experiments

No.	Reaction	k	Ref. /Notes
1.	$CH_3CHO + h\upsilon \rightarrow CH_3 + CHO$	2.52×10^{-4} s^{-1}	a
2.	$CH_3 + O_2 (+ M) \rightarrow CH_3O_2 (+ M)$	1.1×10^{-11}	16 b
3.	$CHO + O_2 \rightarrow CO + HO_2$	5.5×10^{-12}	16
4a.	$CH_3O_2 + CH_3O_2 \rightarrow 2CH_3O + O_2$	1.23×10^{-11}	16 c
4b.	$CH_3O_2 + CH_3O_2 \rightarrow CH_3OH + HCHO + O_2$	1.23×10^{-11}	16 c
4c.	$CH_3O_2 + CH_3O_2 \rightarrow CH_3OOCH_3 + O_2$	1.23×10^{-11}	16 c
5.	$CH_3O_2 + HO_2 \rightarrow CH_3O_2H + O_2$	5.2×10^{-12}	16
6a.	$HO_2 + HO_2 \rightarrow H_2O_2 + O_2$	1.6×10^{-12}	16
6b.	$HO_2 + HO_2 (+ M) \rightarrow H_2O_2 + O_2 (+ M)$	6.4×10^{-13}	16 d
7.	$CH_3O + O_2 \rightarrow HCHO + HO_2$	1.9×10^{-15}	16
8$_f$.	$HCHO + HO_2 \rightarrow HOCH_2O_2$	7.9×10^{-14}	16
8$_b$.	$HOCH_2O_2 \rightarrow HCHO + HO_2$	1.5×10^{2} s^{-1}	16
9a.	$HCHO + h\upsilon \rightarrow H + CHO$	1.26×10^{-4} s^{-1}	e
9b.	$HCHO + h\upsilon \rightarrow H_2 + CO$	1.26×10^{-4} s^{-1}	e
10.	$CH_3CHO + OH \rightarrow CH_3CO + H_2O$	1.6×10^{-11}	16
11.	$CH_3CO + O_2 \rightarrow CH_3COO_2$	5.0×10^{-12}	16
12.	$CH_3COO_2 + CH_3COO_2 \rightarrow 2CH_3CO_2 + O_2$	1.6×10^{-11}	16
13.	$CH_3CO_2 (+ O_2) \rightarrow CH_3O_2 + CO_2$	1.1×10^{-11}	16 f
14a.	$CH_3COO_2 + HO_2 \rightarrow CH_3CO_2H + O_3$	2.5×10^{-12}	g
14b	$CH_3COO_2 + HO_2 \rightarrow CH_3CO_3H + O_2$	5.9×10^{-12}	g
15a.	$CH_3COO_2 + CH_3O_2 \rightarrow CH_3CO_2H + HCHO + O_2$	5.5×10^{-12}	h
15b.	$CH_3COO_2 + CH_3O_2 \rightarrow CH_3O + CH_3CO_2 + O_2$	5.5×10^{-12}	h
16.	$CH_3CO_2H + OH \rightarrow CH_3CO_2 + H_2O$	8.0×10^{-13}	16

Notes

a)   See sections 3.2.5 and 3.2.6 for the explanation of how this rate was determined.

b) $k_o = 1.0 \times 10^{-30}$ molecule^2 cm^{-6} s^{-1}, $k_{inf} = 2.2 \times 10^{-12}$ molecule cm^{-3} s^{-1}, $f_c = 0.27$

c)   See *Atkinson et al.* [1992] for a discussion on this reaction

d) $k = 5.2 \times 10^{-32}[N_2]$ molecule cm^{-3} s^{-1}

e)   Calculated by scaling the photolysis rate used for CH_3CHO according to the respective absorption cross-sections at 254nm.

f)   The rate used is that for reaction 2 as $CH_3CO_2 \rightarrow CH_3 + CO_2$ is assumed to be effectively instantaneous.

g)   Overall rate from *Atkinson et at.* [1992]. Branching ratio determined as k14a/(k14$_a$ + k14$_b$) = 0.3 by Sanderson [1994].

h)   Rate constants used are k($CH_3O_2 + CH_3O_2$), see note c.
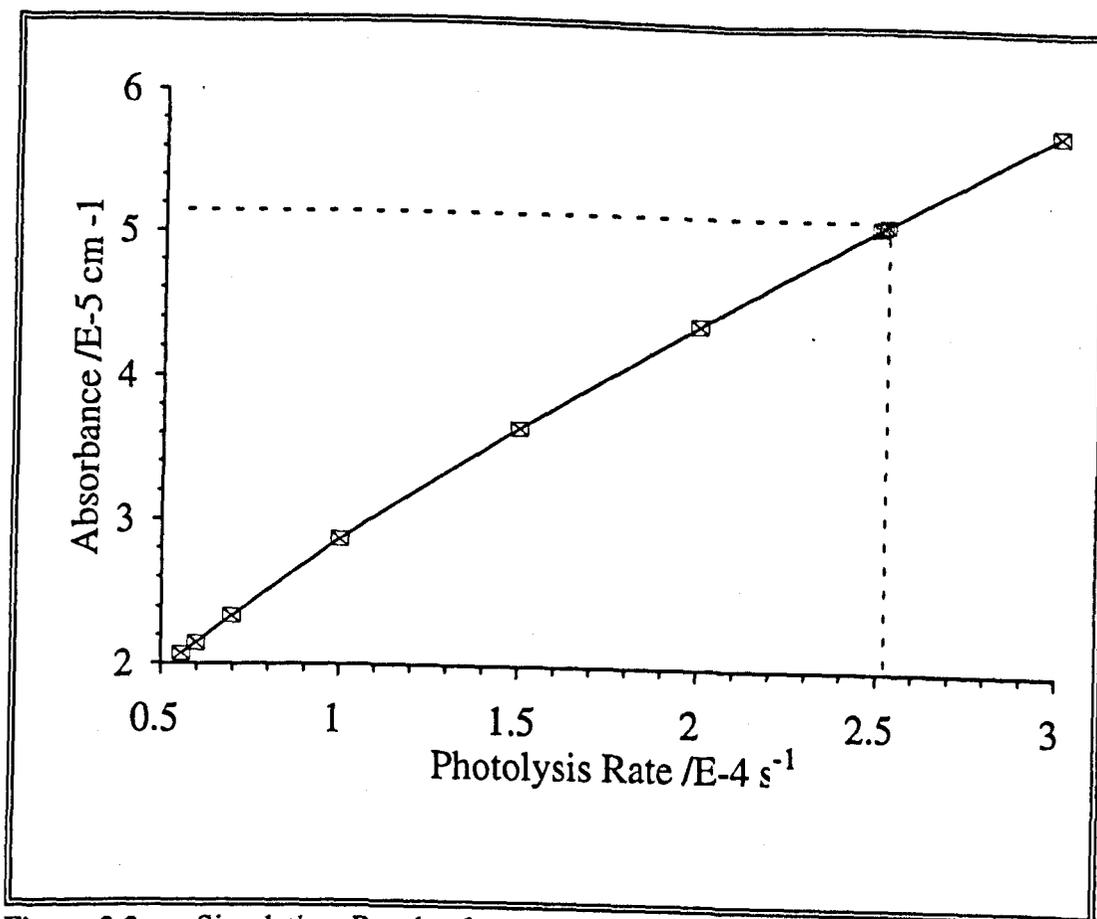
Figure 3.3   Simulation Results for the Total Absorbance after 5s for Varying Ethanal photolysis Rate Constants

### 3.2.6   Profile of the Photolysis Lamp Output

In order to justify using the γ value calculated above, it was necessary to measure the intensity profile of the lamp over the flash durations used in the chemical amplification work.   This is because the photolysis rate was calculated using photolysis periods of greater than 1s, while the amplification studies were performed with photolyses of 1ms.   While it may be reasonable to assume that the output from the lamp is a square wave at the longer times it cannot be assumed that this is still true at 1ms.   A fast sampling A-D converter system was used to monitor the profile at short photolysis periods.
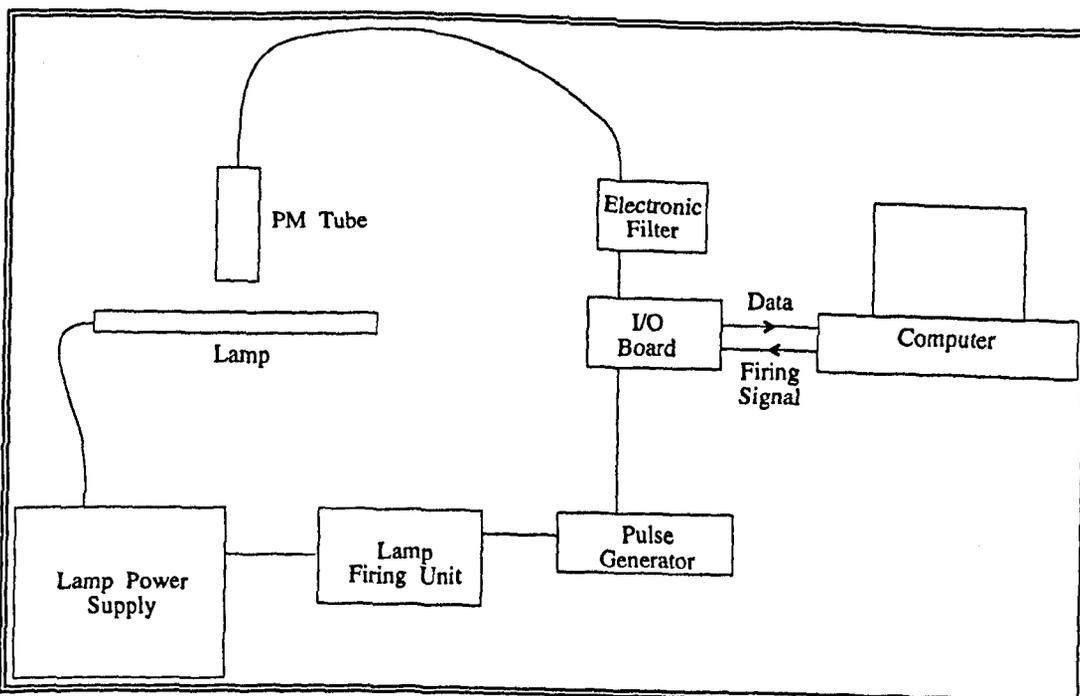
Figure 3.4   Schematic Diagram of the Apparatus used to Measure the Intensity Profile of the Photolysis Lamp

The apparatus used is shown in Figure 3.4. When the lamp was fired using a signal from a computer, the I/O chip sent the signal to the pulse generator which output a signal of the required duration to the lamp. The PM tube detected the output from the lamp and sent a signal, via electronic alias filtering, back to an input channel on the I/O chip. One reading was taken every 24.8μs. During the sampling the data were stored in the transputer chip memory, from where it was passed to the computer once the sampling was complete, and stored as an ASCII text file. For details of the software used to control this operation see the work of *Lawes* [1993; 1994].

The lamp intensity was measured for 10 independent flashes at durations of 1, 2, 5 and 10ms each, and for 5 flashes at 500ms. Measuring flashes in excess of this length would have created data files of unmanageable size, and was not necessary as all the required information could be obtained from these flash durations. A plot of typical profiles at these flash lengths is shown in Figure 3.5.
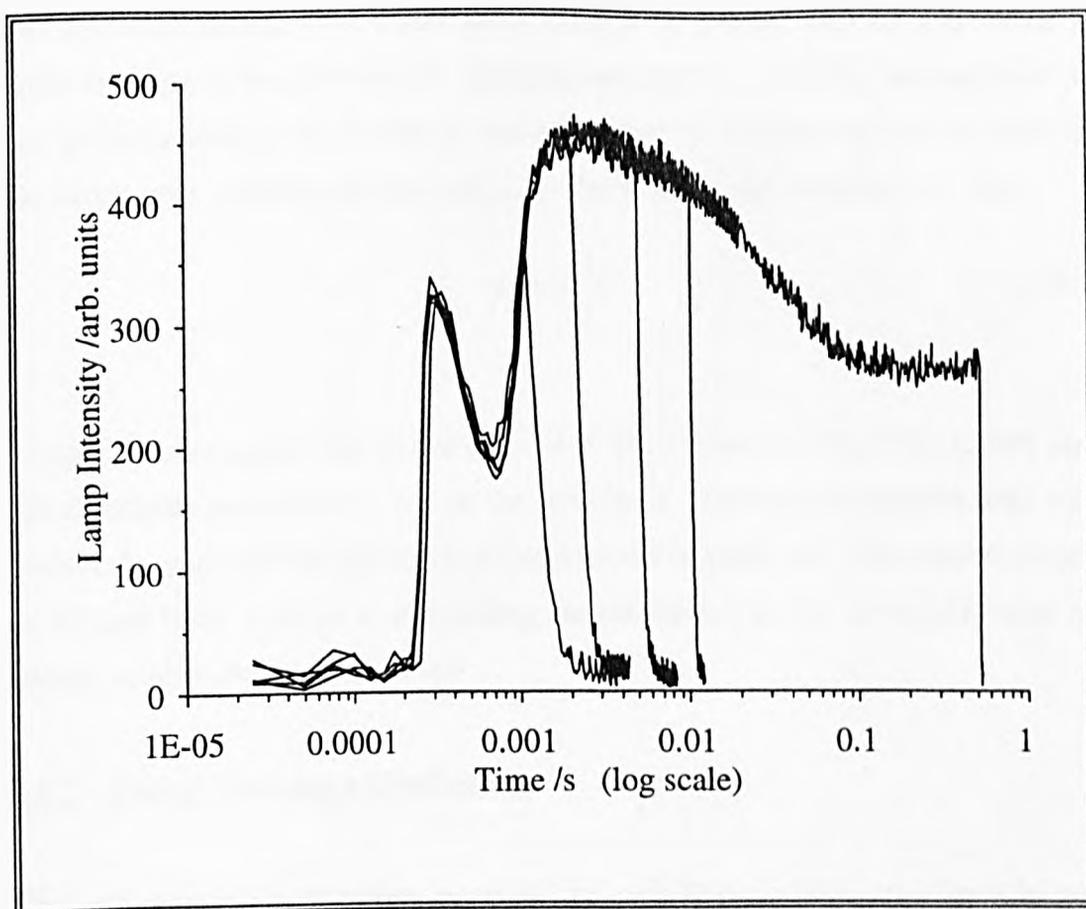
Figure 3.5   Lamp Intensity Profiles for Flash Durations of 1, 2, 5, 10 and 500ms

It was found that the intensity profiles were very consistent, but were not the square form that had been expected. Instead they showed that the lamps had an initial rise and fall, followed by a further rise, after which the intensity fell to a constant value. The lamp did not reach a uniform intensity for almost 100ms. As a result the value of γ calculated in section 3.2.5 could not be used directly, but instead the intensity profile had to be simulated. A model reaction scheme was used to calculate the number of radicals generated during each flash. An integral part of the model was a variable ethanal photolysis rate constant, γ, so that the profiles shown in Figure 3.5 could be recreated.

In order to perform this simulation, it was necessary to match the intensity at any point on a profile with a γ value that could be used in the model. The γ value calculated from the MMS modelling (6.3×10^{-5} s^{-1}) was assumed to be a result of the steady intensity shown after 100ms, I_u, (the error involved in doing this is small;

73

the difference between the actual area under a 5s profile, and the area under a uniform output at that intensity is approximately 0.5%). The rate constant used at any particular time in the model, γ_t, was calculated by multiplying γ by the ratio of the actual lamp intensity at that time, I_t, to the steady lamp intensity, I_u. Thus:

$$\gamma_t = \gamma \cdot \frac{I_t}{I_u} \qquad (3.3)$$

Using this information, the model calculated the number of HO_2, CH_3O_2, HO and CH_3O radicals present at the end of the photolysis. The reaction scheme used was that for the amplification chemistry of DME shown in Table 3.iii. The concentrations of NO and DME were set to zero during the simulations so that no amplification of radical number density could occur.

3.2.7 Radical Generation Conclusions

The total radical concentrations generated by each flash duration are shown below, in Table 3.ii.

Table 3.ii Radical Number Densities Generated by Each Photolysis Duration.

Photolysis Period /ms	[Radicals]				
	$[HO_2]$ $/x10^9$ cm^{-3}	$[CH_3O_2]$ $/x10^9$ cm^{-3}	$[HO]$ $/x10^3$ cm^{-3}	$[CH_3O]$ $/x10^4$ cm^{-3}	Total $/x10^9$ cm^{-3}
1.0	2.06	2.21	2.39	0.02	4.27
1.5	3.28	3.52	2.38	0.04	6.80
2.0	4.47	4.81	2.39	0.09	9.28
3.0	7.05	7.58	2.39	0.22	14.6
5.0	12.0	13.0	2.42	0.66	25.0
25.0	61.0	65.7	2.96	17.4	127

In all cases $[CH_3CHO] = 2.46 \times 10^{16}$ molecule cm^{-3} ($\equiv$1mbar at T = 298K), $[O_2] = 4.90 \times 10^{18}$ molecule cm^{-3} (199mbar) and the total cell pressure was 500mbar. The uncertainties involved in calculating the densities shown above are considered in section 3.3.7.

The initial concentration of ethanal was chosen as 2.46×10^{16} molecule cm^{-3} because it was believed that a 1ms photolysis of this would provide an HO$_2$ concentration of the order of 10^8 cm^{-3}, the same order believed to be present in the atmosphere. Unfortunately, Table 3.ii shows that the HO$_2$ yield was actually greater, around 10^9 cm^{-3}. This is a result of the photolysis rate of ethanal being faster than that indicated by the primary analysis of the MMS data. However, the total radical concentration is of the same order as that found in the troposphere [*Cantrell et al.*, 1992], and the elevated HO$_2$ concentration is not expected to compromise the study, as the system response to the initial radical concentration is predicted to be linear (see Chapter 4).

3.3   Chemical Amplification Experiments

3.3.1   Experimental Procedure

All the experiments discussed below were performed following the same procedure. A reaction mixture containing the appropriate amounts of NO, DME, ethanal and O$_2$, was made in a mixing bulb using N$_2$ as the bath gas. All mixtures were mechanically stirred, and left for over 30 minutes to ensure complete mixing occurred.

A typical mixture contained 0.6 ppm (1.48×10^{13} molecule cm^{-3}) NO, 160 mbar (3.94×10^{18} molecule cm^{-3}) DME, 2 mbar (4.92×10^{16} molecule cm^{-3}) ethanal and 398 mbar (9.79×10^{18} molecule cm^{-3}) O$_2$, diluted to 1000 mbar with N$_2$. These concentrations were chosen so that the concentration of O$_2$ was that of ambient air, while those for NO and DME were predicted by initial modelling of the system to provide the optimum chain length. The concentration of ethanal, as stated above, was chosen as it was believed that a 1ms photolysis would produce a number density of radicals close to that found in ambient air. Although it has been shown that this was not the case, it does not affect the experiments.

Unphotolysed blank samples (henceforward referred to as 'blanks') were passed into the NO$_x$ analyser using a sample loop, similar to those used for gas chromatographic analysis of gas samples. The sample loop was filled to a pressure of 400 mbar with the mixture and then closed. Argon, from the NO$_x$ analyser carrier stream, was

allowed into the loop, to a pressure of around 970 mbar and the loop was again closed. This diversion of argon caused a drop in the pressure of the carrier stream which in turn caused a peak in the output from the analyser. Once this pressure peak had subsided and the baseline was re-established the carrier flow was redirected through the loop, thus flushing the entire sample into the analyser. This was done three times for each mixture so that the uncertainties involved in the procedure could be reduced by averaging the results.

The reaction cell was then filled with 500 mbar of the mixture. While the sample was being introduced to the cell, the lamp RF pre-ionizer was kept on, but the lamp heaters were switched off. Once the cell was filled, the lamp heaters were switched on, and after 5s the lamp was fired. The heaters and pre-ionizer were switched off immediately after the flash. This was to reduce any photolysis of the sample not due to the actual lamp flash. Ideally, the pre-ionizer would also have been off when the sample was added to the cell, but it did not prove possible to recharge reliably the pre-ionizer immediately before a flash, and so the charging had to be done at a time when the lamp could safely be allowed to come on.

The contribution to the photolysis of the pre-ionizer was assessed by several experiments where mixtures were placed in the cell, with the pre-ionizer on, without being photolysed and left for equivalent times to a normal experiment before the samples were taken. In addition, other experiments were carried out, as above, except that the pre-ionizer was off throughout the experiment. Although these experiments showed no significant difference from the 'blanks', the procedure of keeping the light level in the cell to a minimum at all times was continued in an attempt to reduce the errors involved.

The mixture in the cell was allowed to stand for at least 5 minutes before the first sample was admitted into the sample loop. Three samples of the mixture were passed into the analyser in the same way as the blanks, with, typically, around 10 minutes between each sample. No systematic difference between the peaks that would suggest that either the reaction, or the mixing, was incomplete when the samples were taken, could be detected. The subject of the time it took for the reaction to come to completion is discussed further in section 3.4.1.

Several experiments were performed with a further series of 'blanks' after the photolysed samples taken. These showed no change in peak area between the two sets of 'blanks'. In addition, several samples containing only N_2 were passed through the analyser to test for any peak due to the sampling method. No such peak could be detected. As a final check for systematic errors in the experimental method several experiments were performed in exactly the same way as normal except that the lamp was not fired. These showed no significant difference between the blanks and the samples that had been in the cell.

The analogue output from the analyser was passed to an A-D card in a computer which sampled every 1s. The digitised data set was stored as an ASCII file and the peak areas were integrated using the data analysis functions of the WinFirst programme. Although this programme is intended for the control of Matteson Fourier Transform Infrared Spectrometers, the spectrum analysis functions proved effective in dealing with the output from the A-D card. However, before this could be used a column of time data had to be added to the file in order to provide an x-axis for the plot. This was performed by a programme listed in Appendix 2.

The concentration of NO in the samples was calculated using the calibration method discussed in section 2.3.1 and the average of the three peak areas obtained. The chain length, CL, was calculated as the difference between the concentration of NO in the unphotolysed and photolysed samples, divided by the concentration of radicals produced by the flash that were calculated in section 3.2.

During the experiments, it was found that the ethanal would degrade over a period of a few days if it was not kept cool and in the dark. Failure to do so resulted in the production of insufficient numbers of radicals, and no amplification could be detected. In order to test the purity of the ethanal, mixtures of 4% ethanal in O_2 were occasionally made, and photolysed in the MMS. The P and Q counts were compared with earlier results. In the event of a significant (>5%) decrease in the counts the ethanal was discarded and replaced. All ethanal handling was performed under vacuum or a nitrogen atmosphere.

3.3.2 Laser-Induced Fluorescence Analysis

Laser-induced fluorescence was first used for monitoring NO_2 by *Birnbaum* and co-workers. In their original work, either an Ar^+ ion or HeCd laser was used to excite the NO_2 at 488nm or 442nm respectively [*Gelbwachs et al.*, 1972]. In later work, only the HeCd laser was used [*Tucker et al.*, 1973 and 1974], as is the case in the present study. They developed a detector for measuring ambient concentrations of NO_2 [*Birnbaum*, 1974] with a reported detection limit of approximately 1.8×10^{10} molecule cm^{-3} (0.6ppb) [*Birnbaum and Tucker*, 1974; *Tucker et al.*, 1975; *Birnbaum*, 1976 and *Fincher et el.*, 1978]. It has also been used successfully in evaluating the kinetics of some NO_2 reactions [*Anastasi and Hancock*, 1988; *Broomfield*, 1992].

It was believed that using the laser-induced fluorescence of NO_2 to follow the chemical amplification chemistry *in situ*, was potentially more accurate than taking samples from the cell and passing them through the chemiluminescence analyser. The principal advantage was that the growth in the signal would be followed from a baseline, rather than being taken from the difference in two larger signals. However, the work on the experiments involving the photolysis of NO_2 in the presence of 2-butyne suggested that the existing LIF apparatus would not be sensitive enough for this. Accordingly, several aspects of the system were considered and improved.

The fluorescence collection optics were redesigned so that greater discrimination between genuine NO_2 fluorescence and light from other sources, such as scattered laser radiation or component fluorescence, could be achieved. Originally, the light was collected by a 50mm focal length ($f = 50mm$) biconvex lens placed directly under the top of the cell complex, close to its focal length above the line of the laser so that light from the fluorescence would be passed as a parallel beam through the filter and into the PM tube. The region between the lens and the PM tube was shielded by a blackened cylinder (Figure 3.6a).

Photomultiplier
Tube Surface

Filter

Cell complex top

Photolysis Lamp

40mm focal
length lens

Quartz cell

HeCd
Laser
in

(a). Original Optical Arrangement

Photomultiplier
Tube Surface

Mounted Filters
Iris Diaphragm

Spacer

Cell complex top

Photolysis Lamp

20mm focal
length lens

Quartz cell

HeCd
Laser
in

(b). Modified Optics
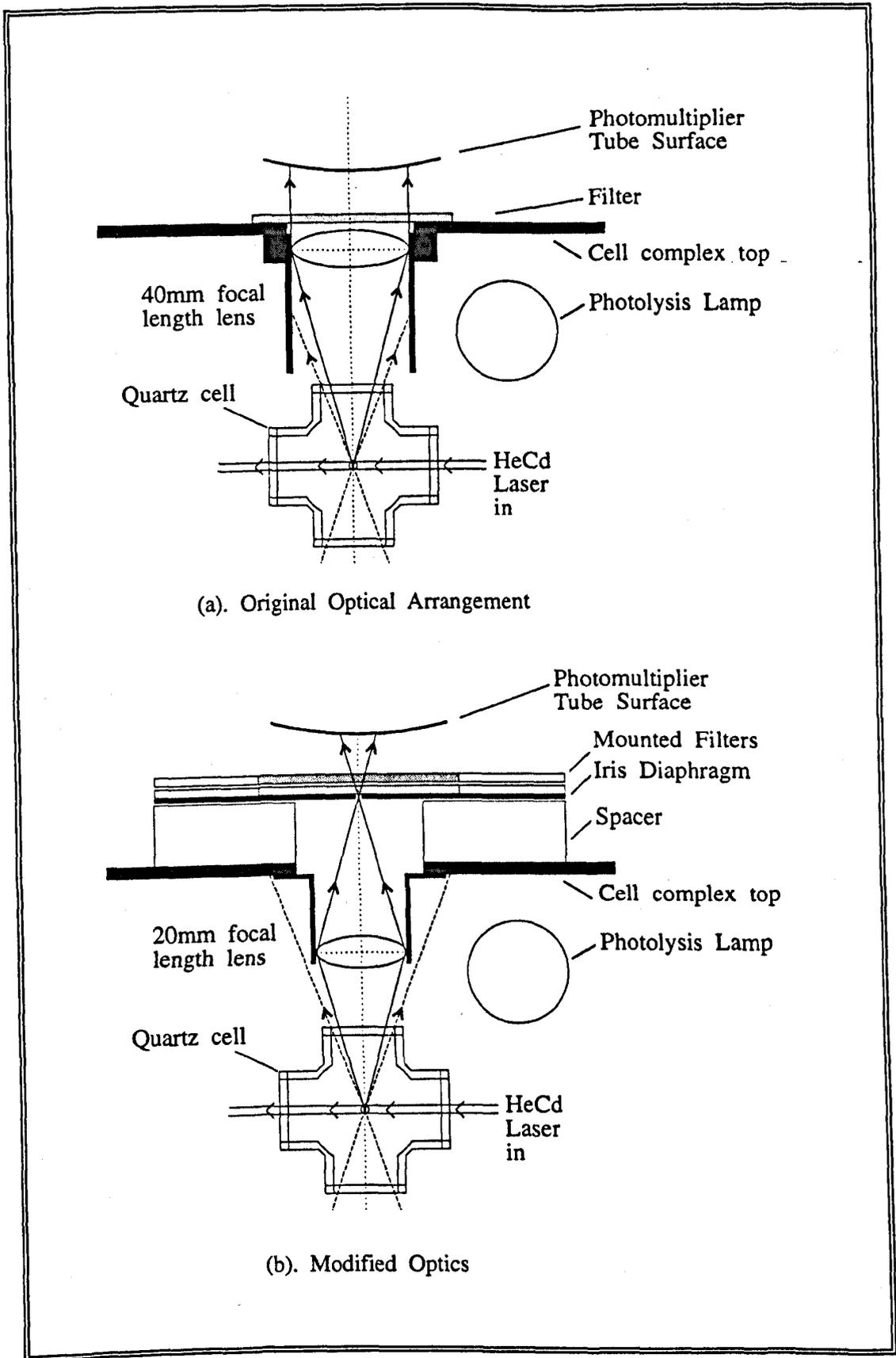
Figure 3.6   Changes Made to the Optical Design of the LIF Apparatus. (a) shows the original arrangement, (b) shows the arrangement used in this work.

79

This was changed so that the light was collected by a 20mm biconvex lens situated 40mm above the fluorescence source. With this configuration, the lens was $2f$ from the source, so genuine fluorescence would be collected by the lens and focused to a point $2f$ above the lens. An iris was placed $2f$ above the lens so that only light focused in this way could pass through (Figure 3.6b). Consequently, the amount of scattered laser radiation reaching the PM tube was reduced. It should be noted that the fluorescence is, of course, not a point source, but a column along the path of the laser. This, however, is only important when considering the diameter of the iris.

The lens used had a diameter of 22.4mm, as this was all that was available commercially at that time. Assuming the fluorescence had come from a point source, then the cone of light passing through the top window of the cell would have reached a diameter of approximately 28mm at the height of the lens. If the effects of distortion at the edge of the lens are ignored and it is assumed that focusing is performed correctly over the entire area of the lens, then an analysis of the area of light that would be collected, compared to that available, shows that approximately 36% of the signal is lost. If lens edge distortion is considered, and hence it is assumed that light is only focused properly over the central region within, say, 10mm of the centre, then 51% of the signal is lost.
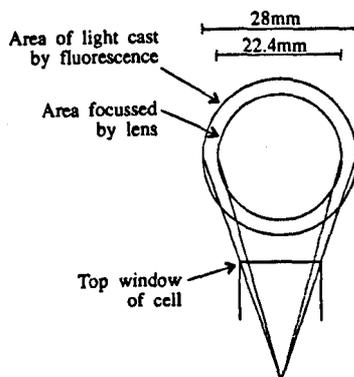
Area of outer circle $= \pi.r^2$

$= \pi.14^2$

$= 616$ mm^2

Area of inner circle $= \pi.11.2^2$

$= 394$ mm^2

$\therefore$ Signal lost $= 36\%$

Filters were placed immediately above the iris. In the NO_2/2-butyne work a single 590nm cut-on filter was used to help reduce the effect of non-genuine signals. This was modified so that 495nm, 530nm or 590nm filters could be used, either individually, or in combination; two of each filter were available. While using multiple filters would reduce the amount of stray light, they would also reduce the strength of the fluorescence signal, as reflections occur at each surface of the filters. Experiments were carried out to determine which filter, or combination of filters gave the best signal-to-noise ratio. The fluorescence signal was measured for 5 minutes to establish a background value, before approximately 125 mbar of 1% NO_2 in N_2 were added and the signal measured for a further 5 minutes. In this way, it was determined that the best signal-to-noise ratio was obtained using a single 495nm filter.

It was also found that the signal contained more noise when the fluorescence lights that provide ambient lighting for the laboratory were on, so all measurements were performed with these lights off. Ambient lighting was provided by an incandescent bulb scattered off a wall. As the cell complex was thoroughly sealed to make it light-proof, it is assumed that this increase in noise was due to electronic interference. Figure 3.7 below shows a typical result from one of these experiments. The reduction in the noise when the lights are off can clearly be seen.

If the fluorescence had emanated from a true point source, it could then have been focused and passed through a point iris. However, the beam width of the laser was around 2mm, which suggested the use of an iris with a diameter, ϕ, of 2mm. Additionally, even if the width of the beam is considered, it must also be born in mind that the fluorescence will emanate, not just from the centre of the cell, but from the entire length of the beam inside the cell. Hence the image produced by the lens on the iris will not be of a point, but an elipse. Consequently, the diameter of the iris had to be such that it collected as much of the fluorescence as possible, while preventing the passage of light from other sources. It was found that using a 4mm iris provided the best signal-to-noise ratio.
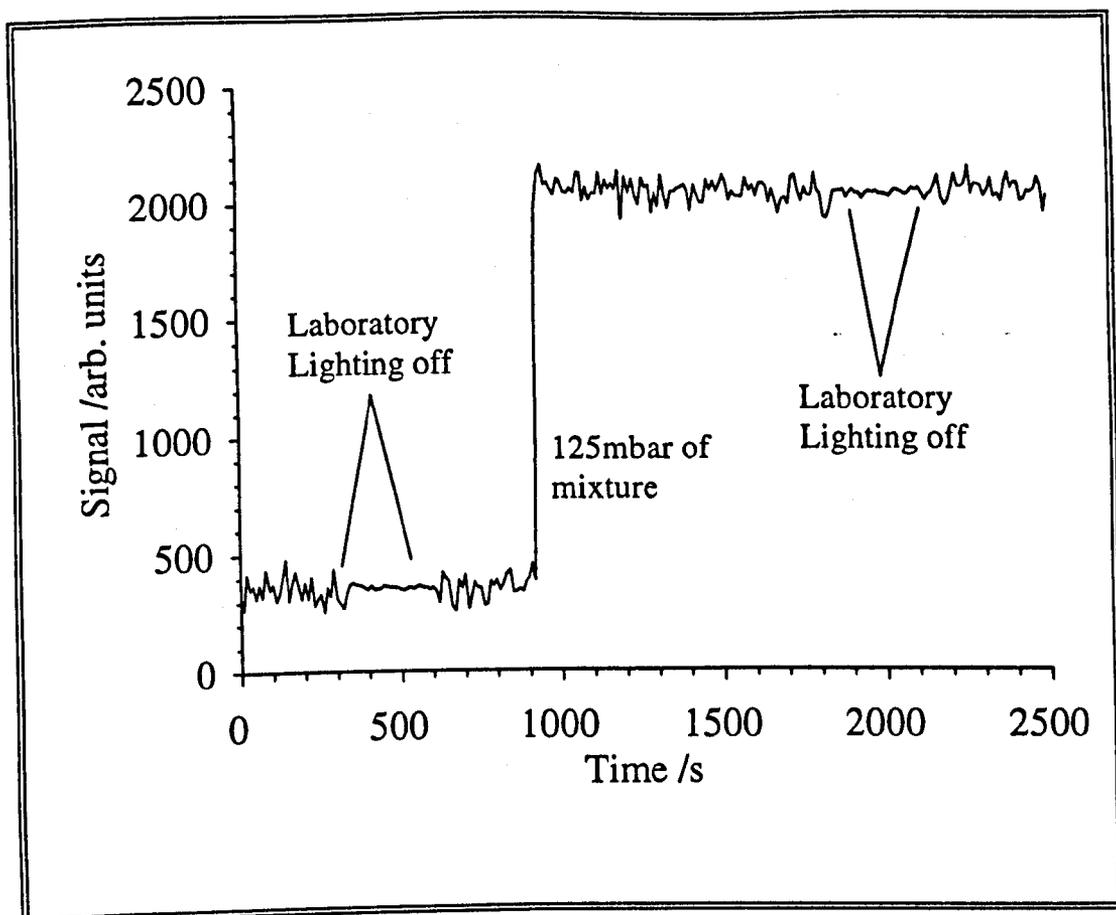
Figure 3.7   Typical Laser-induced Fluorescence Result.
125 mbar 1% NO_2/N_2; Filter = 495nm only; ϕ = 2.5mm; υ = 497Hz.

The frequency of the chopper, υ, used to attenuate the signal for the phase-sensitive detection was also considered. Different frequencies were tried at 100Hz intervals between 497Hz, the frequency used in the NO_2/2-butyne work, and 993Hz. Multiples of 50Hz were avoided to limit interference from signals produced by the mains electricity supply.

Varying the frequency of the chopper had a marked effect on the results from a 50 mbar sample of 1% NO_2/N_2, with the signal-to-noise ratio apparently more than doubling, from 361:1 at the original 497Hz, to 847:1 at 793Hz (Figure 3.8). While increasing the frequency of the chopper reduced the noise in the signal, it also reduced the signal itself and so the optimum frequency was a compromise between the size of the noise, and that of the signal.
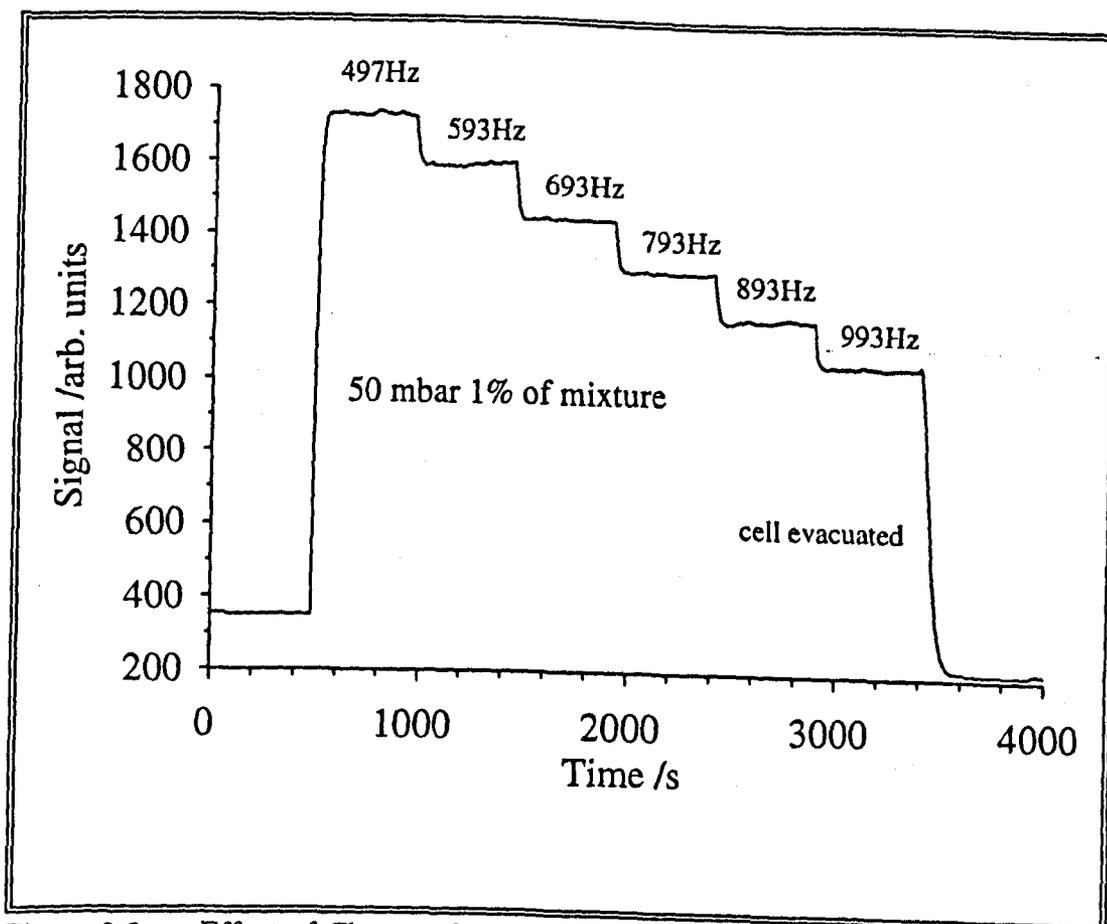
Figure 3.8   Effect of Chopper frequency on Fluorescence Signal.
50 mbar of 1% NO_2/N_2; Filter = 495nm; ϕ = 4.0mm

Ultimately, the optimum conditions for this apparatus were found to be those shown in Figure 3.8, and listed below:

Filter = 495nm only

ϕ = 4mm

υ = 793Hz

Under these conditions, a signal-to-noise ratio of 847:1 could be obtained for a 50 mbar sample of 1% NO_2/N_2. Unfortunately, some of the sources of noise were independent of the signal strength; among these was a periodic sine wave fluctuation in the power of the laser. Consequently, the signal-to-noise ratio for a 50 mbar sample of 100ppm NO_2/N_2 was only 26:1 and it was not possible to distinguish the fluorescence from the background for 1ppm mixtures.

The largest production of NO_2 in the chemical amplification experiments carried out with chemiluminescence analysis, was of the order of 1ppm. Also, in the amplification experiments the NO_2 is formed in a mixture containing large quantities of DME and ethanal, both of which are more effective at quenching fluorescence than N_2 on its own. Consequently, having established that the optimum conditions for LIF in the present system were not sufficiently sensitive to detect the expected concentrations of NO_2, no chemical amplification experiments involving monitoring by LIF were performed.

3.3.3 Computer Modelling of Results

Computer models of the chemistry (Table 3.iii and Table 3.iv) were used to simulate the experiments discussed below. In order to replicate accurately the conditions in the cell it was necessary to account for the heterogeneous loss of radicals following their diffusion to the cell walls. The first order loss rate constant was calculated as follows (equations from [Semenov, 1959]):

$$\text{Diffusion Coefficient, } D = \frac{\eta}{n.m} \qquad (3.4)$$

where η = coefficient of viscosity, n = number density, and m = mass.

As diffusion rates are temperature sensitive, the following correction was used:

$$D_T = D\left(\frac{T}{273}\right)^{\frac{1}{2}} \qquad (3.5)$$

$$k_{diff} = \frac{23.2D_T}{d^2} \qquad (3.6)$$

84

where d is the cell diameter. For N_2 and O_2, η is 16.6 x 10^{-6} Nsm^{-2} and 19.2 x 10^{-6} Nsm^{-2} respectively, which gives unimolecular diffusion rates of:

$$k_{diff}(N_2) = 1.22 \text{ s}^{-1}$$
$$k_{diff}(O_2) = 1.24 \text{ s}^{-1}$$

These rates are for a molecule in a single species gas (e.g. N_2 only) diffusing to the walls of a cylindrical cell. For the model it was assumed that the radicals would diffuse in a similar way, although their larger size and different character would slow their diffusion down slightly. It was also assumed that all radicals were destroyed upon reaching the cell walls.

Consequently, a common loss rate of 1.2 s^{-1} was used for all of the principal radical species. This is in good agreement with the previous work of *Hastie et al.* [1991] who found that a value for k_{diff} of 2.5 s^{-1} was appropriate for their apparatus. A slower loss rate is to be expected in the present work, as the internal diameter of the cell was 20mm, significantly larger than that used by *Hastie* and co-workers. The reaction chamber in that work consisted of a nylon tube which was only 3.6mm in diameter.

Equation 3.6 suggests that such a difference in diameter would lead to a diffusion rate constant for the smaller chamber approximately 30 times faster than that for the larger one. However, direct comparisons cannot be made as other factors are not the same. As well as the nature of the walls being different (glass in this work as opposed to nylon in the work of *Hastie et al.*), the cell used here was static, while that of *Hastie et al.* was a flow system. Both of these factors will affect the radical loss kinetics.

Table 3.iii   The DME Model

No.	Reaction	k	Ref./Notes
1.	$CH_3OCH_3 + OH \rightarrow CH_3OCH_2 + H_2O$	2.98×10^{-12}	16
2.	$CH_3OCH_2 + O_2 \rightarrow CH_3OCH_2O_2$	3.00×10^{-12}	111 a
3.	$CH_3OCH_2O_2 + NO \rightarrow CH_3OCH_2O + NO_2$	7.23×10^{-12}	21, 180 b
4.	$CH_3OCH_2O + O_2 \rightarrow CH_3OCHO + HO_2$	8.40×10^{-15}	12, 13 c
5.	$CH_3OCHO + OH \rightarrow CH_2OCHO + H_2O$	2.27×10^{-13}	184 d
6.	$CH_2OCHO + O_2 \rightarrow HCOOCH_2O_2$	4.50×10^{-12}	15, 111 e
7.	$HCOOCH_2O_2 + NO \rightarrow HCOOCH_2O + NO_2$	7.23×10^{-12}	21, 180 b
8.	$HCOOCH_2O \rightarrow HCO_2 + HCHO$	$1.50 \times 10^5 \, s^{-1}$	12, 13 f
9.	$HCO_2 + O_2 \rightarrow HO_2 + CO_2$	5.60×10^{-12}	15 g
10.	$HCHO + HO_2 \rightarrow HOCH_2O_2$	7.90×10^{-14}	15
11.	$HOCH_2O_2 \rightarrow HCHO + HO_2$	$1.50 \times 10^2 \, s^{-1}$	15
12.	$HCHO + OH \rightarrow CHO + H_2O$	9.56×10^{-12}	16
13.	$HCHO + OH \rightarrow HCOOH + H$	1.9×10^{-13}	12
14.	$CH_2OH + NO \rightarrow HNO + CH_2O$	2.4×10^{-12}	121
15.	$CH_2OH + O_2 \rightarrow CHO + HO_2$	9.4×10^{-12}	16
16.	$HNO + O_2 \rightarrow NO + HO_2$	3.31×10^{-14}	58
17.	$CH_2OH + NO_2 \rightarrow HONO + HCHO$	8.3×10^{-12}	121
19.	$CHO + O_2 \rightarrow CO + HO_2$	5.6×10^{-12}	16
21.	$CHO + O_2 \rightarrow CO_2 + OH$	2.0×10^{-14}	169
22.	$CHO + O_2 \rightarrow HCOO_2$	4.0×10^{-13}	169
23.	$CHO + NO \rightarrow CO + HNO$	1.23×10^{-11}	90,118,179 h
24.	$CHO + NO_2 \rightarrow HONO + CO$	5.19×10^{-11}	170
25.	$CHO + NO_2 \rightarrow HCO_2 + NO$	2.07×10^{-11}	31, 170
26.	$HO_2 + NO \rightarrow OH + NO_2$	8.1×10^{-12}	15
27.	$OH + CO \rightarrow H + CO_2$	2.4×10^{-13}	70
28.	$H + O_2 \rightarrow HO_2$	1.2×10^{-12}	15
29.	$OH + NO \rightarrow HONO$	5.2×10^{-12}	15
30.	$CH_3O_2 + NO \rightarrow CH_3O + NO_2$	7.7×10^{-12}	15
31.	$CH_3O + O_2 \rightarrow HCHO + HO_2$	1.9×10^{-15}	15
32.	$CH_3 + O_2 \rightarrow CH_3O_2$	1.0×10^{-12}	16
33.	$CH_3COO_2 + NO \rightarrow CH_3 + CO_2 + NO_2$	2.0×10^{-11}	16
34.	$OH + HCHO \rightarrow H_2O + CHO$	1.1×10^{-11}	15
35.	$OH + O_3 \rightarrow HO_2 + O_2$	6.8×10^{-14}	16
36.	$OH + HNO_3 \rightarrow H_2O + NO_3$	1.5×10^{-13}	16
37.	$OH + HONO \rightarrow H_2O + NO_2$	4.9×10^{-12}	16
38.	$OH + HO_2NO_2 \rightarrow H_2O + NO_2 + O_2$	4.98×10^{-12}	16
39.	$OH + NO_2 \rightarrow HNO_3$	1.1×10^{-11}	70
40.	$OH + NO_3 \rightarrow HO_2 + NO_2$	2.3×10^{-11}	15
41.	$OH + OH \rightarrow H_2O + O$	1.9×10^{-12}	15
42.	$OH + OH \rightarrow H_2O_2$	4.8×10^{-12}	15
43.	$OH + HO_2 \rightarrow H_2O + O_2$	1.1×10^{-10}	15
44.	$OH + H_2O_2 \rightarrow H_2O + HO_2$	1.7×10^{-12}	16
45.	$OH + CH_4 \rightarrow H_2O + CH_3$	7.3×10^{-15}	16
46.	$OH + CH_3O_2 \rightarrow O_2 + CH_3OH$	1.0×10^{-11}	70

Table 3.iii   The DME Model (cont.)

No.	Reaction	k	Ref./Notes
47.	$OH + CH_3O_2NO_2 \rightarrow H_2O + HCHO + NO_3$	4.0×10^{-12}	70
48.	$OH + CH_3O \rightarrow H_2O + HCHO$	1.0×10^{-11}	70
49.	$HO_2 + HO_2 \rightarrow H_2O_2 + O_2$	1.7×10^{-12}	16
50.	$HO_2 + NO_2 \rightarrow HO_2NO_2$	1.4×10^{-12}	70
51.	$HO_2 + O_3 \rightarrow OH + 2 O_2$	1.9×10^{-15}	15
52.	$PAN \rightarrow CH_3COO_2 + NO_2$	8.0×10^{-4} s^{-1}	16
53.	$CH_3COO_2 + NO_2 \rightarrow PAN$	1.2×10^{-11}	16
54.	$HO_2NO_2 \rightarrow HO_2 + NO_2$	8.1×10^{-2} s^{-1}	16
55.	$CH_3COO_2 + CH_3COO_2 \rightarrow 2 CH_3 + 2 CO_2$	1.6×10^{-11}	16
56.	$CH_3COO_2 + CH_3O_2 \rightarrow CH_3 + CH_3O + O_2 + CO_2$	5.5×10^{-13}	16
57.	$CH_3COO_2 + CH_3O_2 \rightarrow CH_3COOH + HCHO + O_2$	5.5×10^{-13}	16
58.	$CH_3O_2 + NO_2 \rightarrow CH_3O_2NO_2$	1.08×10^{-13}	70
59.	$CH_3O_2 + CH_3O_2 \rightarrow 2 CH_3O + O_2$	8.0×10^{-14}	16
60.	$CH_3O_2 + CH_3O_2 \rightarrow CH_3OH + HCHO + O_2$	2.5×10^{-13}	16
61.	$CH_3O_2 + CH_3O_2 \rightarrow CH_3OOCH_3 + O_2$	3.0×10^{-14}	16
62.	$CH_3O_2NO_2 \rightarrow CH_3O_2 + NO_2$	1.9 s^{-1}	16
63.	$CH_3CO + O_2 \rightarrow CH_3COO_2$	5.00×10^{-12}	15, 112
64.	$CH_3CO + OH \rightarrow CH_2CO + H_2O$	2.00×10^{-11}	72
65.	$CH_2CO + OH \rightarrow HCHO + CHO$	9.00×10^{-12}	12
66.	$CH_2CO + OH \rightarrow CH_2OH + CO$	9.00×10^{-11}	12
67.	$NO + O_3 \rightarrow NO_2 + O_2$	1.8×10^{-14}	16
68.	$NO_2 + O_3 \rightarrow NO_3 + O_2$	3.41×10^{-17}	16
69.	$NO_3 + NO_2 \rightarrow N_2O_5$	1.4×10^{-12}	70
70.	$N_2O_5 \rightarrow NO_3 + NO_2$	5.2×10^{-2} s^{-1}	70
71.	$HO \rightarrow WALL$	1.2 s^{-1}	i
72.	$HO_2 \rightarrow WALL$	1.2 s^{-1}	i
73.	$CH_3O_2 \rightarrow WALL$	1.2 s^{-1}	i
74.	$CH_3CO_3 \rightarrow WALL$	1.2 s^{-1}	i
75.	$CHO \rightarrow WALL$	1.2 s^{-1}	i
76.	$CH_3CHO + h\upsilon \rightarrow CH_3 + CHO$	variab.	j
77.	$OH + CH3CHO \rightarrow CH3CO + H2O$	1.58×10^{-11}	15

Table 3.iv   The Carbon Monoxide Model

No.	Reaction	k	Ref./Notes
1.	$HO_2 + NO \rightarrow HO + NO_2$	8.1×10^{-12}	70
2.	$HO + CO \rightarrow H + CO_2$	2.4×10^{-13}	70
3.	$H + O_2 \rightarrow HO_2$	1.2×10^{-12}	70
4.	$HO + NO \rightarrow HONO$	5.2×10^{-12}	70
5.	$CH_3O_2 + NO \rightarrow CH_3O + NO_2$	7.7×10^{-12}	70
6.	$CH_3O + O_2 \rightarrow HCHO + HO_2$	1.9×10^{-15}	70
7.	$CH_3 + O_2 \rightarrow CH_3O_2$	1.0×10^{-12}	70
8.	$CH_3COO_2 + NO \rightarrow CH_3 + CO_2 + NO_2$	1.4×10^{-11}	70
9.	$HO + HCHO \rightarrow H_2O + CHO$	1.1×10^{-11}	70
10.	$CHO + O_2 \rightarrow HO_2 + CO$	5.6×10^{-12}	70
11.	$HO + O_3 \rightarrow HO_2 + O_2$	6.8×10^{-14}	70
12.	$HO + HNO_3 \rightarrow H_2O + NO_3$	1.0×10^{-13}	70
13.	$HO + HONO \rightarrow H_2O + NO_2$	4.9×10^{-12}	70
14.	$HO + HO_2NO_2 \rightarrow H_2O + NO_2 + O_2$	4.7×10^{-12}	70
15.	$HO + NO_2 \rightarrow HNO_3$	1.1×10^{-11}	70
16.	$HO + NO_3 \rightarrow HO_2 + NO_2$	2.3×10^{-11}	70
17.	$HO + HO \rightarrow H_2O + O$	1.9×10^{-12}	70
18.	$HO + HO \rightarrow H_2O_2$	4.8×10^{-12}	70
19.	$HO + HO_2 \rightarrow H_2O + O_2$	1.1×10^{-10}	70
20.	$HO + H_2O_2 \rightarrow H_2O + HO_2$	1.7×10^{-12}	70
21.	$HO + CH_4 \rightarrow H_2O + CH_3$	7.7×10^{-15}	70
22.	$HO + CH_3O_2 \rightarrow O_2 + CH_3OH$	1.0×10^{-11}	70
23.	$HO + CH_3O_2NO_2 \rightarrow H_2O + HCHO + NO_3$	4.0×10^{-12}	70
24.	$HO + CH_3O \rightarrow H_2O + HCHO$	1.0×10^{-11}	70
25.	$HO_2 + HO_2 \rightarrow H_2O_2 + O_2$	1.7×10^{-12}	70
26.	$HO_2 + NO_2 \rightarrow HO_2NO_2$	1.4×10^{-12}	70
27.	$HO_2 + O_3 \rightarrow HO + 2\ O_2$	2.1×10^{-15}	70
28.	$PAN \rightarrow CH_3COO_2 + NO_2$	$3.7 \times 10^{-4}\ s^{-1}$	70
29.	$HO_2NO_2 \rightarrow HO_2 + NO_2$	$8.1 \times 10^{-2}\ s^{-1}$	70
30.	$CH_3COO_2 + CH_3COO_2 \rightarrow 2\ CH_3 + 2\ CO_2$	1.6×10^{-11}	70
31.	$CH_3COO_2 + CH_3O_2 \rightarrow CH_3 + CH_3O + O_2 + CO_2$	4.5×10^{-13}	70
32.	$CH_3COO_2 + CH_3O_2 \rightarrow CH_3COOH + HCHO + O_2$	4.5×10^{-13}	70
33.	$CH_3O_2 + NO_2 \rightarrow CH_3O_2NO_2$	4.0×10^{-12}	70
34.	$CH_3O_2 + CH_3O_2 \rightarrow 2\ CH_3O + O_2$	8.0×10^{-14}	70
35.	$CH_3O_2 + CH_3O_2 \rightarrow CH_3OH + HCHO + O_2$	2.5×10^{-13}	70
36.	$CH_3O_2 + CH_3O_2 \rightarrow CH_3OOCH_3 + O_2$	3.0×10^{-14}	70
37.	$CH_3O_2NO_2 \rightarrow CH_3O_2 + NO_2$	$1.9 \quad s^{-1}$	70
38.	$NO + O_3 \rightarrow NO_2 + O_2$	1.8×10^{-14}	70
39.	$NO_2 + O_3 \rightarrow NO_3 + O_2$	3.2×10^{-17}	70
40.	$NO_3 + NO_2 \rightarrow N_2O_5$	1.4×10^{-12}	70
41.	$N_2O_5 \rightarrow NO_3 + NO_2$	$5.2 \times 10^{-2}\ s^{-1}$	70
42.	$HO \rightarrow WALL$	$1.2\ s^{-1}$	i
43.	$HO_2 \rightarrow WALL$	$1.2\ s^{-1}$	i
44.	$CH_3O_2 \rightarrow WALL$	$1.2\ s^{-1}$	i
45.	$CH_3CO_3 \rightarrow WALL$	$1.2\ s^{-1}$	i
46.	$CH_3CHO + h\upsilon \rightarrow CH_3 + CHO$	variab.	j
47.	$OH + CH_3CHO \rightarrow CH_3CO + H_2O$	1.58×10^{-11}	15

Notes for the Models

(a)   The rate constant used is $k(HOCH_2CH_2 + O_2)$, as $HOCH_2CH_2$ and CH_3OCH_2 are isomeric.

(b)   The rate constant is an average of $k(HOCH_2O_2 + NO) = 5.60 \times 10^{-12}$ [*Veyret et al.* 1982] and $k(HOCH_2CH_2O_2 + NO) = 9.0 \times 10^{-12}$ [*Becker et al.*, 1991] $= 7.3 \times 10^{-12}$; allowing for 2% nitrate formation $= 7.23 \times 10^{-12}$

(c)   The rate constant used is $k(HOCH_2CH_2O + O_2)$ [*Atkinson*, 1986; 1990]

(d)   There is an alternative product from this reaction, CH_3OCO. However, a study of similar reactions (OH with HCOOH [*Singleton et al.*, 1988], CH_3COOH [*Singleton et al.*, 1989] and CH_3COOCH_3 [*Campbell and Parkinson*, 1978]) show that the attack predominantly occurs at the alkoxy end and so this second channel is unimportant.

(e)   The rate constant used is an average of $k(HOCH_2CH_2 + O_2) = 3.00 \times 10^{-12}$ [*Miyoshi et al.*, 1989a] and $k(CH_3CH_2CH_2 + O_2) = 6.00 \times 10^{-12}$ [*Atkinson et al.*, 1989]

(f)   k is equal to $k(HOCH_2CH_2O \rightarrow CH_2OH + CH_2O)$ [*Atkinson*, 1986; 1990]

(g)   The rate constant used is that for the reaction of CHO with O_2

(h)   The rate constant used is an average of 1.26×10^{-11} [*Langford and Moore*, 1984], 1.23×10^{-11} [*Veyret and Lesclaux*, 1981] and 1.20×10^{-11} [*Nadtochenko et al.*, 1980]

(i)   Calculated in section 3.3.3

(j)   Calculated in section 3.2.6

3.3.4 Variation of the Photolysis Time

The duration of the flash, τ, was varied between 1 and 25ms using mixtures of the same concentration as is given above. It can be seen from the results, shown in Figure 3.9, that there is a distinct fall in the chain length as the duration of the photolysis increases.
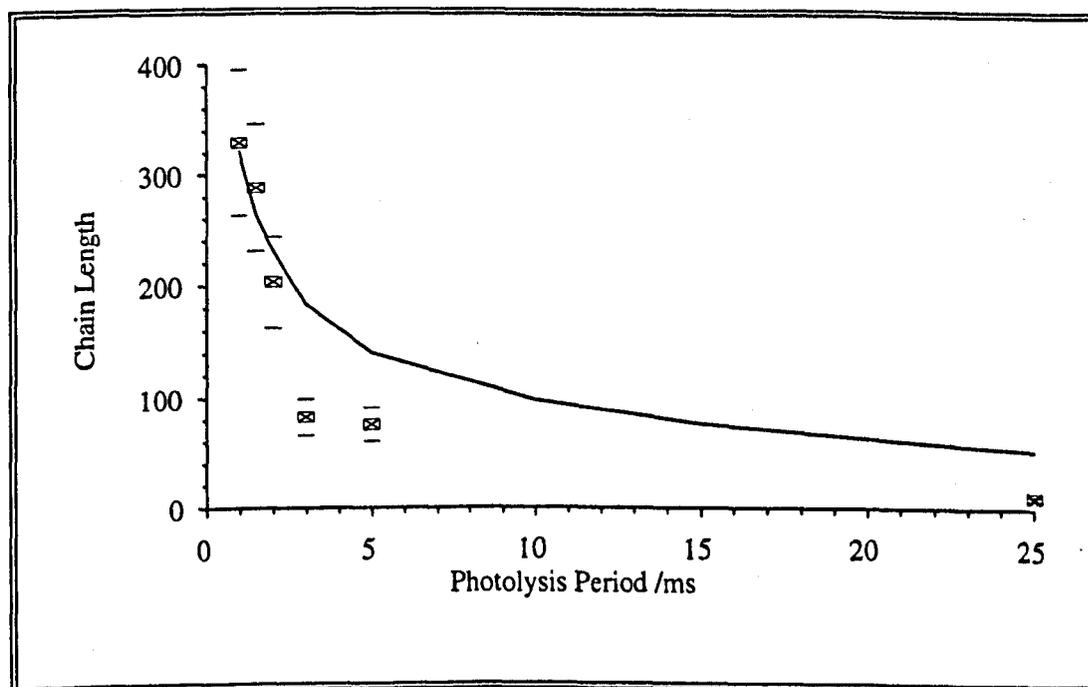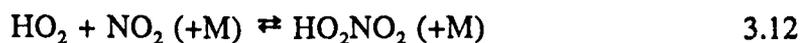

Figure 3.9 Variation of the Chain Length with the Flash Duration. Experimental points are shown by ⊠. The solid line is the model prediction.

[DME] = 80 mbar; [CH$_3$CHO] = 1 mbar; [NO] = 0.6 ppm; [O$_2$] = 199 mbar; [N$_2$] = 220 mbar

This decrease in the chain length is predicted by modelling to be a result of the increase in the concentration of NO$_2$ during the photolysis. Initially, under the conditions used, the only significant reaction channel for HO$_2$ and CH$_3$O$_2$ is with NO, a chain initiation reaction (only 0.2% of the peroxy radicals are lost by diffusion to the cell walls). However, as the photolysis continues, the rise in the concentration of NO$_2$ means that the following, chain termination reactions, become more important:

$$HO_2 + NO_2 \ (+M) \rightleftarrows HO_2NO_2 \ (+M) \qquad\qquad 3.12$$

$$CH_3O_2 + NO_2 \ (+M) \rightleftarrows CH_3O_2NO_2 \ (+M) \qquad\qquad 3.13$$

The amount of the peroxy radicals reacting in this way is small, after 10ms less than 0.1% of HO_2 and approximately 0.2% of CH_3O_2 are consumed in this way, but the effect of terminating a chain, rather than initiating a new one, is significant. At 25ms, the reaction of the peroxy radicals with NO_2 is the largest loss channel after the reaction with NO, accounting for around 0.2% of the HO_2 and 1.3% of the CH_3O_2. If the photolysis were to last for 100ms, then around 16% of the CH_3O_2 would react with NO_2.

The difference in the proportions of HO_2 and CH_3O_2 reacting with NO_2 is a consequence of the difference in their respective rate constants for the reaction [*Atkinson et al.*, 1989]:

$$k_{(HO_2 + NO_2)} = 1.4 \times 10^{-12} \text{ molecule cm}^{-3} \text{ s}^{-1}$$
$$k_{(CH_3O_2 + NO_2)} = 8.0 \times 10^{-12} \text{ molecule cm}^{-3} \text{ s}^{-1}$$

The reaction of HO with NO_2, when compared with its reaction with DME, is not sufficiently fast to have an effect on the chain length, even at the higher concentrations of NO_2.

It should be noted that the agreement between the experimental results and the model prediction is poor at the longer photolysis periods. This could be due to a combination of the increased uncertainties associated with measuring the small change in the concentration of NO_2, and any errors in the rate constants used the model having an increased effect at the longer times. The error bars shown in Figure 3.9 are the average error in the chain length, ±20%, although the error in these points could be around ±30% (see the discussion of the uncertainties in section 3.3.7 below).
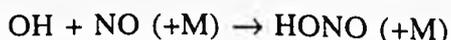
3.3.5 Variation of the NO Concentration

A series of experiments was performed to test the response of the chain length to the concentration of NO in the sample. All other concentrations were maintained at those given in section 3.3.1 while the concentration of NO was varied between 0.6 and 10.0 ppm (7.38×10^{12} - 1.23×10^{13} molecule cm^{-3}). The results are shown in Figure 3.10.
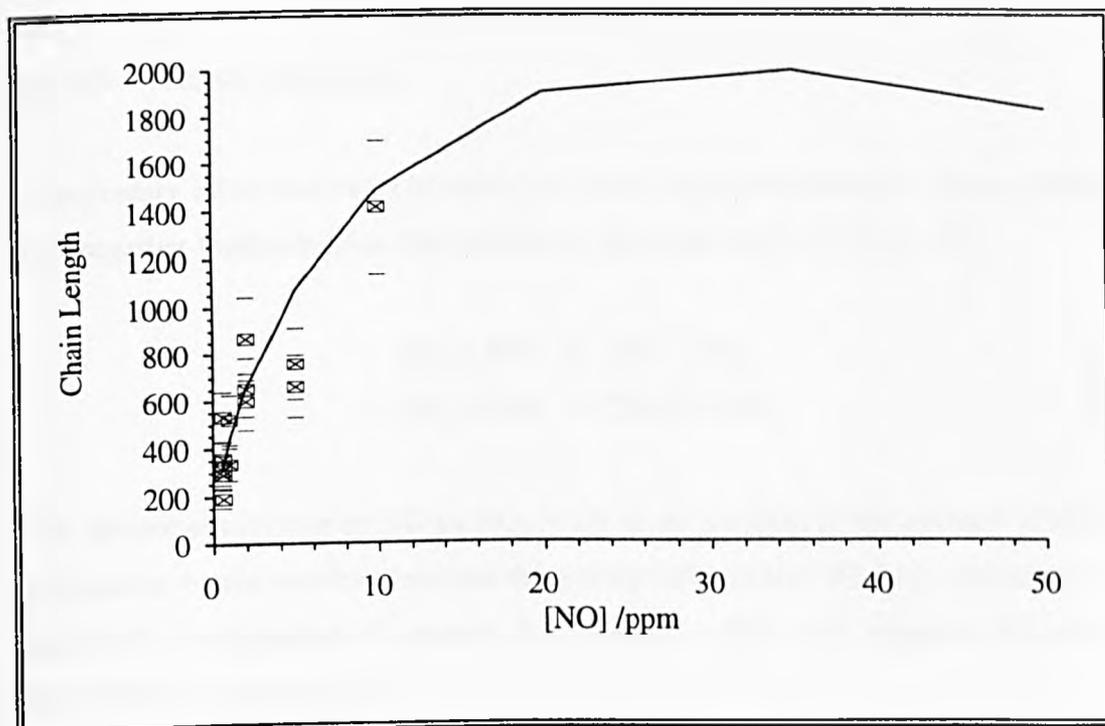
Figure 3.10 Variation of the Chain Length with [NO]. Experimental points are denoted by ⊠. The solid line is the model prediction.

[DME] = 80 mbar; [CH$_3$CHO] = 1 mbar; [O$_2$] = 199 mbar;
[N$_2$] = 220 mbar; τ = 1ms

As the concentration of NO increases, more of the peroxy radicals react with it rather than being lost to the cell walls, or reacting with NO$_2$. The reduction in the proportion of the radicals undergoing termination reactions increases the chain length, as shown in Figure 3.10. However, NO may also provide a chain termination channel for OH through the reaction:

$$OH + NO\ (+M) \rightarrow HONO\ (+M) \qquad\qquad 3.5$$

The increase in the NO concentration, therefore, also inhibits the chain by restricting the amount of OH that reacts with DME:

$$OH + CH_3OCH_3 \rightarrow H_2O + CH_3OCH_2 \qquad 3.14$$
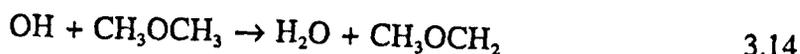
The concentration of NO at which the increase in reactions with peroxy radicals, such as 3.1 and 3.2, is outweighed by the rise in reactions 3.5 and decline of 3.14 depends on the branching ratios between the different routes. Accordingly, several factors, including the rates for each reaction and the rate of radical loss through diffusion to the cell walls, are important.

A secondary effect that helps to reduce the chain length at higher NO concentrations is a negative feedback from the increase in reactions such as 3.1 and 3.2:

$$HO_2 + NO \rightarrow OH + NO_2 \qquad 3.1$$
$$CH_3O_2 + NO \rightarrow CH_3O + NO_2 \qquad 3.2$$
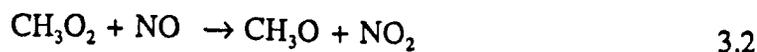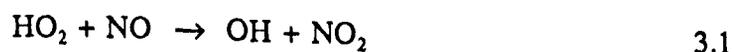
The greater conversion of NO to NO_2 leads to an increase in the amount of chain termination by the reactions between the peroxy radicals and NO_2 (e.g. reactions 3.12 and 3.13) as discussed in section 3.3.4 above. This will augment the direct termination by reaction 3.5.

Another factor in the apparent decline of the chain length at higher NO concentrations is the reaction between NO and the methyl radical, CH_3:

$$CH_3 + NO\ (+M) \rightarrow CH_3NO\ (+M) \qquad 3.15$$
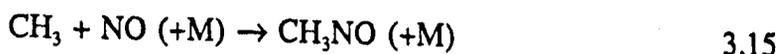
The CH_3 is formed by the photolysis of ethanal (reaction 3.4) and is the immediate precursor of the methyl peroxy radical, CH_3O_2 (reaction 3.6).

$$CH_3CHO + h\upsilon \rightarrow CH_3 + CHO \qquad 3.6$$
$$CH_3 + O_2\ (+ M) \rightarrow CH_3O_2\ (+ M) \qquad 3.8$$

93
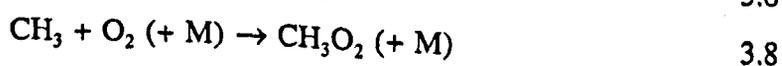
Although the concentration of O_2 (2.45×10^{18} molecule cm^{-3}) is always much greater than that of NO, the reaction between NO and CH_3 is 25 times faster than that between O_2 and CH_3 ($k(CH_3 + NO) = 2.5 \times 10^{-11}$ molecule cm^{-3} s^{-1} while $k(CH_3 + O_2) = 1.0 \times 10^{-12}$ molecule cm^{-3} s^{-1} under the conditions used in this work). When the concentration of NO is 100ppm (1.23×10^{15} molecule cm^{-3}) the branching ratio between the reactions of CH_3 with NO and O_2 is 1.26%, which, although small, is significant in curtailing the chain propagation. In fact, this reduces the number of radicals available to initiate chains, and so the amount of NO converted to NO_2, rather than actually reducing the length of the chain. However, the chain lengths shown in Figure 3.10 are calculated using the number of radicals generated in the absence of NO, rather than the actual number of radicals available. Since the chain length is defined by:

$$C.L. = \frac{[NO]_i - [NO]_f}{[Radicals]}$$

reducing the NO converted, while using the same figure for the number density of radicals, will reduce the calculated chain length. As such, this is an artifact of this experimental conditions, rather than the chemical amplification chemistry.

3.3.6   Experiments with CO

Several experiments were performed using CO instead of DME in order to provide a direct comparison between the two systems as the former is the established chain carrier. However, it was found that under the 'normal' conditions used (cell pressure = 500mbar; [DME/CO] = 80mbar [ethanal] = 1mbar; [NO] = 0.6ppm; [O_2] = 199mbar; τ = 1ms) no amplification could be detected in the CO system. Consequently the concentration of NO was increased to 10ppm and the results are shown in Figure 3.11.
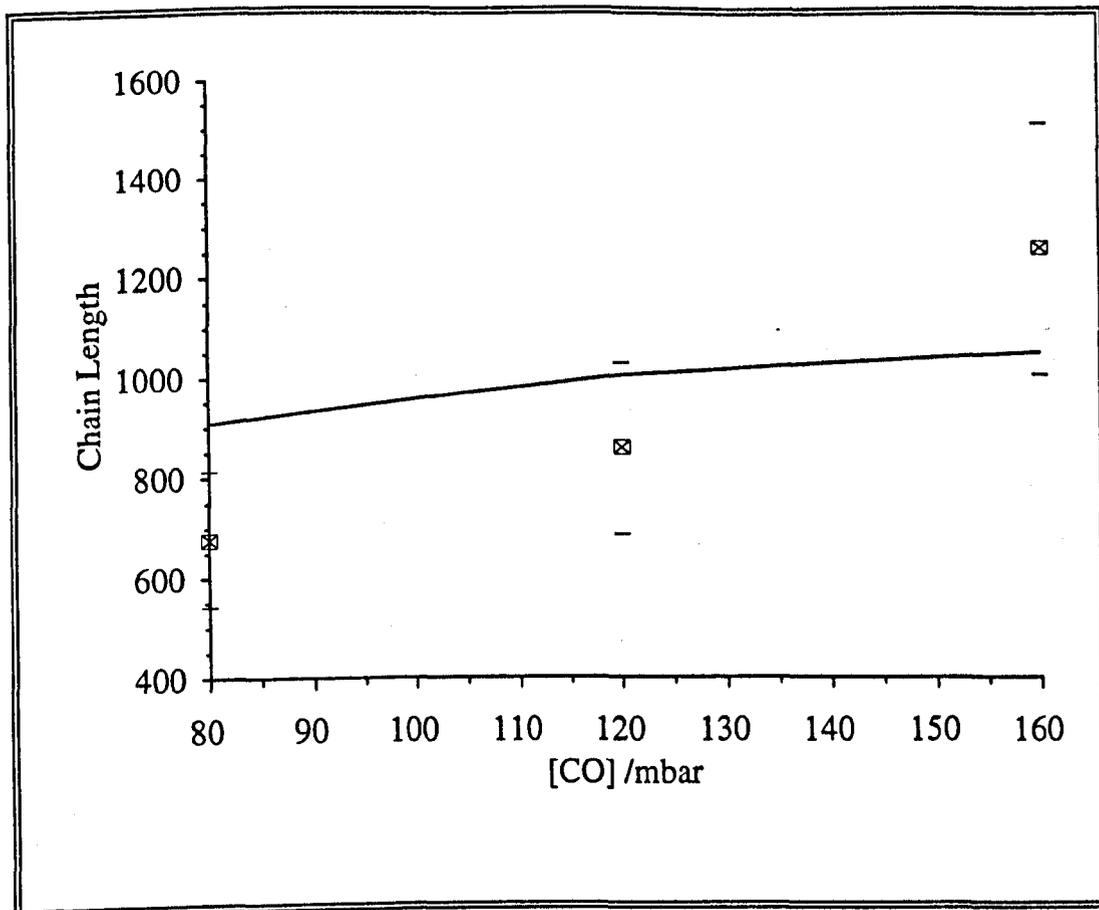
Figure 3.11   Variation in Chain Length with [CO].
⊠ experimental data; —— model prediction

[CH$_3$CHO] = 1 mbar; [NO] = 0.6ppm; [O$_2$] = 199mbar; cell pressure
(N$_2$ bath gas) = 500mbar; τ = 1ms

It had been expected that it would be difficult to detect the change in the NO concentration in these experiments. With the chain lengths obtained in the DME experiments, the difference in the NO concentration was only just visible above the noise. The chain lengths expected in the CO experiments were lower than those for DME and accordingly, the conversion of NO to NO$_2$ would be more difficult to monitor. However, the elevated concentrations of NO and CO resulted in chain lengths comparable with those obtained in the experiments with DME.

Figure 3.11 shows a relatively poor agreement between the model predictions and the experimental results, with the model predicting larger chain lengths, and a weaker

dependence on the concentration of CO. However, care must be taken when interpreting these results, because of the small number of measurements, and the error in each of them.

Figure 3.11 suggests that in the model, either the rate constant for the reaction of OH with CO is too low, or the rate constants for the radical loss processes are too high. With the exception of the first order rate constant for radical diffusion to the cell wall, the rate constants for the termination reaction are relatively well known, as is the OH/CO rate constant. Other modelling studies [e.g. *Hastie et al.*, 1991; *Cantrell et al.*, 1993 and other modelling in this work] have used similar rate constants and have been able to reproduce accurately the experimental results. It must be concluded that the poor agreement in the present study is due to the error in the experimental results, although no exceptional reason for this has been identified.

3.3.7 Error Analysis

For the purpose of this analysis, the following were considered to be the principal primary sources of error:

(a) P_{max}
Scatter in the data for the maximum number of P counts in the MMS experiments.
The standard deviation in the P counts for experiments where $\tau \geq 5.0s$ was 8.1%.

(b) Calibrations
Quality of the fit of the data to the calibration curve. For the MMS calibration the fit was excellent, with a 2σ error of 0.4%. The fit of the NO calibration data was less good. The figure used, 5%, was an assumption based on the 2σ error for a linear fit of 10%.

(c) Photolysis

Slight variations in the actual duration and intensity of the lamp output. The standard deviation in the area under the intensity/time curves for ten independent flashes of 1ms duration was 2.4%.

(d) NO analysis

Random equipment noise, variations arising from the precise sampling method, and uncertainties associated with the integration of the areas of the peaks. These are reduced slightly by the practice of taking three samples for each measurement, and hence the value used in the error analysis was typical for the difference between the mean and the extreme values, 10%. It was found that this varied between <5% and >15%. The greatest error was associated with the experiments with low NO concentrations, where the effect of equipment noise was very marked.
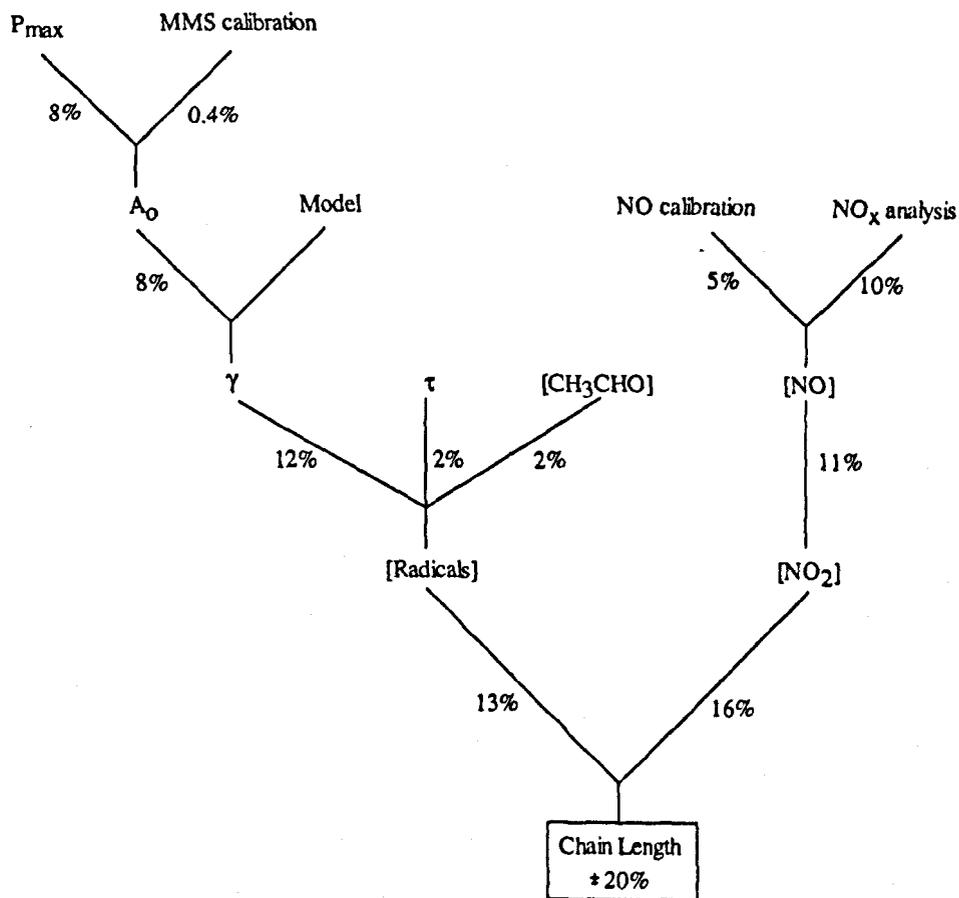
(e) Mixtures

Errors in the reagent concentrations originating from the uncertainties involved in measuring gas pressures. These were considered to be negligible for DME and O_2, and ethanal in the MMS experiments as the pressures of each used were so high. However, in the chemical amplification experiments, the uncertainty in the ethanal concentration was calculated to be 2%. While the equivalent error for NO was calculated to vary between 1.4 and 2.2%, depending on the concentration used, this uncertainty was, in fact, included in the overall uncertainty of the calibration.

The flow diagram shown below illustrates how these errors combine in the calculation of the chain length.

The errors were propagated through the scheme using the following formulae:

If x = u + v or u - v, then the variance in x is

$$\sigma_x^2 = \sigma_u^2 + \sigma_v^2 \tag{3.8}$$

P$_{max}$ MMS calibration

8%   0.4%

A$_0$ Model

8%

NO calibration   NO$_x$ analysis

5%   10%

γ   τ   [CH$_3$CHO]   [NO]

12%   2%   2%   11%

[Radicals]   [NO$_2$]

13%   16%

Chain Length
± 20%

If $x = u.v$ or u/v, then

$$\left(\frac{\sigma x}{x}\right)^2 = \left(\frac{\sigma u}{u}\right)^2 + \left(\frac{\sigma v}{v}\right)^2 \qquad (3.9)$$

The error in the value of γ, the photolysis rate constant, was determined by applying the 8% error in A$_0$ to the plot of A$_0$ against photolysis rate, and reading off the range thus created in the value γ. This assumed that there was no error associated with the model used to match the experimental and predicted total absorbances. Whilst there are very definite differences in the published literature for both rate constants and absorption cross-sections, the errors resulting from this are difficult to quantify. Hence the actual uncertainty in the chain length could be higher than the calculated figure of ±20%.

It should be noted that at the low NO concentrations, the results show a greater variation than would be predicted from the calculation. The standard deviation in the values of the chain lengths when the NO concentration was 0.6ppm is actually 31% of the mean. The principal cause of this increased spread is the greater influence of instrument noise and integration error in the measurement of the smaller peak areas. The deviations in the peak areas were around ±15% of the mean, and if this value is used in the analysis, the calculated error in the chain length becomes ±26%.

3.4   Conclusions and Future Work

The work detailed above in sections 3.3.4-6 demonstrates that DME can be used as a chain carrier in a chemical amplification system, and that it yields a larger chain length than CO. The comparison between the performances of DME and CO, as well as several other alternative organic compounds, was extended using computer modelling. In order to evaluate the potential of the various species for use in an atmospheric monitor, the investigation also involved the response to several ambient species that could cause an interference. This is discussed in Chapter 4.

3.4.1   Time for Reaction Completion

As has been stated above, reaction mixtures were left for at least 500s after photolysis before any samples were analysed. This was intended to ensure that the reaction involved in the chemical amplification process had reached completion and so remove a potential source of error. While no systematic difference could be detected in the experimental results that would suggest that the reaction was indeed continuing after samples were taken, the production of NO_2 over time was modelled.

The modelling was performed by simulating the standard conditions used for the experiments; cell pressure = 500 mbar; [DME] = 80 mbar; [ethanal] = 1 mbar; [O_2] = 199 mbar; τ = 1ms: with [NO] at both 1 and 10 ppm. The results, shown in Figure 3.12, indicate that in fact the reactions are not quite complete after 500s.

However, as the concentration of NO_2 is measured as the difference between the concentration of NO before and after the photolysis, the small growth in NO_2 after around 200s would not be distinguishable above the noise.
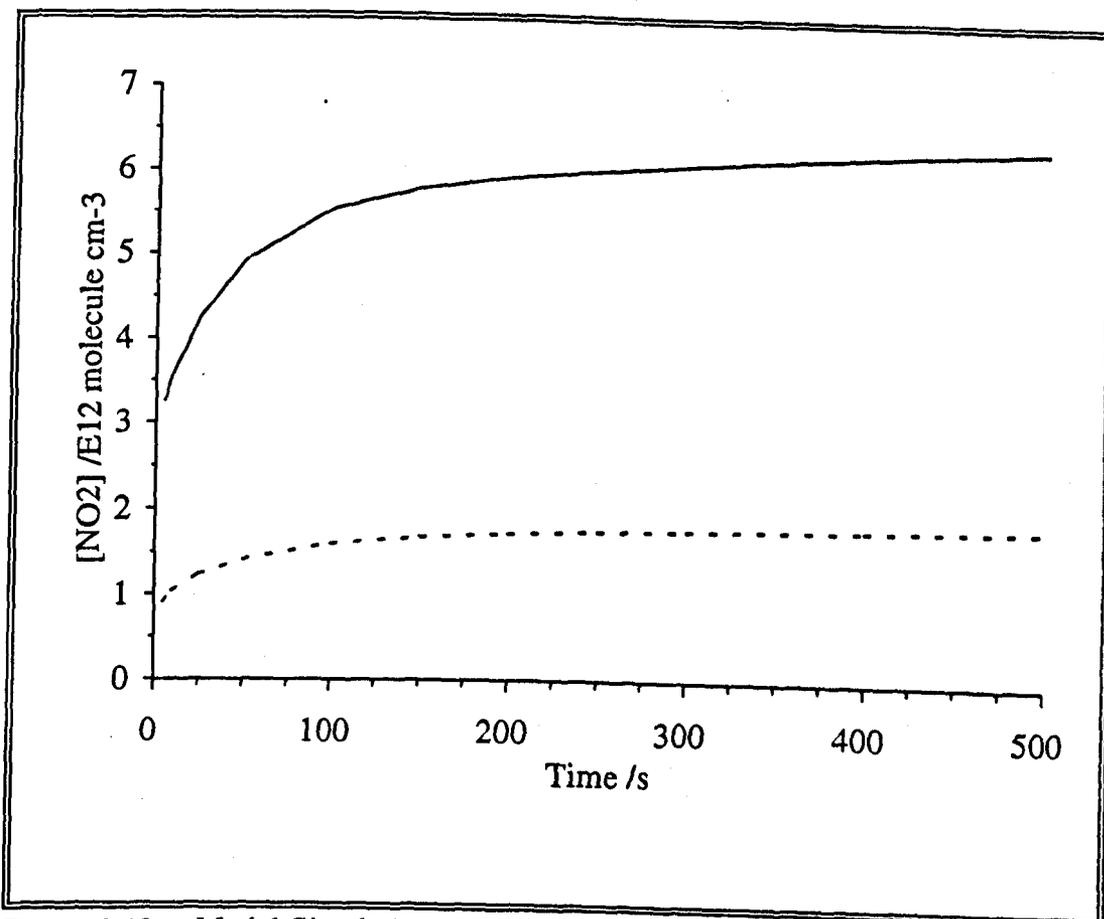

Figure 3.12 Model Simulations of the Production of NO_2 over Time.
—— [NO] = 1 ppm; ---- [NO] = 10 ppm.

[DME] = 80 mbar; [ethanal] = 1 mbar; [O$_2$] = 199 mbar; [N$_2$] = 220 mbar; τ = 1ms

3.4.2 Future Work

The experiments intended to investigate the response of the DME system to different radical densities yielded unexpected results not directly related to the different number densities. There are two alternative methods for generating the different concentrations desired, but both have problems associated with them. Essentially

they both involve changing the photolysis rate of ethanal. In this way larger or smaller radical densities could be generated in the same photolysis time, so avoiding the problem of increased NO_2 concentrations.

This could be achieved if the initial concentration of ethanal in the reaction mixtures were altered. However, such an change would also lead to a change in the chemistry of the system. For example, if the concentration were increased, a greater proportion of the OH produced would react with the ethanal, rather than the DME, as desired. This would yield peroxyacyl radicals and ultimately PAN (peroxyacetyl nitrate, $CH_3COO_2NO_2$) which could act as a sink for NO_2.

$$OH + CH_3CHO \rightarrow CH_3CO + H_2O \qquad\qquad 3.16$$
$$CH_3CO + O_2 \;(+M) \rightarrow CH_3COO_2 \;(+M) \qquad\qquad 3.17$$
$$CH_3COO_2 + NO_2 \;(+M) \rightleftharpoons CH_3COO_2NO_2 \;(+M) \qquad\qquad 3.18$$
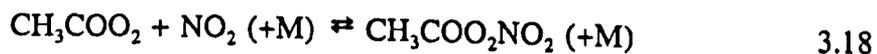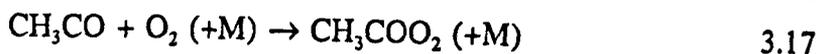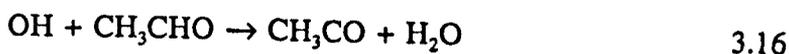
Consequently, an elevated concentration of ethanal would interfere with the amplification chemistry. This could be countered by increasing the concentration of DME accordingly.

The alternative method would be to use more than one lamp. This would increase the effective rate constant for the photolysis, while leaving the chemistry unchanged. The problem with this method is that, when tried, it proved difficult to ensure that the lamps fired for exactly the same duration at photolysis periods of around 1ms. Thus, calculating the number of radicals actually generated would have been very difficult. If the total intensity output was monitored as discussed in section 3.2.6 for each experiment, then such a calculation would be possible.

Figure 3.10 illustrates the possible increase in the chain length that can be achieved in the DME system. At present, the experimental data do not cover the predicted optimum conditions so this requires further investigation. In addition, the concentration of DME could be varied to investigate the response of the system.

Experiments using greater concentrations of NO than those already described could not be performed reliably in the existing apparatus. Problems of excessive tailing in the peaks from the NO_x analyser, and measuring the difference in the areas of the peaks, meant that the data from such experiments were unreliable; as the concentration of NO increases, the percentage conversion to NO_2 becomes smaller. Changing the design of the sample loop would reduce the tailing problem, while the difficulties in measuring a small difference between two large areas can only be directly addressed by increasing the precision of each measurement.

However, changing to a detection method where the growth in NO_2 is measured directly, rather than as a difference, would improve the accuracy of the data significantly. Attempts were made to monitor the NO_2 concentration using LIF, but the equipment was not sensitive enough to detect the small levels of NO_2 formed. Further improvements to the design of the LIF apparatus, together with those discussed in section 3.3.2, could improve the sensitivity to a degree that would enable its use in these experiments. The layout of the reaction cell was not ideal for use in LIF work, as it was designed primarily for use in absorption experiments. The laser entry and exit windows were close to the region from which the fluorescence was collected (about 20mm away). Moving these windows away from the centre of the cell, and changing them from perpendicular to the Brewster angle, would reduce the influence of scattered radiation. This would be further reduced by the use of a Wood's Horn on the underside of the cell, opposite the fluorescence collection window. However, both of the alterations would reduce the uniformity of the photolysis by a single lamp, leading to different amounts of NO_2 being produced in different regions of the cell.

It would be possible to design a cell specifically to allow the combination of LIF analysis and photolysis, but it would be unlikely that such a design would be compatible with the absorption experiments that are vital for the MMS work. Consequently, one of the major advantages of this system, the ability to study the radical creation and loss kinetics in the same equipment as the chemical amplification experiments, would be lost.

While the effect of fluorescence from some of the components in the cell complex, such as the complex walls and the filters, has not been assessed in this work, it has previously been reported (see [*Gelbwachs et al.*, 1972] and subsequent work by this group). Filters made of an aqueous solution of $Na_2Cr_2O_7.2H_2O$ have been used to solve this problem. It is also possible that dielectric filters could be used to the same effect.

The uncertainty in the chain length could also be improved by a better knowledge of the kinetics of the radical generation. The scatter in the data at short photolysis periods could easily be improved by using an improved counter chip. A new system could be run from a desktop computer which would generate the square wave output to fire the lamps and perform the up-down counting, as well as log and analyse the data. Such a system would provide a more versatile apparatus, and would be capable of running other experiments such as the LIF detection.

The mixed radical products from the photolysis of ethanal also complicated the elucidation of the kinetics. Using a radical precursor that yielded only one radical species would simplify the analysis of the data, as the standard procedures for second order loss could be used. Azomethane ($(CH_3)_2N_2$) and azoethane ($(C_2H_5)_2N_2$) are frequently used as radical precursors. When photolysed in the presence of oxygen, they yield N_2 and, respectively, either methylperoxy or ethylperoxy radicals. While single radical products are an advantage in evaluating the performance of the DME and CO systems under laboratory conditions, the production of both hydroperoxy and methylperoxy radicals by ethanal is more reflective of the ambient atmosphere. Product analysis by gas chromatography with flame-ionisation detection (GC-FID) could be used to improve the understanding of the radical generation calibration.

The comparison between the performances of DME and CO is very limited at present. For a more thorough study, experiments mirroring those performed with DME, should be carried out. While a thorough comparison has been carried out using computer modelling (see Chapter 4), the results of such work need to be confirmed by experimental data.

In order for the performance of the system to be assessed under ambient conditions, it must first be converted to operate in a continuous, flow mode, including providing a method of modulating the radical signal so that the background signal could be removed. No major problems are anticipated in providing a continuous detection method, as the possible methods, LIF, NO_2/luminol and NO/O_3 chemiluminescence, are all designed primarily for flowing samples. Included in the development of the equipment for an ambient chemical amplifier would be the design of both the reactor chamber and the sample intake nozzle, as previous studies have shown that these can greatly affect the performance of the system.

It may also be possible to use an alternative chain carrier to DME or CO that would provide improvements in the sensitivity. Some potential alternatives are considered in Chapter 4, although other species could also be investigated.
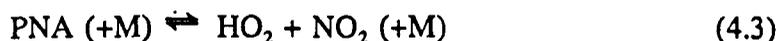
Chapter 4

Chemical Amplification: Modelling Studies

4.1 Introduction

The work detailed in Chapter 3 demonstrated that there are potential alternative chain carriers to CO for use in a Peroxy Radical measurement by Chemical Amplification (PERCA) monitor that may offer improved performance. However, the scope of the experimental studies were limited to proving the viability of dimethyl ether (DME) in this role and to demonstrating that it could provide some performance benefits over CO. This study was extended, using the chemical model of the system that was validated in the experimental work, in order to predict the chain length that could be obtained under different conditions, including assessing the interference effects of several ambient species. In addition, the modelling was used to examine the suitability of several other potential chain carriers.

The sensitivity of the monitor, and hence its detection limit, depends primarily on the length of the chain which, as in all chain reactions, is the result of a balance between the chain propagation reactions (in this case the reaction of OH with the chain carrying agent) and the chain termination reactions. The chain length can be improved in four ways: (i) using a carrier that has a faster reaction with OH; (ii) use of chain carriers which undergo further reactions to produce more than one HO_2 radical per molecule; (iii) minimizing the side reactions of the carrier; (iv) reducing the radical wall loss rate. In the light of these characteristics several potential organic agents, ethene, propene, ethanol and ethyne, as well as DME, were investigated.

Techniques that monitor levels of NO_2 in the presence of excess NO under ambient conditions will be subject to interferences from the reaction of NO with ozone and

also from the thermolysis of PAN (peroxyacetyl nitrate, $CH_3COO_2NO_2$) and PNA (pernitric acid, HO_2NO_2), all of which yield NO_2:

$$O_3 + NO \rightarrow O_2 + NO_2 \tag{4.1}$$

$$PAN\ (+M) \rightleftharpoons CH_3COO_2 + NO_2\ (+M) \tag{4.2}$$

$$PNA\ (+M) \rightleftharpoons HO_2 + NO_2\ (+M) \tag{4.3}$$

In practice these interferences cause an increase in the background level of NO_2 and so can be removed by modulating the signal. However, if the NO_2 due to the amplification process is only a small part of a large overall concentration of NO_2 then the sensitivity of the system is considerably reduced. Accordingly, this aspect of the chemistry was also investigated in this study.

The CO model is different to the organic carrier models in several ways. After the initiation OH reacts with CO as follows:

$$HO_2 + NO \rightarrow OH + NO_2 \tag{4.4}$$

$$OH + CO \rightarrow H + CO_2 \tag{4.5}$$

$$H + O_2\ (+M) \rightarrow HO_2\ (+M) \tag{4.6}$$
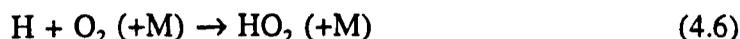
The regenerated HO_2 is able to start the chain again via reaction (4.4). As the only other product is CO_2, which is inert, few complications from side reactions occur. However, this system has two major disadvantages, the most important one being the slow rate of reaction between OH and CO. This means that other OH loss channels compete with the reaction between OH and CO. Secondly, only one HO_2 radical is produced per molecule of CO undergoing reaction.

The prospective chain carriers proposed in this study react more rapidly with OH (except ethyne) and can produce more than one HO_2 radical per molecule reacted, giving higher degrees of amplification. However, in some cases the more complicated chemistry causes new problems to arise. Unlike CO_2, the other products

106

from the reactions are not inert, and so additional secondary chemistry can occur; this may involve OH, HO_2, NO and NO_2, and affect the degree of amplification of the system.

For example, following the initiation, one molecule of ethene could ultimately lead to the production of a further six molecules of NO_2, assuming that all the secondary chemistry associated with the degradation of the products occurs. In practice, however, some of the subsequent reactions do not contribute to the propagation of the chain under the conditions modelled.

However, the major disadvantage of ethene as a chain carrier is due to its reaction with ozone (almost always present in ambient air), which is thought to produce approximately 0.12 HO_2 per molecule of ethene [Atkinson, 1990]. This will initiate new chains which are not derived from the ambient peroxy radicals, and the latter's concentration will be overestimated. Similar arguments can be constructed for propene and this aspect is discussed in detail later.

Ethanol and ethyne, like the alkenes, can produce several HO_2 radicals per molecule. The chemistry of the ethanol and ethyne systems are reasonably well known, and are similar to that for ethene; however, the branching ratios for their reaction with OH are such that the major channels only produce one radical. The channels that result in greater radical production are the minor routes.

DME has the advantage of being gaseous at room temperature, and not reacting with other ambient species, such as ozone. Although its rate of reaction with OH is slower than that of ethanol (but faster than that of CO) it has the potential to perform well as a chain carrier because the chemistry which follows the attack by OH results in more conversion of NO to NO_2. This is because DME and the first stable product, CH_3OCHO, do not produce species which react with OH (except for CH_2O), whereas the alkenes do, e.g. $HOCH_2CHO$ and CH_3CHO.

4.2 Model Simulations

The form of modelling that was used here assumes a static reaction vessel with no concentration gradients and no addition or removal of species, apart from loss to the walls. The model is simply initialised with appropriate concentrations of the particular species, and then allowed to proceed.

The models used here build on the CO model used by *Hastie et al.* [1991] the details of which were unaltered. The additional chemistry for each of ethene, propene, ethanol, dimethyl ether (DME), and ethyne was simply added to the CO model. All schemes include loss of OH and HO_2 via wall reactions, as well as other reactions not directly involved in the amplification process. Tables 4.i to 4.vi (given in section 4.3) show the chemistry used in each of the models (although, as each one contained all of the reactions from the CO model in addition to the specific chemistry of that compound, the CO chemistry is not repeated in the individual tables). Also, there are some reactions in the models which are shown by the results to make a negligible contribution to the overall mechanism but are included for completeness (e.g. the reactions of CHO, which are unimportant because degradation of the parent HCHO via OH is minimal).

4.2.1 Chain Length

One of the most important factors in the performance of the chemical amplifiers is the chain length of the reaction and this was calculated for the range of HO_2 concentrations believed to be found in the troposphere. The chain length is defined as:

$$(CL)_x = \frac{[NO_2]_{final}}{[HO_2]_{initial}} \qquad 4.1$$

were x refers to the chain carrier being investigated. For a direct comparison with the CO system the Relative Chain Length is used:

$$RCL = \frac{(CL)_x}{(CL)_{co}} \qquad\qquad 4.2$$

or, for a given concentration of HO_2:

$$RCL = \frac{[NO_2]_x}{[NO_2]_{co}} \qquad\qquad 4.3$$

In the first instance the models assumed that the background air stream was 'clean', i.e. it contained only nitrogen and oxygen. In order to compare directly the results of this study with the work of *Hastie et al.* [1991], the same initial conditions were employed in the first instance; namely, a reaction time of 1.1s and initial concentrations of chain carrier and NO of 8% (1.97×10^{18} molecules cm^{-3}) and 6ppm (1.48×10^{14} molecules cm^{-3}) respectively. The concentrations of HO_2 were varied between 1×10^7 and 50×10^7 molecules cm^{-3}. This range is believed to cover all concentrations found in the troposphere (see Chapter 1).

4.2.2 Sensitivity to Reactor Conditions

Simulations were carried out to assess the sensitivity of the chain length to the initial concentrations of the chain carrier and NO, as well as to the radical wall loss rate coefficients.

As stated above, the conditions reported by *Hastie et al.* [1991] were used as the base, and then varied to both higher and lower concentrations from this point (or higher and lower rate constants in the investigation of the radical wall loss rate). Accordingly, the concentration of the chain carriers was varied from the base value of 1.97×10^{18} molecules cm^{-3}, between 2.46×10^{18} and 1.57×10^{19} molecule cm^{-3}, while the effect of the initial NO concentration was modelled for concentrations between 1.84×10^{13} and 1.18×10^{15} molecules cm^{-3} (with the base value of 1.48×10^{14}

molecules cm^{-3}). Similarly, the first order radical diffusion loss rate was set at 2.5 s^{-1} in all the models initially, and varied between 0.0 and 5.0 s^{-1}.

Although no attempt was made to quantify the effect of temperature on the different systems, Hastie *et al.* [1991] reported that the chain length in the CO system varied by only 0.3% per degree over the range 273-308 K. In our studies the temperature was assumed to be 298K.

4.2.3   Simulation of Chemical Interferences

The thermolysis of PAN and PNA, and the reaction of NO with ozone all produce NO_2 which increases the background signal. The extent of these interferences were assessed using various concentrations of these species, up to 2.5×10^{12} molecule cm^{-3} (i.e. up to 100ppb). In the case of the alkenes there is a further interference from the reaction of the alkene with ozone. The contribution of ambient OH to the chain reactions was also investigated.

In order to compare the performances of the various systems in discriminating against the NO_2 produced by interferences, a Discriminating Power (DP) of each system is defined as:

$$DP_i = \frac{[NO_2]_o}{[NO_2]_{Total}}$$

4.4

where i is the interference source, $[NO_2]_o$ is the final concentration of NO_2 in the absence of the interference (and therefore produced by chemical amplification) and $[NO_2]_{Total}$ is the final NO_2 concentration in the presence of the interference.

4.3   Model Listings

Table 4.i   The Carbon Monoxide Model

No.	Reaction	k	Ref./Notes
1.	$HO_2 + NO \rightarrow OH + NO_2$	8.1×10^{-12}	70
2.	$OH + CO \rightarrow H + CO_2$	2.4×10^{-13}	70
3.	$H + O_2 \rightarrow HO_2$	1.2×10^{-12}	70
4.	$OH + NO \rightarrow HONO$	5.2×10^{-12}	70
5.	$CH_3O_2 + NO \rightarrow CH_3O + NO_2$	7.7×10^{-12}	70
6.	$CH_3O + O_2 \rightarrow HCHO + HO_2$	1.9×10^{-15}	70
7.	$CH_3 + O_2 \rightarrow CH_3O_2$	1.0×10^{-12}	70
8.	$CH_3COO_2 + NO \rightarrow CH_3 + CO_2 + NO_2$	1.4×10^{-11}	70
9.	$OH + HCHO \rightarrow H_2O + CHO$	1.1×10^{-11}	70
10.	$CHO + O_2 \rightarrow HO_2 + CO$	5.6×10^{-12}	70
11.	$OH + O_3 \rightarrow HO_2 + O_2$	6.8×10^{-14}	70
12.	$OH + HNO_3 \rightarrow H_2O + NO_3$	1.0×10^{-13}	70
13.	$OH + HONO \rightarrow H_2O + NO_2$	4.9×10^{-12}	70
14.	$OH + HO_2NO_2 \rightarrow H_2O + NO_2 + O_2$	4.7×10^{-12}	70
15.	$OH + NO_2 \rightarrow HNO_3$	1.1×10^{-11}	70
16.	$OH + NO_3 \rightarrow HO_2 + NO_2$	2.3×10^{-11}	70
17.	$OH + OH \rightarrow H_2O + O$	1.9×10^{-12}	70
18.	$OH + OH \rightarrow H_2O_2$	4.8×10^{-12}	70
19.	$OH + HO_2 \rightarrow H_2O + O_2$	1.1×10^{-10}	70
20.	$OH + H_2O_2 \rightarrow H_2O + HO_2$	1.7×10^{-12}	70
21.	$OH + CH_4 \rightarrow H_2O + CH_3$	7.7×10^{-15}	70
22.	$OH + CH_3O_2 \rightarrow O_2 + CH_3OH$	1.0×10^{-11}	70
23.	$OH + CH_3O_2NO_2 \rightarrow H_2O + HCHO + NO_3$	4.0×10^{-12}	70
24.	$OH + CH_3O \rightarrow H_2O + HCHO$	1.0×10^{-11}	70
25.	$HO_2 + HO_2 \rightarrow H_2O_2 + O_2$	1.7×10^{-12}	70
26.	$HO_2 + NO_2 \rightarrow HO_2NO_2$	1.4×10^{-12}	70
27.	$HO_2 + O_3 \rightarrow OH + 2 O_2$	2.1×10^{-15}	70
28.	$PAN \rightarrow CH_3COO_2 + NO_2$	$3.7 \times 10^{-4} \ s^{-1}$	70
29.	$HO_2NO_2 \rightarrow HO_2 + NO_2$	$8.1 \times 10^{-2} \ s^{-1}$	70
30.	$CH_3COO_2 + CH_3COO_2 \rightarrow 2\ CH_3 + 2\ CO_2$	1.6×10^{-11}	70
31.	$CH_3COO_2 + CH_3O_2 \rightarrow CH_3 + CH_3O + O_2 + CO_2$	4.5×10^{-13}	70
32.	$CH_3COO_2 + CH_3O_2 \rightarrow CH_3COOH + HCHO + O_2$	4.5×10^{-13}	70
33.	$CH_3O_2 + NO_2 \rightarrow CH_3O_2NO_2$	4.0×10^{-12}	70
34.	$CH_3O_2 + CH_3O_2 \rightarrow 2\ CH_3O + O_2$	8.0×10^{-14}	70
35.	$CH_3O_2 + CH_3O_2 \rightarrow CH_3OH + HCHO + O_2$	2.5×10^{-13}	70
36.	$CH_3O_2 + CH_3O_2 \rightarrow CH_3OOCH_3 + O_2$	3.0×10^{-14}	70
37.	$CH_3O_2NO_2 \rightarrow CH_3O_2 + NO_2$	$1.9 \ s^{-1}$	70
38.	$NO + O_3 \rightarrow NO_2 + O_2$	1.8×10^{-14}	70
39.	$NO_2 + O_3 \rightarrow NO_3 + O_2$	3.2×10^{-17}	70
40.	$NO_3 + NO_2 \rightarrow N_2O_5$	1.4×10^{-12}	70
41.	$N_2O_5 \rightarrow NO_3 + NO_2$	$5.2 \times 10^{-2} \ s^{-1}$	70
42.	$OH \rightarrow WALL$	$2.5 \ s^{-1}$	70
43.	$HO_2 \rightarrow WALL$	$2.5 \ s^{-1}$	70
44.	$CH_3O_2 \rightarrow WALL$	$2.5 \ s^{-1}$	70
45.	$CH_3CO_3 \rightarrow WALL$	$2.5 \ s^{-1}$	70

Table 4.ii   The DME Model

No.	Reaction	k	Ref./Notes
1.	$CH_3OCH_3 + OH \rightarrow CH_3OCH_2 + H_2O$	2.98×10^{-12}	16
2.	$CH_3OCH_2 + O_2 \rightarrow CH_3OCH_2O_2$	3.00×10^{-12}	111 (a)
3.	$CH_3OCH_2O_2 + NO \rightarrow CH_3OCH_2O + NO_2$	7.23×10^{-12}	21, 180 (b)
4.	$CH_3OCH_2O + O_2 \rightarrow CH_3OCHO + HO_2$	8.40×10^{-15}	12, 13 (c)
5.	$CH_3OCHO + OH \rightarrow CH_2OCHO + H_2O$	2.27×10^{-13}	184 (d)
6.	$CH_2OCHO + O_2 \rightarrow HCOOCH_2O_2$	4.50×10^{-12}	15, 111 (e)
7.	$HCOOCH_2O_2 + NO \rightarrow HCOOCH_2O + NO_2$	7.23×10^{-12}	21, 180 (b)
8.	$HCOOCH_2O \rightarrow HCO_2 + HCHO$	1.50×10^{5} s^{-1}	12, 13 (f)
9.	$HCO_2 + O_2 \rightarrow HO_2 + CO_2$	5.60×10^{-12}	15 (g)
10.	$HCHO + HO_2 \rightarrow HOCH_2O_2$	7.90×10^{-14}	15
11.	$HOCH_2O_2 \rightarrow HCHO + HO_2$	1.50×10^{2} s^{-1}	15
12.	$HCHO + OH \rightarrow CHO + H_2O$	9.21×10^{-12}	16
13.	$HCHO + OH \rightarrow HCOOH + H$	1.90×10^{-13}	12
14.	$CH_2OH + NO \rightarrow HNO + HCHO$	2.40×10^{-11}	121
15.	$HNO + O_2 \rightarrow NO + HO_2$	3.31×10^{-14}	58
16.	$CH_2OH + NO_2 \rightarrow HONO + HCHO$	8.30×10^{-12}	121
17.	$CHO + O_2 \rightarrow CO + HO_2$	5.60×10^{-12}	16
19.	$CHO + O_2 \rightarrow CO_2 + OH$	2.00×10^{-14}	169
21.	$CHO + O_2 \rightarrow HCOO_2$	4.00×10^{-13}	169
22.	$CHO + NO \rightarrow CO + HNO$	1.23×10^{-11}	90,118,179 h
23.	$CHO + NO_2 \rightarrow HONO + CO$	3.53×10^{-11}	31, 170
24.	$CHO + NO_2 \rightarrow HCO_2 + NO$	2.07×10^{-11}	31, 170
25.	$CHO \rightarrow WALL$	2.5 s^{-1}	(i)

Table 4.iii   The Ethyne Model

No.	Reaction	k	Ref./Notes
1.	$C_2H_2 + OH \rightarrow C_2H_2OH$	9.1×10^{-13}	16
2.	$C_2H_2OH \rightarrow CH_2CHO$	1.92×10^{6} s^{-1}	72 (j)
3.	$C_2H_2OH + O_2 \rightarrow HOC_2H_2O_2$	2.60×10^{-13}	72 (j)
4.	$CH_2CHO + O_2 \rightarrow HCOCHO + OH$	2.60×10^{-13}	97
5.	$HOC_2H_2O_2 \rightarrow HCOOH + CHO$	5.00×10^{4} s^{-1}	72
6.	$HOC_2H_2O_2 + NO \rightarrow HCOCHO + HO_2 + NO_2$	8.89×10^{-12}	16
7.	$HCOCHO + OH \rightarrow HO_2 + 2 CO$	1.14×10^{-11}	13
8.	$C_2H_2 + O_3 \rightarrow HCOOH + CO$	1.95×10^{-21}	16
9.	$C_2H_2 + O_3 \rightarrow CO_2 + H_2 + CO$	5.85×10^{-21}	16
10.	$C_2H_2 + NO_3 \rightarrow NO_3C_2H_2$	3.00×10^{-12}	16
11.	$NO_3C_2H_2 + O_2 \rightarrow NO_3C_2H_2O_2$	4.98×10^{-17}	72 (k)
12.	$NO_3C_2H_2O_2 + NO \rightarrow 2 NO_2 + HCOCHO$	8.89×10^{-12}	16
13.	$NO_3C_2H_2O_2 + HO_2 \rightarrow NO_3C_2H_2O_2H + O_2$	4.98×10^{-12}	16 (l)
14.	$NO_3C_2H_2O_2H + OH \rightarrow NO_3C_2H_2O_2 + H_2O$	3.60×10^{-12}	16 (m)
15.	$CHO \rightarrow WALL$	2.5 s^{-1}	(i)

Table 4.iv   The Ethene Model

No.	Reaction	k	Ref./Notes
1.	$C_2H_4 + OH \rightarrow HOCH_2CH_2$	9.00×10^{-12}	15
2.	$HOCH_2CH_2 + O_2 \rightarrow HOCH_2CH_2O_2$	3.00×10^{-12}	111
3.	$HOCH_2CH_2O_2 + NO \rightarrow HOCH_2CH_2O + NO_2$	9.00×10^{-12}	21
4.	$HOCH_2CH_2O \rightarrow HCHO + CH_2OH$	1.50×10^5 s^{-1}	4
5.	$CH_2OH + O_2 \rightarrow HCHO + HO_2 \cdot$	9.20×10^{-12}	(o)
6.	$HCHO + HO_2 \rightarrow HOCH_2O_2$	7.90×10^{-14}	15
7.	$HOCH_2O_2 \rightarrow HCHO + HO_2$	1.50×10^2 s^{-1}	15
8.	$HCHO + OH \rightarrow CHO + H_2O$	9.21×10^{-12}	(p)
9.	$HCHO + OH \rightarrow HCOOH + H$	1.90×10^{-13}	12
10.	$HOCH_2CH_2O + O_2 \rightarrow HOCH_2CHO + HO_2$	8.40×10^{-15}	4, 12
11a.	$HOCH_2CHO + OH \rightarrow HOCH_2CO + H_2O$	8.00×10^{-12}	15
12.	$HOCH_2CO + O_2 \rightarrow HOCH_2COO_2$	5.00×10^{-12}	(q)
13.	$HOCH_2COO_2 + NO_2 \rightarrow HOCH_2COO_2NO_2$	8.40×10^{-12}	(r)
14.	$HOCH_2COO_2NO_2 \rightarrow HOCH_2COO_2 + NO_2$	5.80×10^{-4} s^{-1}	(r)
15.	$HOCH_2COO_2 + NO \rightarrow CH_2OH + CO_2 + NO_2$	1.40×10^{-11}	(r)
16.	$CH_2OH + NO \rightarrow HNO + CH_2O$	2.40×10^{-11}	120
17.	$HNO + O_2 \rightarrow NO + HO_2$	3.31×10^{-14}	58
18.	$CH_2OH + NO_2 \rightarrow HONO + CH_2O$	8.30×10^{-12}	120
11b.	$HOCH_2CHO + OH \rightarrow HCOCHOH + H_2O$	2.00×10^{-12}	15
19.	$HCOCHOH + O_2 \rightarrow HCOCHO + HO_2$	1.56×10^{-11}	(s)
20.	$HCOCHO + OH \rightarrow HCOCO + H_2O$	1.12×10^{-11}	12, 15
21.	$HCOCO \rightarrow CHO + CO$	4.80×10^7 s^{-1}	(t)
22.	$CHO + O_2 \rightarrow CO + HO_2$	5.60×10^{-12}	15, 90, 125
23.	$CHO + O_2 \rightarrow OH + CO_2$	2.00×10^{-14}	169
24.	$CHO + O_2 \rightarrow HCOO_2$	4.00×10^{-13}	169
25.	$CHO + NO \rightarrow CO + HNO$	1.23×10^{-11}	(i)
26.	$CHO + NO_2 \rightarrow HONO + CO$	3.53×10^{-11}	31, 170
27.	$CHO + NO_2 \rightarrow HCO_2 + NO$	2.07×10^{-11}	31, 170
28.	$HCO_2 + O_2 \rightarrow HO_2 + CO_2$	5.60×10^{-12}	(h)
29.	$C_2H_4 + O_3 \rightarrow HO_2 + PRODUCTS$	2.04×10^{-19}	13
30.	$C_2H_4 + O_3 \rightarrow PRODUCTS$	1.50×10^{-18}	13
31.	$CHO \rightarrow WALL$	2.5 s^{-1}	(j)

113

Table 4.v   The Propene Model

No.	Reaction	k	Ref./Notes
1a.	$CH_3CHCH_2 + OH \rightarrow CH_3CHCH_2OH$	1.95×10^{-11}	12, 15
2.	$CH_3CHCH_2OH + O_2 \rightarrow CH_3CH(O_2)CH_2OH$	1.16×10^{-13}	113
3.	$CH_3CH(O_2)CH_2OH + NO \rightarrow CH_3CH(O)CH_2OH + NO_2$	8.16×10^{-12}	(u)
4.	$CH_3CH(O)CH_2OH \rightarrow CH_3CHO + CH_2OH$	$6.00 \times 10^{6} \, s^{-1}$	71
5.	$CH_3CH(O)CH_2OH + O_2 \rightarrow CH_3COCH_2OH + HO_2$	3.00×10^{-14}	71
6.	$CH_3COCH_2OH + OH \rightarrow CH_3COCHOH + H_2O$	3.00×10^{-12}	41
7.	$CH_3COCHOH + O_2 \rightarrow CH_3COCHO + HO_2$	1.56×10^{-11}	(v)
1b.	$CH_3CHCH_2 + OH \rightarrow CH_3CH(OH)CH_2$	1.05×10^{-11}	12, 15
7.	$CH_3CH(OH)CH_2 + O_2 \rightarrow CH_3CH(OH)CH_2O_2$	3.82×10^{-12}	113
8.	$CH_3CH(OH)CH_2O_2 + NO \rightarrow CH_3CH(OH)CH_2O + NO_2$	8.40×10^{-12}	(w)
9.	$CH_3CH(OH)CH_2O \rightarrow CH_3CHOH + HCHO$	$6.00 \times 10^{5} \, s^{-1}$	71
10.	$CH_3CH(OH)CH_2O + O_2 \rightarrow CH_3CH(OH)CHO + HO_2$	6.90×10^{-15}	(x)
11.	$CH_3CH(OH)CHO + OH \rightarrow CH_3C(OH)CHO + H_2O$	2.00×10^{-12}	(y)
12.	$CH_3C(OH)CHO + O_2 \rightarrow CH_3COCHO + HO_2$	1.56×10^{-11}	(v)
13.	$CH_3COCHO + OH \rightarrow CH_3CO + CO + H_2O$	1.70×10^{-11}	15
14.	$CH_3CO + OH \rightarrow CH_2CO + H_2O$	2.00×10^{-11}	72
15.	$CH_2CO + OH \rightarrow HCHO + CHO$	9.00×10^{-12}	12
16.	$CH_2CO + OH \rightarrow CH_2OH + CO$	9.00×10^{-12}	12
17.	$CH_3CH(OH)CHO + OH \rightarrow CH_3CH(OH)CO + H_2O$	8.00×10^{-12}	(z)
18.	$CH_3CH(OH)CO + O_2 \rightarrow CH_3CH(OH)COO_2$	3.82×10^{-12}	(†)
19.	$CH_3CH(OH)COO_2 + NO_2 \rightarrow CH_3CH(OH)COO_2NO_2$	8.40×10^{-12}	(s)
20.	$CH_3CH(OH)COO_2NO_2 \rightarrow CH_3CH(OH)COO_2 + NO_2$	$5.80 \times 10^{-4} \, s^{-1}$	(s)
21.	$CH_3CH(OH)COO_2 + NO \rightarrow CH_3CHOH + CO_2 + NO_2$	1.40×10^{-11}	(s)
22.	$CH_3CHOH + O_2 \rightarrow CH_3CHO + HO_2$	1.56×10^{-11}	5, 111
23.	$CH_3CHO + OH \rightarrow CH_3CO + H_2O$	1.60×10^{-11}	15
24.	$CH_3CO + O_2 \rightarrow CH_3COO_2$	5.00×10^{-12}	15, 112
25.	$CH_2OH + O_2 \rightarrow HCHO + HO_2$	9.20×10^{-12}	(p)
26.	$HCHO + HO_2 \rightarrow HOCH_2O_2$	7.90×10^{-14}	15
27.	$HOCH_2O_2 \rightarrow HCHO + HO_2$	$1.50 \times 10^{2} \, s^{-1}$	15
28.	$HCHO + OH \rightarrow CHO + H_2O$	9.21×10^{-12}	(c)
29.	$HCHO + OH \rightarrow HCOOH + H$	1.90×10^{-13}	121
30.	$CH_2OH + NO \rightarrow HNO + HCHO$	2.40×10^{-11}	121
31.	$HNO + O_2 \rightarrow NO + HO_2$	3.31×10^{-14}	58
32.	$CH_2OH + NO_2 \rightarrow HONO + HCHO$	8.30×10^{-12}	14
33.	$CHO + O_2 \rightarrow CO + HO_2$	5.60×10^{-12}	15, 90, 125
34.	$CHO + O_2 \rightarrow OH + CO_2$	2.00×10^{-14}	169
35.	$CHO + O_2 \rightarrow HCOO_2$	4.00×10^{-13}	169
36.	$CHO + NO \rightarrow CO + HNO$	1.23×10^{-11}	(i)
37.	$CHO + NO_2 \rightarrow HONO + CO$	3.53×10^{-11}	31, 170
38.	$CHO + NO_2 \rightarrow HCO_2 + NO$	2.07×10^{-11}	31, 170
39.	$HCO_2 + O_2 \rightarrow HO_2 + CO_2$	5.60×10^{-12}	(h)
40.	$CH_3CHCH_2 + O_3 \rightarrow HO_2 + PRODUCTS$	2.82×10^{-18}	13
41.	$CH_3CHCH_2 + O_3 \rightarrow PRODUCTS$	8.48×10^{-18}	13
42.	$CHO \rightarrow WALL$	$2.5 \, s^{-1}$	(j)

Table 4.vi   The Ethanol Model

No.	Reaction	k	Ref./Notes
1a.	$CH_3CH_2OH + OH \rightarrow CH_3CHOH + H_2O$	2.67×10^{-12}	(‡)
1b.	$CH_3CH_2OH + OH \rightarrow HOCH_2CH_2 + H_2O$	3.90×10^{-13}	(‡)
1c.	$CH_3CH_2OH + OH \rightarrow CH_3CH_2O + H_2O$	3.40×10^{-13}	(‡)
2.	$HOCH_2CH_2 + O_2 \rightarrow HOCH_2CH_2O_2$	3.00×10^{-12}	111
3.	$HOCH_2CH_2O_2 + NO \rightarrow HOCH_2CH_2O + NO_2$	9.00×10^{-12}	21
4.	$HOCH_2CH_2O \rightarrow HCHO + CH_2OH$	$1.50 \times 10^5 \ s^{-1}$	4
5.	$CH_2OH + O_2 \rightarrow HCHO + HO_2$	9.20×10^{-12}	(o)
6.	$HCHO + HO_2 \rightarrow HOCH_2O_2$	7.90×10^{-14}	15
7.	$HOCH_2O_2 \rightarrow HCHO + HO_2$	$1.50 \times 10^2 \ s^{-1}$	15
8a.	$HCHO + OH \rightarrow CHO + H_2O$	9.21×10^{-12}	(p)
8b.	$HCHO + OH \rightarrow HCOOH + H$	1.90×10^{-13}	12
9.	$HOCH_2CH_2O + O_2 \rightarrow HOCH_2CHO + HO_2$	8.40×10^{-15}	4, 12
10a.	$HOCH_2CHO + OH \rightarrow HOCH_2CO + H_2O$	8.00×10^{-12}	15
11.	$HOCH_2CO + O_2 \rightarrow HOCH_2COO_2$	5.00×10^{-12}	(q)
12.	$HOCH_2COO_2 + NO_2 \rightarrow HOCH_2COO_2NO_2$	8.40×10^{-12}	(r)
13.	$HOCH_2COO_2NO_2 \rightarrow HOCH_2COO_2 + NO_2$	$5.80 \times 10^{-4} \ s^{-1}$	(r)
14.	$HOCH_2COO_2 + NO \rightarrow CH_2OH + CO_2 + NO_2$	1.40×10^{-11}	(r)
15.	$CH_2OH + NO \rightarrow HCHO + HNO$	2.40×10^{-11}	121
16.	$HNO + O_2 \rightarrow NO + HO_2$	3.31×10^{-14}	58
17.	$CH_2OH + NO_2 \rightarrow HONO + CH_2O$	8.30×10^{-12}	121
10b.	$HOCH_2CHO + HO \rightarrow HOCHCHO + H_2O$	2.00×10^{-12}	15
18.	$HOCHCHO + O_2 \rightarrow HCOCHO + HO_2$	1.56×10^{-11}	(s)
19.	$HCOCHO + HO \rightarrow HCOCO + H_2O$	1.12×10^{-11}	12, 15
20.	$HCOCO \rightarrow CHO + CO$	$4.80 \times 10^7 \ s^{-1}$	(t)
21a.	$CHO + O_2 \rightarrow CO + HO_2$	5.60×10^{-12}	15, 90, 125
21b.	$CHO + O_2 \rightarrow CO_2 + OH$	2.00×10^{-14}	169
21c.	$CHO + O_2 \rightarrow HCOO_2$	4.00×10^{-13}	169
22.	$CHO + NO \rightarrow CO + HNO$	1.23×10^{-11}	(i)
23a.	$CHO + NO_2 \rightarrow HONO + CO$	3.53×10^{-11}	31, 170
23b.	$CHO + NO_2 \rightarrow HCO_2 + NO$	2.07×10^{-11}	31, 170
24.	$CH_3CHOH + O_2 \rightarrow CH_3CHO + HO_2$	1.56×10^{-11}	5, 111
25.	$CH_3CH_2O + O_2 \rightarrow CH_3CHO + HO_2$	8.00×10^{-15}	15
26.	$CH_3CHO + OH \rightarrow CH_3CO + H_2O$	1.60×10^{-11}	15
27.	$CH_3CO + O_2 \rightarrow CH_3COO_2$	5.00×10^{-12}	15, 112
28.	$CH_3CO + OH \rightarrow CH_2CO + H_2O$	2.00×10^{-11}	72
29a.	$CH_2CO + OH \rightarrow HCHO + CHO$	9.00×10^{-12}	(¶)
29b.	$CH_2CO + OH \rightarrow CH_2OH + CO$	9.00×10^{-12}	(¶)
30.	$HCO_2 + O_2 \rightarrow HO_2 + CO_2$	5.60×10^{-12}	(h)
31.	$CHO \rightarrow WALL$	$2.5 \ s^{-1}$	(j)

115

4.3.2 Notes for the Models

(a) All rate constants are in cm^3 molecule^{-1} s^{-1} unless otherwise stated

(b) The rate constant used is $k(HOCH_2CH_2 + O_2)$, as $HOCH_2CH_2$ and CH_3OCH_2 are isomeric.

(c) The rate constant is an average of $k(HOCH_2O_2 + NO) = 5.60 \times 10^{-12}$ [*Veyret et al.* 1982] and $k(HOCH_2CH_2O_2 + NO) = 9.0 \times 10^{-12}$ [*Becker et al.,* 1991] $= 7.3 \times 10^{-12}$; allowing for 2% nitrate formation $= 7.23 \times 10^{-12}$

(d) The rate constant used is $k(HOCH_2CH_2O + O_2)$ [*Atkinson,* 1986; 1990]

(e) There is an alternative product from this reaction, CH_3OCO. However, a study of similar reactions (OH with HCOOH [*Singleton et al.,* 1988], CH_3COOH [*Singleton et al.,* 1989] and CH_3COOCH_3 [*Campbell and Parkinson,* 1978]) show that the attack predominantly occurs at the alkoxy end and so this second channel is unimportant.

(f) The rate constant used is an average of $k(HOCH_2CH_2 + O_2) = 3.00 \times 10^{-12}$ [*Miyoshi et al.,* 1989a] and $k(CH_3CH_2CH_2 + O_2) = 6.00 \times 10^{-12}$ [*Atkinson et al.,* 1989]

(g) k is equal to $k(HOCH_2CH_2O \rightarrow CH_2OH + HCHO)$ [*Atkinson,* 1986; 1990]

(h) The rate constant used is that for the reaction of CHO with O_2, as in reaction 21

(i) The rate constant used is an average of 1.26×10^{-11} [*Langford and Moore,* 1984], 1.23×10^{-11} [*Veyret and Lesclaux,* 1981] and 1.20×10^{-11} [*Nadtochenko et al.,* 1980]

(j) The rate of various wall reactions were taken by *Hastie et al.* [1991] to be $2.5 s^{-1}$, this rate constant has been adopted here.

(k) The rate constant is arrived at by fitting the product yields reported by *Hatakeyama et al.* [1985] to the rate data from *Lorenz et al.* [1985].

(l) Assumed to be the same as $k(C_2H_5OH + O_2)$, see note (k) above.

(m) Assumed to be the same as $k(HO_2 + C_2H_5O_2)$

(n) Assumed to be the same as $k(OH + CH_3OOH \rightarrow CH_3O_2 + H_2O)$

(o) The given rate constant is an average of the following values (all $\times 10^{-12}$): 9.3 [*Cvetanovic,* 1987]; 8.59 [*Wayne,* 1988]; 9.5, 10.5, 8.6, 8.8 (all from

116

[Pagsberg et al., 1989]); and 8.61 [Nesbitt et al., 1988]

(p) k is an average of the following values (all $\times 10^{12}$) 9.0 [Atkinson, 1986], 11.0 [Atkinson, 1989] and 8.1 [Temps and Wagner, 1984a]

(q) The rate constant was taken as that for $k(CH_3CO + O_2) = 5.0 \times 10^{-12}$ [Atkinson et al. 1991]

(r) The rate constants were assumed to be the same as $k(CH_3COO_2 + NO_2)$, $k(CH_3COO_2NO_2 \rightarrow CH_3COO_2 + NO_2)$ and $k(CH_3COO_2 + NO)$ [Atkinson et al. 1991]

(s) The rate constant used in the model was assumed to be the same as $k(CH_3CHOH + O_2) = 1.56 \times 10^{-11}$ [Miyoshi et al., 1989a; Anastasi et al., 1989]

(t) The rate constant was estimated from data quoted by Niki et al. [1985] and Atkinson [1986]

(u) $k(CH_3CH(O_2)CH_2OH + NO)$ was assumed to be equal to $k(i\text{-}C_3H_7O_2 + NO)$ [Atkinson et al., 1989] $= k(sec\text{-}C_4H_9O_2 + NO)$ [Atkinson et al., 1987] $= 8.5 \times 10^{-12}$. Allowing for 4% nitrate formation, $k = 8.16 \times 10^{-12}$

(v) The rate constant used is $k(CH_3CHOH + O_2)$

(w) $k(CH_3CH(OH)CH_2O_2 + NO)$ was assumed to equal $k(n\text{-}C_3H_7O_2 + NO)$ [Atkinson et al., 1989] $= k(n\text{-}C_4H_9O_2 + NO)$ [Atkinson et al., 1987] $= 8.7 \times 10^{-11}$. Allowing for 4% nitrate formation, $k = 8.4 \times 10^{-11}$

(x) The rate constant is for $k(HOCH_2CH_2O + O_2)$ [Anastasi et al., 1991]

(y) The rate constant is for $k(HOCH_2CHO + OH \rightarrow HOCHCHO + H_2O)$ [Atkinson et al., 1989]

(z) The rate constant is for $k(HOCH_2CHO + HO \rightarrow OHCH_2CO + H_2O)$ [Atkinson et al., 1989]

(†) The rate constant is for $k(CH_3CH(OH)CH_2 + O_2)$ [Miyoshi et al., 1990]

(‡) The overall rate constant k_1 is 3.4×10^{-12} [Atkinson et al., 1989]. The only known value for k_{1a}/k_1 is 0.75 ± 0.15 [Meier et al., 1985]. k_{1b} was estimated as $1/3\ k(OH + t\text{-}C_4H_9OH)$ [Wallington et al., 1988a] assuming alcoholic H abstraction is negligible. k_{1c} was estimated at 10% of k_1.

(¶) Overall rate constant for $OH + CH_2CO$ is 1.8×10^{-11}, the branching ratio was taken to be 1:1 as the actual value is not known.

4.4 Results and Discussion

4.4.1 Chain Length

All the chain carrying agents investigated gave higher chain lengths than CO, and the actual values are presented in Figure 4.1. The improvement over CO is also demonstrated by the fact that the Relative Chain Lengths were between 1.7 for ethanol and 2.7 for propene and DME .
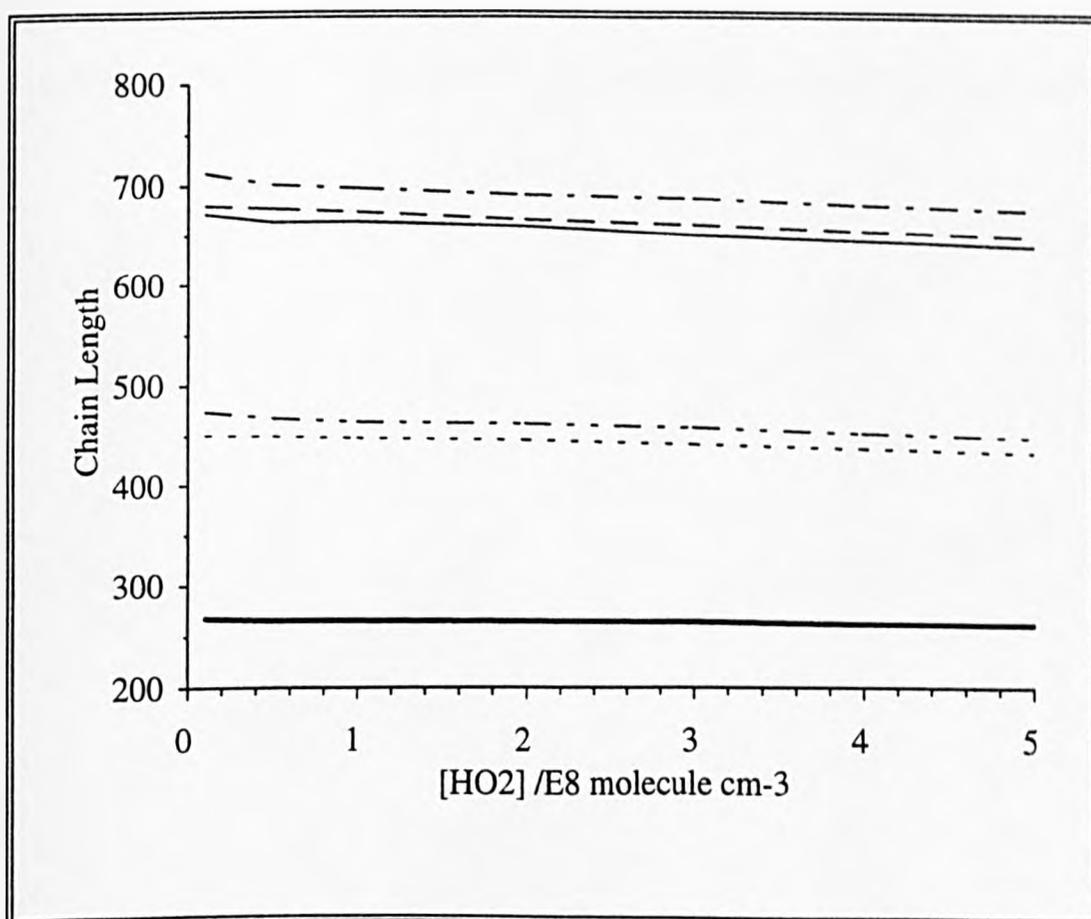
Figure 4.1   Chain Length as a Function of HO_2 Concentration

—— DME; ▬ CO; — — — ethene; — – — propene;
— – – — ethanol; - - - - - - ethyne.
[Chain carrier] = 1.97 $\times 10^{18}$ molecule cm^{-3}; [NO] = 1.48 $\times 10^{14}$ molecule cm^{-3}

118

This was due to a faster initial reaction with OH and the subsequent reactions that produce further HO_2 radicals. Also the chain lengths were found to be virtually constant over the range of HO_2 concentrations investigated, an important feature in an atmospheric monitor. If this were not so, there could have been problems interpreting the data from a monitor to provide a unique measurement.

At all the concentrations of HO_2 investigated the final concentration of NO_2 produced (Figure 4.2) was sufficiently large to be detectable by existing methods such as luminol chemiluminescence[*Wendel et al.*, 1983; *Maeda et al.*, 1980; *Drummond et al.*, 1990] and laser-induced fluorescence [*Birnbaum*,1976; *Fincher et al.* 1978].
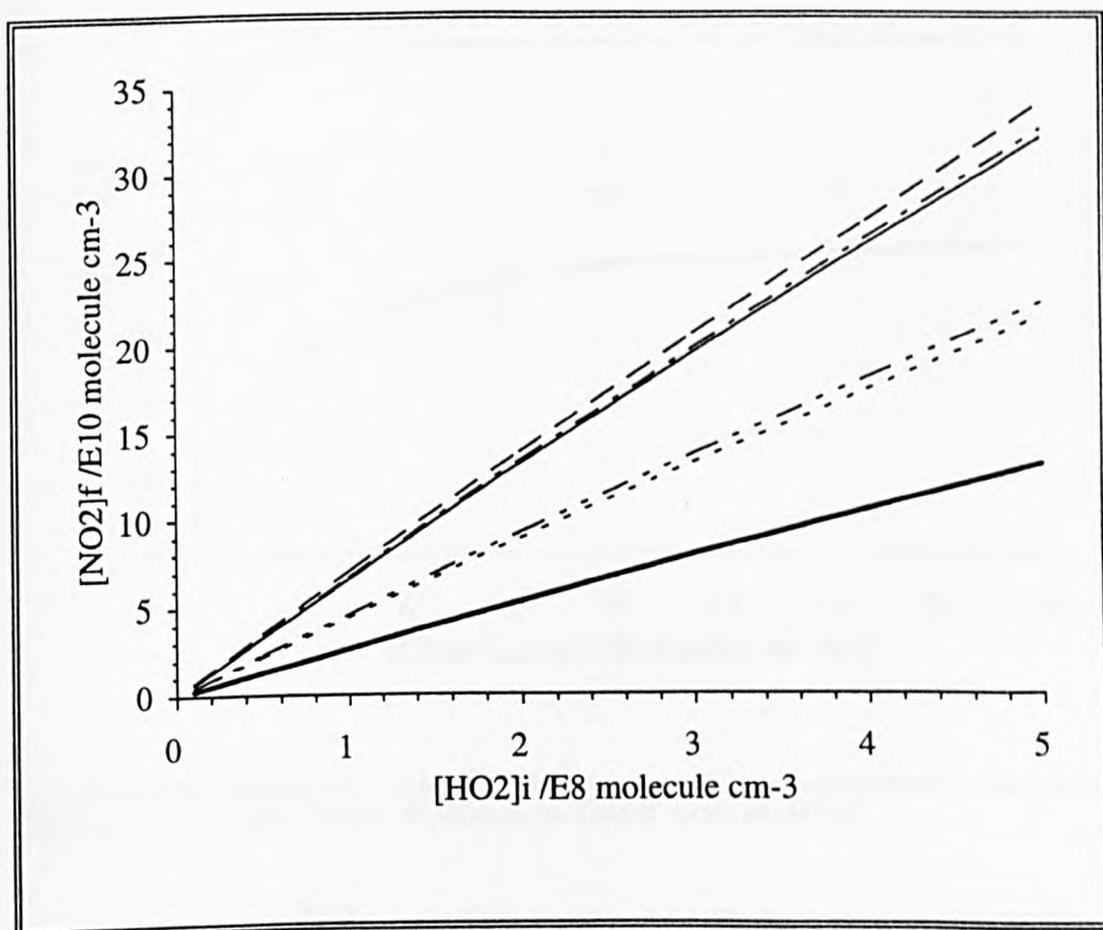
Figure 4.2   Final NO_2 Concentrations

—— DME; —— CO; — — — ethene; — – — propene; — – – — ethanol; - - - - - - ethyne.
[Chain carrier] = 1.97 x10^{18} molecule cm^{-3}; [NO] = 1.48 x10^{14} molecule cm^{-3}

119

4.4.2 Simulated Reactor Conditions

With the exception of the CO system, it was found that varying the amount of chain carrier added by a factor of two in either direction from the value used by *Hastie et al.* [1991] had little effect on the final concentration of NO_2 and hence on the chain length. However, lowering the amount of chain carrier by more than a factor of four to below 4.9×10^{17} molecule cm^{-3}, resulted in a reduction in the chain lengths observed (Figure 4.3).
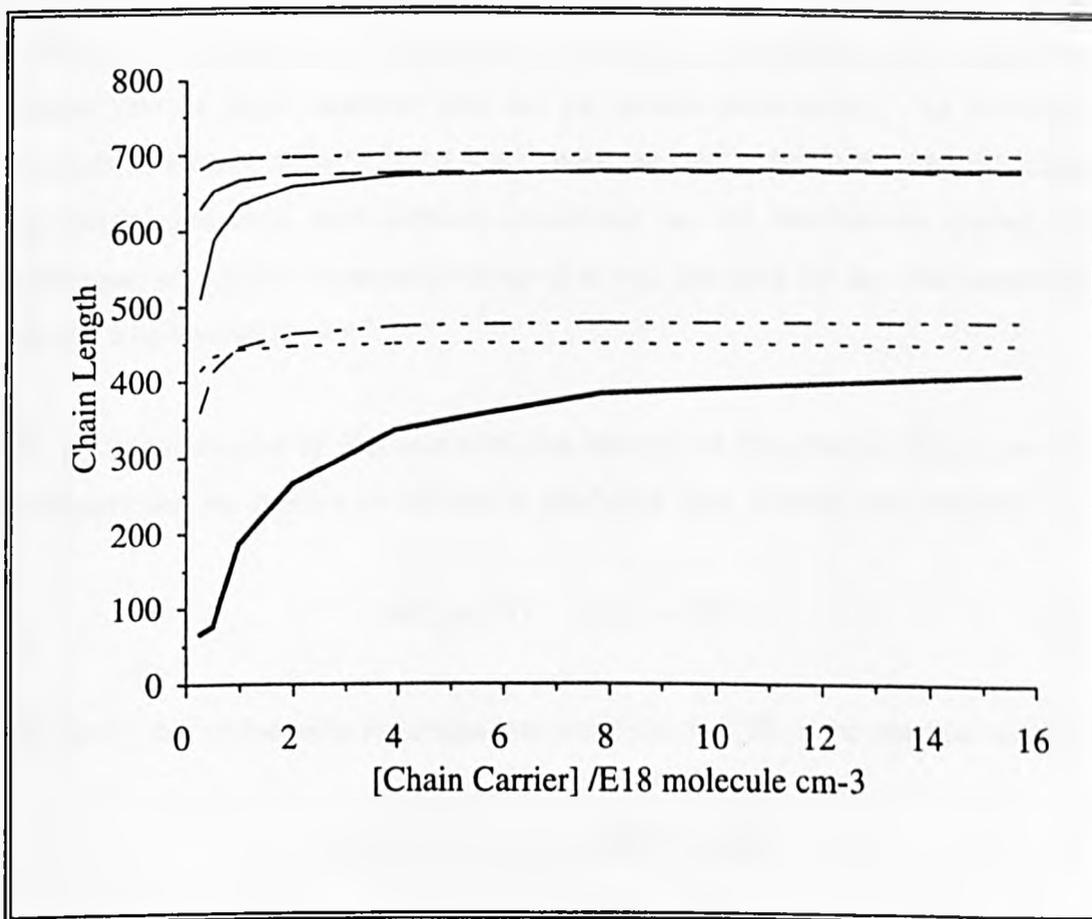
Figure 4.3   Chain Length Response to Carrier Concentration

―――― DME;   ▬▬ CO;   ― ― ― ethene;   ― – ― propene;
― – – ― ethanol; - - - - - - ethyne.
[NO] = 1.48×10^{14} molecule cm^{-3}; [HO_2] = 1.0×10^{8} cm^{-3}

This relative lack of response of the chain lengths of the organic systems to the amount of chain carrier present is due to the reactor being saturated with the chain

120

carrier and thus the reaction of the carrier with OH is the only significant removal process for the radical. At lower concentrations of the carrier other processes, including wall loss and reaction with NO, compete. In the case of the CO system the radical loss processes are still playing a role at the higher CO concentrations because the rate of the reaction between CO and OH is relatively slow.

The ability to reduce the concentration of the chain carrier has three advantages: (i) the consumption of the chain carrier, and so the running cost of the apparatus, is reduced; (ii) secondary reactions of the carrier (e.g. with ozone in the case of the alkenes) are minimized; (iii) for ethanol the lower concentrations make addition of vapour from a liquid reservoir into the gas stream much easier. As the vapour pressure of ethanol at 298K is 1.1 $\times 10^{18}$ molecule cm^{-3} [CRC, 1982] the subsequent modelling concerned with ambient conditions, i.e. the interference studies, was performed with initial concentrations equal to half that used for the other amplifiers, i.e. 9.8 $\times 10^{17}$ molecule cm^{-3}.

As the concentration of NO increases, the amount of HO$_2$ that is lost to the wall decreases and the amount of OH that is produced rises, through the reaction:

$$HO_2 + NO \rightarrow NO_2 + OH \qquad (4.4)$$

However, one of the most important loss processes for OH is the reaction with NO:

$$OH + NO \ (+M) \rightarrow HONO \ (+M) \qquad (4.7)$$
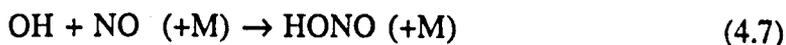
This reaction competes with the loss of OH to the reactor walls and the reaction between OH and the chain carrier. Hence there is a balance between increasing the production of OH by reducing the wall loss of HO$_2$, and the loss of OH by reaction with NO.

Where this balance lies for each of the chain carriers is again dependent on the rate of their reaction with OH. Hence, for CO the initial concentration of NO used in this

work and by Hastie et al. (1.48×10^{14} molecule cm^{-3}) is optimum while for the other chain carriers increasing the NO concentration results in an increase in the chain length. For ethene and propene the increase does not tail off significantly until four times the original level, reflecting the high rate of reaction with OH (Figure 4.4).
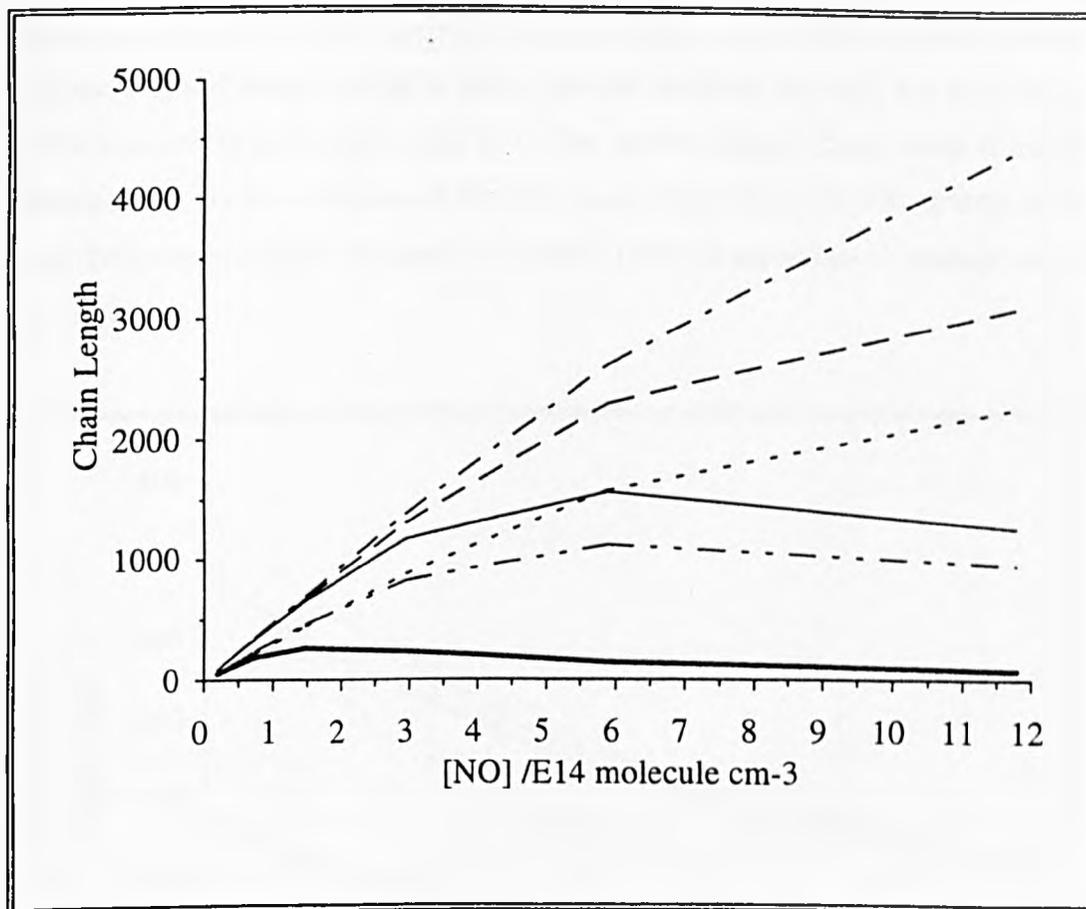
Figure 4.4   Chain Length Response to NO Concentration

——— DME; ▬▬ CO; — — — ethene; — – — propene;
— – – — ethanol; - - - - - - ethyne.
[Chain carrier] = 1.97×10^{18} molecule cm^{-3}; [HO$_2$] = 1.0×10^{8} cm^{-3}

As indicated earlier, under these simulated conditions the most important limitation on the chain length is imposed by the loss of the radicals to the walls of the reactor. Figure 4.5 shows that in all the systems, reduction of this rate greatly increases the chain length.

As with the response of the different systems to the changes in NO concentration, the extent to which the chain length is affected depends on the proportion of radicals that were lost to the wall, and the secondary chemistry of the system. While the relatively slow rate of the OH/CO reaction means that a larger proportion of the OH radicals diffuse to the walls rather than react with CO, the subsequent chemistry of the system means that this terminates only one chain. However, the faster reaction between OH and ethene results in fewer radicals reaching the wall, but each radical that is lost has the potential to start up to five further chains. Thus, while it may be expected that, on the evidence of the OH attack rates alone, the CO system would show the greatest change, the positive feedback from the secondary chemistry reduces the effect.
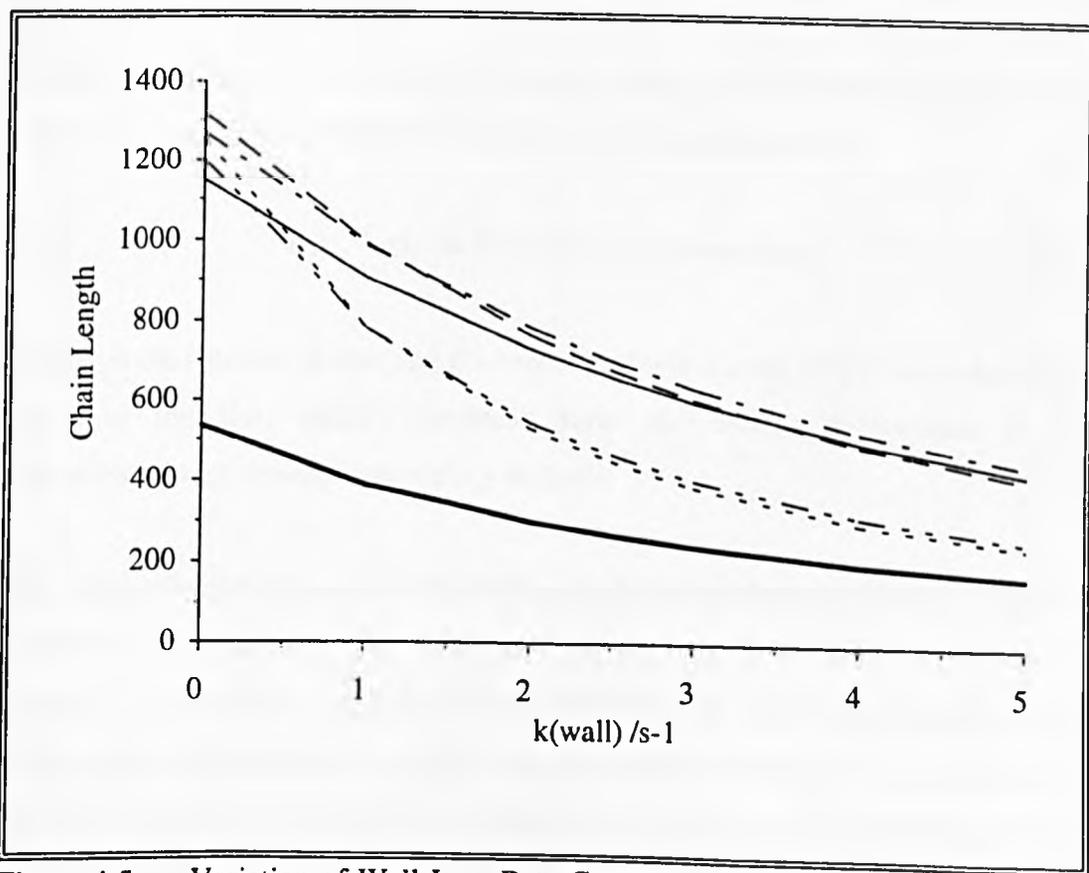
Figure 4.5   Variation of Wall Loss Rate Constant

—— DME; —— CO; — — — ethene; — – — propene;
— – – — ethanol; - - - - - - ethyne.
[Chain carrier] = 1.97 $\times 10^{18}$ molecule cm^{-3}; [NO] = 1.48 $\times 10^{14}$ molecule cm^{-3}; [HO$_2$] = 1.0 $\times 10^8$ cm^{-3}

4.4.3 Effects of the Simulation of Interferences

Ambient ozone in the air stream will react with the excess NO to form NO_2:

$$O_3 + NO \rightarrow O_2 + NO_2 \qquad\qquad (4.1)$$

This increase of the background NO_2 signal makes it more difficult to discriminate between the NO_2 produced by the chemical amplification process and the background. Consequently the sensitivity to atmospheric radicals is reduced. A higher chain length, and so a higher final NO_2 concentration, improves the discrimination possible.

As indicated earlier the alkenes also suffer from attack by ozone which can form HO_2 radicals [Atkinson et al., 1989] and further reduce the discrimination power. For example, in the case of ethene the reaction can be represented by:

$$C_2H_4 + O_3 \rightarrow 0.12 \; HO_2 + \text{other products} \qquad\qquad (4.8)$$
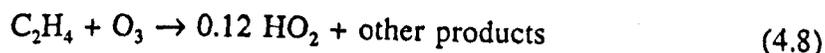
Although the reaction is slow and the branching ratio is only 0.12 it has a significant effect as the HO_2 radicals produced form new chains independent of the concentrations of atmospheric peroxy radicals.

The ozone discrimination potentials (DP_{ozone}) of each of the systems over a range of ambient ozone concentrations (6-25 $x10^{11}$ molecule cm^{-3}) are shown in Figure 4.6. The DP_{ozone} of the ethene system could be improved from that shown by reducing the ethene concentration and increasing the concentration of NO, as the ozone was forced to react with the NO rather than the ethene, and the extra NO also improved the chain length. Despite the high chain length of the propene system, it suffered badly from a fast attack by ozone with a branching ratio for HO_2 production twice that for ethene. In addition to HO_2 several other radicals, such as CH_3O_2, CH_3CHO_2 and CH_2O_2, are formed [Atkinson et al., 1989] that can cause further interference. For these reasons no further simulation work was carried out on the propene system.

Figure 4.6   Ozone Discrimination

―― DME; ▬ CO; ― ― ― ethene; ― – ― propene;
― – – ― ethanol; - - - - - - ethyne.
[Chain carrier] =1.97×10^{18} molecule cm^{-3}, except [ethanol] = 9.87×10^{17}
molecule cm^{-3}; [NO] = 1.48×10^{14} molecule cm^{-3}; [HO$_2$] = 1.0×10^{8} cm^{-3}

The thermolyses of PAN and PNA contribute to the background NO$_2$ in two ways. In both cases the products are NO$_2$, which adds to the background directly, and a peroxy radical, CH$_3$COO$_2$ for PAN and HO$_2$ for PNA.

The simulations show that only 0.04% of the PAN would break down in the 1.1s residence time in the chamber, as would be predicted from its relatively long lifetime at 298K of 45mins [*Hastie et al.*, 1991]. As a result, the contribution of the NO$_2$ produced directly was almost negligible compared to other background sources, despite PAN concentrations being typically a factor of 2000 times greater than HO$_2$ concentrations.

Where significant interferences did arise, however, was from the reactions of the CH_3COO_2 radical. This rapidly underwent a series of reactions that resulted in the formation of a further two molecules of NO_2 and a HO_2 radical. It is this radical that is the critical aspect of the interference as it can start a new amplification chain, making the three molecules of NO_2 produced more directly from the thermolysis effectively insignificant. Even at low PAN concentrations (1 $\times 10^{10}$ molecule cm^{-3}) the contribution to the final NO_2 concentration was significant (Figure 4.7).

Within experimental error the DP_{PAN} of each systems was affected equally as the additional HO_2 was released at the same rate in each case. The independence of the thermolysis rate to the system was confirmed by following the amount of NO_2 produced directly by the thermolysis.
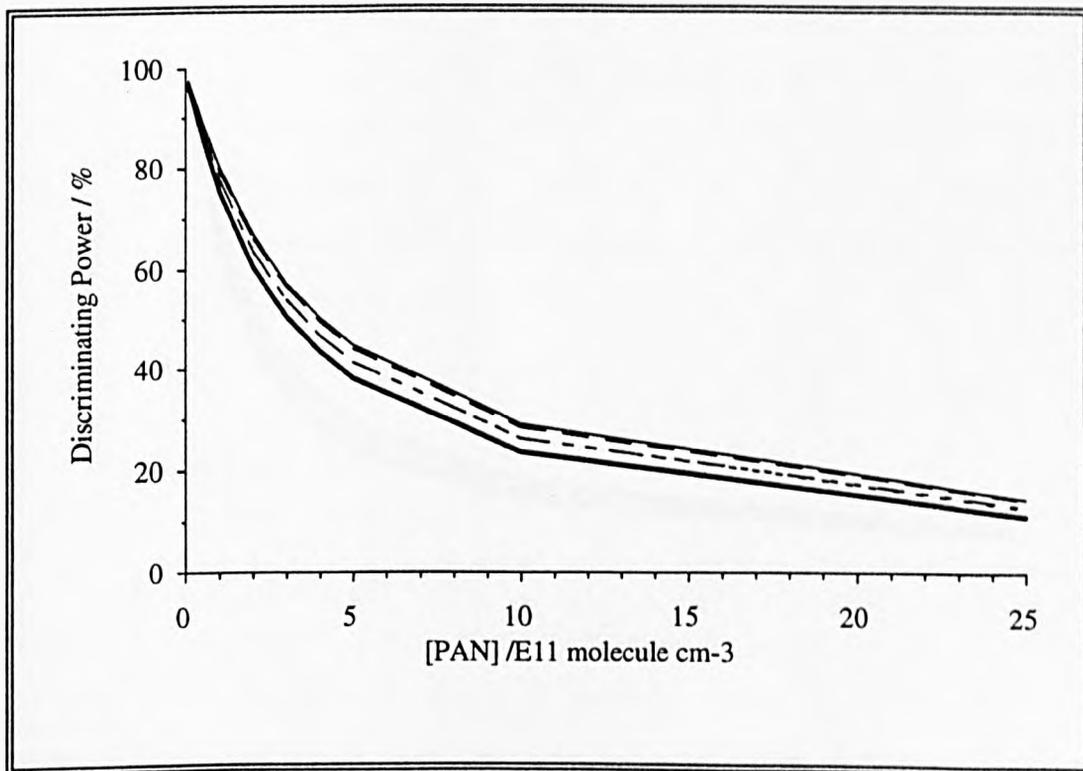
Figure 4.7   PAN Discrimination

—— DME; —— CO; — — — — ethene; — - — propene; — - - — — ethanol; - - - - - - ethyne.
[Chain carrier] $=1.97 \times 10^{18}$ molecule cm^{-3}, except [ethanol] $= 9.87 \times 10^{17}$ molecule cm^{-3}; [NO] $= 1.48 \times 10^{14}$ molecule cm^{-3}; [HO_2] $= 1.0 \times 10^8$ cm^{-3}

126

In the PNA interference simulations the NO_2 produced directly by the thermolysis was again virtually negligible, although this was due to the low levels of PNA present rather than its lifetime. It was found that approximately 8.5% of the PNA decomposed during the 1.1s reaction time (compared with 0.04% of the PAN), but because the PNA concentrations investigated were a factor of 100 lower than those for PAN, approximately double the amount of HO_2 was produced by the thermolysis. The result was that PNA concentrations of $(1-25)$ $x10^9$ molecule cm^{-3} produced an equivalent DP to PAN levels 100 times greater (Figure 4.8). At present, typical ambient concentrations of PNA are not known, though the short lifetime suggests that the concentration is lower than that of PAN. On the other hand, as the PNA precursor, HO_2, is present in higher levels than the peroxyacetyl radical precursor for PAN, it is also possible that the steady state concentration of PNA is comparable with that of PAN.
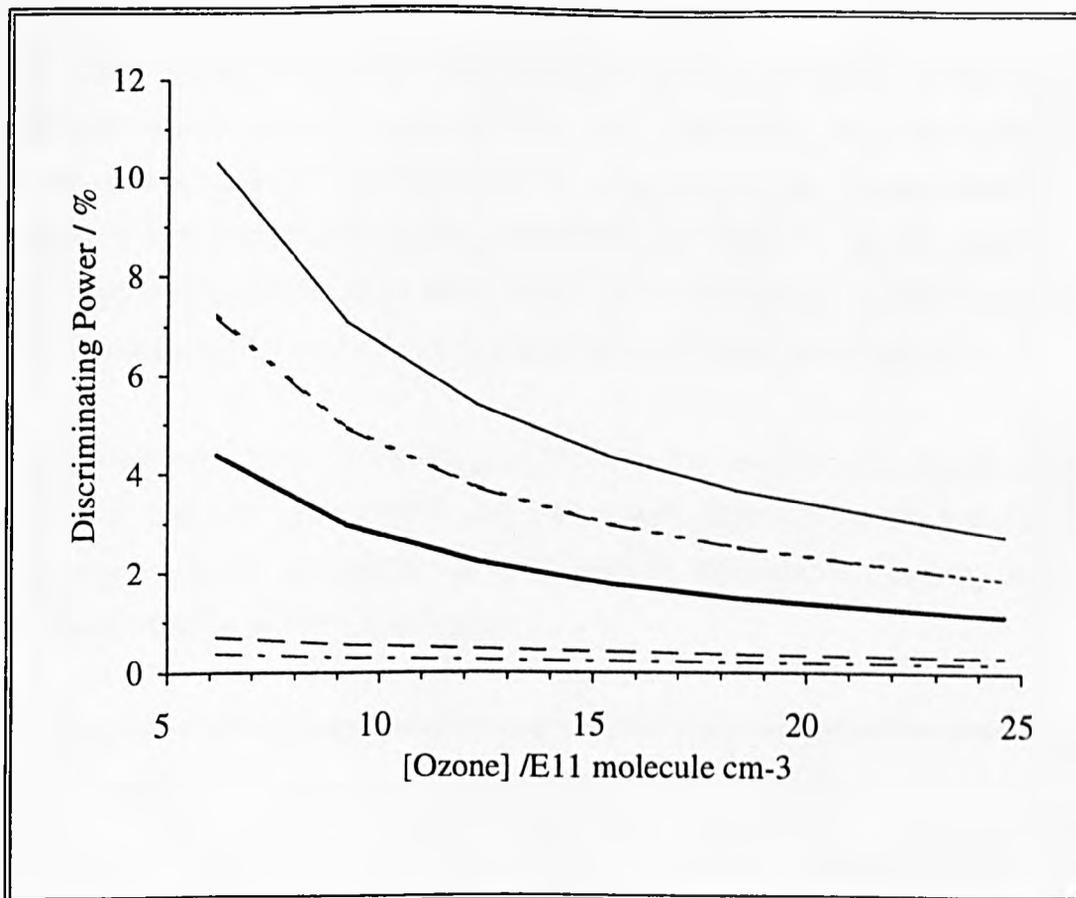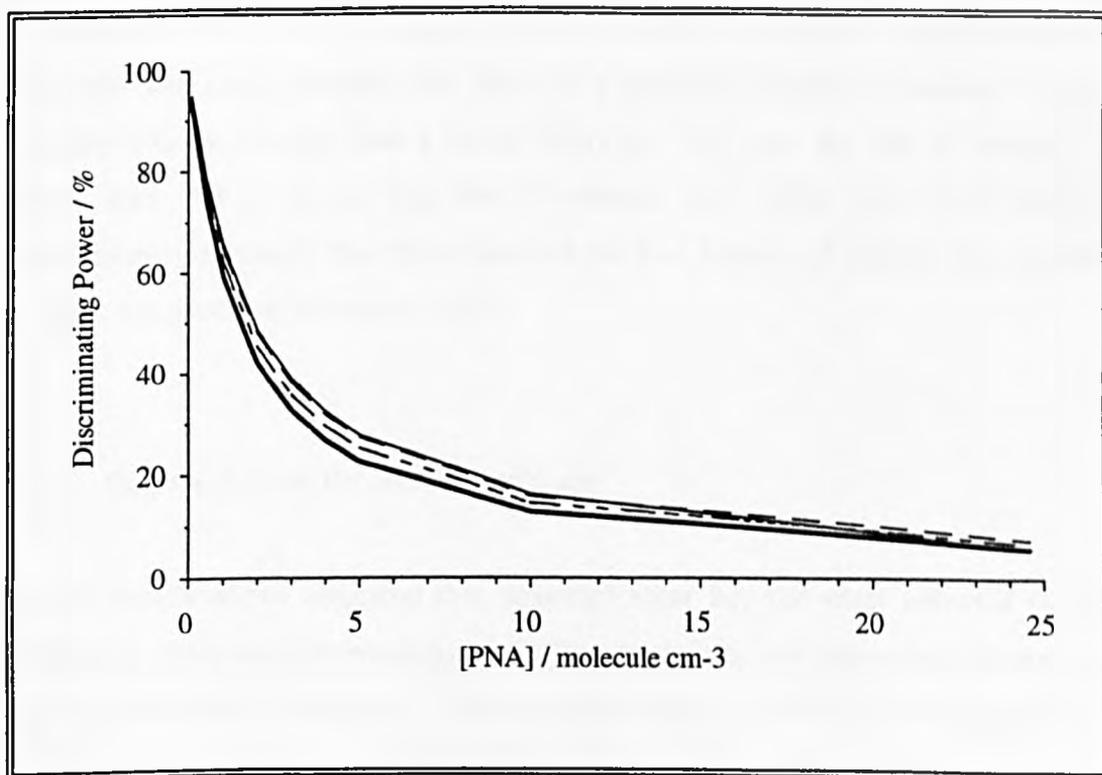

Figure 4.8   PNA Discriminaton

—— DME; —— CO; — — — ethene; — – — propene;
— – – — ethanol; - - - - - - ethyne.
[Chain carrier] $=1.97x10^{18}$ molecule cm^{-3}, except [ethanol] $= 9.87x10^{17}$ molecule cm^{-3}; [NO] $= 1.48x10^{14}$ molecule cm^{-3}; [HO_2] $= 1.0x10^8$ cm^{-3}

Although the chemical amplification technique measures the sum of all atmospheric odd-hydrogen radicals, simulations show that the contribution to the total from ambient OH concentrations are so small as to be well within experimental error. This is because OH concentrations are between a factor of 100 and 1000 less than HO_2 concentrations. Ambient OH concentrations therefore cannot reliably be resolved with this method.

4.4.4   Conclusions

All the systems investigated appear to perform better than CO as chain carrying agents. However, they all have weaknesses as well as strengths; the alkenes have a fast initial OH reaction and at least one further conversion of NO to NO_2 but suffer from the attack by ozone. Ethanol and ethyne have no important interferences but relatively low chain lengths; also, there is a practical problem of ethanol vapour delivery into the reactor from a liquid reservoir. Although the rate of reaction of ethers with OH is slower than that of ethanol they suffer little from ambient interferences; it appears that ethers combine the best features of alkenes and alcohols without the problems discussed above.

4.5   Optimisation of the DME Conditions

As the results above indicated that dimethyl ether has the most potential of the alternative chain carriers investigated, further modelling was performed to establish the optimum reactor conditions. The work above has shown that the chain length can be improved by adjusting the initial concentrations of both NO and DME. However, the optimum conditions for a 'clean' sample may not provide the best discrimination against the interferences present in ambient air. For this reason, the optimum reactor conditions were determined by maximising the discrimination against the NO_2 produced in the monitor by ozone, where:

$$DP_{ozone} = \frac{[NO_2]_o}{[NO_2]_{Total}}$$

The discrimination against ozone was chosen, rather than against PAN or PNA as these cause false signals as a result of thermolysis, and as such are very dependent upon residence time in the reactor. The ozone interference, however, is more closely linked to the initial concentrations of the reaction mixture.

4.5.1   Initial Concentration of NO

The base conditions for the simulation were those used in the earlier simulations, i.e. 1.1s reaction time and initial concentrations of HO_2 and DME of 1×10^8 cm^{-3} and 1.97×10^{18} molecules cm^{-3} respectively. The concentration of ozone used was 2.46 $\times 10^{12}$ molecule cm^{-3} as this represents a relatively high tropospheric concentration [*Finlayson-Pitts and Pitts*, 1986 and references therein]. The NO concentration was increased from the base value of 1.48×10^{14} molecules cm^{-3} (6ppm) and the DP_{ozone} calculated. These are shown in Figure 4.9.

The discrimination initially increases with NO concentration as the chain length of the system increases. This is due to the increase in the proportion of peroxy radicals undergoing initiation reactions, such as:

$$HO_2 + NO \rightarrow OH + NO_2 \qquad\qquad 4.4$$

and the consequent decrease in radical loss reactions. However, as the concentration of NO rises, so does the amount of NO_2 formed by:

$$NO + O_3 \rightarrow NO_2 + O_2 \qquad\qquad 4.1$$

and the proportion of the OH radicals lost by the reaction with NO also increases:

$$OH + NO\ (+M) \rightarrow HONO\ (+M) \qquad\qquad 4.7$$

129
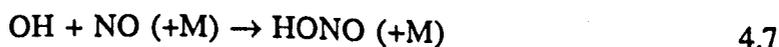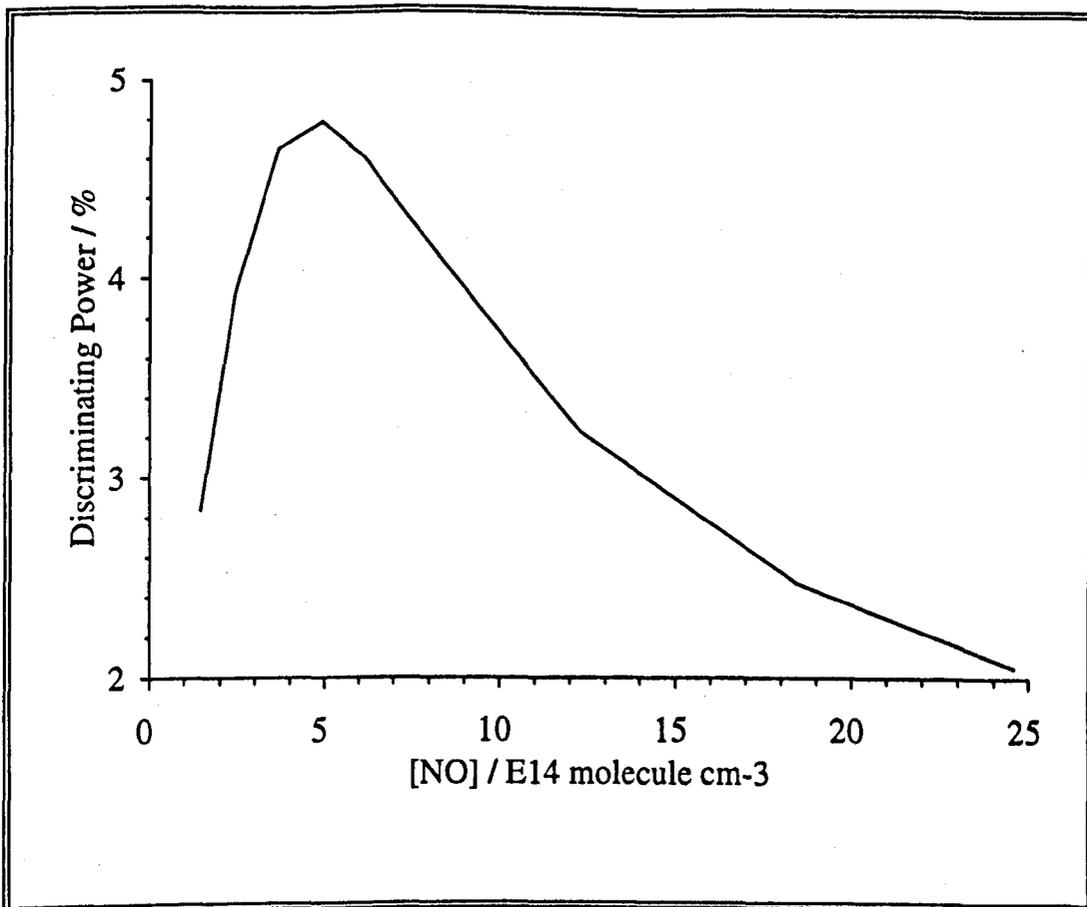
Figure 4.9   Effect of [NO] on the Ozone Discriminating Power

[DME] = 1.97 $\times 10^{18}$ molecule cm^{-3}; [HO$_2$] = 1 $\times 10^8$ cm^{-3};
[O$_3$] = 2.46 $\times 10^{12}$ molecule cm^{-3}; Time = 1.1s

Hence, there is an optimum NO concentration, which is shown by Figure 4.9 to be around 5 $\times 10^{14}$ molecule cm^{-3}.

4.5.2   DME Concentration

The concentration of DME was also varied, using the optimum NO concentration found above, and keeping other conditions the same ([HO$_2$] = 1 $\times 10^8$ cm^{-3}, [O$_3$] = 2.46 $\times 10^{12}$ molecule cm^{-3}, reaction time = 1.1s). It was found that increasing the concentration of DME from the initial value of 1.97 $\times 10^{18}$ molecule cm^{-3} resulted in a steady increase in the ozone discriminating power of the system, as shown in Figure 4.10.

When the 'clean' system was modelled above (section 4.4), it was found that increasing the concentration of DME above approximately 3×10^{18} molecule cm^{-3} had little effect on the chain length, as effectively all the OH radicals produced were reacting with DME. As Figure 4.10 shows, this is obviously not the case here, as the discriminating power continues to rise beyond 8×10^{18} molecule cm^{-3}. This continuing rise in discriminating power is a result of the increased concentration of NO making reaction 4.7 more significant.

However, the use of such high concentrations of DME is not to be recommended, not only because of the quenching of the chemiluminescence or fluorescence signal used to detect the NO_2, but also because it would significantly increase the cost of operating the chemical amplifier. Although the actual optimum concentration of DME would need evaluating in conjunction with the detection method, a higher concentration than that modelled above may used. Consequently the subsequent modelling was performed using a DME concentration of 3.7×10^{18} molecule cm^{-3}, as this is not an excessive amount, and it provides a 30% increase in the discriminating power.

It was also found that at the higher concentration of DME chosen (3.7×10^{18} molecule cm^{-3}) subsequent improvements in the discriminating power could be obtained by increasing the concentration of NO further, as a consequence of the reduced influence of the termination reaction 4.7. Accordingly, the optimum concentration of NO was found to be 6.15×10^{14} molecule cm^{-3}.

4.5.3   Reactor Residence Time

As discussed above, the extent of the interferences from PAN and PNA depend strongly on the residence time of the sample in the reactor. In order to determine the optimum residence time, both the PAN and ozone discriminations were plotted as a function of time, along with the concentration of NO_2. Although PAN and PNA have different dissociation rates, Figures 4.7 and 4.8 show that they have similar

131
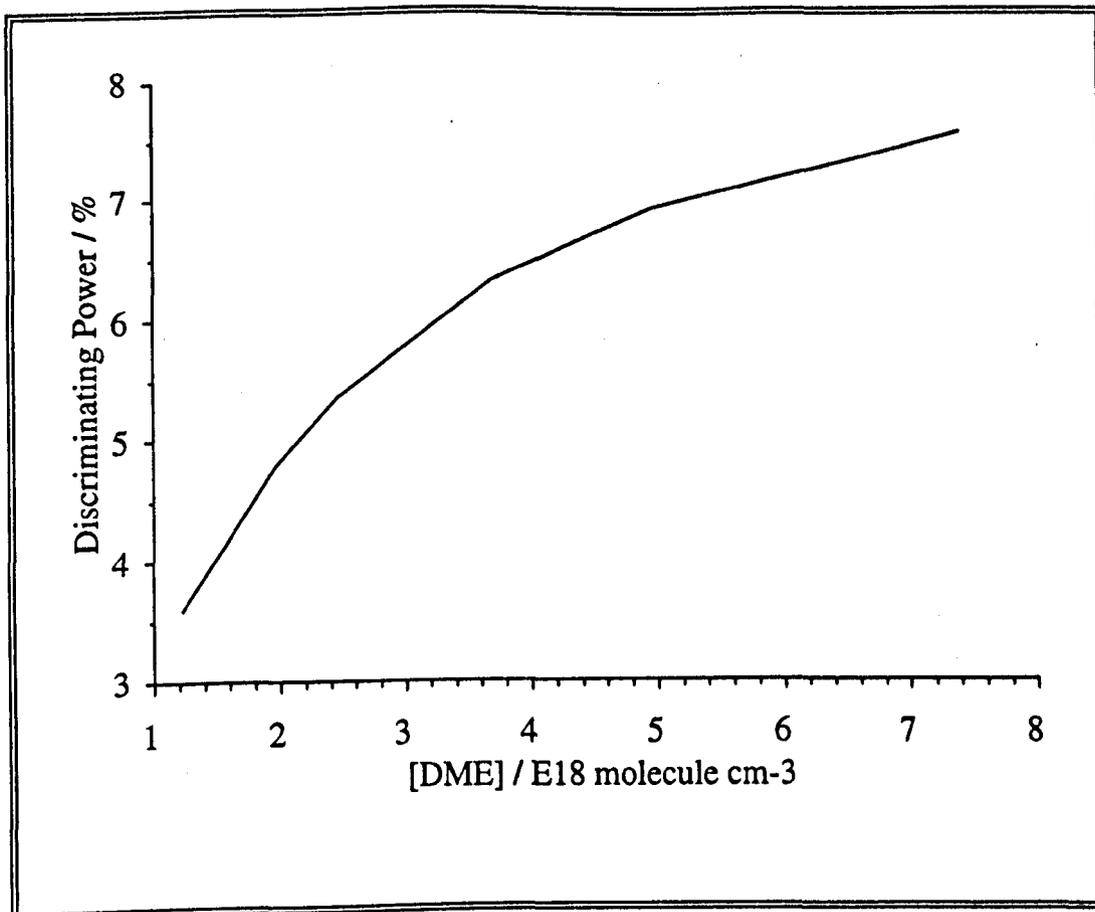
Figure 4.10 Effect of [DME] on the Ozone Discrimination Power

$$[NO] = 4.92 \times 10^{14} \text{ molecule cm}^{-3}; [HO_2] = 1 \times 10^8 \text{ cm}^{-3};$$
$$[O_3] = 2.46 \times 10^{12} \text{ molecule cm}^{-3}; \text{ Time } = 1.1s$$

interferences, as a result of the difference in their concentrations. Therefore, the PAN discrimination was taken to be indicative of that of both species.

It can be seen from Figure 4.11 that there is little increase in either the concentration of NO_2 or the ozone discrimination after 1s. The similar shape of these two curves suggests that the ozone chemistry is over more quickly than the amplification chemistry, as had the increasing NO_2 concentration been due to reaction of ozone with NO (reaction 4.1), it would have been accompanied by a corresponding decrease in the discrimination. While the ozone discrimination increases with time, the PAN discrimination decreases rapidly, as more of the PAN undergoes thermolysis. This would suggest that in order to maximize the discrimination of the system, the residence time of the sample in the chamber should be around 1s.
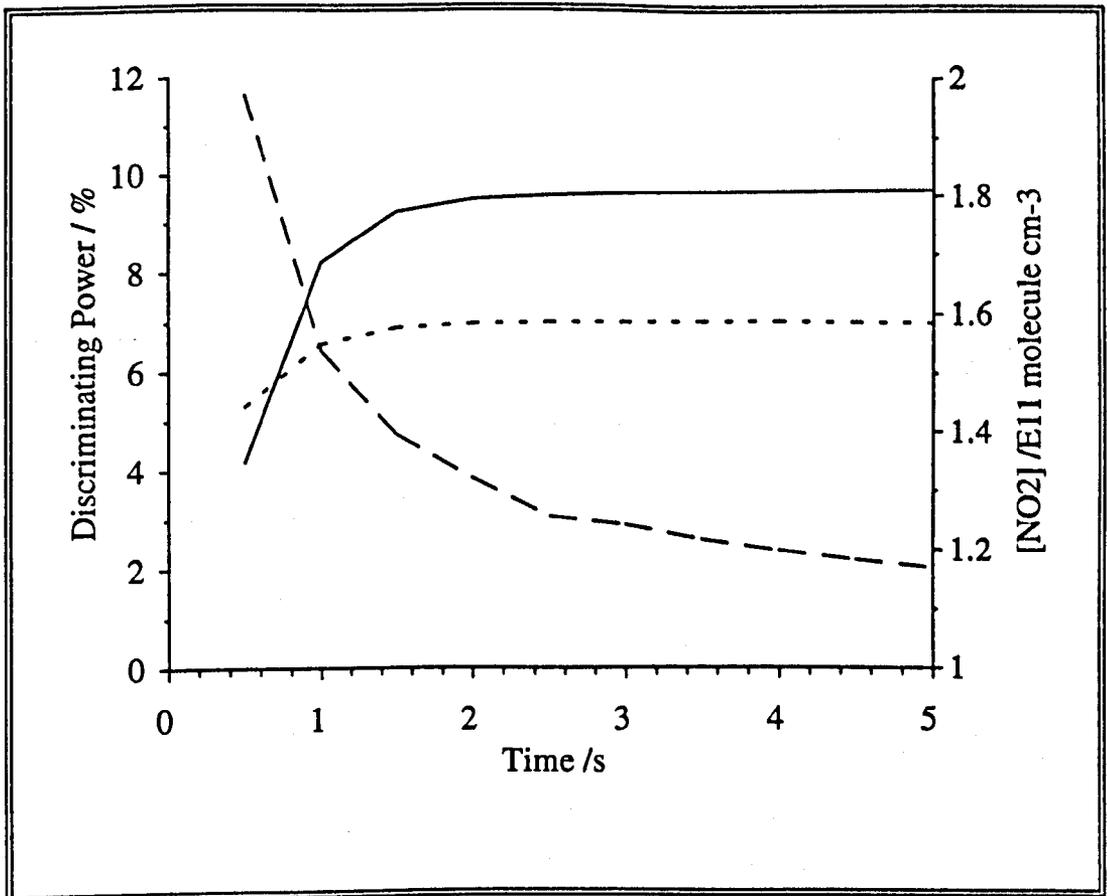
Figure 4.11 Effect of Reaction Time on [NO$_2$] and Discriminating Power

———— [NO$_2$] (right axis); - - - DP$_{ozone}$ (left axis); — — DP$_{PAN}$ (left axis)
[NO] = 3.69 x10^{18} molecule cm^{-3}; [NO] = 4.92 x10^{14} molecule cm^{-3};
[O$_3$] = 2.46 x10^{12} molecule cm^{-3}; [PAN] = 2.46 x10^{12} molecule cm^{-3};
[HO$_2$] = 1 x10^8 cm^{-3}

4.5.4 Summary

The above work suggests that the optimum conditions for an ambient chemical amplification monitor, based on the reactor design of *Hastie et al.* [1991] using DME as the chain carrier, are as follows:

[DME]	3.7 x10^{18} molecule cm^{-3}
[NO]	6.2 x10^{14} molecule cm^{-3}
Residence Time	1s

133

The modelling of chain carrier performance should be an on-going study, with existing models being refined as rate constants become better understood, and new models of alternative carriers being tried. In this way, the chemical amplifier system can be continually improved.

In order for the models to simulate accurately the conditions in an operational chemical amplifier, the processes of the modelling programme need to be altered to reflect the flow dynamics of the system. In the chemical amplifiers currently in use [*Hastie et al.*, 1991 and *Hu and Stedman*, 1994] the reactor chamber is a relatively narrow tube (around 40mm in diameter) where the sample flow is reasonably described as a plug. There is little mixing along the length of the chamber and any chosen 'section' of the sample will have little interaction with its adjacent 'sections'. As such, the conditions are similar to those of the static systems modelled here. However, consideration would need to be made of the contribution to the mixing caused by the laminar flow and the flow characteristics of the "nitrogen wall" used by *Hu and Stedman* [1994] would need particularly careful consideration.

Chapter 5

The Photolysis of Nitrogen Dioxide
in the Presence of 2-Butyne

5.1   Introduction

The photolysis of NO_2 is one of the fundamental steps in the oxidation of
tropospheric trace gases. It has a crucial role in the formation of the OH radical, the
primary day-time oxidant. As such, it is very important to be able to monitor the rate
of NO_2 photolysis in order to test the current theories of tropospheric chemistry.

There are several problems associated with measuring the ambient photolysis rate of
NO_2. These are related, principally, to the passage of light into the apparatus, the
effect of scattered light and the subsequent chemistry of the $O(^3P)$ atom produced by
the photolysis. In a system where a dilute mixture of NO_2 in a bath gas, typically
N_2, is continuously flowed through the photolysis cell [for example, *Parrish et al.*,
1983; *Dickerson et al.*, *1982*], the secondary chemistry is limited to the reaction of
O with NO_2 itself, producing NO and O_2. Hence each photolysis event has a
effective quantum yield, Φ_{eff} of 2. However, in a static system, the build-up of
reaction products can lead to more complicated chemistry, including the production
of O_3. Consequently, Φ_{eff} can vary over the course of the experiment.

The purpose of this work was to investigate the possibility that doping the mixture
with a trap for the O atoms will produce a chemical system with a constant Φ_{eff}.
For a variety of reasons, the dopant chosen was 2-butyne. The first of these reasons
was that the reaction between it and O is relatively fast (approximately five times
faster than the reaction of O with NO_2) so trapping all the O atoms would not require
excessive amounts of the 2-butyne. Secondly, while the reaction is believed to
proceed through a radical intermediate, the final products are largely stable
hydrocarbons and CO, potentially limiting the secondary chemistry. Thirdly, it is a
simple matter to obtain sufficient quantities of gaseous 2-butyne from a liquid
sample. Another consideration was that 2-butyne is relatively cheap and easy to
obtain, an important consideration if is to have a wide-spread use in atmospheric monitoring.

5.2   Experimental Procedure

5.2.1   Method 1: End Product Analysis via a Chemiluminescent Method

The reaction mixtures consisted of NO_2 in an excess of 2-butyne, with N_2 as a bath gas. These were photolysed in a looped cell and the products were examined by a chemiluminescence NO_x analyzer. Most photolyses were performed at 500 mbar total pressure and with the 2-butyne in approximately a 160 times excess over NO_2. This ratio provided a sufficient excess for all the O atoms to react with the 2-butyne, and it also involved the handling of convenient quantities of the materials. A schematic diagram of the apparatus is shown in Figure 5.1.

The lamp was placed 'face on' to the cell so that both arms of the loop were irradiated equally (Figure 2.1). A Pyrex dome that had been coated on the outside surface with silver paint, was placed over the cell. This served two purposes: preventing interference from ambient lighting, and increasing the effectiveness of the lamp. The coated glass acted as a mirror and so made the irradiance more uniform, as well as making use of a larger proportion of the lamp output.

The analyser was used predominantly in the NO sampling mode in order to determine the amount of NO produced in each photolysis experiment. It was found that the optimum peak size for the NO_x channel was obtained with the converter running at 673K. At this temperature, peaks of the same size were obtained for mixtures with 50ppm (6.15×10^{14} molecule cm^{-3}) of NO or NO_2, in N_2 containing 0.8% (9.84×10^{16} molecule cm^{-3}) 2-butyne at 500 mbar (1.23×10^{19} molecule cm^{-3}) pressure.

Above and below this temperature, the NO_2 peaks were smaller than those for NO. It was assumed that at the lower catalyst temperatures, not all of the NO_2 was reduced to NO and at the higher temperatures, the presence of the 2-butyne in the catalyst interfered with the reduction. Also, it was observed that there were, in fact, two peaks when the converter was run at temperatures above 900K. These peaks were of equal intensity, and separated by approximately 2s. Increasing the distance

between the cell and the analyser had no effect on the separation between the peaks, suggesting that the separation was not caused by different products from a dark reaction travelling at different speeds through the connecting tubing. As the catalyst converts other nitrogen-containing species to NO, as well as NO_2, this chromatographic effect could have been responsible for the observed separation. However, as reducing the catalyst temperature removed the problem, no further time was spent investigating this unusual phenomenon.

Initially, a tungsten riband lamp was used to provide the radiation for the photolysis of NO_2 as it had a broad emission spectrum. However, it was found that at the operating temperatures obtainable, this did not emit a sufficient amount of light below 400nm. Consequently, very little NO was produced, even after photolyses of up to 2 hours in duration. The tungsten lamp was replaced by a D_2 lamp, but while the lamp had a suitable spectrum to photolyse NO_2, the Pyrex cell cut out most of the useable radiation from this source. Finally a medium pressure Hg arc lamp was used as this provided suitable levels of photolysis; its spectrum was measured, and is shown in Figure 2.2.

While using a quartz cell would have allowed the use of the D_2 lamp, it was felt that using Pyrex, which cuts out radiation with a wavelength less than around 300nm, provided a desirable reproduction of the atmospheric filtering caused by O_3 and, to a lesser extent, O_2.

The output from the Hg lamp was monitored with a photodiode behind the cell so that the lamp consistency could be checked. The diode produced a voltage, proportional to the intensity of incident light, which was displayed on a digital voltmeter. However, it proved very difficult to get a stable reading from the diode due to fluctuations in the ambient light levels. As it proved difficult to light-proof the apparatus without overheating the lamp, and as the experimental results showed no evidence of variations in the lamp power, no extra time was spent on attempting to improve the photodiode stability.
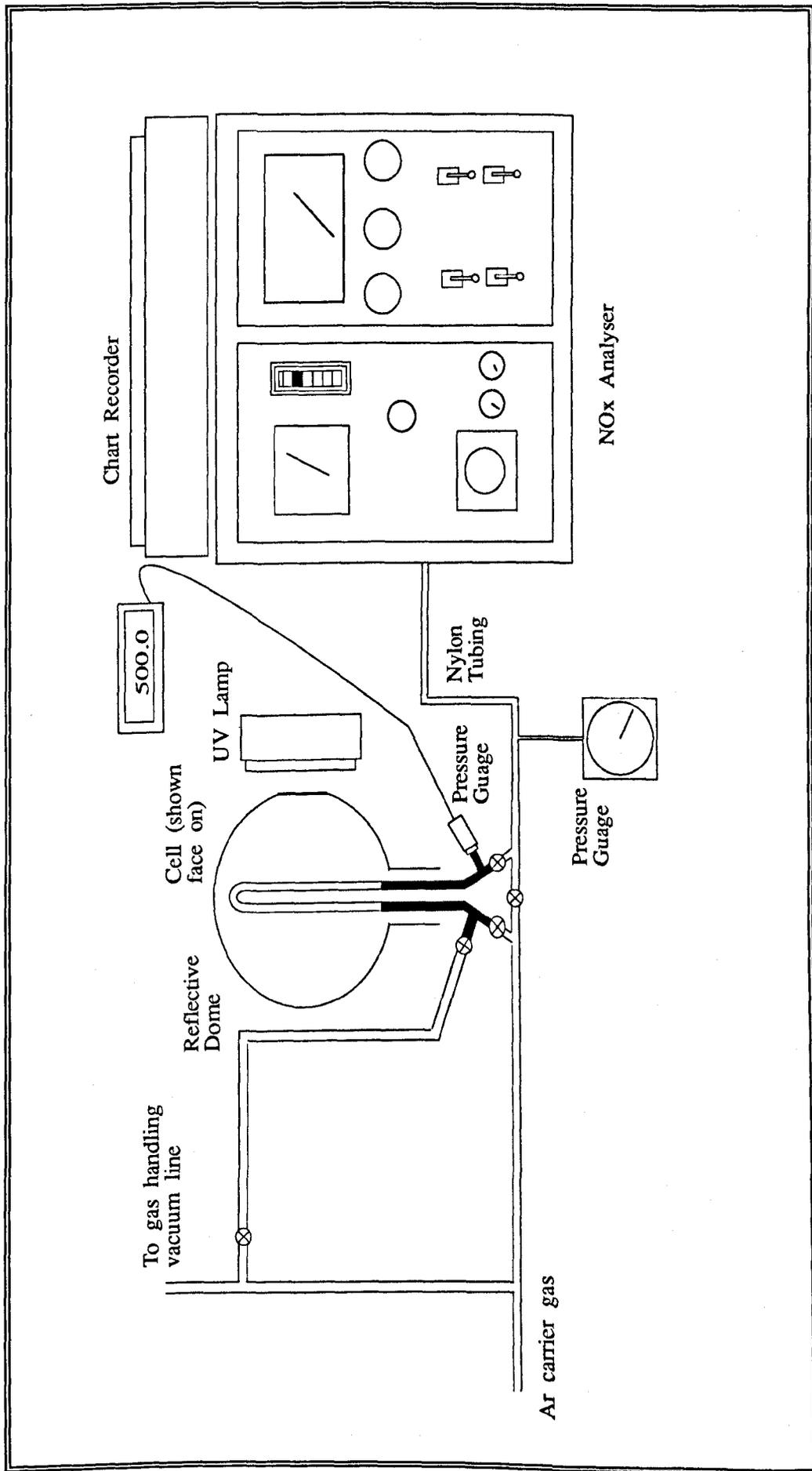
Figure 5.1 Schematic Diagram of the Apparatus used in the NO$_x$ Analysis

Even with the use of the reflective dome, it was not possible to irradiate the entire cell evenly. Consequently, the cell was designed so that only the region that could be illuminated equally was exposed, with the rest blackened. The extent of the blacking was determined by examining the geometry of the layout, using scale drawing to determine the maximum spread of light into the dome. This resulted in only 37% of the volume actually being exposed to the radiation of the lamp (Figure 5.2a). The proportion of the cell exposed was measured, after all the photolyses had been concluded, by filling the cell with water, first to the limit of the blacking and then fully, and weighing it. Once the dry weight of the cell was subtracted, the difference in the amount of water provided the difference in the volume exposed.

However, it was possible to get diffusion between the exposed and blackened regions of the cell during an experiment. While the small internal diameter of the cell (9mm) provided a limited area for the diffusion, the possibility that the latter could occur was investigated. The volume exposed to the photolysis radiation was reduced to approximately 25% of the total volume (Figure 5.2b), so that the area over which diffusion could occur would be greater in relation to the actual photolysis volume. Several samples, containing 50ppm NO_2 (6.15 x10^{14} molecule cm^{-3}), 0.8% 2-butyne (9.84 x10^{16} molecule cm^{-3}) and N_2 were photolysed at 500 mbar (1.23 x10^{19} molecule cm^{-3}) for 600s. After this time, the mixtures were passed into the chemiluminescence analyser and the amount of NO produced was measured. The photolyses were repeated once the pattern of the blackening had been changed so that while the total volume exposed was maintained at 25%, both the top and bottom sections of the cell were covered instead of just the bottom (Figure 5.2c), effectively doubling the area where diffusion could occur. The effect of this is discussed in section 5.4.1 .

Also, constrictions were put in the cell at the limit of the blacking, reducing the internal diameter to approximately 2mm. This minimised the available diffusion area, making any subsequent diffusion insignificant.
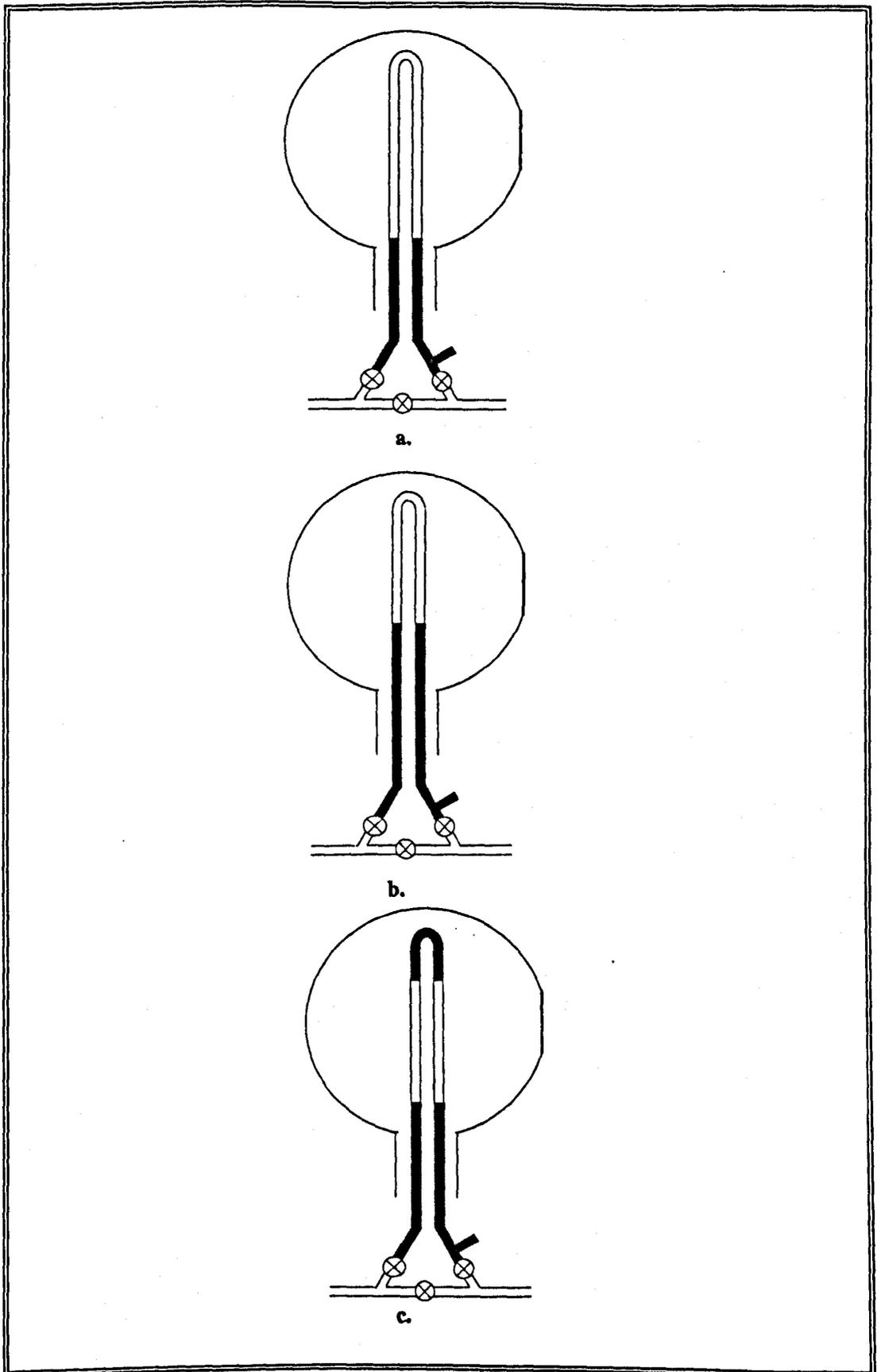
Figure 5.2   The three configurations of cell used in this study

Following these simple alterations, a series of photolyses of 2-butyne/NO_2/N_2 mixtures (4.0 mbar 2-butyne made up to 500 mbar with a stock mixture of 50 ppm NO_2 in N_2) was performed at times between 30 and 1500 seconds. After each photolysis, the amount of NO present in the mixture was measured. Computer modelling of the system was also performed to aid the interpretation of results (for a listing of the model see Table 5.i).

Table 5.i   Reactions and Rate Constants for the 2-Butyne Model

	Reaction	k or k_o	k_{inf}	f_c	Ref./ Notes
1_f	$NO_2 + h\upsilon \rightarrow NO + O$	6.00×10^{-4} s^{-1}	-	-	(b)
1_b	$O + NO \rightarrow NO_2$	9.72×10^{-32}	3.00×10^{-11}	0.85	16
2	$O + NO_2 \rightarrow NO + O_2$	9.70×10^{-12}	-	-	16
3a	$O + CH_3CCCH_3 \rightarrow CO + SP$	3.42×10^{-12}	-	-	(c)
3b	$O + CH_3CCCH_3 \rightarrow DMK$	5.80×10^{-13}	-	-	(c)
3c	$O + CH_3CCCH_3 \rightarrow C_2H_3 + CH_3 + CO$	8.80×10^{-13}	-	-	(c)
4	$CH_3 + NO_2 \rightarrow CH_3O + NO$	2.50×10^{-11}	-	-	197
5	$CH_3O + NO_2 \rightarrow CH_3ONO_2$	3.40×10^{-29}	2.00×10^{-11}	0.48	16
6	$CH_3 + NO \rightarrow CH_3NO$	1.29×10^{-29}	1.10×10^{-11}	0.65	83
7a	$CH_3O + NO \rightarrow CH_3ONO$	6.00×10^{-28}	2.00×10^{-11}	0.60	16
7b	$CH_3O + NO \rightarrow CH_2O + HNO$	3.50×10^{-12}	-	-	16
8	$C_2H_3 + NO_2 \rightarrow CH_2CHO + NO$	2.50×10^{-11}	-	-	(d)
9	$CH_2CHO + NO \rightarrow ONCH_2CHO$	6.53×10^{-29}	2.51×10^{-11}	0.54	63
10	$CH_2CHO + NO_2 \rightarrow HONO + CH_2CO$	1.94×10^{-11}	-	-	18
11	$OH + NO \rightarrow HONO$	7.40×10^{-31}	1.00×10^{-11}	0.80	16
12	$OH + NO_2 \rightarrow HNO_3$	2.60×10^{-30}	5.20×10^{-11}	0.43	16
13	$OH + CH_3CCCH_3 \rightarrow PRODUCTS$	5.00×10^{-30}	8.30×10^{-13}	0.60	13
14	$DMK + O \rightarrow CH_3COCH_3 + CO$	4.05×10^{-11}	-	-	40 (e)
15	$SP + O \rightarrow RADICALS$	3.96×10^{-12}	-	-	40 (f)

<u>Notes</u>

(a) k = cm^3 molecule^{-1} s^{-1} , unless otherwise stated; k_o = cm^6 molecule^{-2} s^{-1}; k_{inf} = cm^3 molecule^{-1} s^{-1}; f_c = dimensionless

(b)   Rate constant is that found for the Method 1 apparatus, in Method 2 the rate was 1.23×10^{-3} s^{-1}

(c) k_3 = 4.86×10^{-12} cm^3 molecule^{-1} s^{-1} [*Herbrechtsmeier and Wagner*, 1975], see section 5.5.4 for discussion of the branching ratios

(d)   Rate constant used is $k(CH_3 + NO_2)$

(e)   DMK = Dimethylketene

(f)   SP = Stable Products, rate constant is $k(O + C_3H_6)$. Reported products are C_3H_6, C_2H_2, C_2H_6, C_2H_4, CH_4, and C_3H_4 (see section 5.5.4)

The reduced fall-off curves used for pressure dependent reactions in the models are derived from the formulae given by *Atkinson et al* [1989], using the low pressure limit, k_o, the high pressure limit, k_{inf} and the fall-off factor f_c. A thorough discussion of the calculation is given by *Atkinson et al* [1989].

The chemistry of ethene has been more extensively studied than that of 2-butyne. Accordingly, it was possible to construct a model for a system (Table 5.ii) in which ethene had replaced 2-butyne. Although this model contained more reactions than the 2-butyne model, the rate constants for them are known with a greater degree of confidence.

Had the results of both the 2-butyne and ethene experiments not agreed with their respective models, it would have indicated a problem in either the experimental or analysis procedures, rather than the modelling. It should be noted that while ethene is a suitable reagent for this role, it was not thought to be suitable as an alternative to 2-butyne in an ambient photolysis rate monitor, as the addition of O to ethene rapidly forms CH_3 radicals which react with NO and NO_2, thus complicating the overall process.

$$O + C_2H_4 \rightarrow CH_3 + CHO \qquad\qquad 5.1$$
$$CH_3 + NO\ (+M) \rightarrow CH_3NO\ (+M) \qquad\qquad 5.2$$
$$CH_3 + NO_2 \rightarrow CH_3O + NO \qquad\qquad 5.3$$
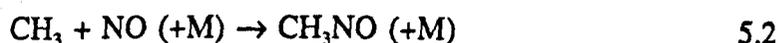
Accordingly, in addition to the experiments containing 2-butyne, a series of photolyses using ethene was carried out. Mixtures consisted of 20 mbar of ethene made up to 500 mbar with 50 ppm NO_2/N_2. The increased concentration of ethene, compared to 2-butyne, was intended *to compensate for the difference in their* respective rate constants for their reactions with O ($k(O + C_2H_4) = 7.25 \times 10^{-13}$ cm^3 molecule^{-1} s^{-1} [*Cvetanovic*, 1987]; $k(O + CH_3CCCH_3) = 2.66 \times 10^{-12}$ cm^3 molecule^{-1} s^{-1} [*Umstead and Lin*, 1977]).

Table 5.ii   The Ethene Model

	Reaction	k or k_o	k_{inf}	f_c	Ref./Notes
1_f	$NO_2 + h\upsilon \rightarrow NO + O$	6.00×10^{-4} s^{-1}	-	-	(b)
1_b	$NO + O \rightarrow NO_2$	9.72×10^{-32}	3.00×10^{-11}	0.85	16
2	$O + O_2 \rightarrow O_3$	5.80×10^{-34}	2.80×10^{-12}	0.65	16
3	$O + NO_2 \rightarrow NO + O_2$	9.72×10^{-12}	-	-	16
4	$NO + O_3 \rightarrow NO_2 + O_2$	1.70×10^{-14}	-	-	16
5_f	$NO_2 + NO_2 \rightarrow N_2O_4$	1.70×10^{-15}	-	-	16
5_b	$N_2O_4 \rightarrow NO_2 + NO_2$	6.00×10^{3} s^{-1}	-	-	16
6a	$O + C_2H_4 \rightarrow CH_3 + CHO$	5.00×10^{-13}	-	-	16
6b	$O + C_2H_4 \rightarrow H + CH_2CHO$	4.50×10^{-13}	-	-	16
6c	$O + C_2H_4 \rightarrow OH + C_2H_3$	2.42×10^{-15}	-	-	16
6d	$O + C_2H_4 \rightarrow PRODUCTS$	5.00×10^{-14}	-	-	16
7	$CH_3 + NO \rightarrow CH_3NO$	1.29×10^{-29}	1.1×10^{-11}	0.65	83
8	$CH_3 + NO_2 \rightarrow CH_3O + NO$	2.50×10^{-11}	-	-	197
9	$CH_3O + NO \rightarrow CH_3ONO$	6.00×10^{-27}	2.00×10^{-11}	0.60	16
10	$CH_3O + NO_2 \rightarrow CH_3ONO_2$	2.60×10^{-28}	1.50×10^{-11}	0.40	16
11	$CHO + NO \rightarrow HNO + CO$	1.23×10^{-11}	-	-	(c)
12	$CHO + NO_2 \rightarrow H + NO + CO_2$	5.19×10^{-11}	-	-	170
13	$H + C_2H_4 \rightarrow C_2H_5$	2.10×10^{-29}	1.14×10^{-12}	0.68	133
14	$H + NO \rightarrow HNO$	5.66×10^{-13}	-	-	(d)
15	$H + NO_2 \rightarrow OH + NO$	1.49×10^{-10}	-	-	190
16	$C_2H_5 + NO \rightarrow C_2H_5NO$	2.00×10^{-13}	-	-	140
17a	$C_2H_5 + NO_2 \rightarrow C_2H_5NO_2$	1.13×10^{-11}	-	-	127
17b	$C_2H_5 + NO_2 \rightarrow C_2H_5O + NO$	3.37×10^{-11}	-	-	127
18	$C_2H_5O + NO \rightarrow C_2H_5ONO$	2.63×10^{-11}	-	-	16
19	$C_2H_5O + NO_2 \rightarrow C_2H_5ONO_2$	1.50×10^{-11}	-	-	16
20	$OH + NO_2 \rightarrow HONO_2$	2.52×10^{-30}	5.20×10^{-11}	0.70	16
21	$OH + C_2H_4 \rightarrow HOC_2H_4$	9.50×10^{-29}	9.00×10^{-12}	0.70	16
22	$HOC_2H_4 + NO \rightarrow HOC_2H_4NO$	2.60×10^{-11}	-	-	111
23a	$HOC_2H_4 + NO_2 \rightarrow HOC_2H_4O + NO$	1.13×10^{-11}	-	-	(e)
23b	$HOC_2H_4 + NO_2 \rightarrow HOC_2H_4NO_2$	3.37×10^{-11}	-	-	(e)

Notes

(a)   Units as in Table 5.i

(b)   The rate shown here is the Method 1 apparatus. No ethene experiments were performed using Method 2

(c)   The rate constant is an average of 1.26×10^{-11} [*Langford and Moore*, 1984], 1.23×10^{-11} [*Veyret and Lesclaux*, 1981] and 1.20×10^{-11} [*Nadtochenko et al.*, 1980]

(d) $k_o = 4.6 \times 10^{-32}$ cm^6 molecule^{-2} s^{-1} [*Ishikawa et al.*, 1979]. k is assumed to be $k_o[M]$

(e)   Overall rate constant and branching ratio assumed to be equall to $k(C_2H_5 + NO_2)$

Table 5.ii   The Ethene Model (cont.)

	Reaction	k or k_o	k_{inf}	f_c	Ref./ Notes
24	$CH_3O + O_2 \rightarrow CH_2O + HO_2$	1.90×10^{-15}	-	-	16
25	$CH_3O + NO \rightarrow CH_2O + HNO$	4.00×10^{-12}	-	-	16
26	$CH_3O + NO_2 \rightarrow CH_2O + OH + NO$	3.00×10^{-13}	-	-	16
27	$HO_2 + NO \rightarrow OH + NO_2$	8.30×10^{-11}	-	-	16
28_f	$HO_2 + NO_2 \rightarrow HO_2NO_2$	1.74×10^{-31}	4.7×10^{-12}	0.60	16
28_b	$HO_2NO_2 \rightarrow HO_2 + NO_2$	1.23×10^{-20}	2.3×10^{-1}	0.60	16
29	$CHO + O_2 \rightarrow HO_2 + CO$	5.60×10^{-12}	-	-	16
30	$C_2H_5O + O_2 \rightarrow CH_3CHO + HO_2$	8.00×10^{-15}	-	-	16
31	$C_2H_5O + NO \rightarrow CH_3CHO + HNO$	6.12×10^{-12}	-	-	16
32	$C_2H_5O + NO_2 \rightarrow CH_3CHO + OH + NO$	7.00×10^{-12}	-	-	16
33	$HOC_2H_4 + O_2 \rightarrow HOC_2H_4O_2$	3.00×10^{-12}	-	-	(f)
34	$HOC_2H_4O_2 + NO \rightarrow HOC_2H_4O + NO_2$	8.90×10^{-12}	-	-	21
35	$HOC_2H_4O + O_2 \rightarrow HOCH_2CHO + HO_2$	8.00×10^{-15}	-	-	(g)
36a	$HOC_2H_4O + NO \rightarrow HOCH_2CHO + HNO$	1.30×10^{-11}	-	-	(h)
37a	$HOC_2H_4O + NO_2 \rightarrow HOCH_2CHO + HO + NO$	7.00×10^{-12}	-	-	(i)
36b	$HOC_2H_4O + NO \rightarrow HOC_2H_4ONO$	4.40×10^{-11}	-	-	(h)
37b	$HOC_2H_4O + NO_2 \rightarrow HOC_2H_4ONO_2$	2.80×10^{-11}	-	-	(h)
38	$CH_2CHO + NO \rightarrow ONCH_2CHO$	6.53×10^{-29}	2.51×10^{-11}	0.54	63
39	$CH_2CHO + NO_2 \rightarrow CH_2CO + OH + NO$	1.94×10^{-11}	-	-	18
40	$CH_2CHO + O_2 \rightarrow CH_2O + OH + CO$	3.00×10^{-14}	-	-	(i)
41	$CH_2CHO + O_2 \rightarrow O_2CH_2CHO$	2.24×10^{-14}	-	-	(i)
42	$O_2CH_2CHO + NO \rightarrow OCH_2CHO + NO_2$	8.90×10^{-12}	-	-	(g)
43	$OCH_2CHO \rightarrow CH_2O + CHO$	$1.5 \times 10^5 \ s^{-1}$	-	-	(j)
44	$OCH_2CHO + O_2 \rightarrow HO_2 + CHOCHO$	8.00×10^{-15}	-	-	(g)
45	$C_2H_5 + O_2 \rightarrow C_2H_5O_2$	2.00×10^{-28}	5.0×10^{-12}	0.70	16
46	$C_2H_5O_2 + NO \rightarrow C_2H_5O + NO_2$	8.90×10^{-11}	-	-	16

Notes

(f)   Rate constant assumed to be equall to $k(C_2H_5 + O_2)$

(g)   Rate constant assumed to be equall to $k(C_2H_5O + O_2)$

(h)   Rate constant assumed to be equall to $k(C_2H_5O + NO/NO_2)$ as appropriate

(i) k_{inf} from *Lorenz et al.* [1985] fitted for k_o with pressure dependence from *Gutman and Nelson* [1983]

(j)   Assumed to be very fast

5.2.2 Method 2: Laser-induced Fluorescence Analysis of NO_2

To complement the work in section 5.2.1, the NO_2/2-butyne system was also studied using Laser-Induced Fluorescence (LIF) to follow the photolysis of NO_2 *in situ* and in real time. The details of the LIF apparatus are discussed in section 2.3.2 and will not be repeated here, though a diagram of the apparatus used in this work is shown in Figure 5.3. The photolysis radiation was provided by a blacklamp with a broad emission spectrum with λ_{max} at 350nm. The lamp spectrum is shown in Figure 2.2.

As these LIF experiments were performed primarily to help develop a chemical model that would be able to predict accurately the results of a photolysis, it was important to reduce the number of unknown parameters associated with the system, amongst which was the photolysis rate of NO_2 itself. Consequently, mixtures of 1% NO_2/N_2, with no 2-butyne present, were photolysed at various pressures up to 100 mbar. The results of these were fitted to a simple chemical model (see Table 5.iii). The modelling was necessary in order to account for the secondary chemistry, and the possibility of Φ_{eff} varying during the experiment. This photolysis rate, J_{NO_2} was then used in the model of the 2-butyne system.

Table 5.iii   The NO_2 Model

	Reaction	k or k_o	k_{inf}	f_c	Ref./ Notes
1	$NO_2 + h\upsilon \rightarrow NO + O$	1.23×10^{-3} s^{-1}	-	-	(b)
2	$O + NO \rightarrow NO_2$	1.00×10^{-31}	3.0×10^{-11}	0.85	15
3	$O + NO_2 \rightarrow NO + O_2$	2.22×10^{-12}	-	-	15
4	$O + O_2 \rightarrow O_3$	5.80×10^{-35}	2.80×10^{-13}	0.65	15
5	$O_3 + NO \rightarrow NO_2 + O_2$	1.81×10^{-14}	-	-	70

Notes
(a)   Units as given for Table 5.i
(b)   Found by fitting to decay traces

Photolyses were then carried out on a series of mixtures of 2-butyne/NO_2/N_2 at pressures between 10 and 100 mbar. The 2-butyne excess was varied between 10- and 100-fold. However, with the excess greater than 25-fold, the effects of laser scattering and fluorescence quenching made analysis of the results unreliable.

After the experiments containing 2-butyne had been carried out, another series of photolyses of NO_2/N_2 was performed to ensure that no variation in J_{NO_2} had occurred during the course of the experiments.
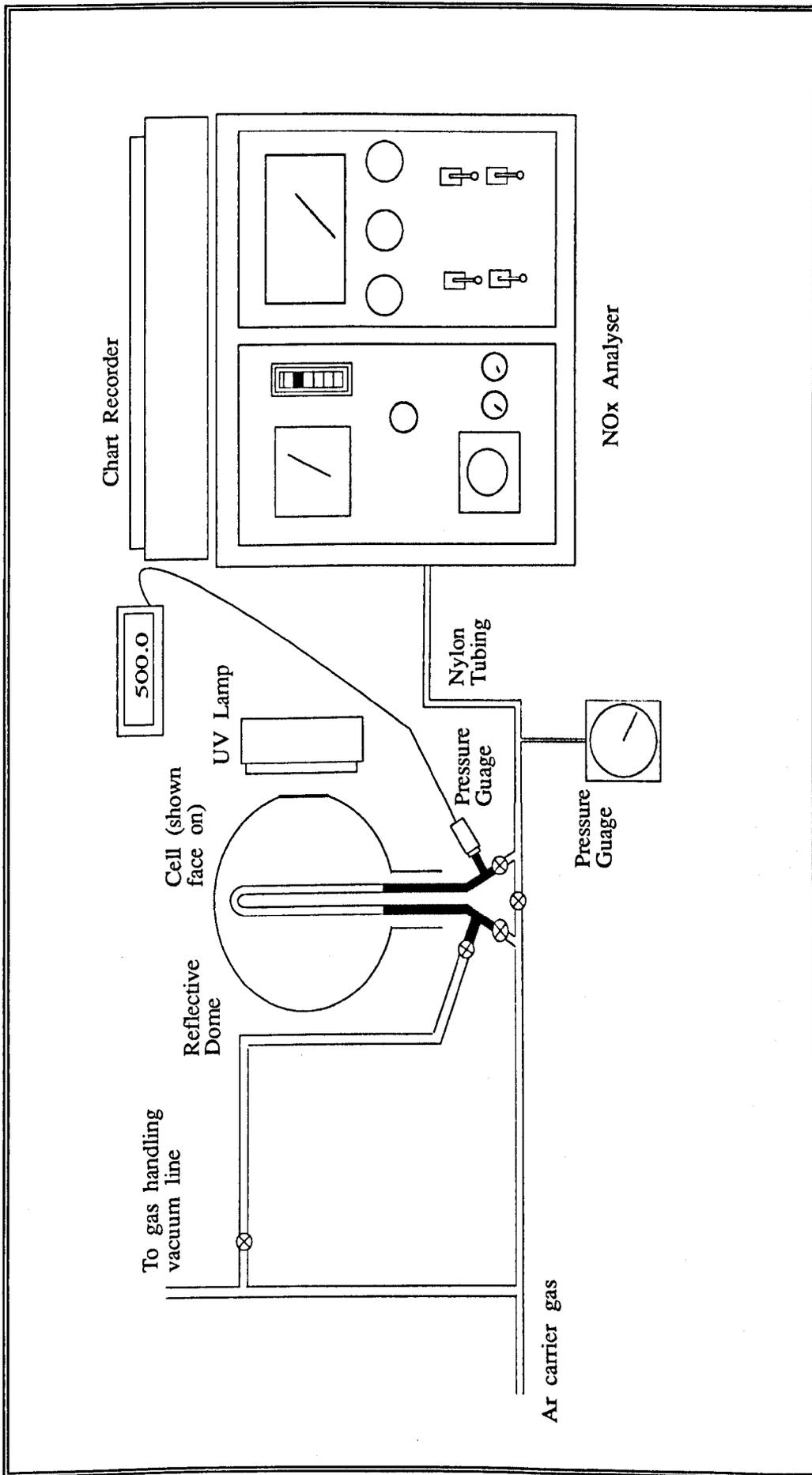
Figure 5.1 Schematic Diagram of the Apparatus used in the NO$_x$ Analysis

5.3 Results

5.3.1 Mathematical Treatment of the Results from Method 1

If the intermediates discussed in Section 5.1 proceeded solely to the stable products, the following simple mathematical treatment could be assumed:

$$\frac{-d[NO_2]}{dt} = J_{NO_x}[NO_2]$$

$$\int \frac{1}{[NO_2]}d[NO_2] = -\int J_{NO_x} \, dt$$

$$\ln[NO_2]_t = -J_{NO_x}t + c$$

When $t = 0$, $[NO_2]_t = [NO_2]_o$, $\therefore c = \ln[NO_2]_o$

$$\ln[NO_2]_t = -J_{NO_x}t + \ln[NO_2]_o$$

Therefore a plot of $\ln[NO_2]_t$ against time would be expected to yield a straight line with the gradient equal to $-J_{NO_2}$ and an intercept on the y-axis of $\ln[NO_2]_o$. In Method 1 it is actually $[NO]_t$ that is followed with the NO_x analyser, so instead $\ln([NO_2]_o - [NO]_t)$ is plotted against time.

$$\ln([NO_2]_o - [NO]_t) = -J_{NO_x}t + \ln[NO_2]_o$$

Since the peak height is proportional to $[NO_x]$ (as demonstrated in the calibration results in Section 2.3.1) it is possible to substitute the respective peak heights for $[NO_2]_o$ and $[NO]_t$.

However, it was found that plotting the above graph (shown in Figure 5.4) did not give a straight line, indicating that the mechanism is more complex. Analysis of the initial section of the slope (up to around 250s) yields:

$$J_{NO_2} = 1.0 \times 10^{-3} \, s^{-1}$$

147
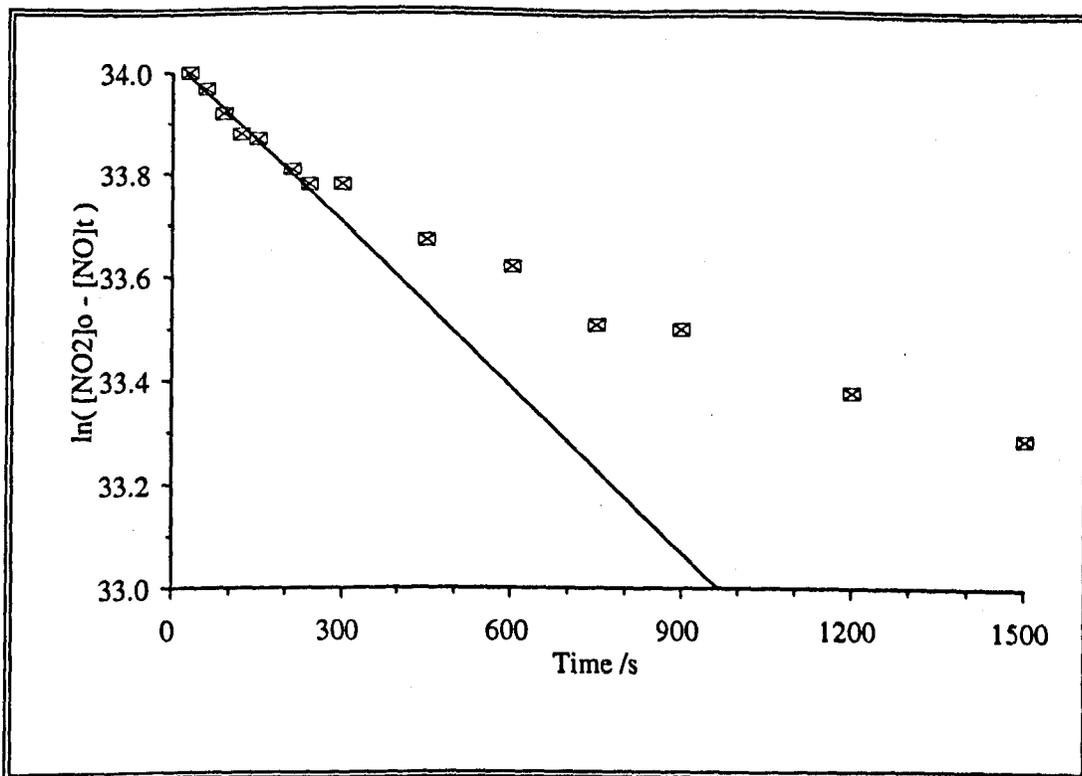
Figure 5.4   Results of the Simple Kinetic Analysis on the Data from Method 1

$[NO_2] = 2.5 \times 10^{-2}$ mbar; [2-butyne] = 4.0 mbar; $[N_2] = 496$ mbar

5.3.2   Method 1: End Product Analysis via a Chemiluminescent Method

When comparing the results of the experiments with different configurations of blacking on the cell it was necessary to compensate for the difference in the actual volume photolysed.   This was achieved by scaling the peak heights from the experiments with increased blacking according to the ratio 37:25, the proportions of the volumes exposed.

Once this had been performed it was noted that increasing the potential diffusion area relative to the volume exposed to photolysis also increased the amount of NO produced. Thus when the exposed volume was reduced from 37% to 25 % (blacking changed from that shown in Figure 5.2a to that in Figure 5.2b) the amount of NO produced was greater, in proportion to the volume of the cell exposed. Similarly, when the volume exposed was maintained at 25% with the diffusion area increased (Figure 5.2c) the NO produced increased again.

148

The results for the NO production after different photolysis times for the 2-butyne and ethene experiments, along with their respective model predictions are shown in Figure 5.5 and Figure 5.6 respectively. It can be seen that both models agree well with the experimental data. The quality of this agreement suggests that there are no systematic errors in the experimental or analysis procedures, or that any that do exist are common to both the 2-butyne and ethene experiments.
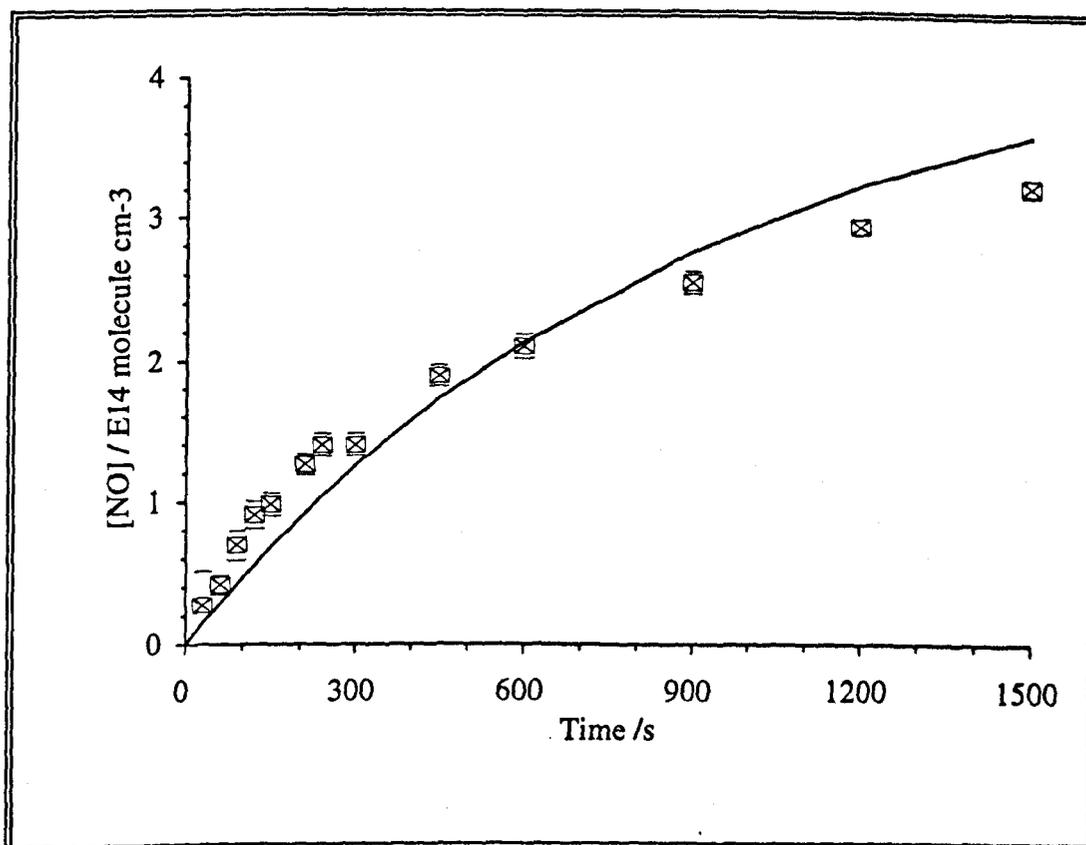
Figure 5.5   The Method 1 2-butyne Results. The solid line is the model fit.

$[NO_2] = 2.5 \times 10^{-2}$ mbar; [2-butyne] = 4.0 mbar; $[N_2] = 496$ mbar

5.3.3   Method 2: Laser-Induced Fluorescence Analysis

Before the data could be properly analysed the decay traces had to be treated, in order to allow for several anomalies of the experimental apparatus. There was a non-zero reading in the absence of NO_2 which had to be removed. This background signal was caused by radiation scattering from the laser, and also, by the fluorescence
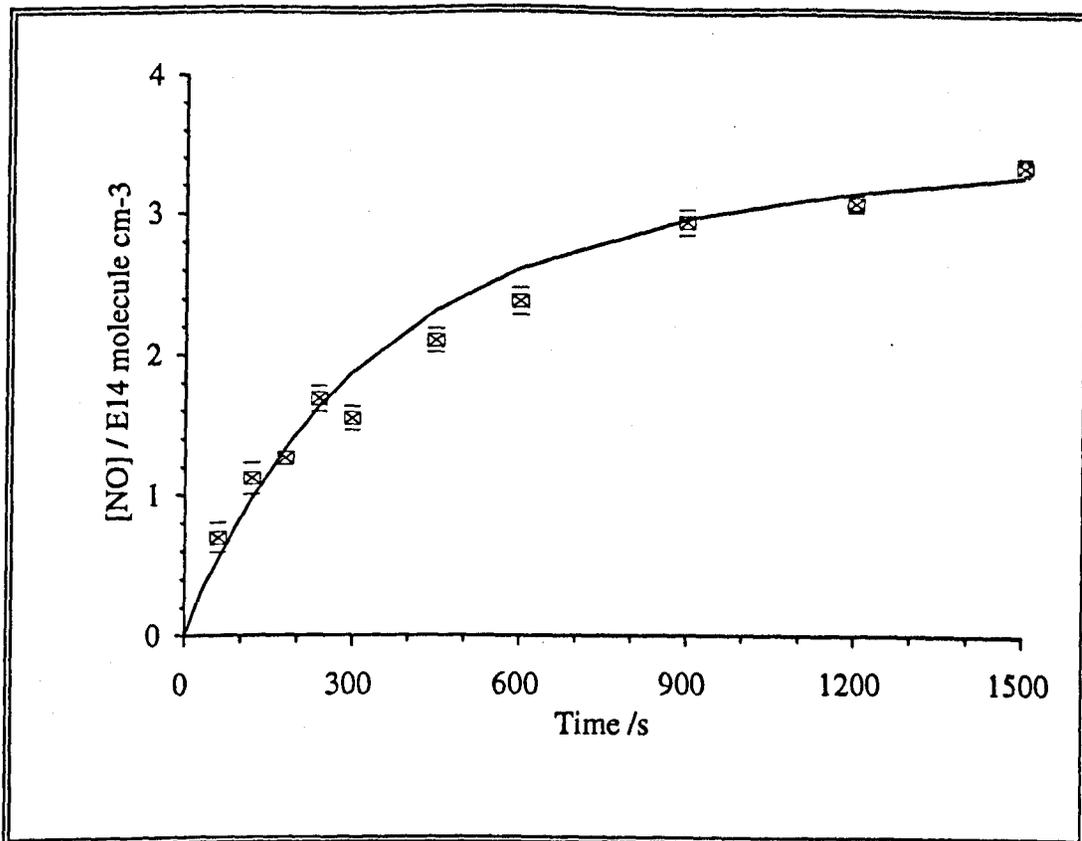
Figure 5.6   Method 1 Ethene Results. The solid line is the model fit.

$[NO_2] = 2.5 \times 10^{-2}$ mbar; [ethene] = 20.0 mbar; $[N_2] = 480$ mbar

of components in the apparatus, such as the filters or contaminants on the cell walls. Also, switching on the photolysis lamp caused a spike in the signal which settled down after approximately 60 seconds at a level higher than that before the spike. Although the optical design of the experiment was intended to minimise light from the photolysis lamp entering the PM tube, it is such an intense source, in comparison with the fluorescence, that a very small amount can have a noticeable effect on the reading.

It was shown that this increase in signal was a constant feature, and therefore likely to be due to stray photolysis radiation, by putting 50 mbar of N_2 in the cell and turning the lamp on. After the spike, the signal stayed at the higher level with no discernable decrease over a period of 15 minutes. It was, therefore, assumed that this signal increase was due to stray light from the lamp entering the PM tube, rather than

an electronic interference in the signal caused by turning the lamp on. *The mixing time for the* NO_2 *and 2-butyne, and the steadiness of the fluorescence signal in the absence of photolysis is shown in* Figure 5.7, *while the background signal and the spike can be clearly seen in* Figure 5.8, *which is a typical result of an experiment containing 2-butyne before any treatment of the data.*

An exponential decay curve was fitted to each set of normalized data. In the case of the NO_2/N_2 photolyses a curve could be fitted to all the data sets, for over 750 seconds, with an R^2 correlation greater than 93%. An example of a normalized decay trace is shown in Figure 5.9. When fitted to a simple model (see Table 5.iii) these provided a JNO_2 value of 1.23×10^{-3} s^{-1}. It was observed from the results of the photolyses of NO_2/N_2 mixtures that the decay traces showed little scattering, and that they decayed back to the background level.
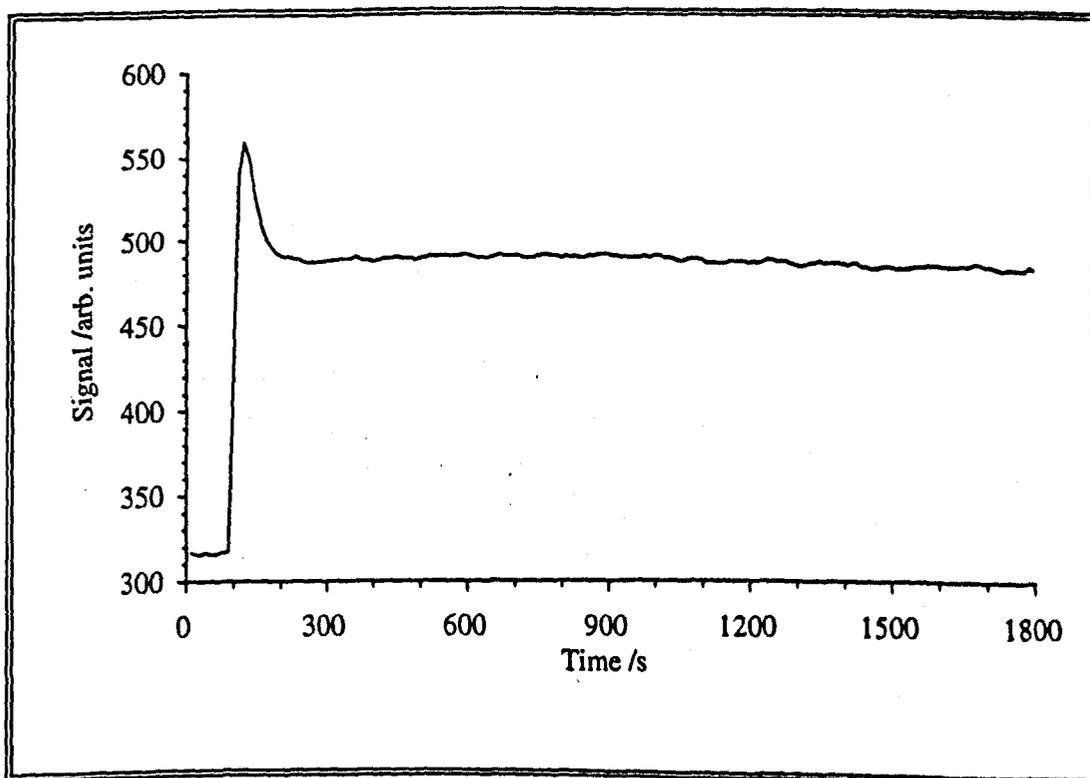
Figure 5.7   Fluorescence Trace with no Photolysis.

0.4 mbar NO_2; 8.0 mbar 2-butyne; 39.6 mbar N_2
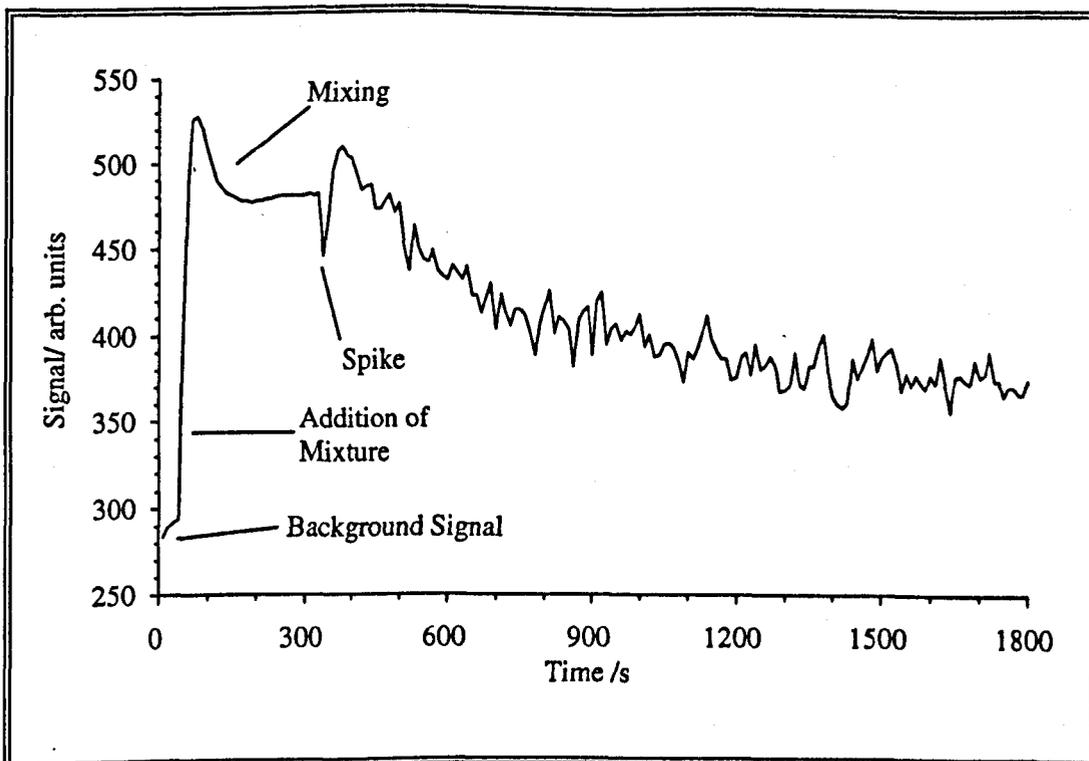
Figure 5.8   Decay trace showing the background signal and the lamp spike.

0.4 mbar NO_2; 8.0 mbar 2-butyne; 39.6 mbar N_2
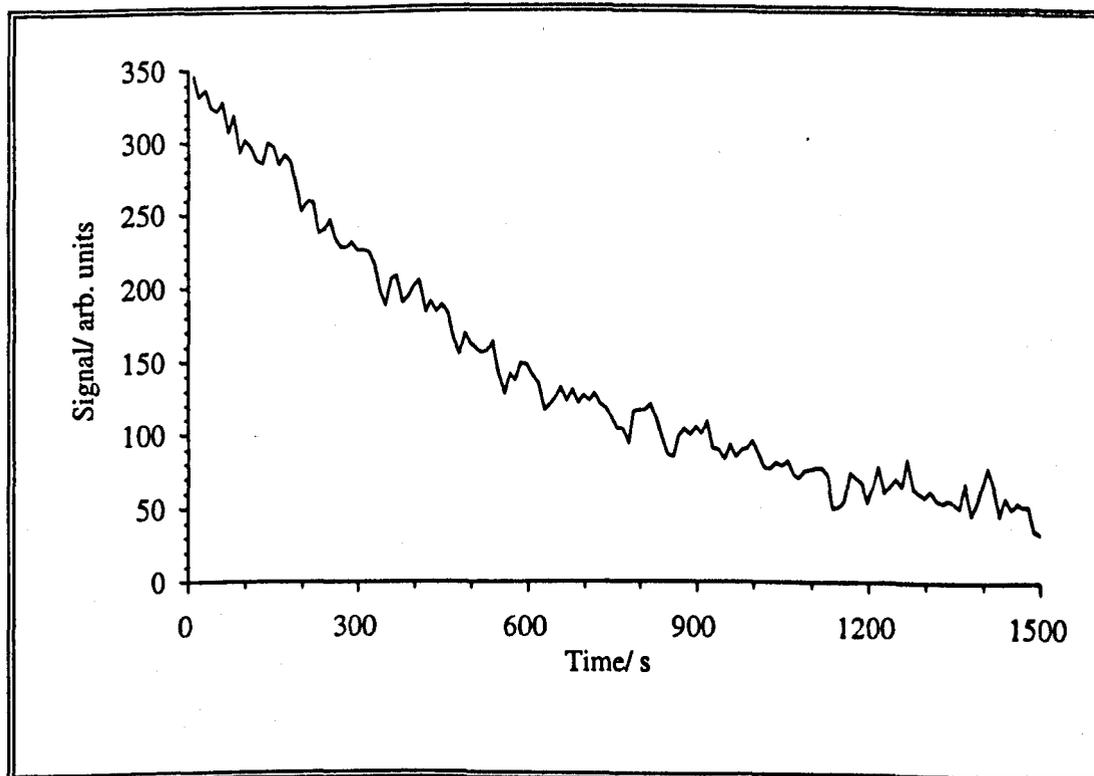
Figure 5.9   Fluorescence Decay During Photolysis of NO_2.

10 mbar of 1% NO_2/N_2; no 2-butyne present

152

It was found that when 2-butyne was present in the reaction mixtures, the decay traces showed a lower signal-to-noise ratio than when it was absent, and did not approach their background levels, even if the photolysis was continued for over 2 hours. In addition, it was noted that over the course of the LIF experiments, the background signal rose by a factor of four and the observed laser power appeared to drop by approximately 10%. This suggested that the light from the laser was being absorbed or scattered by something generated by the reaction in the cell. It may be that aerosols are produced in the cell, which scatter the laser radiation, and these are associated with the build up of a deposit on the cell walls that is responsible for the increase in the background signal.

Out of the twenty five experiments performed that contained 2-butyne, only eight could be fitted with an R^2 correlation value of greater than 90% over the first 400 second period of photolysis. The rest were discarded either because extreme fluctuation in the laser power had caused a discontinuity in the trace, or because the data were too scattered to analyse reliably.

These eight data sets were used to compare with the chemical model (already shown, in its final form, in Table 5.i) and the fits of the model to the results are given in Figure 5.10 and Figure 5.11. The reactions and rate constants contained in the model were taken, where possible, from the literature. Different mechanisms for the attack of the O atom on 2-butyne were tried, varying from 100% stable product yield, to 100% radical yield, and the model was run to simulate the reaction conditions of the eight data sets. The model predictions for each set of conditions were then compared with the exponential decays that had been fitted to the experimental data. The exponential fits, rather than the raw experimental data, were used in the comparison so that the effects of scattering in the trace would be minimised.
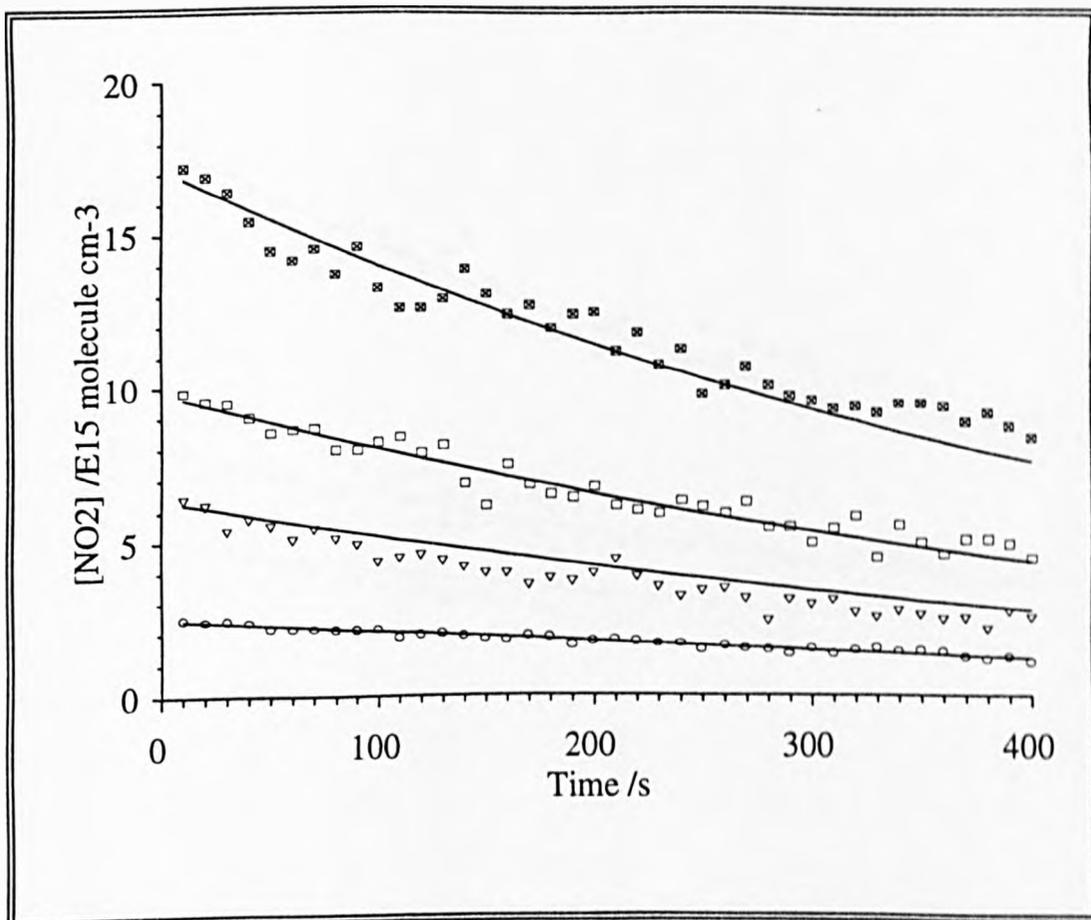
Figure 5.10 Results of the LIF Experiments. The solid lines are the model predictions.

⊠	0.7 mbar NO_2; 7.0 mbar 2-butyne; 69.3 mbar N_2
□	0.8 mbar NO_2; 8.0 mbar 2-butyne; 39.2 mbar N_2
∇	0.3 mbar NO_2; 3.9 mbar 2-butyne; 25.7 mbar N_2
o	0.1 mbar NO_2; 2.0 mbar 2-butyne; 9.9 mbar N_2
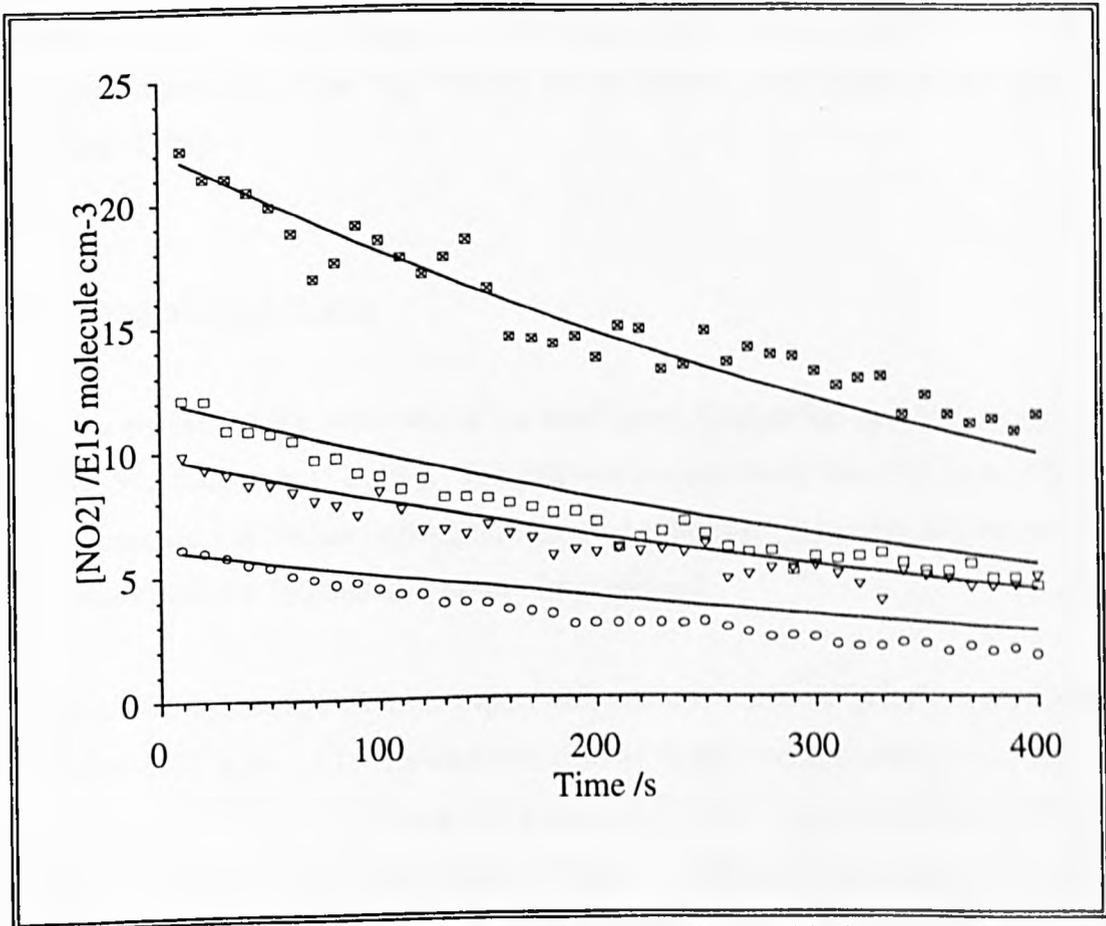
Figure 5.11 Results of the LIF Experiments. The solid lines are the model predictions.

■ 0.9 mbar NO_2; 9.0 mbar 2-butyne; 89.4 mbar N_2

□ 0.5 mbar NO_2; 6.6 mbar 2-butyne; 48.8 mbar N_2

∇ 0.4 mbar NO_2; 10.0 mbar 2-butyne; 39.6 mbar N_2

o 0.2 mbar NO_2; 2.5 mbar 2-butyne; 24.8 mbar N_2

5.4   Preliminary Ambient Measurements

Some preliminary measurements of ambient NO_2 photolysis rates have already been made using a static cell. These experiments, carried out between December 1993 and February 1994, constituted part of an undergraduate research project. A more thorough discussion of the experiments can be found in the report of that project [Vipond, 1994].

5.4.1   Experimental Design

The site chosen for this work was a flat level sports field at this university (latitude 53° 56' 59", longitude 1° 2' 45"). The cell was located more than 100 meters from the nearest vertical feature, although there were buildings (2 stories) or trees on all four sides between 100 and 200 meters from the cell.

The cell was cylindrical with hemispherical ends and made of quartz (dimensions: 310 mm x 33 mm o.d.). At one end a short length (approximately 15mm) of capillary tubing led to a PTFE tap and a bayonet fitting for attachment to a standard glass vacuum line. The cell was secured from the capillary tubing onto a matt grey tripod 150cm above the grass surface and oriented so that it pointed south from the tripod. It was filled in the laboratory to a pressure of 650mbar with a mixture of 1% NO_2 in N_2. The mixtures used did not contain 2-butyne for reasons discussed below (section 5.5.5). Some experiments were also performed using a Pyrex cell. The cell pressure of 650 mbar was chosen as it allowed several experiments to be obtained from bulbs filled to 1000 mbar, while also allowing the sample to be expanded out to a pressure of 500 mbar in the sample loop for the chemiluminescence analyser.

Whilst protected by a black covering to prevent unwanted photolysis, the cell was taken and secured to the tripod. The cover was then removed for a period of 10 minutes before being replaced and the cell returned to the laboratory. The sample was expanded from the cell into a loop before being passed into the

chemiluminescence analyser, which measured the concentration of NO present. A simple chemical model was then used to match the photolysis rate to the observed NO production.

5.4.2 Summary of Results

It was found that on most days the experiment worked well. However, some problems were encountered on the days with little cloud cover, as the increased photolysis rate lead to the consumption of a large proportion of the initial NO_2 (around 80%). Although the frequency of measurements was limited to no more than four per day, by combining results from days with similar weather conditions it was possible to show the expected diurnal variation in the photolysis rate.

The effect of increasing cloud cover was also demonstrated by comparing measurements performed at the same time of day (solar noon). In this way it was shown that the photolysis rate could vary from around 2×10^{-3} s^{-1} with 25% cloud cover (the least cloud cover experienced during the measurement period) to around 2×10^{-4} s^{-1} with 100% cover. These results are in reasonable agreement with previous measurements (see the discussion of previous measurements in Chapter 1).

5.5 Discussion

5.5.1 Method 1: Effect of the Different Cell Configurations

The results of the experiments with different regions of the cell exposed to the lamp can be explained by increased diffusion of NO_2 into the photolysis region, effectively giving higher $[NO_2]_0$ values than used in the analysis. With further experiments, it would have been possible to quantify the diffusion rate. However, this was not necessary once the constrictions had been placed in the cell at the limit of the blacking.

5.5.2   Error Analysis

The uncertainties involved in Method 1 are much less complex than those considered in Chapter 3. They essentially arise from two principal sources: the calibration and the reading of the chemiluminescence analyser. The error associated with the timing of the photolyses is minimal, as most were of the order of 100s or more.

The result of the calibration was (1.72 ± 0.04) mm/ppm NO. The uncertainty in this figure, $\pm2.3\%$, is the 2σ value for the gradient. The readings from the NO channel were very stable and the peak heights from duplicate experiments varied by only around ±2mm, which corresponds to an error of between 17% and 2% depending on the actual peak height, and is 5% in a mid-range reading. Accordingly, the total uncertainty in a mid-range reading is 5.5%.

However, performing a full analysis of the uncertainties involved in Method 2 is much more difficult. The reading errors associated with the apparatus are demonstrated by the noise visible in each trace, while the fact that only one third of the experiments actually produced useable results also indicates the level of difficulty experienced. Despite this, the eight experiments that were used, all agreed very well with the predictions of the model simulations of their conditions. As the aim of this series of experiments was the elucidation of the O/2-butyne reaction mechanism through the chemical model, the true measure of the uncertainty is provided by the variational analysis performed on the model, and discussed in section 5.5.4.

5.5.3   Discussion of the Ethene Experiments

As indicated earlier, the purpose of the experiments using ethene instead of 2-butyne, was to check for systematic errors in the experimental design. The chemistry of the reaction of $O(^3P)$ with ethene is well understood and, as such, can be reliably modelled. Any significant difference between the results of the ethene experiments and the model simulations may have highlighted a problem with the experiment. As

the experimental and simulated data are in good agreement it can be assumed that there is no significant error in either the experimental or analysis procedures.

Also, the photolysis rate of NO_2 in this system was not measured independently and only determined by fitting to the models (it was measured in Method 2, but a different optical layout and photolysis lamp were used and so the same J value cannot be assumed). The excellent agreement between the ethene model and experimental data gives support to the value of J_{NO_2} (6.0×10^{-4} s^{-1}) which is used in both the ethene and 2-butyne models.

5.5.4 Discussion of the 2-Butyne Experiments

The simple kinetic analysis performed in section 5.3.1 demonstrated that a simple mechanism could not be assumed for the reaction of $O(^3P)$ with 2-butyne. It was, therefore, necessary to attempt to elucidate the mechanism using model simulations of the experimental results. As the production of NO is less sensitive to the details of the mechanism than the decay of NO_2, the LIF experiments were performed to provide data on the loss rates of NO_2 that could be simulated, and so help determine the mechanism.

However, it was possible to fit a straight line ($R^2 = 0.983$) through the first 250s of the data, which gave a value for the NO_2 photolysis rate of 1.0×10^{-3} s^{-1}. Although this figure on its own cannot be regarded as reliable, it does provide some support for the rate determined from the modelling, 6.0×10^{-4} s^{-1}

In the model the following three reactions are used to simulate the core of this system, based on the rate constant for the reaction of $O(^3P)$ and 2-butyne given by *Herbrechtsmeier and Wagner* [1975] of 4.86×10^{-12} cm^3 molecule^{-1} s^{-1}.

$$O + C_4H_6 \rightarrow \text{Stable Products} + CO \quad k_{3a} = 3.42 \times 10^{-12} \text{ cm}^3 \text{ molecule}^{-1} \text{ s}^{-1}$$
$$O + C_4H_6 \rightarrow \text{Dimethylketene} \quad k_{3b} = 5.80 \times 10^{-13} \text{ cm}^3 \text{ molecule}^{-1} \text{ s}^{-1}$$
$$O + C_4H_6 \rightarrow C_2H_3 + CH_3 + CO \quad k_{3c} = 8.60 \times 10^{-13} \text{ cm}^3 \text{ molecule}^{-1} \text{ s}^{-1}$$

159
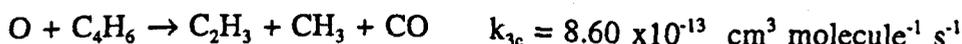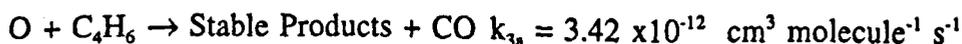
By using these three reactions it is possible to predict a CO yield of around 88% and a stable hydrocarbon yield of around 60%, as reported by *Herbrechtsmeier and Wagner* [1975] (based on 100% 0 atom reaction).

Varying the rate of the $O(^3P)$ attack on 2-butyne, k_3, by a factor of ten in either direction has little effect on the results, suggesting that it is the production of O atoms, and not their reaction with 2-butyne, that is the rate limiting step in the reaction scheme. In the case of the NO production data from Method 1, the concentration of the 2-butyne is such that all the O atoms react with it immediately they are formed, even with the slowest rate constant modelled. The modelling of the NO_2 loss data from the LIF analysis experiments still indicates that the lifetime of the O atoms is very short. However, because the 2-butyne excess is never greater than 25-fold, a proportion of the O atoms react with NO_2 rather than 2-butyne. Obviously this proportion will depend on the actual 2-butyne excess and the value of k_3 that is used.

In fact it is still found that the NO_2 production is relatively insensitive to this rate constant. Analysis of the subsequent chemistry reveals that a branching ratio for k_{3c} of 18%, as used in the model, gives an effective quantum yield, Φ_{eff}, for the photolysis of NO_2 of approximately 1.4. If all the O atoms reacted with NO_2 the Φ_{eff} would be 2.0. Hence it makes little difference to the loss of NO_2 if 70% or 50% of the O-atoms react with 2-butyne.

The branching ratio between the formation of the hydrocarbon products and dimethylketene (k_{3a}:k_{3b}) has little effect on the rate of NO_2 loss or NO production, as they undergo very little subsequent chemistry. Approximately 1% of the O atoms formed react with dimethylketene to form $(CH_3)_2CO$ and CO, and 0.6% of them react with the hydrocarbon products (assuming they all react with the same rate as O + C_3H_6). Although the reaction of O and C_3H_6 (and OH with C_4H_6) yields complex radical products, the modelling suggests that they are formed in such low concentrations that their contribution to the overall scheme will be negligible.

The crucial ratio is $k_{3c}:k_{3a+3b}$ between the formation of the stable products and the radicals C_2H_3 and CH_3, as these react with NO and NO_2. All the C_2H_3 formed reacts with NO_2 to give NO and CH_2CHO. This then reacts with more NO_2, giving HONO and ketene, or with NO to give the nitrite $ONCH_2CHO$. The methyl radical can also form a nitrite, but most reacts with NO_2 producing NO and methoxy, CH_3O, which itself reacts further with NO and NO_2.

In order to assess the sensitivity of the system to this branching ratio it is necessary to use the NO_2 loss data rather than those for NO production. The secondary chemistry of the mechanism involves both the production and loss of NO, while NO_2 is only lost. Hence the Φ_{eff} for NO production is only around 1.2, and this insensitivity of the NO concentration is demonstrated in Figure 5.12.

The variational analysis was performed using the conditions where the model prediction fitted most closely to the NO_2 decay profile. This was in part because it would show the effects of the variation more clearly, and also because that experiment had the highest excess of 2-butyne of all the LIF experiments (25 fold) and so would have the minimum contribution from O atom attack on NO_2. It was found that varying k_{3c} from between 8% and 28% of k_3 resulted in an approximately ±10% difference in the concentration of NO_2 after 400 seconds, compared to the experimental results. However, the base value of k_{3c} was chosen as 18% of k_3 because it provided a reasonable agreement with all the data sets. Using the latter value, the model predictions for the concentration of NO_2 over 400 seconds differ by no more than 15% from the experimental results. While varying k_{3c} improves the fit of some of the data sets, they decrease the fit of others. Consequently, a branching ratio of 18% radical products provides the best overall fit to the results. The effect on the NO_2 decay of varying this ratio is shown in Figure 5.13.
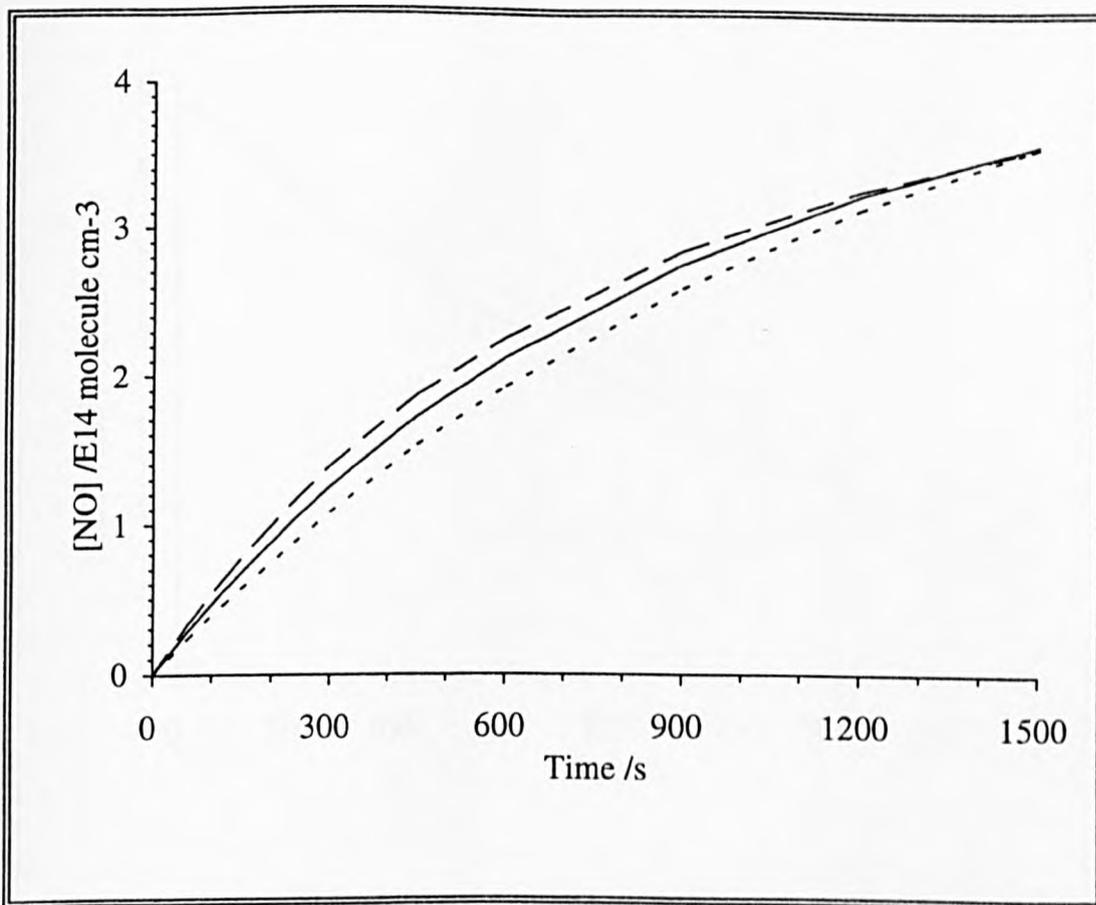
Figure 5.12 Effect on [NO] of Varying the Radical Production Ratio.

— — 30%, —— 18% (base value), - - 5%

$[NO_2] = 2.5 \times 10^{-2}$ mbar; [2-butyne] = 4.0 mbar; $[N_2]$ = 496 mbar

Previously reported studies of this reaction suggest a branching ratio for the production of propene of 0.3 [*Herbrechtsmeier and Wagner*, 1975] or 0.32 [*Deslauriers and Collins*, 1986] with the former also detailing the yield of other hydrocarbons. These were C_2H_2 (11%), C_2H_6 (9%), C_2H_4 (5%), CH_4 (4%) and C_3H_4 (2%). While the mechanism given in the present study does not detail the nature of the stable hydrocarbon products, the proportion of the 2-butyne that follows this channel is the same as that previously reported by *Herbrechtsmeier and Wagner* [1975] (a total of 61% in both cases).
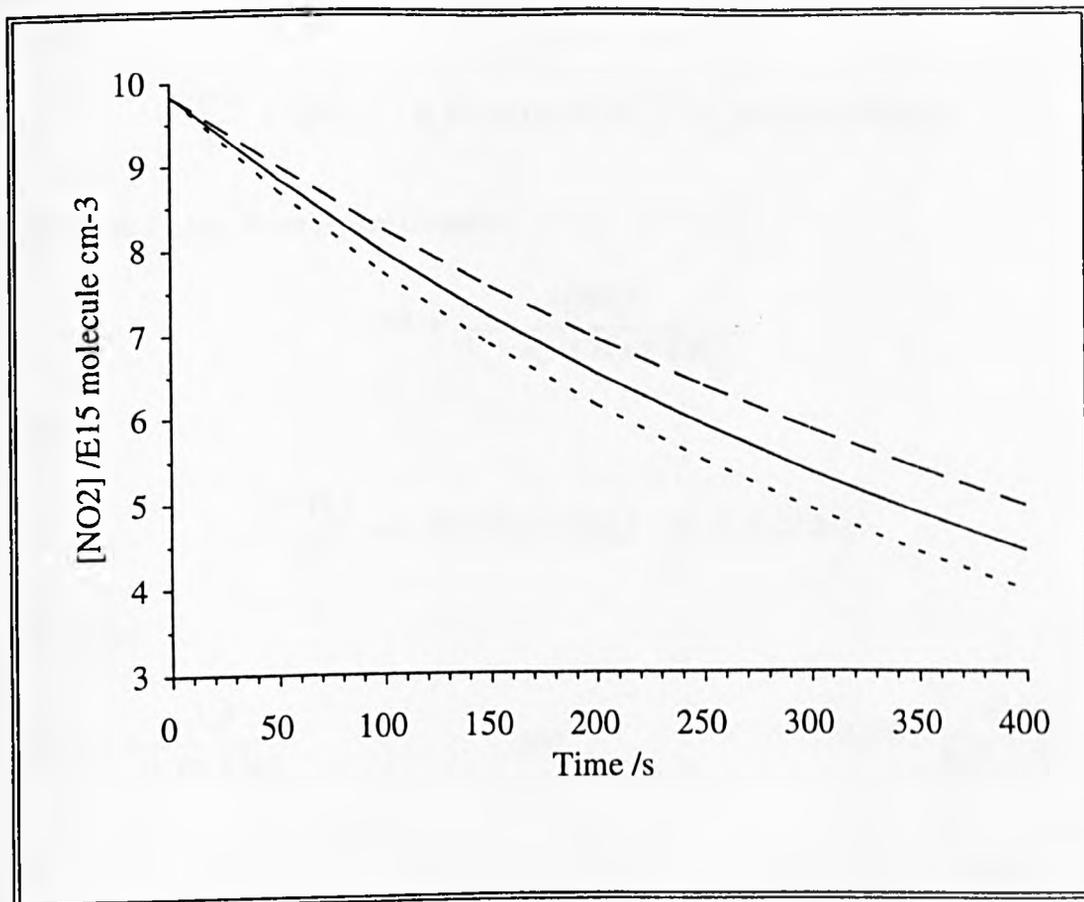
Figure 5.13 Effect on [NO$_2$] of Varying the Radical Production Ratio.

$- -$ 25%, — 18% (base value), - - 10%.

An alternative method of determining the branching ratio involves the examination of the rate equations. The analysis depends on the following summary being an accurate representation of the core of the reaction scheme:

$$NO_2 + h\upsilon \rightarrow NO + O \qquad\qquad J$$
$$O + CH_3CCCH_3 \rightarrow C_2H_3 + CH_3 + CO \qquad\qquad k_a$$
$$O + CH_3CCCH_3 \rightarrow Stable\ Products \qquad\qquad k_b$$
$$CH_3 + NO_2 \rightarrow CH_3O + NO \qquad\qquad k_c$$
$$CH_3O + NO_2 \rightarrow Stable\ Products \qquad\qquad k_d$$
$$C_2H_3 + NO_2 \rightarrow C_2H_3O + NO \qquad\qquad k_e$$
$$C_2H_3O + NO_2 \rightarrow HONO + CH_2CO \qquad\qquad k_f$$

163
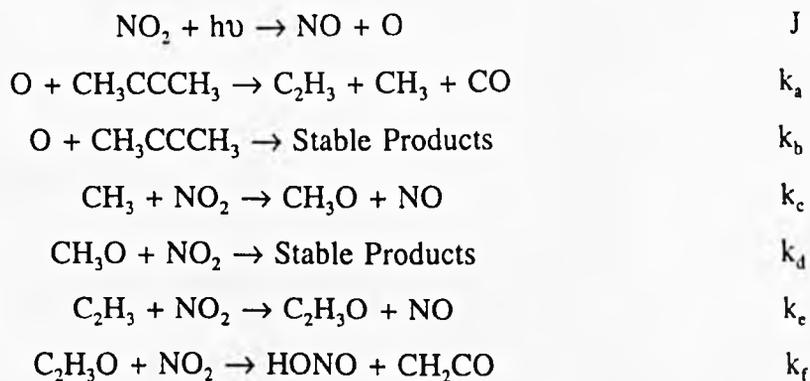
Thus:

$$+\frac{d[O]}{dt} = J[NO_2] - k_a[O][CH_3CCCH_3] - k_b[O][CH_3CCCH_3]$$

Using the Steady State Approximation:

$$[O] = \frac{J[NO_2]}{(k_a + k_b)[CH_3CCCH_3]}$$

Also:

$$+\frac{d[CH_3]}{dt} = k_a[O][CH_3CCCH_3] - k_c[CH_3][NO_2]$$

Therefore:

$$[CH_3] = \frac{k_a J}{k_c(k_a + k_b)} \qquad \text{and} \qquad [CH_3O] = \frac{k_a J}{k_d(k_a + k_b)}$$

$$[C_2H_3] = \frac{k_a J}{k_e(k_a + k_b)} \qquad \text{and} \qquad [C_2H_3O] = \frac{k_a J}{k_f(k_a + k_b)}$$

From the above, the following rate equation can be obtained:

$$-\frac{d[NO_2]}{dt} = J[NO_2]\left(1 + 4\frac{k_a}{k_a + k_b}\right)$$

Integration of this equation gives:

$$\ln[NO_2]_o - \ln[NO_2]_t = J\left(1 + 4\frac{k_a}{k_a + k_b}\right)$$

Plotting the left hand side of the above equation against time, t, will have a gradient m, such that:

164

$$m = 1 + 4\frac{k_a}{k_a + k_b}$$

Therefore, the branching ratio for the reaction of O with 2-butyne is:

$$\text{Branching Ratio} = \frac{k_a}{k_a + k_b} = \frac{1}{4}\left(\frac{m}{J} - 1\right)$$

As stated above, the validity of this approach depends on the simplified reaction scheme being a reasonable representation of the chemistry. For this to be true it is important that the reaction:

$$O + NO_2 \rightarrow NO + O_2 \qquad\qquad k_g$$

is not significant. This is only true for the experiments in Method 1, where 2-butyne was in greater than 100 fold excess. Unfortunately, as discussed above, the NO production rate is less sensitive to the branching ratio than the loss of NO_2. If the reaction of O with NO_2 is included, in order to allow the use of the NO_2 loss data, the following rate expression is obtained, the integration of which is very complex:

$$-\frac{d[NO_2]}{dt} = [NO_2]\left(J + k_g + \frac{4Jk_a[CH_3CCCH_3]}{(k_a + k_b)[CH_3CCCH_3] + k_g[NO_2]}\right)$$

Figure 5.14 shows the plot obtained using the Method 1 data for 2-butyne. It can be seen that it deviates from being linear as the photolysis time increases, showing the increasing influence of the secondary chemistry that is not included in the reaction scheme. However, the plot is reasonably linear up to 120s and this region of the line has a gradient:

$$m = 1.33 \times 10^{-3} \text{ s}^{-1}$$

In Method 1:

$$J = 6.0 \times 10^{-4} \text{ s}^{-1}$$

165
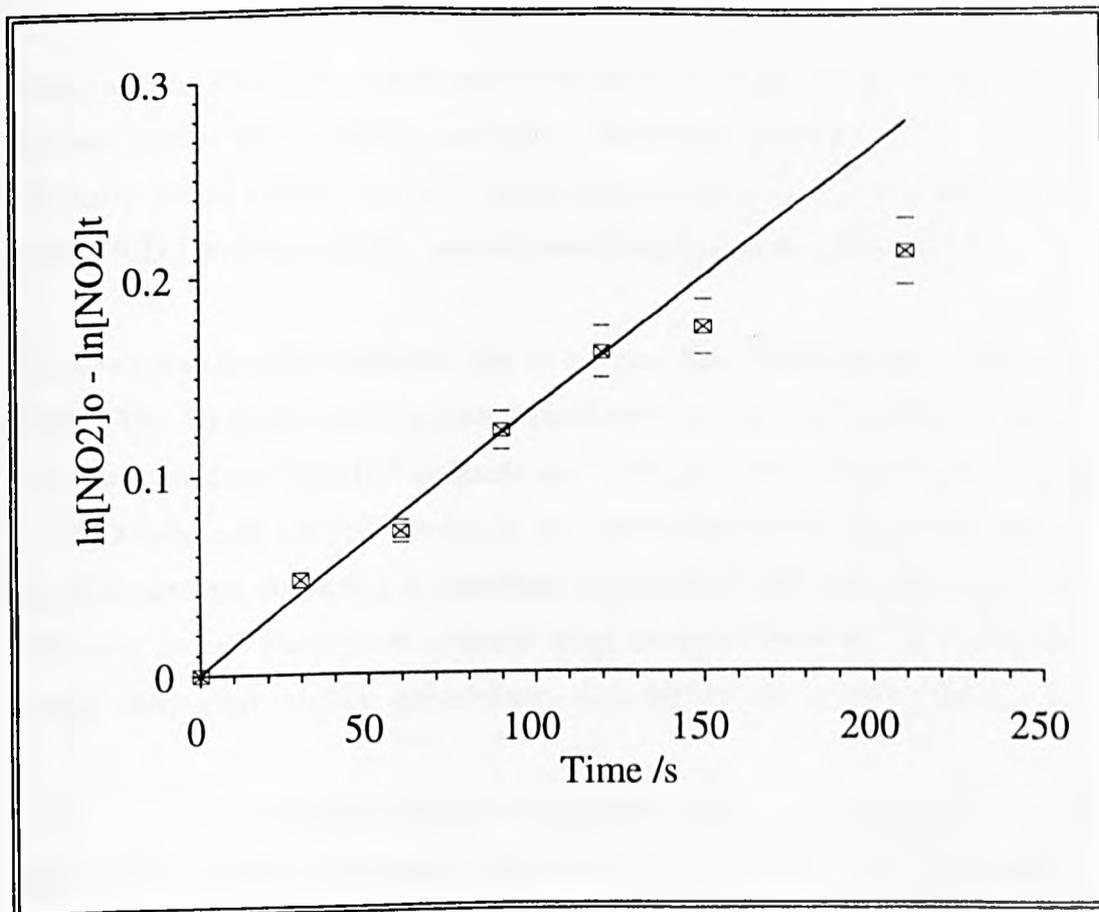
Figure 5.14 Result of the Analysis of the Rate Equations. The line is the least squares fit up to 120s, the gradient of which is 1.33 x10^{-3} s^{-1}

This yields a branching ratio:

$$\frac{k_a}{k_a + k_b} = 0.3$$

Given the simplicity of the reaction scheme, and consequently the poor fit of the data at the longer times to a straight line relationship, this is in reasonable agreement with the branching ratio of 0.18, obtained from the computer modelling.

5.5.5 The Consequences of the Branching Ratio for a Photolysis Rate Monitor

It was stated at the beginning of this chapter that one of the reasons that 2-butyne was chosen as an additive for NO_2 photolysis experiments was that the reaction between it and $O(^3P)$ produced stable hydrocarbon products and CO. It was,

166

therefore, hoped that it would provide a constant quantum yield throughout the duration of the photolysis, and so allow analysis of the results using simple analytical methods, rather than complex modelling. However, it has been shown that the chemistry which follows the O/2-butyne reaction leads to the production of both methyl (CH_3) and vinyl (C_2H_3) radicals which react with both NO_2 and NO.

The effect the secondary chemistry has on the quantum yield is shown in Figure 5.15 below. This figure shows the quantum yield over the course of a 300s photolysis of a mixture containing 1.6×10^{15} molecule cm^{-3} (100ppm) NO_2, 2.4×10^{17} molecule cm^{-3} (1.5%) 2-butyne in 1.6×10^{19} molecule cm^{-3} (650 mbar) of N_2, along with those for identical mixtures containing hypothetical dopants with different radical production branching ratios. These were obtained using the same chemistry as 2-butyne and merely altering the relevant rate constants according to the desired branching ratio.

It can be seen from Figure 5.15 that the quantum yield can vary greatly over 300s, approaching 1 at longer photolysis times, as the concentration of NO_2 decreases. It should be noted that in all the results shown, 90% or more of the NO_2 had been consumed by 300s. This is a consequence of the high photolysis rate, 7.0×10^{-3} s^{-1}, used in the simulations. Although it is higher than any of the rates measured by *Vipond* [1994], it is typical of the rates measured by previous studies, where the solar zenith angles were smaller [e.g. *Parrish et al.*, 1983].

For 2-butyne to simplify the analysis of the results from a photolysis, it has to reduce the variation in the quantum yield to less than approximately 5%, the uncertainty in the NO measurement. The actual value of the quantum yield is not important, as long as it is known. Figure 5.15 shows that a radical production branching ratio of less that 5% would be needed to achieve such a small variation. It should be noted, however, that the quantum yield for the NO_2/N_2 system itself varies from around 1.4 to 1.1 over 300s, approximately the same as that with 2-butyne present (branching ratio of 18%, as found from the earlier experiments). For this reason is was believed that the addition of 2-butyne provided no benefit for the analysis, and indeed increased the uncertainty in the result as the model used was more complex.

167
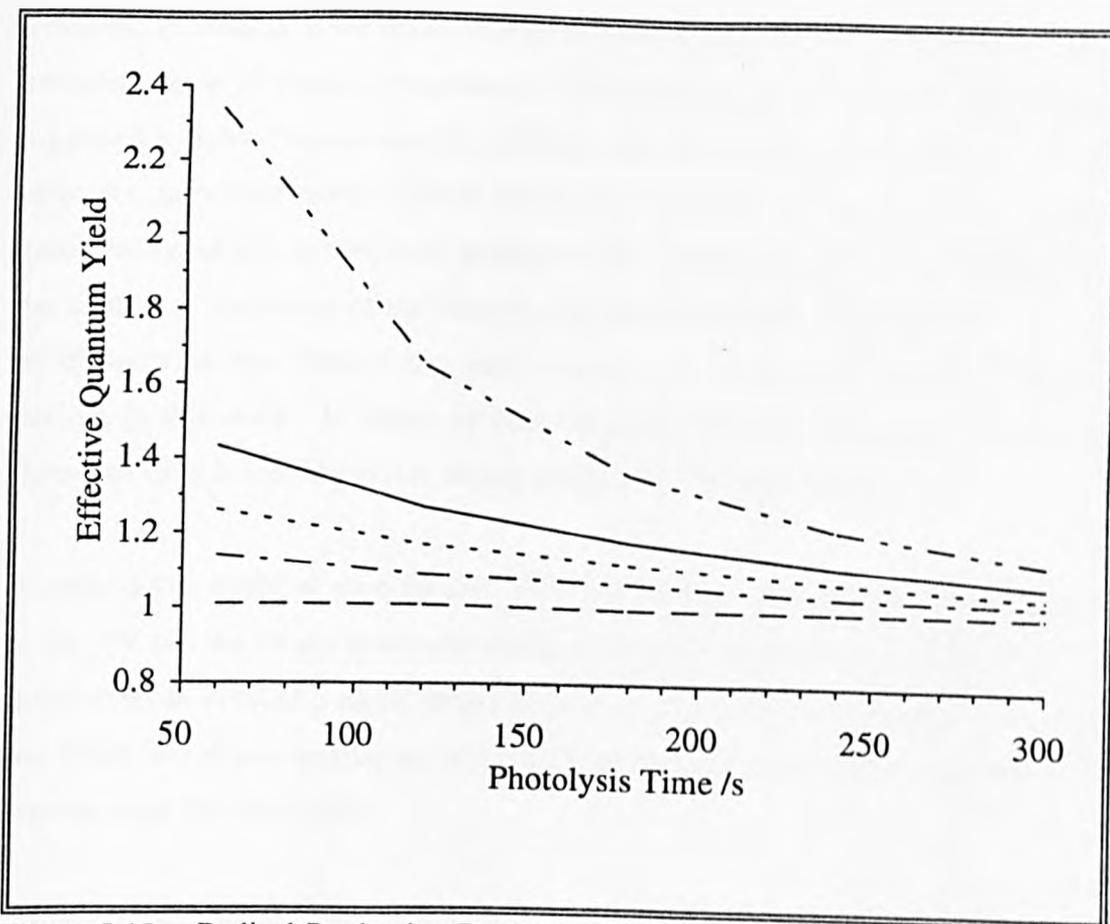
Figure 5.15   Radical Production Branching Ratio and Quantum Yield.

— ·· —	100% Radical Yield
———	18% Radical Yield (base value)
- - - - - -	10% Radical Yield
— · — · —	5% Radical Yield
— — —	0% Radical Yield

<u>5.5.6</u>   <u>Future Work</u>

The initial aim of this work was the creation of a chemical system that would yield a constant quantum yield in a static monitor of atmospheric NO_2 photolysis rates. The production of the methyl and vinyl radicals, and their reactions with NO and NO_2, suggest that 2-butyne is not a suitable species for this role. An alternative dopant would need low radical production (<5%) in order to provide a constant quantum yield.

However, in relation to the determination of the mechanism, the identification of the intermediates is of primary importance. The existence of the biradical $CH_3C:CH_3$ is suggested by both *Umstead and Lin* [1977] and *Herbrechtsmeier and Wagner* [1975]. However, in neither study is there any direct evidence of its role. Both of these groups assigned the formation of propene to the rearrangement of this biradical, but the method of formation of the other hydrocarbon products was believed to involve its dissociation into methyl and vinyl radicals, as is assumed in the mechanism derived in this work. If either, or both, of the methyl or vinyl radicals could be shown to exist it would provide strong support for this mechanism.

A method that could be used for this is UV absorption. Both of the radicals absorb in the UV but the steady state concentrations that are likely to be present would be insufficient to provide a signal strong enough to be measured accurately. By using the MMS technique, smaller concentrations of radicals would be needed than with conventional UV absorption.

5.5.7 Conclusions

This work has shown that the addition of 2-butyne to a mixture of NO_2 in N_2 will not result in any simplification of the data analysis. Because the reaction of $O(^3P)$ with 2-butyne produces both methyl and vinyl radicals which can subsequently react with NO_2 and NO, a constant quantum yield for the photolysis of NO_2 is not obtained.

It can also be concluded that the models used in this study accurately reproduce the two chemical systems investigated (NO_2/2-butyne and NO_2/ethene), and that the branching ratio for the production of the radicals C_2H_3 and CH_3 from the O atom attack on 2-butyne is 0.18 ± 0.03. Using this ratio, it is also possible to simulate the observed concentrations of both NO and NO_2, and also the yield of both CO and stable hydrocarbons previously reported. The diagram below illustrates the reaction scheme suggested by the model. It should be noted that the percentages shown are approximate as some, particularly those involving the reaction of radicals with NO_2, vary greatly over the course of the photolysis.

O + CH_3CCCH_3 $\longrightarrow$ $CH_3\overset{\cdot}{C}=\overset{\overset{O^\cdot}{|}}{C}CH_3$

$(CH_3)_2C=C=O$ $\xrightarrow{+O}$ $(CH_3)_2CO$ + CO

$\downarrow$ 89%

Stable hydrocarbon products $\xleftarrow[\text{Rearrangement}]{68\%}$ $H_3C-\overset{\cdot\cdot}{C}-CH_3$ + CO

$\downarrow$ 32%

C_2H_3 + CH_3 $\xrightarrow[NO]{3\%}$ CH_3NO

100% NO_2 97% NO_2

NO + CH_2CHO CH_3O + NO

20% NO 80% NO_2 60% NO_2 8% NO

$ONCH_2CHO$ CH_2CO + $HONO$ CH_3ONO_2 CH_2O + HNO

0.5%   32% NO

CH_3ONO

NO + OH

99% C_4H_6 0.5% NO_2

Radical Products HNO_3
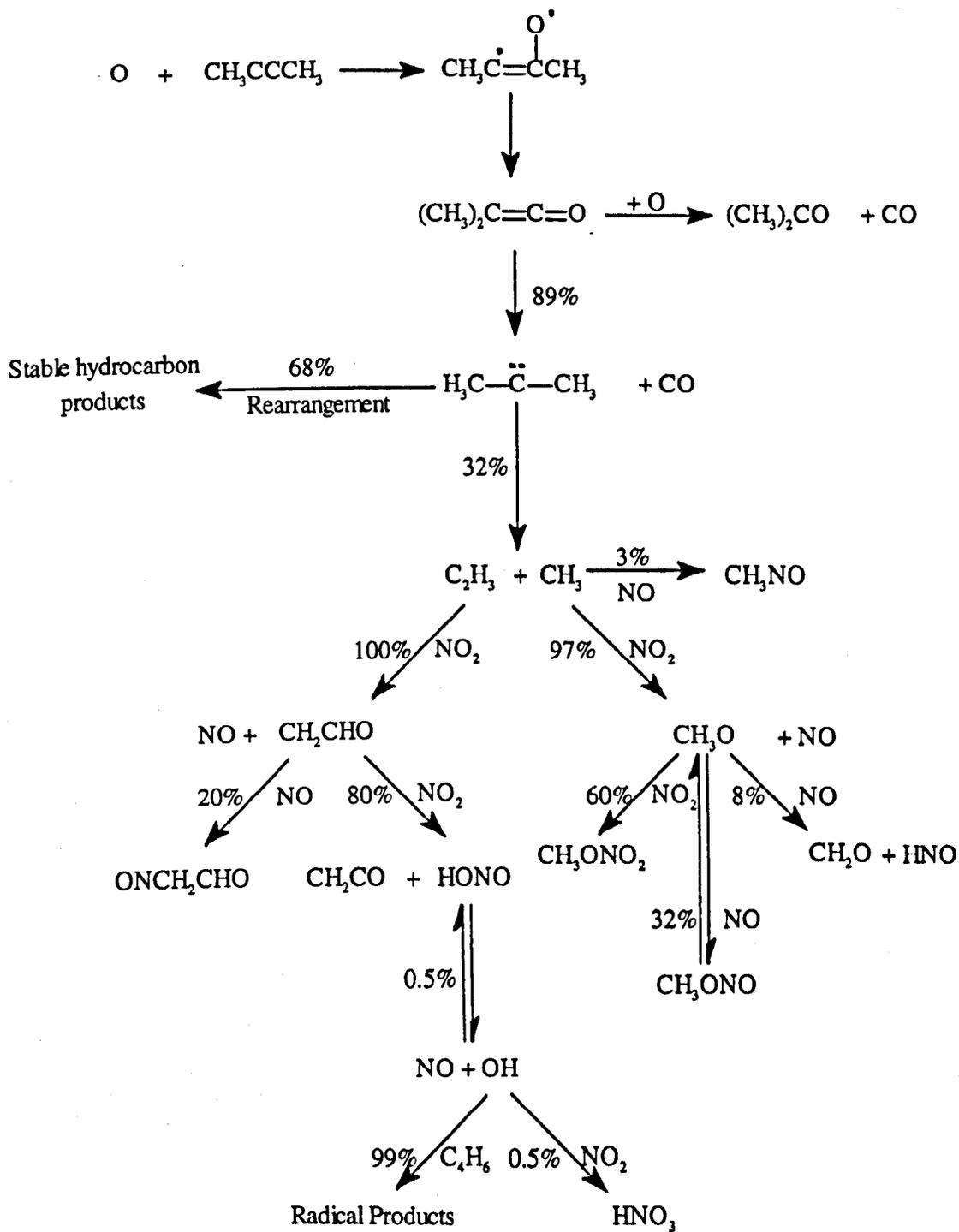
Data Collection Programme for Lock-in Amplifier

```
DECLARE SUB readlia (rd$)
DECLARE SUB writelia (cmd$)
'
'*******************************************************************
******
'           LOCK-IN-AMPLIFIER DATA COLLECTION ROUTINE (RS232)
'
'*******************************************************************
******
'   Author: Richard M. Burdett
'   Date:   1st July 1993
'   Rev:    1.0
'
' This program assumes that the computer is fitted with a serial interface
' and that the lock-in has been set up so that the RS232 settings are:
' 11; for baud rate = 9600; 16; echo, 7 data bits, 1 stop bit, even parity.
' (numbers 11 & 16 refer to models 5209/5210. For other units ensure that
' settings match the above.
'
'
'*******************************************************************
******
' This line sets up the com1/2 RS232 port to 9600 baud,even parity,7 data
' bits, 1 stop bit. Select either com1 or com2 to match the port to which
```

```
' the LIA is cabled.
  OPEN "com1: 9600,e,7,1,cs,ds" FOR RANDOM AS #1
  rd$ = SPACE$(80)
'

'   * * * * * * * * * * * * * * * * * * * * * *   MAIN   PROGRAM   LOOP
*********************************


  CLS : KEY OFF


' Locate model number of LIA
    cmd$ = "ID"
    writelia cmd$
    readlia rd$


' Draw main screen
    PRINT rd$; " Lock in Amplifier Data Collection Routine (RS232)"
    PRINT ""
    PRINT "This program collects a specified number of CH 1"
    PRINT "readings from the attached LIA at specified"
    PRINT "time intervals and writes them to the file 'output.dat'"
    PRINT ""


' Prompt for time per point
    INPUT "Time per point (seconds) ", timepoint


' Prompt for number of points
    INPUT "Number of points       ", numpoints


' Open file for output data
    OPEN "c:\vbdos\output.dat" FOR OUTPUT AS #2
```

```
' Prompt to start experiment
    INPUT "Press ENTER to start", goon$


' Clear input boxes and show working message
    LOCATE 7, 1
    PRINT "                            "
    PRINT "working.......              "
    PRINT "                            "


' Write file header information
    PRINT #2, "CHANNEL 1 v TIME DATA SET"
    filedate$ = DATE$
    PRINT #2, "Date: ", filedate$
    PRINT #2, ""
    PRINT #2, "Point Time", "Ch 1 value"


' Main loop starts here, repeats for specified number of points
    ON TIMER(timepoint) GOSUB collect
    TIMER ON
    DO UNTIL pointno = numpoints
    LOOP


' Write finished message to screen for 2 seconds
    LOCATE 8, 1
    PRINT "finished......"
    SLEEP (2)


    CLOSE : CLS : STOP


' data collection subroutine
collect:
    cmd$ = "Q1"
```

```basic
      pointtime$ = TIME$
      writelia cmd$
      readlia rd$
      PRINT #2, pointtime$, rd$
      pointno = pointno + 1
      RETURN


' * * * * * * * * * * * * * * * * * * * * * *     E N D   O F   P R O G R A M
*********************************


   SUB collect
   END SUB


SUB readlia (rd$)
' ******************** read subroutine *********************************
      A$ = "": prd$ = ""
      WHILE (A$ <> "*" AND A$ <> "?")
      WHILE LOC(1) = 0: WEND
      A$ = INPUT$(1, #1)
      IF (A$ <> CHR$(10) AND A$ <> CHR$(13) AND A$ <> "*") THEN
      prd$ = prd$ + A$
      END IF
      WEND
      IF A$ = "?" THEN
       rd$ = "Command Error"
      ELSE
      IF LEN(prd$) > 0 THEN
       rd$ = prd$
       ELSE
       rd$ = "No response to this command          "
      END IF
      END IF
```

```
END SUB

SUB writelia (cmd$)
REM**********************WriteLiasubroutine**********************
FOR P = 1 TO LEN(cmd$)
c$ = MID$(cmd$, P, 1)
PRINT #1, c$;
WHILE LOC(1) = 0: WEND
A$ = INPUT$(1, #1)
IF A$ <> c$ THEN PRINT "handshake error"
NEXT P
PRINT #1, CHR$(10)
PRINT #1, CHR$(13)
END SUB
```

Appendix 2

Data Extraction Programme for A-D Converter

This programme was written by Stephen Laws, Electronics Department, University of York, U.K. It reads a data file output by the "Data Capture" software supplied with the A-D converter card and creates a seperate, single column, ASCII text file consisting of the data contained in the first column of the original file.

```
PROGRAM extract;
{extracts first 12 characters of data file}

var
  infile  : string[12];
  outfile : string[12];
  line    : string[12];
  linenumber : INTEGER;
  input   : TEXT;
  output  : TEXT;
  data    : char;
  i       : INTEGER;

begin
  write('Enter input file name: ');
  readln(infile);
  Assign(input,infile);
  write('Enter output file name: ');
  readln(outfile);
  Assign(output,outfile);
  reset(input);
```

```pascal
    rewrite(output);
    linenumber := 1;
    while not Eof(input) do
    begin
      i:=1;
      line:='            ';
      while (i <= 12) do
       begin
         read (input,data);
         line[i]:=data;
         i:=i+1;
       end;
     readln(input);
     write(output,linenumber);
     writeln(output,line);
     linenumber := linenumber + 1;
   end;
   writeln('Data Extraction Complete');
   close(input);
   close(output);
 end.
```

Appendix 3

Data Analysis Programme for NO_x Analyser Results

'   This programme was written by Rob Gladstone 21/06/94

'   Dept. of Chemistry, University of York, Heslington, York, YO1 5DD, UK

'   It is for use in analysing the results from chemical amplification

'   experiments, where the difference in the concentration of NO, before and

'   after a photolysis-induced chain reaction, is determined by a NOx Box.

'

'   *****   Introduction   *****

'

```
        CLS
        PRINT
        PRINT
        PRINT
        PRINT "      *****      NOx Box Results Analysis      *****"
        PRINT
        PRINT
        PRINT "This programme takes the integrated peak areas from the NOx
Box"
        PRINT "and calculates the chain length of the reaction and the"
        PRINT "percentage of NO converted."
10      PRINT
        PRINT
```

'

'   *****   Data input   *****

'

```
        PRINT "IMPORTANT!  Only use this programme for a 1ms flash
```

duration."

```
        INPUT "Please enter the AVERAGE peak areas of the BLANKS: ", B
        INPUT "Now enter the AVERAGE peak areas of the SAMPLES: ", S
        INPUT "Finally, enter the pressure (in mbar): ", P
        PRINT
        PRINT "Thank you"
        PRINT
        PRINT

'

'       *****    Calculations    *****

'


        MRB = ((-20.77 + SQR(431.49 + (2.394 * (7.25 - B)))) / -1.197) / 10 ^ 6
        MRS = ((-20.77 + SQR(431.49 + (2.394 * (7.25 - S)))) / -1.197) / 10 ^ 6
        DNO = 2.46 * 10 ^ 16 * P * (MRB - MRS)
        R = 3.59 * 10 ^ 9 * (P / 500)
        CL = DNO / R
        CON = (MRB - MRS) * 100 / MRB

'

'       *****    Results output    *****

'


        PRINT "The chain length is "; CL
        PRINT "The percentage of NO converted is "; CON; "%"

'

'       *****    Repeat calculations    *****

'


        INPUT "Do you want to do more calculations? (y/n): ", Y$
        IF Y$ = "n" OR Y$ = "N" THEN 100
        GOTO 10
100     PRINT "Goodbye"
        END
```

179

References

1   Altshuller, A.P. *J. Air Pollut. Control Assoc.* **1989**, *39*, 704-708

2   Anastasi, C.; Gladstone, R.V.; Sanderson, M.G. *Environ. Sci. Technol.* **1993**, *27* (3), 474-482

3   Anastasi, C.; Hancock, D.U. *J. Chem. Soc. Farad. Trans. 2* **1988**, *84* (10), 1697-1706

4   Anastasi, C.; Muir, D.J.; Simpson, V.J.; Pagsberg, P. *J. Phys. Chem.* **1991**, *95*, 5791-5797

5   Anastasi, C.; Simpson, V.J.; Monk, J.; Pagsberg, P. *Chem. Phys. Lett.* **1989**, *164*, 18-22

6   Anderson, J.G. *Geophys. Res. Lett.* **1976**, *3*, 165-168

7   Armerding, W.; Herbert, A.; Schindler, T.; Spiekermann, M.; Comes, F.J. *Ber. Bunsenges. Phys. Chem.* **1990**, *94* (7), 776-781

8   Armerding, W.; Herbert, A.; Spiekermann, M.; Walter, J.; Comes, F.J. *Fresnius J. Anal. Chem.* **1991**, *340* (10), 654-660

9   Armerding, W.; Spiekermann, M.; Comes, F.J. *J. Geophys. Res.* **1994**, *99* (D1), 1225-1239

10   Armerding, W.; Spiekermann, M.; Grigonis, R.; Walter, J.; Herbert, A.; Comes, F.J. *Ber. Bunsenges. Phys. Chem.* **1992**, *96* (3), 314-318

11   Ashmead, B.V.; Thomas, J.H. *Symp. Int. Combust. Proc.* **1973**, *14*, 493

12   Atkinson, R. *Chem. Rev.* **1986**, *86*, 69-201

13   Atkinson, R. *Atmos. Envi.* **1990**, *24A*, (1) 1-41

14   Atkinson, R.; Aschmann, S.M.; Winer, A.M. *J. Atmos. Chem.* **1987**, *5*, 91

15   Atkinson, R.; Baulch, D.L.; Cox, R.A.; Hampson, R.F.Jr; Kerr, J.A.; Troe, J. *J. Phys. Chem. Ref. Data* **1989**, *18*, 881-1097

16   Atkinson, R.; Baulch, D.L.; Cox, R.A.; Hampson, R.F.Jr; Kerr, J.A.; Troe, J *J. Phys. Chem. Ref. Data* **1992**, *21*, 1125

17   Bahe, F.C.; Schurath, U.; Becker, K.H. *Atmos. Environ.* **1980**, *14*, 711-718

18   Barnhard, K.I.; Santiago, A.; He, M.; Asmar, F.; Weiner, B.R. *Chem. Phys. Lett.* **1991**, *178*, 150

19   Baulch, D.L.; Cobos, C.J.; Cox, R.A.; Esser, C.; Frank, P.; Just, T.; Kerr, J.A.; Pilling, M.J.; Troe, J.; Walker, R.W.; Warnatz, J. *J. Chem. Phys. Ref. Data* **1992**, *21*, 411

20   Beck, S.M.; Bendura, R.J.; McDougal, D.S.; Hoell, J.M.Jr.; Gregory, G.L.; Curfman, H.J.Jr.; Davis, D.D.; Bradshaw, J.; Rodgers, M.O.; Wang, C.C.; Davis, L.I.; Campbell, M.J.; Torres, A.L.; Carroll, M.A.; Ridley, B.A.; Sachse, G.W.; Hill, G.F.; Condon, E.P., Rasmussen, R.A. *J. Geophys. Res.* **1987**, *92* (D2), 1977-1985

21   Becker, K.H.; Geiger, H.; Weissen, P. *Chem. Phys. Lett.* **1991**, *184*, 256-261

22   Birnbaum, M. United States Patent 3,829,696 **1974**

23   Birnbaum, M. in "Modern Fluorescence Spectroscopy Vol. 1" Ed. Wehry, E.L. plenum Publishing Corp., New York, U.S.A. **1976**, 121-157

24   Bradshaw, J.D.; Rodgers, M.O.; Davis, D.D. *App. Opt.* **1984**, *23*, 2134-2145

25   Broomfield, M. D.Phil. Thesis; Department of Chemistry, University of York, U.K. **1992**

26   Buhr, M.P. MSc. Thesis; Faculty of Natural Sciences, University of Denver, USA, **1986**

27   Butler, J.D. "Air Pollution Chemistry" Academic Press, London, U.K. **1979**

28   Campbell, I.M.; Parkinson, P.E. *Chem. Phys. Lett.* **1978**, *53*, 385-387

29   Campbell, M.J.; Sheppard, J.C.; Au, B.F. *Geophys. Res. Lett.* **1979**, *6*, 175-178

30   Campbell, M.J.; Farmer, J.C.; Fitzner, C.A.; Henry, M.N.; Sheppard, J.C.; Hardy, R.J.; Hooper, J.F.; Muralidhar, V.J. *J. Atmos. Chem.* **1986**, *4*, 413-427

31   Canosa, C.; Penzhorn, R-D.; von Sonntag, C. *Ber. Bun. Phys. Chem.* **1979**, *83*, 217

32   Cantrell, C.A.; Stedman, D.H. *Geophys. Res. Lett.* **1982**, *9*, 846-849

33   Cantrell, C.A.; Stedman, D.H.; Wendel, G.J. *Anal. Chem.* **1984**, *56*, 1496-1502

34   Cantrell. C.A.; Lind, J.A.; Shetter, R.E.; Calvert, J.G.; Goldan, P.D.; Kuster, W.; Fehsenfeld, F.C.; Montzka, S.A.; Parrish, D.D.; Williams, E.J.; Buhr, M.P.; Westberg, H.H.; Allwine, G.; Martin, R. *J. Geophys. Res.* **1992**, *97* (D18), 20671-20686

35   Cantrell. C.A.; Shetter, R.E.; Lind, J.A.; McDaniel, A.H.; Calvert, J.G.; Parrish, D.D.; Fehsenfeld, F.C.; Buhr, M.P.; Trainer, M. *J. Geophys. Res.* **1993a**, *98* (D2), 2897-2909

36   Cantrell. C.A.; Shetter, R.E.; Calvert, J.G.; Parrish, D.D.; Fehsenfeld, F.C.; Goldan, P.D.; Kuster, W.; Williams, E.J.; Westberg, H.H.; Allwine, G.; Martin, R. *J. Geophys. Res.* **1993b**, *98* (D10), 18355-18366

37   Cantrell, C.A.; Shetter, R.E.; McDaniel, A.H.; Calvert, J.G. *Adv. Chem. Series* **1993**, *232*, 291-322

38   Chan, C.Y.; Hard, T.M.; Mehrabzadeh, A.A.; George, L.A.; O'Brien, R.J. *J. Geophys. Res.* **1990**, *95* (D11), 18569-18576

39   CRC Handbook of Chemistry and Physics *63rd Edition* Ed. R.C. Weast. CRC Press, Inc., Boca Raton, Florida, USA. **1982**

40   Cvetanovic, R.J. *J. Phys. Chem. Ref. Data* **1987**, *16*, 261

41   Dagaut, P.; Liu, R.; Wallington, T.J.; Kurylo, M.J. *J. Phys. Chem.* **1989**, *93*, 7838-7840

42   Davis, D.D.; Heaps, W.; McGee, T. *Geophys. Res. Lett.* **1976**, *3*, 331-333

43   Davis, D.D.; Rodgers, M.O.; Fischer, S.D.; Asai, K.; *Geophys. Res. Lett.* **1981**, *8*, 69-72

44   Demerjian, K.L.; Schere, K.L.; Peterson, J.T. *Adv. Environ. Sci. Technol.* **1980**, *10*, 369-459

45   De Zafra, R.L.; Parrish, A.; Soloman, P.M.; Barret, J.W. *J. Geophys. Res.* **1984**, *89*, 1321-1326

46   Dickerson, R.R.; Stedman, D.H.; Delany, A.C. *J. Geophys. Res.* **1982**, *87* (C7), 4933-4946

47   Drummond, J.W.; Castledine, C.; Green, J.; Denno, R. Mackay, G.I.; Schiff, H.I. *Monitoring Methods for Toxics in the Atmosphere, ASTM STP 1052* Zielinski, W.L.Jr. and Dorko, W.D. Eds. American Society for Testing and Materials, Philadelphia, U.S.A. **1990**, 133-149

48   Eisele, F.L.; Bradshaw, J.D. *Anal. Chem.* **1993**, *65* (21), 927A-933A

49   Eisele, F.L.; Tanner, D.J. *J. Geophys. Res.* **1991**, *96*, 9295-9308

50   Ehhalt, D.H. *Sci. of the Total Environ.* **1994**, *143*, 1-15

51   Ehhalt, D.H.; Dorn, H.-P.; Poppe, D. *Proc. R. Soc. of Edinburgh* **1991**, *97B*, 17-34

52   Feister, U. *J. Atmos. Chem.* **1994**, *19* (3), 289-315

53   Felton, C.C.; Sheppard, J.C.; Campbell, M.J. *Nature* **1988**, *335*, 53-55

54   Felton, C.C.; Sheppard, J.C.; Campbell, M.J. *Environ. Sci. Technol.* **1990**, *24*, 1841-1847

55   Felton, C.C.; Sheppard, J.C.; Campbell, M.J. *J. Atmos. Environ.* **1992**, *26A*, 2105-2109

56   Fincher, C.L.; Tucker, A.W.; Birnbaum, M. *Proc. Soc. Photo. Opt. Instrum. Eng.* **1978**, *158*, 137-140

57   Finlayson-Pitts, B.J.; Pitts, J.N.Jr. "Atmospheric Chemistry" John Wiley, Chichester, U.K. **1986**

58   Fujii, N.; Miyama, H.; Koshi, M.; Asoda, T. *Symp. Int. Combust. Proc.* **1981**, *18*, 873

59   Gardner, E.P.; Sperry, P.D.;Calvert, J.G. *J. Geophys. Res.* **1987**, *92* (D6), 6642-6652

60   Gelbwachs, J.A.; Birnbaum, M.; Tucker, A.W.; Fincher, C.L. *Optoelectronics* **1972**, *4*, 155-160

61   Ghim, B.T. MSc. Thesis; Faculty of Natural Sciences, University of Denver, USA, **1988**

62   Greenwood, N.N.; Earnshaw, A. "Chemistry of the Elements" **1986**, Pergammon Press, London, U.K.

63   Gutman, D.; Nelson, H.H. *J. Chem. Phys.* **1983**, *87*, 3902

64   Hard, T.M.; O'Brien, R.J.; Chan, C.Y.; Mehrabzadeh, A.A. *Environ. Sci. Technol.* **1984**, *18*, 768-777

65   Hard, T.M.; Chan, C.Y.; Mehrabzadeh, A.A.; Pan, W.H.; O'Brien, R.J. *Nature* **1986**, *322*, 617-620

66   Hard, T.M.; Chan, C.Y.; Mehrabzadeh, A.A.; O'Brien, R.J. *App. Opt.* **1989**, *28* (1), 26-27

67   Hard, T.M.; Chan, C.Y.; Mehrabzadeh, A.A.; O'Brien, R.J. *J. Geophys. Res.* **1992a**, *97* (D9), 9785-9794

68   Hard, T.M.; Mehrabzadeh, A.A.; Chan, C.Y.; O'Brien, R.J. *J. Geophys. Res.* **1992b**, *97* (D9), 9795-9817

69   Harvey, R.B.; Stedman, D.H.; Chameides, W. *J. Air Pollut. Control Assoc.* **1977**, *27*, 663-666

70   Hastie, D.R.; Weissenmayer, M.; Burrows, J.P.; Harris, G.W. *Anal. Chem.* **1991**, *63*, 2048-2057

71   Hatakeyama, S.; Akimoto, H.; Washida, N. *Environ. Sci. Technol.* **1991**, *25*, 1884

72   Hatakeyama, S.; Honda, S.; Washida, N.; Akimoto, H. *Bull. Chem. Soc. Japan* **1985**, *58*, 2157-2162

73   Helton, M.; Pätz, W.; Trainer, M.; Fark, H.; Klein, E.; Ehhalt, D.H. *J. Atmos. Chem.* **1984**, *2*, 191-202

74   Herbrectsmeier, P.; Wagner, H.G. *Berbunsenges. Phys. Chem.* **1975**, 673-675

75   Herzberg, G. *Electronic Structure and Electronic Spectra of Polyatomic Molecules* Van Nostrand, Princeton, New Jersey, **1967**

76   Hoell J.M. (ed.) *NASA Conference Publication 2332*, **1984**

77   Hofzumahaus, A.; Dorn, H-P.; Callies, J.; Platt, U.; Ehhalt, D.H. *Atmos. Environ.* **1991**, *25A* (9), 2017-2022

78   Hübler, G.; Perner, D.; Platt, U.; Tonnissen, A.; Ehhalt, D.H. *J. Geophys. Res.* **1984**, *89*, 1309-1319

79   Houghton, J.T.; Callander, B.A.; Varney, S.K. (Eds.) "Climate Change 1992: The Supplementary Report to the IPCC Scientific Assessment" Cambridge University Press, Cambridge, U.K. **1992**

80   Hu, J.; Stedman, D.H. *Anal. Chem.* **1994**, *66* (20), 3384-3393

81   Ishikawa, Y.; Sugawara, K.; Sato, S. *Bull. Chem. Soc. Jpn.* **1979**, *52*, 3503

82   Jackson, J.O.; Stedman, D.H.; Smith, R.G.; Heckler, L.H.; Warner, P.O. *Rev. Sci. Instrum.* **1975**, *46* (4), 376

83   Jodkowski , J.T.; Ratajczak, E.; Sillesen, A.; Pagsberg, P. *Chem. Phys. Lett.* **1993** *203*, 490

84   Johnston, H.S., McGraw, S.E.; Paukert, T.T.; Richards, L.W.; van der Bogaerde, J. *Proc. Nat. Acad. Sci. (U.S.)* **1967**, *57*, 1146-1153

85   Jones, I.T.N.; Bayes, K.D. *J. Chem. Phys.* **1973**, *59* (9), 4836-4844

86   Jones, J.L.; Miksad, R.W.; Laird, A.R.; Middleton, P. *J. Air Pollut. Control Assoc.* **1981**, *31* (1), 42-45

87   Junkermann, W.; Platt, U.; Volz-Thomas, A. *J. Atmos. Chem.* **1989**, *8*, 203-227

88   Kanakidou, M.; Singh, H.B.; Valentin, K.M.; Crutzen, P.J. *J. Geophys. Res.* **1991**, *96*, 15,395-15,413

89   Kofend, J.B.; Holloway, J.S.; Kwok, M.A.; Heidner, R.F. *J. Quant. Spectrosc. Radiat. Transfer* **1987**, *37*, 449

90   Langford, A.O. and Moore, C.B. *J. Chem. Phys.* **1984**, *80*, 4211-4221

91   Lawes, S.T. D.Phil Thesis; Department of Electronics, University of York, U.K. **1994**

92   Lawes, S.T.; Elphick, J.R.; Clarke, T. *Syst. Eng. for Real-time Applications* **1993**, *Sept.* 13-14

93   Lee, E.K.C.; Uselman, W.M. *Farad. Discuss. Chem. Soc.* **1972**, *53*, 125-131

94   Leroy, B.; Rigaud, P.; Hicks, E. *Annales Geophysicae* **1987**, *5A*, 247

95   Lightfoot, P.D.; Cox, R.A.; Crowley, J.N.; Destriau, M.; Hayman, G.D.; Jenkin, M.E.; Moortgat, G.K.; Zabel, F. *Atmos. Environ.* **1992** 26A (10), 1805-1961

96   Lippmann, M. *Environ. Sci. Technol.* **1991**, *25* (12), 1954-1962

97   Lorenz, K.; Rhasa, D.; Zellner, R. Fritz, B. *Ber. Bunsenges. Phys. Chem.* **1985**,*89*, 341

98   Lu, Y.; Khalil, M.A.K. *Chemosphere* **1991** 23 (3), 397-444

99   Madronich, S.; Hastie, D.R.; Ridley, B.A.; Schiff, H.I. *J. Atmos. Chem.* **1984**, *1*, 3-25

100   Madronich, S. *Atmos. Environ.* **1987** 21 (3), 569-578

101   Maeda, Y.; Aoki, K.; Munemori, M. *Anal. Chem.* **1980**, *52*, 307-331

102 Manahan, S.E. "Environmental Chemistry" 5th Edition. Lewis Publishers Inc., Michigan, U.S.A. **1991**

103 Madronich, S. *J. Geophys. Res.* **1987**, *92* (D8), 9740-9752

104 McKeen, S.A.; Trainer, M.; Hsie, E.Y.; Tallamraju, R.K.; Liu, S.C. *J. Geophys. Res.* **1990**, *95* (D6), 7493-7500

105 Meier, U.; Grotheer, H.H.; Riekert, G.; Just, T. *Ber. Bun. Phys. Chem.* **1985**, *89*, 325-327

106 Mihelcic, D.; Ehhalt, D.H.; Kulessa, G.F.; Klomfass, J.; Trainer, M.; Schmidt, U.; Rohrs, H. *Pure. Appl. Geophys.* **1978a**, *116*, 530-542

107 Mihelcic, D.; Ehhalt, D.H.; Klomfass, J.; Kulessa, G.F.; Schmidt, U.; Trainer, M. *Ber. Bunsenges. Phys. Chem.* **1978b**, *82*, 16-19

108 Mihelcic, D.; Klemp, D.; Musgen, P.; Pätz, H.W.; Volz-Thomas, A. *J. Atmos. Chem.* **1993**, *16* (4), 313-335

109 Mihelcic, D.; Musgen, P.; Ehhalt, D.H. *J. Atmos. Chem.* **1985**, *3*, 341-361

110 Mihelcic, D.; Volz-Thomas, A.; Pätz, H.W.; Kley, D.; Mihelcic, M. *J. Atmos. Chem.* **1990**, *11*, 271-297

111 Miyoshi, A.; Matsui, H.; Washida, N.; *Chem. Phys. Lett.* **1989a**, *160*, 291-294

112 Miyoshi, A.; Matsui, H.; Washida, N. *J. Phys. Chem.* **1989b**, *93*, 5813-3019

113 Miyoshi, A.; Matsui, H.; Washida, N. *J. Phys. Chem.* **1990**, *94*, 3016-3019

114 Möller, D.; Mauersberger, G. *J. Atmos. Chem.* **1992**, *14*, 153-165

115 Mount, G.H. *J. Geophys. Res.* **1992**, *97* (D2), 2427-2444

116 Mount, G.H.; Eisele, F.L. *Science* **1992**, *256*, 1187-1190

117 Mugnai, A.; Petroncelli, P.; Fiocca, G. *J. Atmos. Terr. Phys.* **1979**, *41*, 351-359

118 Nadtochenko, V.A.; Sarkisov, O.M.; Suividenkov W.A.; Ceskis, J. *Kinet. Catal.* **1980**, *21*, 520

119 Nelson, L.; Rattigan, O.; Neavyn, R.; Sidebottom, H. *Int. J. Chem. Kinet.* **1990**, *22*, 1111

120   Nesbitt, F.L.; Payne, W.A., Steif, L.J. *J. Phys. Chem.* **1988**, *92*, 4030-4032

121   Nesbitt, F.L.; Payne, W.A.; Steif, L.J. *J.Phys. Chem.* **1989**, *93*, 5158

122   Niki, H.; Mater, P.D.; Savage, C.M.; Breitenvach, L.P. *Int. J. Chem. Kinet.* **1985**, *17*, 547-558

123   O'Brien, R.J.; George, L.A. *Am. Chem. Soc. Symp. Series* **1992** *483*, 64-116

124   Ortgies, G.; Comes, F.J. *Appl. Phys. B Photophys. and Laser Chem.* **1984**, *33* (2), 103-113

125   Osif, T.L. and Heicklen, J. *J. Phys. Chem.* **1976**, *80*, 1526-1531

126   Pagsberg, P.; Monk, J.; Anastasi, C.; Simpson, V.J. *J. Phys. Chem.* **1989**, *93*, 5162-5165

127   Park, J.Y.; Gutman, D. *J. Phys. Chem.* **1983**, *87*, 1844

128   Parkes, D.A.; Paul, D.M.; Quinn, C.P. *J. Chem. Soc. Farad. Trans. I* **1976**, *72*, 1935-1951

129   Parrish, D.D.; Murphy, P.C.; Albritton, D.L.; Fehsenfeld, F.C. *Atmos. Environ.* **1983**, *17* (7), 1365-1379

130   Paukert, T.T.; Johnston, H.S. *J. Chem. Phys.* **1974**, *56*, 2824

131   Perner, D.; Ehhalt, D.H.; Paetz, H.W.; Platt, U.; Roth, E.P.; Volz, A *Geophys. Res. Lett.* **1976**, *3*, 446-468

132   Perner, D.; Platt, U.; Trainer, M.; Hübler, G.; Drummond, J.; Junkermann, W.; Rudolph, J.; Schubert, B.; Volz, A.; Ehhalt, D.H. *J. Atmos. Chem.* **1987**, *5*, 185-216

133   Pilling, M.J.; Lightfoot, P.D. *J. Phys. Chem.* **1987**, *91*, 3373

134   Peterson, J.T. *Atmos. Environ.* **1977**, *11*, 689-695

135   Platt, U. *Fresnius J. Anal. Chem.* **1991**, *340* (10), 633-637

136   Platt, U.; Hausmann, M. *Res. Chem. Intermed.* **1994**, *20* (3-5), 557-578

137   Platt, U.; Rateike, M.; Junkermann, W.; Rudolph, J.; Ehhalt, D.H. *J. Geophys. Res.* **1988**, *93* (D5), 5159-5166

138   Poppe, D.; Wallasch, M.; Zimmermann, J.; Dorn, H.P.; Ehhalt, D.H. *Ber. Bunsenges. Phys. Chem.* **1992**, *96* (3), 286-290

139   Poppe, D.; Zimmermann, J.;Bauer, R.; Brauers, T.; Bruning, D.; Callies, J.; Dorn, H.P.; Hofzumahaus, A.; Johnen, F.J.; Khedim, A.; Koch, H.; Koppmann, R.; London, H.; Muller, K.P.; Neuroth, R.; Plassdulmer, C.; Platt, U.; Rohrer, F.; Roth, E.P.; Rudolph, J.; Schmidt, U.; Wallasch, M.; Ehhalt, D.H. *J. Geophys. Res.* **1994**, *99* (D8), 16633-16642

140   Pratt, G.; Veltmann, I. *J. Chem. Soc Farad. Trans.* **1974**, *70*, 1840

141   Prinn, R.G. *Geophys. Res. Lett.* **1985**, *12*, 597

142   Prinn, R.G.; Cunnold, D.; Rasmussen, R. *Science* **1987** *238*, 945

143   Prothero, A. Report TRCP.1657(a), Shell Research Ltd., Thornton Research Centre, Chester, U.K. **1970**

144   Rodgers, M.O.; Bradshaw, J.D.; Sandholm, S.T.; KeSheng, S.; Davis, D.D. *J. Geophys. Res.* **1985**, *90* (D7), 12819-12834

145   Rasmussen, O.L.; Bjergbakke, E. Report Risø-R-395, Chemical Reactivity Section, Risø National Laboratory, Denmark **1984**

146   Sackett, P.B.; Yardley, J.T. *Chem. Phys. Lett.* **1970**, *6* (4), 323-325

147   Sanderson, M.G. D.Phil. Thesis; Department of Chemistry, University of York, U.K. **1994**

148   Schneider, W.; Moortgat, G.K.; Tyndall, G.S.; Burrows, J.P. *J. Photochem. Photobiol.* **1987**, *A40*, 195

149   Schwartz, S.E.; Johnston, H.S. *J. Chem. Phys.* **1969**, *51* (4), 1286-1302

150   Semenov, N.N. "Some Problems of Chemical Kinetics and Reactivity Vol.2" Pergamon Press, London, UK. **1959**

160   Sickles, J.E.II; Ripperton, L.A.; Eaton, W.C.; Wright, R.S. Contract 68-02-2258 Report, United States Environment Protection Agency **1977**

161   Singleton, D.L.; Parastevopoulos, G.; Irwin, R.S. *J. Am. Chem. Soc.* **1989**, *111*, 5248-5251

162   Singleton, D.L.; Parastevopoulos, G.; Irwin, R.S.; Jolly, G.S.; McKenny, D.L. *J. Am. Chem. Soc.* **1988**, *110*, 7786-7790

163   Shetter, R.E.; McDaniel, A.H.; Cantrell, C.A.; Madronich, S.; Calvert, J.G. *J. Geophys. Res.* **1992**, *97* (D10) 10349-10359

164   Shirinzadeh, B.; Wang, C.C.; Deng, D.Q. *App. Opt.* **1987**, *26* (11), 2102-2105

165   Smith, G.P.; Crosley, D.R. *J. Geophys. Res.* **1990**, *95* (D10), 16427-16442

166   Stedman, D.H.; Chameides, W.; Jackson, J.O. *Geophys. Res. Lett.* **1975**, *2* (1), 22-25

167   Stokes, N.J.; Tabner, B.J.; Hewitt, C.N. *Chemosphere* **1994**, *28* (5), 999-1008

168   Spinherne, J.D.; Green, A.E.S. *Atmos. Environ.* **1978**, *12*, 2449-2454

169   Temps, F. and Wagner, H.G. *Ber. Bun. Phys. Chem.* **1984a**, *88*, 410-414

170   Timonen, R.S.; Ratajazak, E.; Gutman, D. *J. Phys. Chem.* **1988**, *92*, 651-655

171   Turco, R.P. *Geophys. Surv.* **1975**, *2*, 153-192

172   Tucker, A.W.; Peterson, A.B.; Birnbaum, M. *App. Opt.* **1973**, *12* (9), 2036-2038

173   Tucker, A.W.; Birnbaum, M.; Fincher, C.L. *Proc. Soc. Photo. Opt. Instrum. Eng.* **1974**, *49*, 103-109

175   Tucker, A.W.; Birnbaum, M.; Fincher, C.L. *App. Opt.* **1975**, *14* (6), 1418-1422

176   Tucker, A.W.; Birnbaum, M. United Startes Environmental Protection Agency Report EPA-650/2-74-059 **1974**

177   Tzŭ, Sun "The Art of War" Ed. Clavell, J.Hodder and Stoughton, London, U.K. **1990**

178   Umstead, M.E.; Lin, M.C. *Chem. Phys.* **1977**, *25*, 353

179   Veyret, B. and Lesclaux, R. *J. Phys. Chem.* **1981**, *85*, 1918-1922

180   Veyret, B.; Rajex, J-C.; Lesclaux, R. *J. Phys. Chem.* **1982**, *86*, 3424-3430

181   Vipond, A. Undergraduate Research Report, Department of Chemistry, University of York, U.K. **1994**

182   Wallington, T.J.; Adino, J.M.; Skewes, L.M.; Siegel, W.O.; Japar, S.M. *Int. J. Chem. Kinet.* **1989**, *21*, 993-1001

183   Wallington, T.J.; Dagaut, P.; Liu, R.; Kurylo, M.J. *Int. J. Chem. Kinet.* **1988**, *20*, 177

184   Wallington, T.J.; Dagaut, P.; Liu, R.; Kurylo, M.J. *Environ. Sci. Technol.* **1988a**, 22, 842-844

185   Wallington, T.J.; Liu, R.; Dagaut, P.; Kurylo, M.J. *Int. J. Chem. Kinet.* **1988b**, *20*, 41

186   Wang, C.C.; Davis, L.I.Jr. *Geophys. Res. Lett.* **1982** *9* (1) 98-100

187   Wang, C.C.; Davis, L.I.Jr.; Wu, C.H.; Japar, S.; Niki, H.; Weinstock, B. *Science* **1975**, *189*, 797-800

188   Wang, C.C.; Davis, L.I.Jr.; Selzer, D.M.; Munoz, R. *J. Geophys. Res.* **1981**, *86* (C2), 1181-1186

189   Watanabe, T.; Yoshida, M.; Fujiwara, S.; Abe, K.; Onoe, A.; Horota, M.; Igarashi, S. *Anal. Chem.* **1982**, *54*, 2470-2474

190   Wategaonkar, S.J.; Setser, D.W. *J. Chem. Phys.* **1989**, *90*, 251

191   Waterson, B. "The Days Are Just Packed" Warner Books, London, U.K. **1993**

192   Wayne, R.P. "Chemistry of Atmospheres" 2nd Edition, Oxford University Press, Oxford, U.K. **1991**

193   Wayne, W.A. *Int. J. Chem. Kinet.* **1988**, *20*, 63

194   Wennberg, P.O.; Cohen, R.C.; Hazen, N.L.; Lapson, L.B.; Allen, N.T.; Hanisco, T.F.; Oliver, J.F.; Lanham, L.W.; Demusz, J.N.; Anderson, J.G. *Rev. Sci. Instrum.* **1994**, *65* (6), 1858-1876

195   Wendel, G.J.; Stedman, D.H.; Cantrell, C.A.; Demrauer, L. *Anal. Chem.* **1983**, *55*, 937-940

196   WMO "Scientific Assessment of Ozone Depletion: 1991" World Meteorological Organisation Global Ozone Research and Monitoring Project - Report No.25 **1991**

197   Yamada, F.; Slagle, I.R.; Gutman, D. *Chem. Phys. Lett.* **1981**, *83*, 409

198   Zafonte,L.; Rieger, P.L.; Holmes, J.R. *Environ. Sci. Technol.* **1977**, *11*, 483-487

199   Zellner, R.; Hägele, J. *Opt. and Laser Technol.* **1985**, *17* (2), 79-82